Sb Doped CuMnAs for Antiferromagnetic Spintronics

Luke Xavier Barton, BSc.

School of Physics and Astronomy
University of Nottingham

This dissertation is submitted for the degree of
Doctor of Philosophy

October 2023

Acknowledgements

The effort and guidance of a host of people surrounding me is bound within these pages, foremost of all my supervisors Andrew Rushforth and Richard Campion. Richard has been an unmatched tutor in MBE and an ever ready source of friendly chat. Andy's judgement and considerate oversight have been invaluable, regularly bringing back my focus and bearing when set adrift. Peter Wadley for his instructive advice and Kevin Edmonds for reliably objective consultation, thank you both. Also to Mu Wang for imparting on me what skill I have obtained in an experimental laboratory.

To the denizens of C26, thanks for years of laughs and, periodically, the motivation to come in when the results pushed me away. Special mention has to go to: Sonka who was settled in the office when I joined and had already set the bar exceedingly high; Ollie, the most annoying member of the office but just enough fun to keep around; Stu, who can't help but solve your problems for you and the last member to join, Sam, who we endeavoured to impress our chickpea eating ways upon to no avail. My appreciation also to past members Debi, Mohammed and Syamashree.

On a near daily basis I benefitted from the help and expertise of the school's technical staff of whom there are more than I can adequately thank by name here. However, I would be remiss to not express my gratitude to Andy Solomon, Jas Chauhan and Matt Wooley.

For welcoming me into your lab and facilitating what evolved into a significant undertaking thank you to Kelly Morrison, Guru Venkat and Chris Cox at Loughborough University. Also to Mike Weir and Oleg Makarovskiy for your time in my final weeks in Nottingham, pulling out the stops to see that I complete my work.

To my family, Mum, Dad and Dominic, thank you for your constant belief and refreshing distraction. Finally, saving the best and most indebted to last, thank you, Erica. I would not be where I am today without your unwavering love and support that I wish only to express in kind to you.

Abstract

Enhancement of conventional electronic logic devices has been achieved with the consideration of electron spin, predominantly in ferromagnetic (FM) materials, for more than a decade. In computation and logic devices antiferromagnet (AF) materials have been a more recent hot topic after demonstrating the writing and reading of information with electrical current pulses on thin films of single crystal collinear AF CuMnAs. Desirable for their robust resistance to external fields, terahertz dynamics and lack of stray field, AFs have opened up new avenues for efficient spintronic devices.

In search of high quality, easily synthesised single crystal AF material and greater understanding of the spintronic variables accessible through manipulation of material properties thin film CuMnAs layers were grown via molecular beam epitaxy with an additional Sb doping flux. Producing $\mathrm{CuMnAs}_{1-\alpha}\mathrm{Sb}_{\alpha}$ layers on GaAs at three levels of Sb flux the dopant was successfully incorporated into the tetragonal structure of CuMnAs with the preservation of crystal quality at lower fluxes. FM secondary phase growth was a ubiquitous issue amongst the layers and impacted the surface quality. Evidence of the magnetic phase transition from AF order to a paramagnetic material occurring at a lower temperature with Sb doping flux was found. Polarised X-ray microscopy revealed larger AF domains than observed in CuMnAs layers on the same substrate without Sb but was not yet able to match the highest quality CuMnAs. Recent trends in the electrical writing pulse replicated in the layers but significant improvement in the writing and reading of information was not achieved.

As magnetic materials have been investigated for their use in efficient next generation logical processing so they have also found potential use in improving efficiency through waste thermal energy recovery. Methods in characterising the efficiency of FM conductors for these applications have been applied to $\mathrm{Fe}_{0.79}\mathrm{Ga}_{0.21}$ thin films with a comparison to Fe, both capped with non-magnetic metals during sputter deposition. $\mathrm{Fe}_{0.79}\mathrm{Ga}_{0.21}$ holds promise for efficient thermal energy recovery by harnessing an established large anomalous Nernst effect and complimentary longitudinal spin Seebeck effect. While spin caloritronics measurements confirmed that $Fe_{0.79}Ga_{0.21}$ poses a significant improvement over Fe in waste thermal energy recovery the characterisation approach was found to be flawed. Anomalous peaks observed in the in-plane voltage of Fe samples during in-plane magnetic field sweeps are determined to be an artefact of magnetisation reversal within the thin film layer.

List of Publications

The following poster relates to Chapter 3 of this thesis:

L. X. Barton, V. A. Hills, K. Edmonds, A. W. Rushforth, P. Wadley, R. P. Campion, B. Gallagher "Group V Doped Antiferromagnetic CuMnAs", *Joint European Magnetic Symposia*, Aug 2019

Other publications the author has contributed to:

S. Reimers, D. Kriegner, O. Gomonay, D. Carbone, F. Krizek, V. Novak, R. P. Campion, F. Maccherozzi, A. Bjorling, O. J. Amin, L. X. Barton, S. F. Poole, K. A. Omari, J. Michalicka, O. Man, J. Sinova, T. Jungwirth, P. Wadley, S. S. Dhesi, K. W. Edmonds, "Defect-driven antiferromagnetic domain walls in CuMnAs films", *Nat Commun* 13, 724, Feb 2022

K. A. Omari, L. X. Barton, O. J. Amin, R. P. Campion, A. W. Rushforth, A. J. Kent, P. Wadley, K. W. Edmonds, "Low-energy switching of antiferromagnetic CuMnAs/GaP using sub-10 nanosecond current pulses", *Journal of Applied Physics*, 127 (19), May 2020

S. F. Poole, L. X. Barton, M. Wang, P. Manuel, D. Khalyavin, S. Langridge, K. W. Edmonds, R. P. Campion, V. Novák, P. Wadley, "Probing the manipulation of antiferromagnetic order in CuMnAs films using neutron diffraction", *Appl. Phys. Lett.*, 121 (5), Aug 2022

Table of contents

List of figures

List of tables

Chapter 1

Introduction

1.1 Background

1.1.1 Antiferromagnetic Spintronics

Spintronics is the realm of solid state physics that extends manipulation of electrons beyond their charge into additionally harnessing electron spin. In 1856 William Thomson discovered the dependence of resistance in a ferromagnet on the magnetisation direction now known as magnetoresistance, the nascent beginnings of understanding of the role of magnetism and spin in conductors.[1] Spin dependent conduction of electrons in transition metal ferromagnets (FM) were treated with Nevill Mott's description of two distinct currents dependent on spin and bias in the conductivity between them based on available states and scattering events. [2]

Spintronics took off in earnest in 1988 with the discovery of giant magnetoresistance (GMR) in a FM sandwich device. Significant changes in resistance for a charge current with the realignment of magnetisation in the FM layers between parallel or antiparallel layers compose the first efficient spin valve.[3, 4] This advancement quickly found a commercial home in magnetic recording, allowing smaller read heads and ever denser FM bits on hard drive disks.[5]

The field grew expansively, benefitting from improvements in deposition technology and device fabrication. Magnetic tunnel junctions (MTJs) comprising FM-insulator-FM sandwiches were developed, in which electrons tunnel through the insulator spacer whilst preserving spin under a highly discriminatory selection conditions that achieved magnetoresistances of several hundred % at room temperature.[6, 7] The GMR sandwich architecture of spin valves and MTJs is depicted in fig. 1.1 where a current passing through the contacts can be used to both orient the FM and read the magnetoresistance. Magnetic tunnel junctions became the key to realise magnetic random access memory (MRAM), FM solid state memory controlled by induced fields from charge currents to reorient a FM layer and read the state by probing the magnetoresistance along the same channel.[8] Favoured for its low volatility, resistance to fatigue and nanosecond dynamics this technology evolved over the course of a decade, reducing in scale to a few nm but demanding ever higher current densities to induce a local field.[5]

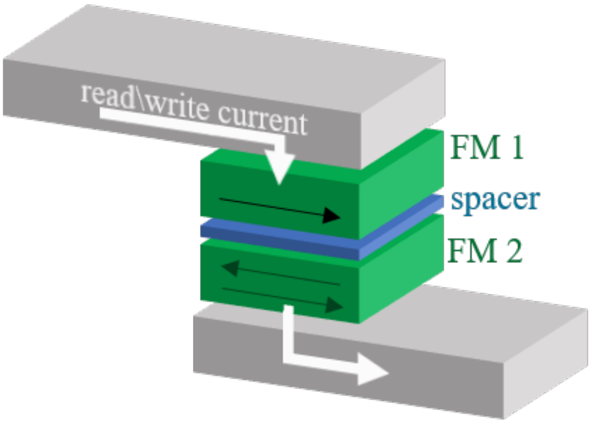

Fig. 1.1 A basic GMR based architecture consisting of FM1 and FM2 seperated by a spacer, such as a non-FM metal for a spin valve or non-FM insulator in the case of a MTJ. The application of a current can reorient one of the layers whether by a nearby induced field or via a current based spin torque. The large difference in resistance of a probe current through the device in parallel or antiparallel configuration provides a clear read out.

The introduction of spin transfer torque reduced the current load needed to write a spin valve or MTJ. Passing a current through a hard FM into a soft FM through an ultrathin spacer the hard magnet acts as a spin polariser transferring spin, experienced as a torque on the magnetisation, to align the soft FM layer parallel with the hard. To reverse the soft layer to the antiparallel configuration charge current is passed from the soft to hard layer, injecting an effective spin moment with opposite magnetisation back into the soft layer.[9] While an improvement, the current densities required were still a limiting factor on their uptake thanks to significant waste heat and damage to the spacer layer.

In the last decade another mechanism of electrical FM bit control emerged. Spin polarised currents originating from normal metals where the charge current's electron spins are strongly coupled with atomic fields and can be used to generate the torque with some efficiency.[10, 11] These spin orbit torques opened up yet more methods to control FM spintronic devices but their potential goes much further, crossing into another class of magnetic materials, antiferromagnets (AFs) that now occupy their own branch of spintronics.[12]

While AFs have played a passive role in FM spintronic devices they offer a host of advantages as active components of logic devices over FMs including no stray magnetic field, robust resistance to external fields and terahertz dynamics. Recently analogous spin orbit torque mechanisms, intrinsic to certain AFs and able to change the AF order were theorised and demonstrated experimentally. Along with an electrical read out of a change in magnetoresistance, the control of FM MTJs can be matched by electrical control of AFs.[13, 14]

This operation, as first reported,[14] employs millisecond pulses of charge current of the order of a few MAcm^{-2}, a fraction of the early MTJ spin transfer currents of 100MAcm^{-2}. When the current pulse is parallel to the AF ordered moments it becomes locally spin polarised by the same conditions as in other spin orbit torques, reorienting the magnetic order parameter by 90°. Orthogonal switching pulses are able to do this reversibly in a sample four terminal device, as schematically illustrated in fig. 1.2.

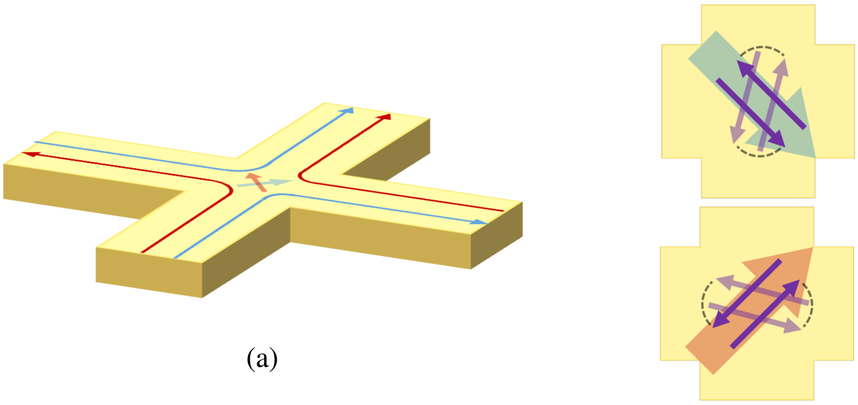

(a)

(b)

Fig. 1.2 (a) A simple AF electrical switching device. Current pulses are applied with a net current direction diagonal to the arms of the 4 terminal device, parallel to the easy axes that AF moments lie along. (b) Orthogonal current pulses (blue and red arrows) reversibly reorient the AF moments by 90° and the change can be read out as a transverse magnetoresistance with a probe along the arms.

The first material to demonstrate this was the AF CuMnAs, which possesses antiparallel alignment of spins along a common axis. Single crystal thin films of this tetragonal semimetal have been grown epitaxially on GaAs substrates, which has a lattice mismatch of 4.3%. However, GaP has a lattice mismatch of just 0.7% with CuMnAs leading to higher quality material that is discernible in both crystallography [15, 16] and in AF properties from X-ray domain imaging [17]. While the material was in high demand, the expense and scarcity of high quality single crystal GaP substrates for growth motivated the improvement of growth on cheaper and widely available GaAs substrates.

In pursuit of high quality GaAs/CuMnAs samples akin to those resulting from growth on a GaP substrate, a method was formulated drawing on group V doping of CuMnAs and the FM semiconductor GaMnAs. With the partial substitution of As in CuMnAs with P, grown on GaP, the out of plane lattice parameter of $\text{CuMnAs}_{1-x}\text{P}_x$ was reduced. This reduction is associated with a tensile strain on the lattice in plane. [15] Sb was successfully incorporated into GaMnAs to create $\text{GaMnAs}_{0.9}\text{Sb}_{0.1}$ in order to enhance the spin orbit coupling. In this case the crystalline anisotropic magnetoresistance (AMR) was enhanced with 10% Sb and the temperature dependence of AMR coefficients was revealed to be dominated by the magnetisation magnitude of the layer.[18][19] In this study[18] growth of CuMnAs doped with Sb was investigated for the potential of well matched in plane lattice parameter of $\text{CuMnAs}_{1-\alpha}\text{Sb}_\alpha$ on GaAs. Characterisation of the material and examination of AF properties in comparison with CuMnAs were carried out to assess the effect of Sb doping and candidacy of material for AF spintronics research.

1.1.2 Spin Caloritronics

Spin caloritronics is concerned with the intersection of spintronics and thermoelectric physics. Chief among problems the field seeks to address is the wasteful Ohmic heating that plagues modern commercial logic devices built from transistors constrained by Moore's law. Thermoelectric energy harvesting can benefit from the supplementation of electron transport with that of electron spin. Interest extends to the inverse case: efficient generation of spin current for spintronics by thermal means.[20]

Curiosity in thermoelectric effects goes back to at least the 18th century before codification of the Peltier and Seebeck effects in terms of thermodynamics by W. Thomson in 1851. Thermoelectric devices based around metals emerged at the turn of the 20th century but were undesirable for their poor efficiency, at the time being compared to a zero entropy Carnot cycle. The search for efficient thermoelectric generators prized large Seebeck coefficients, high electrical conductivity and low thermal conductivity. Semiconductors and semimetals emerged as the best candidates in the middle of the century with Peltier devices finding widespread practical appeal. However, the Wiedermann-Franz law states that in metallic conductors the ratio of the thermal and electrical conductivities is proportional to the temperature and related by a constant, the Lorenz number.[21] As a result, technologies remained limited until attention was directed at other modes of energy conversion such as spin to aid in the conversion of energy, giving rise to spin calitronics.[22]

With the first experimental demonstration of the inverse spin Hall effect (ISHE) in Pt, spin current detection became far more accessible. [23] This was quickly taken up with the experimental discovery of the spin Seebeck effect (SSE) by Uchida et al., the generation of a pure spin current perpendicular to an in plane thermal gradient and non-zero net magnetisation. [24] The NiFe/Pt bilayer (comprising the FM and non-magnetic metal (NM) spin current detector) in the first observation of the SSE was itself a spin mediated thermoelectric generator as well as delivering long range pure spin current pumping. Careful arrangement of the thermal gradient and spin polarisation in a transverse configuration excluded ordinary thermoelectric effects, with any doubt as to the pure spin current mechanism later addressed by replication using the FM insulator $LaY_2Fe_5O_{12}$ [25]. The SSE presented a paradigm shift for thermoelectric generators and exploration of the effect flourished, particularly with the development into a stacked geometry that exploited the longitudinal spin Seebeck effect (LSSE). In this configuration the simple inclusion of a FM/NM bilayer thin film over a thermally lossy surface was well suited to waste energy recovery from the nanoscale architecture of modern logic devices.[26, 27] A simple LSSE energy harvesting device is depicted schematically in fig. 1.3.

After demonstration in YIG, the research field was dominated by investigation of magnetic insulators with metallic spin Hall conversion layers. Magnetic conductors were less favourable for research due to the complication presented by other thermally motivated magnetoelectric phenomena such as the magneto-Seebeck effect and the anomalous Nernst effect. Novel approaches would be required for conducting FMs. Potential benefits of conducting FMs lay in the enhancement of the recovered charge current from complementary thermoelectric and spin Seebeck effects.

Determination of spin Seebeck coefficients and the anomalous Nernst effect (ANE) contribution has been approached by various means: measurements either side of a temperature dependent conducting regime [28], suppression of

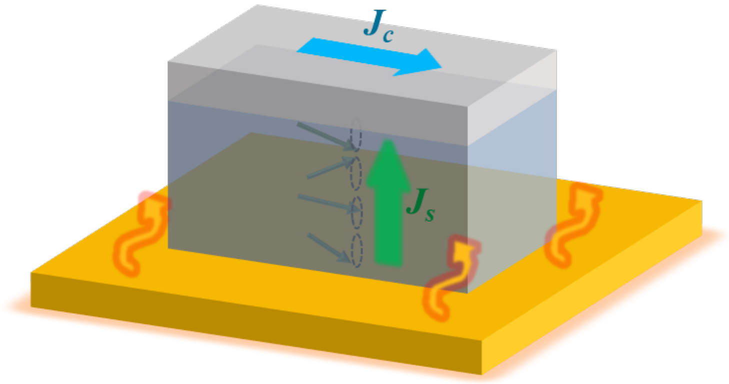

Fig. 1.3 A simple schematic of how a LSSE device might convert waste thermal energy from a surface into recovered electrical energy J_c via the spin Seebeck effect's pure spin current J_s.

spin currents and electron transport via reduced dimensionality [29], compound multilayer devices [30, 31] and via purely analytical methods in terms of electron transport arguments [32]. Reports of the latter promised feasible assessment of almost any FM metal in an LSSE setup. The method treats the two layers as parallel resistors with the anomalous Nernst effect response occurring in the magnetic layer and the spin Seebeck effect in the cap. This approach was key to the inception of the following work.

Motivation for the study of $\mathrm{Fe_{0.79}Ga_{0.21}}$, a FM alloy also referred to as galfenol, was based on the large ANE compared to elemental Fe owing to tuning of the Fermi surface with Ga substitution as shown by other groups immediately prior to the beginning of the study.[33, 34] The reports left an open question surrounding simultaneously harnessing the SSE and ANE kindling interest in combining the two for enhanced thermal recovery. The respective magnitudes of each effect might be determined using the parallel resistor method.

FeGa has enjoyed success in previous work within the group focused on the relation between magnetisation control and strain due to the material's large magnetoelastic coupling.[35–37] With Ga substitution, the Fe lattice is disrupted, giving rise to two structures within the material that couple the magnetisation to strains in the lattice. The magnetostriction is at its highest at 19% and 28% Ga, varying with Ga content as depicted in fig. 1.4[38]. The peak at 19% is attributed to either anisotropic ordering of Ga along the $\langle 100 \rangle$ directions of Fe BCC lattice or the formation of Ga clusters within the Fe lattice inducing local strain and giving rise to magnetostriction.[36, 39, 40]

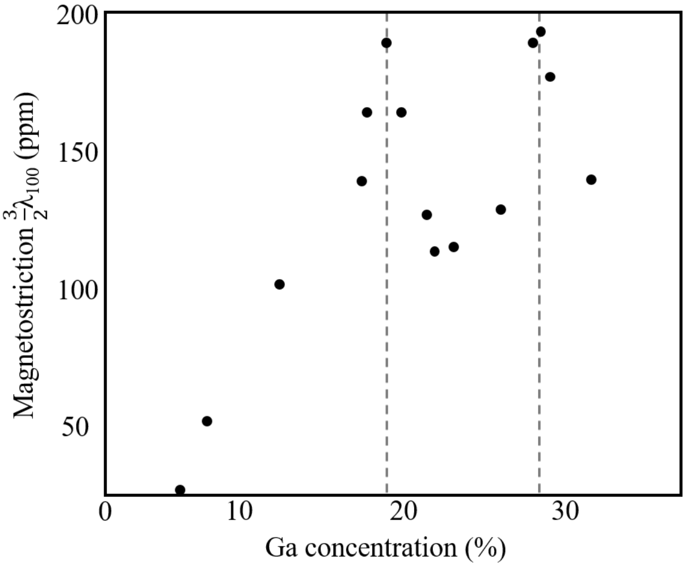

Fig. 1.4 Magnetostriction coefficient $\frac{3}{2}\lambda_{100}$, the fractional change in length with the application of a magnetic field along the [100] direction, with the incorporation of Ga into a Fe lattice. This sketch is adapted from work on "slow cooled" bulk FeGa by Clarke et al.[38]

Reports of other materials with high magnetoelastic coupling professed enhancement of spin caloritronics effects and were attributed to the coupling of spin waves (magnons) and lattice vibrations (phonons), which are also involved in the origins of the spin Seebeck effect.[41–43] The works state that coupling can be induced by tuning the frequency of the magnons via the applied magnetic field strength to coincide with the frequency of phonons. This occurs at the so called 'resonant field'. Although the novelty of resonant magnetoelastic enhancement is of interest within the discourse of spin caloritronics, in the context of energy harvesting the importance is modest. Mostly concerned with insulating ferrimagnets [44, 45], the highest room temperature enhancement of the SSE is reported as 10.21% isolated only at an applied magnetic field of 420mT.[44]

This investigation of spin Seebeck effects in Fe and $Fe_{0.79}Ga_{0.21}$ was intended to supplement the work on AF spintronics during periods of downtime for the epitaxial growth chamber. Using the parallel resistor method the objective was to quantitatively determine the material's spin Seebeck coefficient such that the efficiency might be compared with other candidate materials. The possibility of the observation of resonant magnetoelastic enhancement was of secondary interest.

1.2 Thesis Structure

The following thesis is laid out in six parts beginning with two chapters providing context and background for the reader. Experimental results and discussion are presented across three chapters with a final concluding chapter. Here in the introduction a brief history of the fields of research that lead to the motivation of this work is provided. Then a general description of the theory behind the physics governing phenomena under analysis can be found.

The second chapter portions specific attention to the instruments, systems and techniques used in the experimental research. This includes insight into the physics they rely on and descriptions of their makeup and operation.

The main bulk of the thesis is the presentation and discussion of experimental results with two chapters concerned with the growth and characterisation of $\mathrm{CuMnAs}_{1-\alpha}\mathrm{Sb}_{\alpha}$ an Sb doped variant of the AF CuMnAs. The latter has generated a great deal of interest and been a seminal milestone in the field of AF spintronics due to its facility to electrically switch the magnetic order parameter. The first of these chapters deals with epitaxial growth of $\mathrm{CuMnAs}_{1-\alpha}\mathrm{Sb}_{\alpha}$ thin films from machine calibration to material characterisation. The second chapter examines the AF spintronic properties of $\mathrm{CuMnAs}_{1-\alpha}\mathrm{Sb}_{\alpha}$, assessing their candidacy in comparison to the relatively well studied CuMnAs.

A further results chapter presents a departure from AF spintronics. This chapter is composed of a four pronged study of spin caloritronics effects in both Fe and $\mathrm{Fe}_{0.79}\mathrm{Ga}_{0.21}$ thin films. Starting with sputter deposition and material characterisation of samples, then longitudinal spin Seebeck effect measurements, subsequent investigation of the transverse magneto-Seebeck effect and finally electron transport experiments.

The disconnect between these two subjects is the result of a frustrated compromise. Originally, the spin caloritronic work sought to supplement that on $\mathrm{CuMnAs}_{1-\alpha}\mathrm{Sb}_{\alpha}$ during periods of servicing the epitaxial growth chamber since initial stages of work on Fe and $\mathrm{Fe}_{0.79}\mathrm{Ga}_{0.21}$ required only sputter deposition. Work between the two would later have been drawn together with a study of single crystal epitaxially grown Fe and $\mathrm{Fe}_{0.79}\mathrm{Ga}_{0.21}$ layers in comparison to sputtered layers so that all work was united by composition dependence of spintronic phenomena in epitaxially grown thin films. Ultimately growth of thin films for spin Seebeck effect measurements could not be fulfilled, impacted by technical difficulties and the COVID-19 pandemic, along with a divergence of the objectives of the LSSE investigation.

The thesis concludes with a summary of key results and discussion of further work that might be of interest to future studies relating to the advancement of work presented here.

1.3 Fundamentals of Magnetism and Magnetic Materials

Magnetism is a relativistic effect resulting from magnetic moments of fundamental particles and the dynamics of electrical charge. It is propagated by magnetic fields that exhibit forces across a vast range of length scales and makes up one part of the electromagnetic force. Magnetism is manifested by magnetic dipole moments, vectors that are perpendicular to the relative motion of electric charge and emanating magnetic field from the north to the south pole.

1.3.1 Magnetic Atoms

Classically, magnetic dipole moments μ are related to a loop of current by the product of the current $\mathbf{I}$ and area enclosed A such that $d\mu = \mathbf{I}dA$. A simple calculation can be done to find the moment of an electron orbiting an atomic nucleus. Take an electron of mass m_e and charge e in the ground state orbital of an H atom; the current is the charge of the electron over the period of its 'orbit'. Given that in the ground state the angular momentum is equal to the reduced Planck constant $\hbar$, the result is found to be $\mu_B = \frac{e\hbar}{2m_e}$ known as the Bohr Magneton and is a commonplace unit of reference for atomic moments. However, the concept of a negative point charge circling a positive nucleus is not the origin of magnetism in condensed matter, which is fundamental to the properties and ordering of electrons and cannot be properly treated without quantum mechanics.

To elaborate, in condensed matter magnetic moments originate from two sources of quantised angular momentum of an electron - orbital and spin. Orbital angular momentum follows the same definition as in the classical description and is given by the operator $\hat{\mathbf{L}} = \hat{\mathbf{r}} \times \hat{\mathbf{p}}$. In a hydrogen like atom L is quantised by constraints imposed from coupling of angular equations in the Schrodinger equation of an H-like atom with a wavefunction Ψ for the whole system is given in eqn 1.1:

$$-\frac{\hbar}{2m}\frac{m_e+m_p}{m_e m_p}\nabla^2\Psi(r,\theta,\phi)-\frac{e^2}{4\pi\varepsilon_0 r}\Psi(r,\theta,\phi)=E\Psi(r,\theta,\phi) \tag{1.1}$$

where m_p is the proton mass, ε_0 is the permeability of free space and r, θ and ϕ make up the radial and angular position coordinates.

The spin angular momentum or simply spin, S, is an intrinsic quantum angular momentum of fundamental particles including electrons and the origin of spin magnetic moments that contribute to solid state magnetic behaviour.

Spin Orbit Coupling

For an electron bound to an atom in its ground state, relative to the electron rest frame, the positive nucleus 'orbits' it as depicted in fig. 1.5. This motion of charge appears as a current loop with an associated magnetic field vector (**B**) that in turn dictates a preferred orientation of the electron's spin magnetic moment. This field can be taken as:

$$\mathbf{B}=-\frac{\mathbf{v}\times\varepsilon}{c^2} \tag{1.2}$$

where $\varepsilon=-\frac{\mathbf{r}}{r}\frac{dV(r)}{dr}$ is the electric field at the electron due to the nucleus, $\mathbf{v}$ the velocity and c the speed of light. Considering its interaction with the spin magnetic moment μ_s an energy term $\mathrm{H}_{L,S}$ is contributed to the Hamiltonian:

$$H_{L,S}=-\frac{1}{2}\mu_{\mathbf{s}}\cdot\mathbf{B} \tag{1.3}$$

Here the factor of half is the Thomas factor, a relativistic correction. This energy term can be expanded in terms of **L** and **S**. Taking the spin moment of $\mu_s=-\frac{g\mu_B}{\hbar\mathbf{S}}$ and making use of the orbital angular momentum $\mathbf{L}=\mathbf{r}\times m\mathbf{v}$ the term becomes:

$$H_{L,S}=-\frac{1}{2}\frac{g\mu_B}{m\hbar c^2}\frac{1}{r}\frac{dV(r)}{dr}\mathbf{L}\cdot\mathbf{S} \tag{1.4}$$

This interaction between the spin and orbital angular momentum is spin-orbit coupling (SOC) and gives rise to an apparent Zeeman effect splitting in energy. It is important to note that since $\mathrm{H}_{L,S}$ is proportional to the Coulomb field of an atom the splitting is related to the atomic number Z, consequently it can be found that $H_{L,S}\propto Z^4$.[46] The interaction is instrumental in a multitude of spintronic phenomena handled throughout the following work including magnetostriction, the spin Hall effect and magnetocrystalline anisotropy.[47]

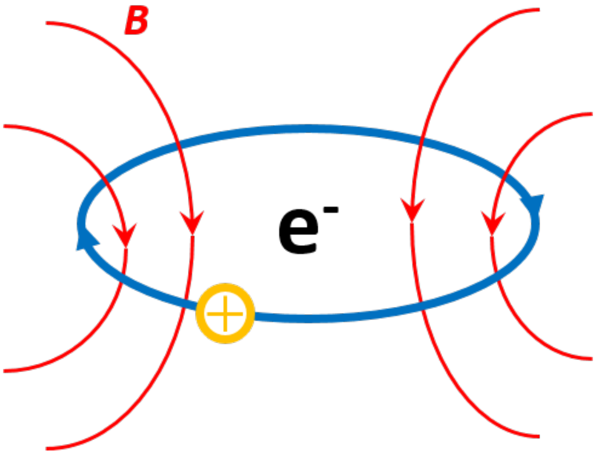

Fig. 1.5 The positive nucleus sweeping out a current loop relative to the rest frame of the electron, creating an apparent magnetic field B that defines spin-orbit coupling.

Hund's Rules

Electron orbitals are filled up to the ground state such that the total energy is minimised, dictating the arrangement and order of electrons within the atomic shells. This energy minimisation follows the empirical Hund's rules, described in terms of total angular momentum $\mathbf{J}$, where $\mathbf{J} = \mathbf{L} + \mathbf{S}$. Hund's rules state firstly within a subshell of equal $\mathbf{L}$ that $\mathbf{S}$ will be maximised to lower the energy i.e. a shell will fill with electrons of parallel spin, the unpaired singlet state, whereby they are spatially distant with reduced nuclear shielding and more tightly bound. Secondly, $\mathbf{L}$ will be maximised, in the classical analogy the electron will move to a higher orbital, to minimise the total energy of the system. The third rule states that for outer shells less than half filled the lowest combined orbital and spin angular momentum offers lowest energy but for a more than half full outer shell energy is lowest when $\mathbf{J}$ is maximised. This rule accommodates spin orbit coupling whereby the electron will have reduced energy if $\mathbf{S}$ is aligned with $\mathbf{L}$ when less than half full and opposite when more than half full and shown in the determination of the total angular momentum first being $J = |L - S|$ and only $J = L + S$ after the shell is half full. With a good estimate of the ground state the total magnetic moment of an atom can be predicted. Hund's rules therefore offer an estimate of the magnetic moment of an atom in the ground state. Whilst these atomic dipole moments play a central role in magnetic materials their interplay within a crystal is more complicated. [46]

1.3.2 Magnetic Metals

Exchange

Even with an atomic magnetic moment simple electromagnetic interactions are too weak to give rise to magnetic ordering above temperatures of 2K. Long range magnetic order between atoms occurs via exchange interactions, a quantum mechanical effect arising from the symmetry (or symmetry breaking) of identical particles being swapped. Exchange can be direct between electrons in neighbouring atoms or indirect via a mediating mechanism. Both direct and indirect classes of interaction are motivated by energy minimisation. However, direct exchange is rarely a dominant influence due to the scarcity of systems with sufficient orbital overlap. Indirect exchange can take many forms including via delocalised conduction electrons, a mediating atomic neighbour of negligible magnetic moment, due to a mix of ions amongst magnetic atoms.

When considering a model of neighbouring spins the energy difference between the singlet and triplet state is characterised by the exchange coupling $\mathbf{J}$. Where $J > 0$ the antisymmetric triplet state is favoured and when $J < 0$ the symmetric singlet state is preferred. This, ultimately, defines the long range magnetic ground state of the material in a uniform direction in a ferromagnet (FM) or with net zero magnetisation ($\mathbf{M}$) as an antiferromagnet (AF) respectively. In the case of a FM, the positive exchange integral will give rise to a molecular field that will act to align local magnetic moments and the system becomes spontaneously magnetised in a single direction as depicted in fig. 1.6a. In an AF the moments are oriented such that the nearest neighbours are not aligned and compensate each other's stray field, each moment is aligned with a distinct FM sublattice. This can occur in many configurations broadly divided into collinear and non-collinear AFs; CuMnAs and its analogues that are relevant to this study are classified as the former. A collinear AF is composed of just two antiparallel FM sublattices A and B of equal and opposite magnetisation such that $M_A = -M_B$. A pair of 2D sublattices are illustrated in fig. 1.6b in red and green where each moment's nearest neighbour is on the opposing sublattice. The magnetic order parameter of a collinear AF, analogous to the magnetisation of a FM, is termed the Néel vector ($\mathbf{L}$) and defined as the difference between the magnetisation of the two sublattices such that $\mathbf{L} = \mathbf{M_A} - \mathbf{M_B}$.

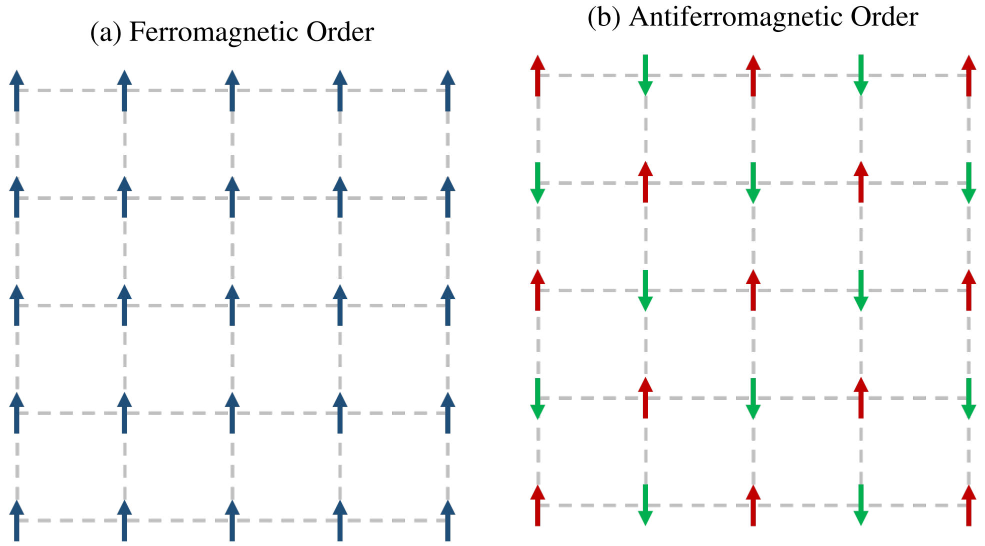
(a) Ferromagnetic Order

(b) Antiferromagnetic Order

Fig. 1.6 Collective alignment of individual magnetic dipole moments represented by arrows on a 2D lattice for a ferromagnet in blue on the left and an antiferromagnet in red and green on the right. The red and green arrows each represent a ferromagnetic sublattice that together have zero net magnetisation.

There is a limit to the exchange and molecular field where it can be overcome at sufficiently high temperatures and undergo a magnetic phase transition. In FMs this is at the Curie temperature T_C and in AFs the Néel temperature T_N.

1.3.3 Magnetic Free Energy

Magnetic Anisotropy

A crystal possessing magnetic order is likely to have an energetic preference leading to anisotropy in the alignment of moments. The magnetocrystalline anisotropy offers an energy difference ΔE_K between the easy axes and hard axes for parallel and antiparallel moments given by $\Delta E_K = E_{hard} - E_{easy}$. The effect's origin lies in the impression of the crystal symmetry on the spin orbit coupling and is inversely proportional to the symmetry of the crystal. Magnetocrystalline anisotropy is axial rather than directional such that opposite magnetisation or Néel vector along the same axis are equivalent.[48]

In cubic structures such as Fe the simplest first order model of the anisotropy energy E_K is a uniaxial system where a single axis is preferred and given by $E_K = K_u \sin(2\theta)$. Here θ is the angle between the magnetic order parameter and the easy axis and K_u is simply the uniaxial anisotropy constant. This can be expanded to include four fold cubic anisotropy term K_{cu}, here reduced to the xy plane given the samples concerned in this study are thin films.

$$E_K = K_u \sin^2\theta - \frac{K_{cu}}{4}\sin^2 2\theta \tag{1.5}$$

Further magnetic anisotropy contributions that are not intrinsic to the crystal but rather induced come from shape, surface, interface and magnetoelastic anisotropy. It is the shape anisotropy, from the morphology of the sample's reduced symmetry, in thin films that constrains moments to be in plane allowing the reduced terms above.[46] Magnetoelastic anisotropy is related to the coupling of the magnetisation with strain in the crystal structure i.e. mangetostriction. Where a sample such as a thin film is grown on a substrate strain in the crystal can arise and induce additional uniaxial anisotropy.[48]

Domains

FM metals are often seen to have no net magnetisation unless a sufficiently strong external field coerces them in a given direction. In a FM, domains are small regions of uniform (saturation) magnetisation and neighbouring domains will align such that the stray demagnetising field is reduced.[46] While AFs do not possess the stray field central to FM domains they still exhibit domains. These are induced by local crystal defects that break exchange, magnetoelastic effects and inhomogeneous occurrence of the magnetic order parameter with the emergence of the AF phase whether in growth or a phase transition.[49]

The interface of neighbouring magnetic domains are bordered by domain walls, regions of canted moments that transition between the differing magnetic order parameters. Domain walls can be classified by the canting angle of the moments within the wall. Broadly these are 90° and 180° domain walls, which separate perpendicular and anti-parallel domains respectively. These can be further categorised by the plane of motion in which the spins are canted with a width determined by the energy cost of rotated neighbouring moments and deviation from the magnetic anisotropy.

Ferromagnets in an Externally Applied Field

When an FM material is exposed to an external magnetic field B it acquires magnetisation M according to its permeability μ, usually given relative to the permeability of free space such that $\mu_r = \frac{\mu}{\mu_0}$. Phenomologically, domain walls move to expand domains that align with the field. This process occurs readily compared to the magnetisation rotation of moments constrained by walls and the magnetic anisotropy, which require more energy and higher fields until all moments are aligned with B and the FM reaches saturation magnetisation M_s, this point is illustrated in fig. 1.7. With a reduction in the applied field towards the opposite direction the magnetisation rotation back to the easy axis is generally lossless and reversible but the domain wall motion loses energy leading to hysteresis and a retention of magnetisation even at zero field, the remanence M_r. The field needed to reverse the magnetisation to zero is the coercive field and a measure of the ease with which a FM can be magnetised.[47]

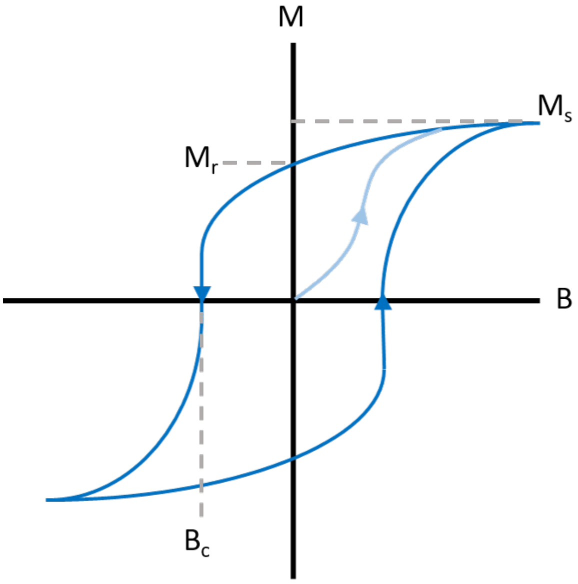

Fig. 1.7 A FM hysteresis loop showing the initial magnetisation in light blue aligning with the field subject to the permeability, until the magnetisation saturates M_s at a sufficiently high field and then falls with the domain wall movement retaining the remnant magnetisation M_r and only changing sign at the coercive field B_c.

1.4 Spintronic Effects and Phenomena

1.4.1 Universal Concepts

Anisotropic Magnetoresistance

Spintronics relies on a read out of the magnetic order to examine the associated logic elements. Changes in the electrical resistivity dependent on the angle between the magnetisation (or rather magnetic order parameter) and current ϕ allow this to be done electrically. This magnetoresistance is widely exploited in FMs and AFs and originates in the influence of spin orbit coupling by opening up scattering between spin up and spin down states in electron transport.[46] This makes up the non-crystalline contribution to anisotropic magnetoresistance (AMR). The difference in resistivity ρ when oriented parallel $\rho_{||}$ and perpendicular $\rho_{\perp}$ to the magnetic order parameter is expressed as the ratio:

$$\frac{\Delta\rho}{\rho} = \frac{\rho_{||} - \rho_{\perp}}{\rho_{av}} \tag{1.6}$$

where ρ_{av} is the resistivity averaged over 360°.[50]

For crystalline structures, the broken symmetry of the lattice can result in a significant uniaxial and biaxial contribution to the AMR introducing a further angle between the magnetic order parameter and crystal axis ψ.[51] A phenomenological model accounting for the allowed symmetries has previously been studied indepth in dilute FM semiconductor (Ga,Mn)As.[52] Following this approach, the longitudinal AMR, i.e. the change in resistivity parallel to the current direction ρ_{xx}, decomposes into the following four terms:

$$\frac{\Delta\rho_{xx}}{\rho_{av}} = \frac{\rho_{xx} - \rho_{av}}{\rho_{av}} = C_I \cos 2\phi + C_U \cos 2\psi + C_C \cos 4\psi + C_{I,C} \cos(4\psi - 2\phi) \tag{1.7}$$

From left to right these terms are the non-crystalline term owing to spin-orbit coupling, the uniaxial and cubic crystalline terms here a function of the angle between the magnetic order parameter and [110] crystal direction. Finally there is a crossed non-crystalline/crystalline term for the contribution of the SOC interaction with the crystal lattice.[53]

The uniaxial and cubic terms are excluded from the transverse AMR, the change in resistivity perpendicular to the current direction ρ_{xy}, whilst still dependent on the crossed term leaving:

$$\frac{\Delta\rho_{xy}}{\rho_{av}} = C_I \sin 2\phi - C_{I,C} \sin(4\psi - 2\phi) \tag{1.8}$$

This effect is often refered to as the planar Hall effect (PHE). For isotropic materials the crystalline terms can be treated as zero, also providing a close approximate for polycrystalline materials with randomly oriented grains. It is useful for detection of the magnetisation in thin magnetic samples where the geometry constrains the moments in plane.[54–56]

Landau Lifshitz Gilbert Equation

Magnetic material behaviour can be simulated by approximations of the composite magnetic elements of a system i.e. micromagnetic simulations. This is principally achieved by the Landau-Lifshitz-Gilbert equation (LLG), which is the time derivative of the magnetisation M and describes the temporal dynamics a FM's magnetisation M in an effective magnetic field H_{eff}. The LLG incorporates any magnetic field considerations in the environment of the magnetic elements, including the demagnetising field and external magnetic field.[57]

$$\frac{\partial \mathbf{M}}{\partial t} = \gamma\prime \mathbf{M} \times \mathbf{H_{eff}} - \frac{\alpha}{M_s} \mathbf{M} \times \frac{\partial \mathbf{M}}{\partial t} \tag{1.9}$$

Here, α is the damping factor determined by the system and $\gamma\prime$ is the coefficient of precession - originally the gyromagnetic ratio relating magnetic moment and angular momentum before Gilbert's modification to depend on damping in 1955.[58]

The first term is formulated from the torque, the rate of change of the angular momentum, on the magnetisation from the effective magnetic field, which leads to the precession of the magnetisation. The second term considers the contribution of damping on the change in magnetisation, which works to bring the system to equilibrium.

Anomalous Hall Effect

For a conducting ferromagnet an additional term to the ordinary Hall effect modifying the transverse resistivity exists that is proportional to the magnetic order parameter of the sample rather than the applied magnetic field. This is the anomalous Hall effect (AHE), a consequence of spin-orbit coupling and present in any material with broken time-reversal symmetry. The AHE is generated by several mechanisms split between intrinsic and extrinsic contributions. The intrinsic band structure adds to the AHE without scattering but instead via a Berry curvature experienced by charge carriers that imparts a Berry phase on them.[59] Extrinsic contributions include skew and side jump scattering that arise as carriers are deflected by interaction with disorder such as a defect of impurity. All three mechanisms produce a transverse displacement on the carrier dependent on spin.[60]

Spin Hall Effect

An electrical current j_c passing through a non-magnetic sample can generate spin accumulation at the lateral surfaces of the sample that constitutes a transverse pure spin current j_s. The spin polarisation σ vector is perpendicular to the currents' plane with a net zero transverse charge current i.e. a pure spin current. This is known as the spin Hall effect, proposed in 1971 and measured three decades later in 2004.[61–64] The pure spin current is defined by:

$$\mathbf{j_s} = (\theta_{SH}\frac{\hbar}{2e})\mathbf{j_c} \times \sigma \tag{1.10}$$

where θ_{SH} is the spin Hall angle, a characteristic coefficient for the efficiency of the effect in a given system.[23]

An illustration is given in fig. 1.8a showing the relevant orientations of electrical current, spin current and polarisation. Like the AHE, spin orbit coupling generates an asymmetric deflection of the charge carriers akin to a spin filter. The effect is a useful spin current generator, utilising the high SOC of heavy metals such as Pt to inject spin currents such as in bilayer Pt/NiO AF spintronic devices.[65]

A complementary effect exists for the reverse case when a spin polarised current is injected into a sample depicted in fig. 1.8b. The spin current undergoes a deflection (equivalent to that described above) perpendicular to both the spin current and polarisation. An electrical charge current is therefore generated with equivalent direction for spins parallel and antiparallel to the spin polarisation vector. This inverse spin Hall effect (ISHE) serves as a valuable spin current detector and is similarly described by:

$$\mathbf{j_c} = (\theta_{SH}\frac{2e}{\hbar})\mathbf{j_s} \times \sigma \tag{1.11}$$

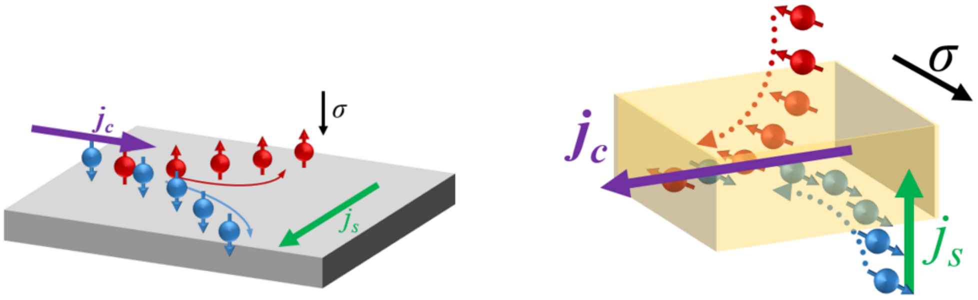

(a) (b)

Fig. 1.8 (a) illustration of the spin Hall effect with a mixed electrical current (purple arrow) composed of spin up (red) and down (blue) electrons diverging to give rise to a spin current (green arrow). (b) an illustration of the inverse spin Hall effect with a charge current arising from the injection of a spin polarised current.

1.4.2 Caloritronic Phenomena

Seebeck Effect

The Seebeck effect is one manifestation of the broader thermoelectric effect concerning the reversible conversion of heat energy and electrical energy. Specifically, the Seebeck effect is the electromotive force that occurs between two points experiencing a temperature difference in a conducting sample mediated by the diffusion of charge carriers from high to low temperature points. The ratio between the Seebeck electromotive force E and the difference in temperature T makes up the Seebeck coefficient S,[22] such that:

$$E_{emf} = -S\nabla T \tag{1.12}$$

Nernst and Magneto-Seebeck Effects

Nernst effect

The Nernst effect is the emergence of an electric field in a conductor subject to a temperature gradient and magnetic field that are perpendicular where the electric field is orthogonal to both.[66] The ratio of the induced electric field E_{NE} to the product of the contributing magnetic field H and temperature gradient ∇T is the material characteristic Nernst coefficient N so the effect can be formulated as:

$$\mathbf{E_{NE}} = N(\mathbf{H} \times \nabla\mathbf{T}) \tag{1.13}$$

It is similar in formulation to the ordinary Hall effect but charge transport is entirely driven by the thermoelectric behaviour of the material.

Anomalous Nernst effect

A further electric field contribution appears in conductors with magnetic ordering that breaks time reversal symmetry such as FMs, the anomalous Nernst effect (ANE). As above the effect emerges perpendicular to the temperature gradient but is dependent on an orthogonal magnetisation rather than magnetic field. It is therefore described by:

$$\mathbf{E_{ANE}} = N_{ANE}(\mathbf{M} \times \nabla\mathbf{T}) \tag{1.14}$$

where N_{ANE} is the anomalous Nernst coefficient of the sample.

It is important to consider the ANE when dealing with the spin Seebeck effect in thin films where the geometry is such that the inverse spin Hall effect and the anomalous Nernst effect signals overlap. This is always pertinent for conducting FMs but even insulating ferromagnets can induce an extrinsic proximity magnetisation in an adjacent capping layer.[67, 43]

Spin Seebeck Effect

In FM materials a spin voltage is generated by a temperature gradient that can drive spin currents, such as when a non-magnetic metal (NM) is in adjacent to the spin voltage and a spin injection across the FM/NM interface is observed.[41] This spin Seebeck effect (SSE), demonstrated in 2008,[24] has potential for spin current generation as well as thermal energy harvesting with the ISHE converting spin to charge current.

In the original transverse configuration, a spin voltage was generated perpendicular to the temperature gradient as depicted in fig. 1.9a and successfully demonstrated the occurrence of the SSE in insulating, semiconducting and metallic FMs. However, experimental design becomes complicated in such a geometry where thermoelectric and thermodynamic effects in a substrate can dominate.[43] Another configuration exists, the longitudinal spin Seebeck effect, where the spin voltage is parallel to the temperature gradient and perpendicular to both the magnetisation and FM/NM interface. The spin polarisation vector σ remains parallel with magnetisation. A schematic diagram for an experimental LSSE is given in fig. 1.9b illustrating the difference to the transverse SSE.

For an SSE device including an inverse spin Hall effect spin-charge current converter the electric field E_{ISHE} in the normal metal from purely spin voltage contribution is given by:

$$\mathbf{E_{ISHE}} = \theta_{SH}\frac{\rho}{A}(\frac{2e}{\hbar})\mathbf{J_s} \times \sigma \tag{1.15}$$

here A is the interfacial area, $\mathbf{J_s}$ the spin current and the spin polarisation vector σ is parallel to the magnetisation $\mathbf{M}$.

The mechanism behind the spin voltage seen in the spin Seebeck effect has predominantly been described as driven by thermal excitation of magnons, collective excitation of localised spins in the FM. However, experimental results have also indicated a role mediated by non-magnetic excitations within the lattice of the FM and substrate, phonons, a matter that is still not fully resolved.[68]

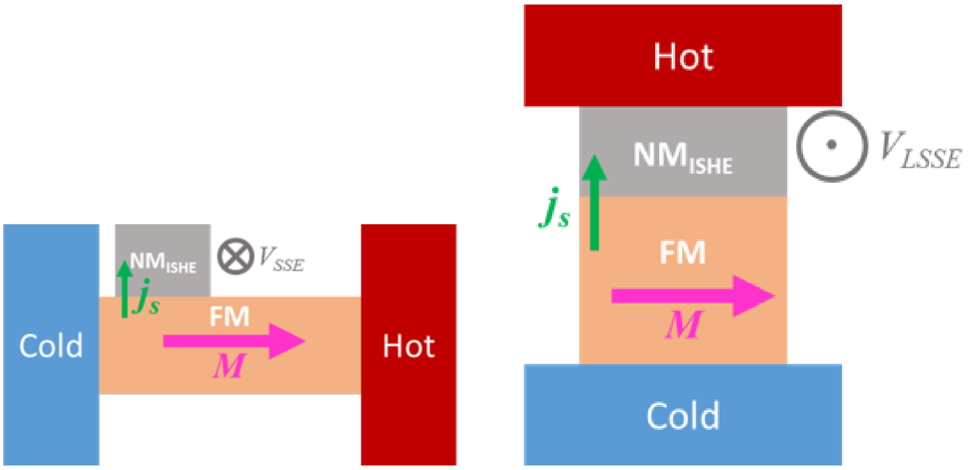

(a)

(b)

Fig. 1.9 A simple experimental set up for the transverse spin Seebeck effect including a non-magnetic ISHE spin-charge current converter and (b) a scheme for the longitudinal spin Seebeck effect.

Magneto-Seebeck Effect

Magneto-thermoelectric effects can also include planar magneto-Seebeck effects (MSE). The MSE is the emergence of an electric field transverse to the temperature gradient in an FM conductor. Unlike the previously described Nernst effects, the MSE occurs for a temperature gradient and magnetisation in the same plane and varies with the angle between the two ϕ.[69] Given the transverse component of the anisotropic magneto-thermopower S_{xy} the transverse electric field induced is: [70]

$$V_{xy} = S_{xy}\nabla T \sin 2\phi \tag{1.16}$$

This effect can appear in spin Seebeck systems with lateral thermal gradients and was prevalent in early studies performed in the transverse scheme of fig. 1.9(a).[43] While setups for longitudinal spin Seebeck effect measurement are, ideally, more resistant to the magneto-Seebeck effect extraneous in-plane temperature gradients must still be taken into account.

1.4.3 Antiferromagnetic Spintronic Phenomena

Spin Orbit Fields

While the model of spin orbit coupling described in section 1.3.1 is helpful in describing relatively simple atomic fields, for a crystal the regular lattice makes up a collective crystal field. It is possible to expand on the Hamiltonian of eqn. 1.4 to account for the electric potential V of the crystal field.[71]

$$H_{L,S} = -\frac{gu_B}{2mc^2}\sigma \cdot (\nabla V \times \mathbf{p}) \tag{1.17}$$

The effective Zeeman field of the crystal can be described simply as a spin orbit field $\mathbf{U}(\mathbf{p})$ such that

$$H_{L,S} = \sigma \cdot \mathbf{U}(\mathbf{p}) \tag{1.18}$$

Time inversion symmetry is preserved in SOC so under the time reversal transformation $\mathscr{T} : H_{L,S} = -H_{L,S}$. However, with the existence of broken spatial inversion symmetry the spin orbit field is an odd function of electron momentum and $-\sigma \cdot \mathbf{U}(-\mathbf{p}) = \sigma \cdot \mathbf{U}(\mathbf{p})$.[72] In environments where spatial asymmetry is structural such as interfaces in a heterostructure, surfaces of conductors or asymmetry in the growth direction such as GaN wurtzite crystals the crystal field and symmetry breaking leads to Rashba SOC.[73, 74] An electron in this asymmetrical structure experiences a non uniform electric field $\mathbf{E_R} = -E_0\hat{z}$ where $\hat{z}$ in the axis of broken symmetry. This makes up the spin orbit field $\mathbf{U}(\mathbf{p}) = (E_0\hat{z} \times \mathbf{p})$ so that the Rashba Hamiltonian is:

$$H_R = -\frac{gu_B}{2mc^2}\sigma \cdot (E_0\hat{z} \times \mathbf{p}) = -\frac{gu_B}{2mc^2}(\sigma_x p_y \hat{x} - \sigma_y p_x \hat{y}) \tag{1.19}$$

Rashba SOC aligns the electron spin perpendicular to momentum to yield a spin texture tangential to the Fermi surface like that illustrated in fig. 1.10a (a).[72] In other crystal structures Rashba spatial inversion asymmetry can be hidden such that the space group symmetry is preserved but broken by atomic site point groups. In this case, Rashba SOC only exists locally within the system.[75] This is true of CuMnAs when considering two Mn sublattices (A and B) that individually break atomic site point group symmetry. When inverted the crystal remains the same but the two FM sublattices making up the AF order are not invariant, they are inversion partners.[13] This is further illustrated in fig. 1.11 where the point on the dashed line indicates an inversion centre between Mn atoms on separate FM sublattices invariant in the space group of the crystal but asymmetric with respect to the magnetic lattice.[14]

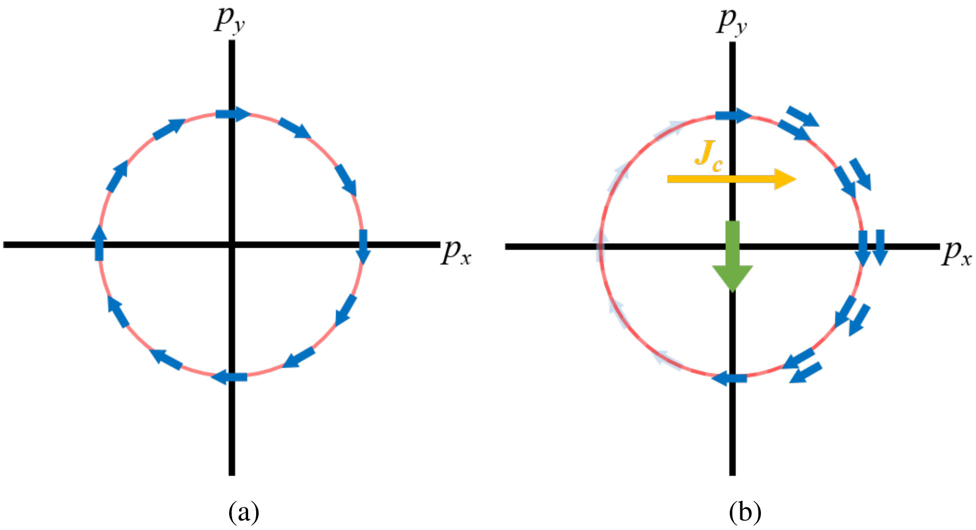

Fig. 1.10 (a) The spin texture at the Fermi surface in a Rashba SOC system where the spin polarisation is perpendicular to the momentum (b) the non-equilibrium spin density with a net spin polarisation in green induced with the application of an in plane current in yellow.

A similar effect is also true for symmetry breaking in the bulk, such as zinc-blend structures where the unit cell has no point of inversion symmetry and is known as Dresselhaus SOC. The two effects are subtly different where the broken spatial inversion symmetry of Dresselhaus SOC produces different spin texture.[76, 72]

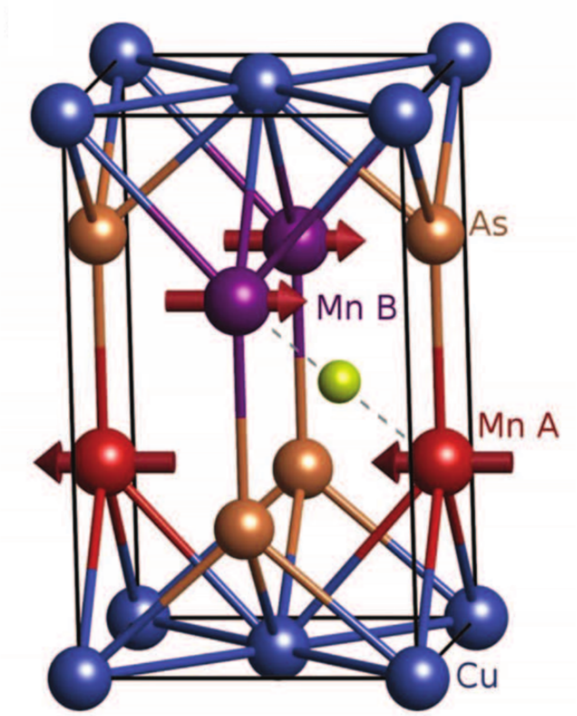

Fig. 1.11 The magnetic unit cell of CuMnAs where the unit cell's centrosymmetric inversion point is indicated at the yellow ball. The Mn sublattices A (red) and B (purple) are asymmetric inversion partners.

Inverse Spin Galvanic Effect

With the injection of an ordinary current J_c, the Rashba spin texture at the Fermi surface shifts in momentum space making for an out of equilibrium spin density,[77] which is further illustrated in fig. 1.10a(b).[78, 79] This is the inverse spin galvanic effect and the current induced non-equilibrium spin density $\hat{D}$ is perpendicular to the current $\hat{D} \sim \hat{z} \times J_c$.[80] For locally asymmetric environments such as CuMnAs the sign of the non-equilibrium local spin density alternates between the two inversion partner sublattices such that it can be described as a staggered spin density.[13]

In CuMnAs the non-equilibrium spin density in turn results in a staggered in plane spin polarisation of the current perpendicular to the current direction, local to each sublattice.[13] The spin polarised current acts as an effective magnetic field where $B_A \sim +\hat{z} \times J_c$ and $B_B \sim -\hat{z} \times J_c$ acting on moments of the sublattice that are parallel to the ordinary current.[77] An illustration of the various physical effects contributing to the NSOT and their directions relative to the magnetic unit cell is provided in fig. 1.12. Given sufficient current density the moments can be reoriented by the field like torque T, which acts in the same direction for both sublattices.

$$T_{A,B} = M_{A,B} \times B_{A,B} \tag{1.20}$$

With the requisite Rashba SOC, an ordinary current induces a Néel order spin orbit torque (NSOT) reorienting the spin pairs of each sublattices by 90° such that the magnetic order parameter is electrically switched.[13, 14]

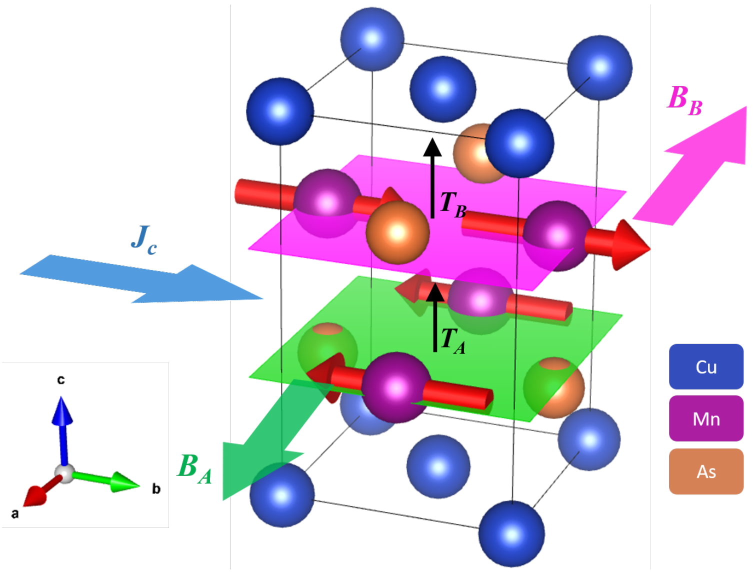

Fig. 1.12 The Néel order spin orbit torque (black arrows) acting on two antiparallel sublattices (green and magenta planes) that form inversion partners within the CuMnAs unit cell. The torque is exerted as a result of an effective field $\mathbf{B}_{\mathbf{A},\mathbf{B}}$ (green and magenta arrows) arising from the influence of hidden Rashba SOC on the injected charge current J_c (blue arrow).

Chapter 2

Material and Techniques

2.1 Material Synthesis

2.1.1 MBE Growth

Principles

Molecular beam epitaxy (MBE) is a crystal growth technique noted for its ability to achieve a high degree of crystal quality, sensitive semiconductor doping control, and atomic interfaces. Operating under ultra-high vacuum (UHV) to reduce background contamination and facilitate long molecular mean-free-paths, a heated substrate is exposed by line of sight to molecular beams of source materials, termed fluxes. The beams can be either molecular or atomic, depending on the material in question, however, the term molecular beam is used to describe both. This arrangement ensures that molecular interactions occur exclusively at the growth surface and this property, when combined with accurate and fast mechanical shuttering of the fluxes, can produce very fine interfaces with monolayer (ML) resolution. Upon adsorption of adatoms on the substrate surface, epitaxial crystal growth is feasible and may be controlled using several key tools: stoichiometry, adatom kinetic energy, surface temperature and the structure of the preceding layer. [81]

Among its capabilities MBE is useful for the synthesis of thin film samples including semiconductor heterostructures, defect induced atomic engineering and single crystal metallic layers as utilised in this work. Whilst MBE is more costly and involved than other thin film deposition techniques, such as sputtering, the value from its vast tool set and high quality is not to be overlooked.

Effusion

The archetypal source for MBE is high purity (>99.999%) material effused from a Knudsen cell (K-cell) composed of a crucible heated by electrical elements. Control of the heating moderates the molecular kinetic energy, species and most significantly the intensity of the flux. A given flux gives rise to a local number density within a unit volume that is dependent both on the flux and on the velocity of the particles. The intensity, the number of particles per unit area per second passing that point, can be thought of as a local pressure, termed the beam equivalent pressure (BEP).

Flux is central to stoichiometry – the ratio of composite source material at the surface - during growth and for a condensed source material is controlled by K-cell temperature. The flux is related to the reciprocal root of the temperature as in the Hertz-Knudsen equation 2.1. Here $\frac{dN}{dT}$ is the rate of molecules evaporating from the source with surface area A. p_{eq} and p_{hs} relate to the equilibrium vapour pressure and ambient hydrostatic pressure respectively, the latter accounts for the return of molecules in the gas phase to the source. T is the temperature of the condensed source, m mass of the vapour molecules and k_B the Boltzmann constant.[82]

$$\frac{1}{A}\frac{dN}{dt} = \frac{(p_{eq} - p_h s)}{\sqrt{2\pi m k_B T}} \tag{2.1}$$

RHEED

Reflection high energy electron diffraction (RHEED) is a real-time surface sensitive technique that is essentially indispensable for MBE. An electron beam between 5 and 50kV is directed at grazing incidence to the sample surface and creates characteristic diffraction patterns on a fluorescent screen. A schematic diagram of these components is presented in fig. 2.1.[83]

RHEED relies on incident electrons, with wave vector $\mathbf{k_0}$, scattering elastically at allowed vectors **k'** as determined by the periodic ordering of atoms at the surface acting as a diffraction grating. An Ewald sphere, a 3D surface in reciprocal space, can be constructed with radius equal to the magnitude of the electron's wave vector and originating about the point of incidence. Where this sphere coincides with the reciprocal lattice – with the form of a grid of periodic rods normal to the sample surface – defines the allowed elastic scattering vectors for diffraction. The low angle of incidence interacts almost exclusively with the xy surface plane, excluding periodicity in z. As such, there are no constraints on scattering vectors normal to the surface, giving rise to the rod form in reciprocal space.

There is a thickness to the Ewald sphere defined by divergence of energy and direction within the electron beam. Similarly, vibrations and defects in the crystal lattice give rise to a divergence in the reciprocal lattice and a spread in the elastic scattering vectors. This is represented in fig.2.1, where the reciprocal lattice is discrete in x and y but continuous in z. Due to the relatively high voltage of the electron beam the wave vector at incidence is much greater than the reciprocal lattice spacing, therefore any small change in the real lattice will result in a significant change in the scattering. This is key to the high sensitivity of RHEED.

The benefit of immediate feedback provided by RHEED is immense. The growth surface can be considered as being made up of a dynamic overlayer and terminal surface of the bulk crystal. Changes in the overlayer, such as the rearrangement of dangling bonds or arrival of adatoms can depart significantly from the bulk lattice structure and are discernible in the diffraction pattern. Rotating the sample, the appearance of known patterns along specific azimuths can provide real time information on the state of the overlayer.

These well-established patterns from the overlayer are classified with respect to the bulk crystal surface by Wood's notation. For a cubic crystal system Wood's notation defines two vectors lying on the growth surface for the sides of the unit cell, $\mathbf{a}_1$ and $\mathbf{a}_2$, which share a common origin. Another pair of vectors are defined for the overlayer, $\mathbf{b}_1$ and $\mathbf{b}_2$, where the angle between b1 and b2 is the same as between $\mathbf{a}_1$ and $\mathbf{a}_2$. Finally, the term in Wood's notation is constructed from the ratio of the overlayer vector to the equivalent surface vector such that

$$\left(\frac{|\mathbf{b_1}|}{|\mathbf{a_1}|} \times \frac{|\mathbf{b_2}|}{|\mathbf{a_2}|}\right) \tag{2.2}$$

where the quotients of vector magnitudes are solved but left in the style of a product by convention. An example would be a cubic overlayer unit cell quadruple the area of the cubic substrate surface, the RHEED pattern associated with this state is then referred to as the (2×2). In this way, it is possible to develop a 2D picture of the surface periodicity at well-defined azimuths. This is shown for GaAs [110] and [$\bar{1}$10] in fig. 2.2 during GaAs(001) growth where As dangling bonds form energetically favourable periodic configurations in the overlayer. Some scattering from the bulk is also visible on the pattern as broad, dim Kikuchi lines emanating from the principle beam spot and can also be seen in fig. 2.2.

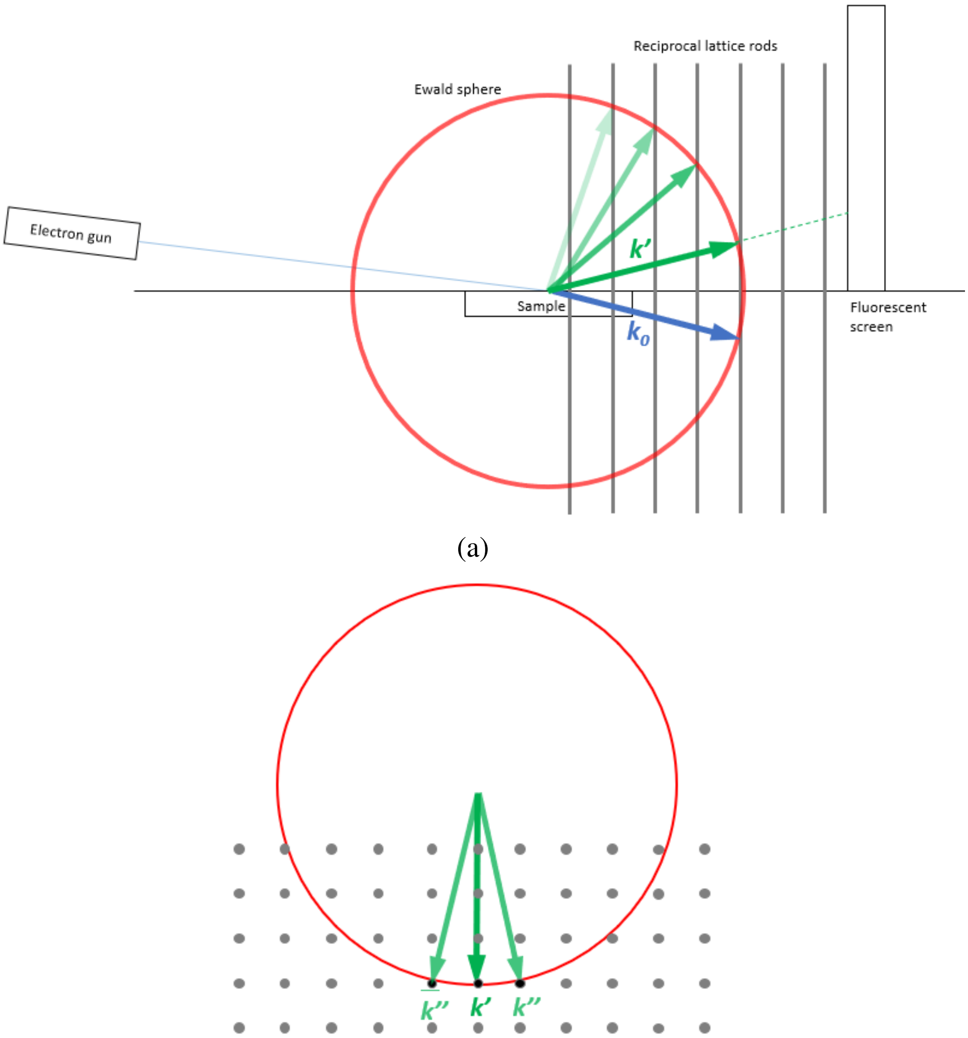

(a)

(b)

Fig. 2.1 The Ewald Spere in context of a RHEED set up (a) the side on perspective showing vertical rods and (b) the top down perspective showing the grid of the reciprocal lattice and allowed scattering vectors coinciding with the Ewald sphere in red.

Analysis of the diffraction pattern allows for calculation of the reciprocal lattice spacing and inference of the periodic surface ordering. However, in this study RHEED has been used as a comparative and qualitative tool to judge surface structure and behaviour in situ rather than to determine the precise arrangement of atoms at the surface.

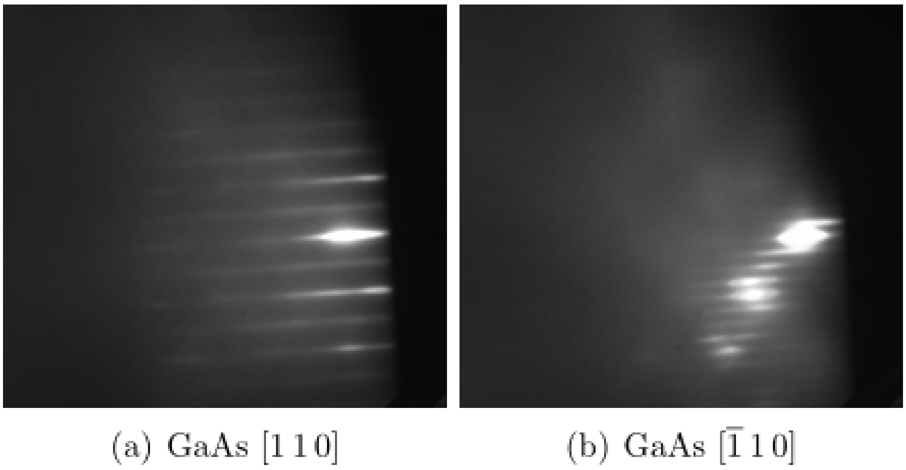
(a) GaAs [1 1 0] (b) GaAs [$\bar{1}$ 1 0]

Fig. 2.2 RHEED pattern of GaAs(001) substrate showing (a) the [110] azimuth and (b) the [$\bar{1}$10] azimuth. Kikuchi lines can be discerned at 45° to the streaks in both images [84]

Crystal Growth

Upon reaching the sample surface adatoms ultimately either remain on the surface and are incorporated into the crystal layer or are desorbed. Before incorporation into the layer, particles may diffuse across the surface given sufficient kinetic energy to overcome the chemical potential of surface atoms or steps. The kinetics of the particle during its existence on the surface bear a significant effect on how it is incorporated and the resulting morphology. [82]

Kinetics govern the route and ultimate state of the particles making up the system. That is to say, the state that is obtained is not necessarily the most stable but is kinetically determined with certain steps within the growth process kinetically prohibited while others occupy a local equilibrium. Despite crystal growth being a non-equilibrium process thermodynamic arguments can be made towards describing processes such as the adsorption-desorption cycle of adatoms or layer vs. island formation dynamics.[85] In the case of the latter a framework for the classification of growth modes based on equilibrium chemical potential or surface free energy can be constructed.

For a hypothetical step free surface growth occurs with particles diffusing along the surface before nucleating, accumulating other adatoms as a single monolayer. As adatoms arrive they diffuse across the surface or off the top of the layer to the step between the two. At the step the adatom is incorporated or diffuses along the step until, without further energy to liberate it, it is incorporated at a kink. In this way 2D islands grow outward, as single monolayers into one another to make up a complete layer before the next nucleates in layer by layer or Frank-van der Merwe growth. The additive propagation of the edge is step flow growth. An illustration of 2D growth is shown in comparison to other models in fig. 2.3(a).[86, 87]

In reality such conditions for monolayer growth are rare. In III-V MBE growth surfaces, even those of high quality, the substrate possesses stacked steps with intermediate surfaces between them described as terraces. However, multiple terraced layers still follow 2D step flow growth local to the terrace surface and are a mainstay of homoepitaxial MBE growth. Additionally, defects can arise from pinned step edges where it will cease to spread and new layers may nucleate before a complete monolayer, potentially causing a break in the periodic lattice.[82]

Applying a thermodynamic approach the surface free energy of the growth surface is greater than that of the adatoms, alternatively it can be described by the change in chemical potential u with the number of layers deposited n, which is positive $\frac{du}{dn} > 0$. If allowed by kinetics Frank-van der Merwe growth occurs. [87, 85]

The incremental roughening and smoothing of 2D growth as monolayer islands nucleate and become whole layers can be observed in the intensity of the RHEED pattern. A smooth, complete layer surface provides good conditions for specular reflection whilst disparate steps result in more diffuse scattering and so the pattern's intensity oscillates. Measurement of the change is exploited growers for in-situ determination of the growth rate. [88]

Step flow growth with a low degree of island nucleation involves little interaction between mobile adatoms but rather a diffusion length longer than the average distance between steps (the terrace width). This assumption breaks down with higher adatom number density (increased flux) or lower substrate temperature. In considering interactions between adatoms as well as strain between the substrate and the layer 3D growth mechanisms emerge. [82]

In the opposite case to layer-by-layer growth arriving adatoms are homophilic and form 3D islands, reducing their surface area to volume ratio. This 3D growth produces a rough surface, which is quickly apparent in the RHEED pattern. Although this regime is undesirable for in growth of thin films it is useful in engineering nanostructures such as quantum dots. As the islands, depicting in fig. 2.3(b), expand they can converge and form a rough but cohesive layer. Referred to as Volmer-Weber growth the difference in chemical potential with deposition of layers can be described by $\frac{du}{dn} < 0$. [89, 87]

A third growth model, common in heteroepitaxy particularly between lattice mismatched substrates and layers, is a two stage hybrid process that shifts from 2D to 3D growth. Layer plus island or Stranski-Krastanov growth begins with step flow growth as the chemical potential of the surface is sufficient to overcome agglomeration of arriving adatoms. However, with increasing thickness the influence of the substrate chemical potential diminishes and an additional degree of strain increases. At a critical thickness $\frac{du}{dn}$ reverses sign from positive to negative and the growth modes shifts from Frank-van der Merwe to Volmer-Weber. This results in complete strained layers at the substrate interface with relaxed 3D islands above as shown in fig. 2.3(c). [87, 90]

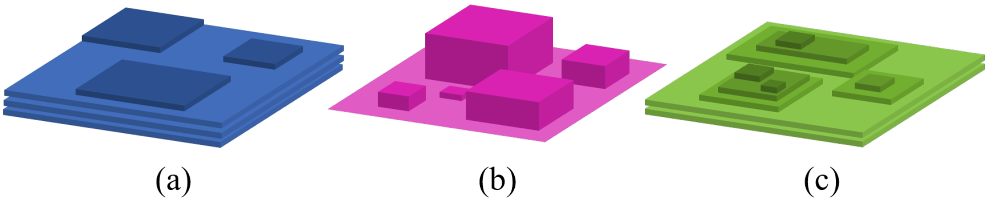

Fig. 2.3 Illustration of epitaxial growth mechanisms (a) Frank-van der Merwe 2D layer by layer growth (b) Volmer-Weber 3D island growth and (c) Stranski-Krastanov layer-island growth.

Metastable Growth

In MBE growth typically occurs far from thermal equilibrium allowing for metastable growth modes. In this state homogeneous films can be deposited that would otherwise favour 3D islands. Consideration of metastable heteroepitaxial growth offers four characteristic modes: floating, pseudomorphic, dislocation and carpet mode. A key variable is the energetic corrugation of the substrate surface, the degree of heterogeneity in the binding energies across the surface for an adatom to the substrate. For low corrugation an adatom is presented with a homogeneous surface that accommodates a lattice mismatch, the layer is not strained to match the substrate lattice constant but can undergo a rotation in it's xy crystallographic orientation. [91]

Substrate surfaces with a stronger corrugation encourage the layer lattice constant to adapt to the substrate, inducing strain in the layer. This is pseudomorphic mode but with sufficient thickness the strain will overcome the interfacial binding energy and the layer will relax and transition into dislocation mode. In the latter a slip between the substrate and layer lattice can occur at the interface.

Defects on the substrate surface such as a step may have an effect on the growth mode. For a small defect the growth layer, with sufficiently high binding energy, may reconcile the defect with a distortion or grain boundary in the film, which induces local strain. This is referred to as carpet mode.[91]

Role of Surface Reconstruction

The surface reconstruction can play a significant role in MBE growth processes, particularly corrugation of the surface. The arrangement of adatoms in the surface overlayer creates a potential well landscape that modulates the growth kinetics from site to site. This landscape leads to anisotropies in mobility and preferential occupation of sites on terraces or alternatively at a step edge, whereas the growth modes described above assume isotropic mobility. Additionally, the reconstruction is largely driven by thermodynamic variables. The role of reconstruction in MBE growth is a second order effect.

For GaAs(001) homoepitaxy, the archetypal case for III-V MBE growth, the phase diagram of surface reconstructions with flux and temperature has long been established. The diagram is presented in fig.2.4 and shows the propensity for the reconstruction to morph into discrete arrangements with subtle changes in thermodynamic variables.[92]

The potential well landscape of the reconstruction leads to anisotropic growth by offering preferential sites along a given crystal direction. An example of this is the As rich step flow regime of GaAs growth with a (2×4) reconstruction. In this case As dimer rows of the reconstruction lie along the [110] direction. The addition of unit cell is determined by the incorporation of Ga atoms, with the preferential site at the end of an As dimer row where there are lone pairs of dangling As bonds. This is equivalent to a $[1\bar{1}0]$ direction step edge perpendicular to the rows of the surface reconstruction. Conversely the [110] direction step edge parallel to the dimer rows of the reconstruction, is unfavourable. As such the growth rate along the [110] direction is greater. [93, 94]

The example of GaAs growth demonstrates the significance of the reconstruction in growth. However, for practical application to growth thorough understanding of the surface is required and at the time of growth there was not a sufficiently well developed picture of CuMnAs growth on GaAs. However,

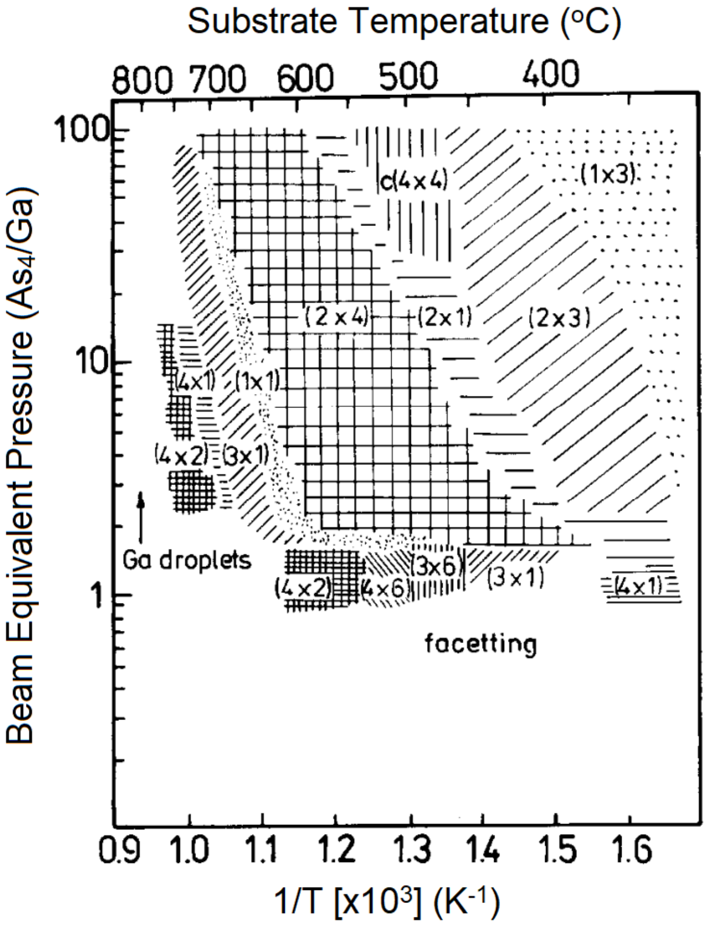

Fig. 2.4 A phase diagram of the surface reconstruction during GaAs homoepitaxial growth on GaAs(001) in the step flow regime. The conditions for given reconstructions are determined by both the substrate temperature and As_4 to Ga flux ratio. Figure obtained from [92]

the typical reconstruction at low temperatures where CuMnAs and CuMnAsSb are grown in this study simple such as a (1×1) structure meaning thermodynamic considerations are diminished and kinetic considerations dominate. For this reason the role of reconstruction and thermodynamics are not discussed in depth.

Band Edge Thermometry

Control of the substrate temperature is a crucial parameter. An effective method of obtaining substrate temperature for semiconductors is to measure their temperature dependent band gap in conjunction with a calibrated dataset. A semiconducting substrate will selectively absorb light below a threshold wavelength in valence band electrons and promote them to the conduction band while longer wavelengths are transmitted elastically.

In 1967 Varshni published work showing the band gap energy of semiconductors increased with temperature following the relation given in eqn. 2.3 where α and β are material specific constants in eVK^{-1}. This is ascribed to two mechanisms: the expansion of the lattice due to increased vibrations and changes in the electron-lattice interaction dependent on temperature.

[95]

$$E_g(T) = E_g(0K) - \frac{\alpha T^2}{T+\beta} \tag{2.3}$$

Utilising optical spectroscopy, the k-Space Associates Inc's kSA BandiT system analyses the absorption edge of the semiconductor sample and infers the temperature from the band gap. This can be configured in a reflection or transmission mode. In reflection a broadband white light lamp is shone on the sample and the solid state spectrometer detects the reflected wavelengths whereas in transmission the heater acts as an infrared lamp. The latter is predominantly useful in circumstances prohibiting a lamp. Reflection has some modest advantages in the range of photon energies and independent intensity control down to low temperatures. Additionally, in reflection light can pass through the sample twice, increasing the chances of absorption and producing a more pronounced step.

While thermocouples and pyrometers are also used for sample thermometry in MBE systems the BandiT offers many benefits. Thermocouples are rarely in good thermal contact with the substrate itself, rather providing feedback on the heater as well as being obscured from radiant heating of K-cells. Pyrometers measure black body radiation, which is subject to the material's emissivity. Emissivity is sensitive to surface changes, unknown for experimental growths and can be skewed by degraded viewports introducing a large uncertainty. Additionally pyrometers can be sensitive to parasitic radiation, such as from K-cells, and operate best above 500°C. Band edge thermometry measures the substrate directly, is ignorant of emissivity and in reflection mode can operate at low enough temperatures for the ideal growth window of tetragonal CuMnAs on III-V substrates.[16]

Growth Setup

This project utilised an existing 'mini-MBE', which is well suited to experimental growth runs. It has a small volume making changes and pumping down to UHV more efficient. In practical terms the reduced capability and size constrains it to be a more dedicated system with less responsibility outside the project scope. A full diagram of the mini-MBE including Bandit and RHEED components is given in fig. 2.5. There is capacity for six material sources occupied by five K-cells and a water cooled Veeco As vapour source. The materials effused from K-cells were Ga, Mn, Al, Sb and Cu. Flux from these sources was under pneumatic shutter control, with the 150W heater controlled via a single thermocouple connected to individual PID controllers. The vapour source is composed of a As reservoir and cracker with flux controlled by a manual needle valve. The As reservoir was held at constant power (around 400°C) and the cracker at a constant temperature of 650°C via PID control.

The rotational heating stage would accept 3" molybdenum sample holders, which were used for single crystal epiready GaAs substrates in conjuction with a PBN backing plate. A prepared substrate holder could be attached to the transfer arm in the load lock chamber at atomspheric pressure. Once pumped down to 1×10^{-6} Torr the holder is introduced to the main chamber and passed to the rotational heating stage. Rotation of the stage is useful for two purposes. Principally it improves homogeneity of stoichiometry over the surface by averaging over local variations in flux and additionally it expands the utility of RHEED by accessing all the azimuths of the surface reconstruction.

The only points of contact between the stage and sample holder are 3 pins passing through holes at the edge and a further 3 sprung pins pushing on the back to keep it in place. The stage has a 2” graphite-PBN element heater capable of reaching temperatures over 900°C and an accompanying thermocouple.

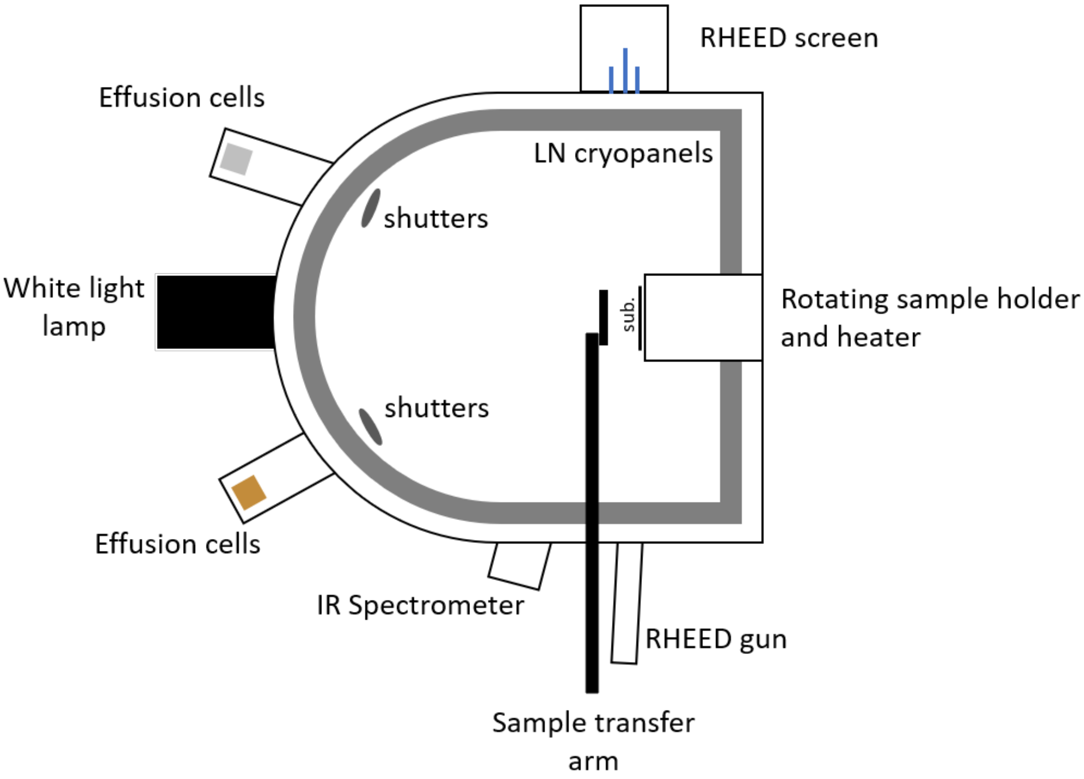

Fig. 2.5 A 2D scheme of the mini-MBE. The 6 effusions cell ports are arranged in a crown about the central view port occupied by the Bandit white light source providing symmetric line of sight to the substrate.

At full operation, UHV is achieved in the main growth chamber via a large turbo-molecular pump (TMP), supported by a backing scroll pump and 2 large ion pumps with a base pressure as low as 10^{-9} Torr. The load lock chamber has a small ion pump and small TMP backed by the same scroll that can be isolated from the main chamber TMP when in the viscous flow pressure regime. To reach pressures below 10^{-9} a liquid nitrogen cooled cryopanel envelopes the growth region, held at -150°C almost all atmospheric gases and impurities condense on the walls of the chamber.

Pressure is monitored in the main chamber by an ion gauge sensitive from 10^{-5} down to 10^{-9} Torr. Mounted on a retractable pole and backed by a 2” shutter plate the ion gauge can be moved in front of the substrate, playing the role of a beam flux monitor for setting fluxes to calibrated BEPs as well as masking the substrate from the sources.

Growth of CuMnAs

Single crystal thin films of collinear antiferromagnet (AF) CuMnAs in its tetragonal polymorph have been grown with success on Si, GaAs and GaP (001) substrates. The lattice orients at a 45° in-plane rotational offset to the substrate such that the substrate [110] direction lies along the CuMnAs [100] direction. GaP is the closest matched lattice of the substrates to be reported at just 0.7% and has been shown to produce smoother films of higher crystal quality with fewer defects than GaAs with a mismatch of 4.3%.[16] III-V substrates are the preferred substrate in MBE for their capacity for thermal oxide removal and buffer layer growth to improve the surface.

During growth of CuMnAs on GaP the optimal temperature window of the substrate is between 190°C and 260°C. Stoichiometry is found at a 1:1 Cu to Mn flux ratio and an As overpressure of up to a factor of 2. Reaching this ratio is a iterative process of trial growths and material characterisation performing magnetometry, X-ray crystallography and atomic force microscopy to identify excess source material and hone flux rates.

The (2x2) CuMnAs reconstruction emerges on the RHEED over the (2x4) of GaAs/P within the first 2nm of growth, at this thickness the CuMnAs is localised to islands multiple unit cells in height, with growth, these coalesce into single layer with elongated holes. After as little as 20nm growth (on GaP) a complete layer can form. Finally, Al capping of the layer at low temperature preserves the layer from oxidation in atmospheric air, an important consideration for material used in electron transport measurements.

2.1.2 Sputter Deposition

Sputter deposition is a highly versatile and well established technique for coating materials on a surface. The scope of control sees its application in research as well as industries from semiconductor fabrication to building materials. Ions in a plasma of a noble gas (the process gas is typically Ar^+) strike an incident target material with sufficient energy to dislodge particles outward. These dislodged particles are sputtered. Sputtered material then deposits on all exposed surfaces including, crucially, the sample substrate.

The energy of the Ar ion plasma is a key variable in consistent yield and sputtering rate but in general sputtered particles have a broad spectrum of energies. This is in contrast to MBE where a flux is made up of a narrow range of particle energies. At low Ar+ energies (<40eV) no significant sputtering occurs. From the binding energy of the surface atoms of the target up to around 1000eV knock-on sputtering occurs, the regime utilised in most depositions applications. A striking particle collides with potentially many target atoms both from the initial collision and subsequent collisions within the bulk. The process is illustrated in fig. 2.6a. The yield above 40eV increases at a steep, roughly linear, rate with striking energy and is best optimised when the process gas and target material's atomic mass are alike. At even higher energies the collisions give off massive yields as striking ions sputter many particles from the surface in craterous collision incidents. Even higher and sputtering becomes suppressed as ions enter the bulk without significant interaction and lose kinetic energy without sputtering.

Magnetron sputtering refers to the process of generating plasma and containing the constituent ions around a target surface to eject material for deposition. Magnetrons operate as a diode where the target is the cathode, typically in a circular geometry and for the system used in this work the anode makes up a sleeve around the target housing or cusp. The plasma is generated by means of a microwave plasma power source. The process gas is released into the chamber locally around the target and at sufficiently high concentration and voltage a current passes through. Due to ion bombardment secondary electrons are emitted from the cathode and held in a ring parallel to the target surface by a magnetic field emerging from below the cusp. The crossed electric and magnetic fields direct secondary electrons perpendicular to both, known as $\mathbf{E} \times \mathbf{B}$ drift. The secondary electrons ionise the Ar gas to generate a dense plasma in the region. In turn Ar^+ ions bombard the cathode sputtering material and providing a feedback loop that sustains the plasma. A simple cross section showing all of the components described above for a cusp like that used in this work is shown in fig. 2.6b.

The magnetron diodes can be run from either a pulsed direct current (DC) or radio frequency (RF) power sources. DC sputter is effective for conductive targets and cheaper to implement with a high degree of control. RF sputter alternates the sign of the applied current making it appropriate for insulators and dielectrics that would otherwise build by charge and arc.

Deposition characteristics are heavily system dependent and due to the plasma ring emission of material is non-uniform. Bespoke calibration of a machine is therefore required on a regular basis to test the rate and composition of film deposition.[96]

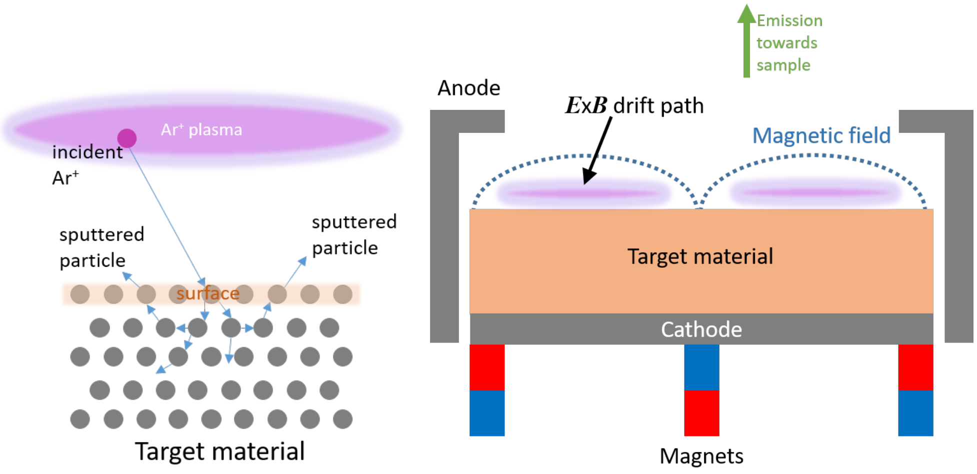

(a) (b)

Fig. 2.6 (a) The mechanism of sputtering in the knock-on regime involving an Ar+ ion colliding with the target to impart kinetic energy, kicking out a source atom. (b) A schematic cross section of the target cusp showing the arrangement of components that give rise to the ring of dense plasma at the target surface for efficient sputtering.

MANTIS Magnetron Sputter Machine

Samples described in 5.1 were sputtered by the author at the University of Nottingham using the MANTIS sputter machine. A cross section of the machine is depicted schematically in fig. 2.7. The main chamber, pumped by a turbomolecular pump and backing scroll pump is held at UHV as low as 1×10^{-9}mbar (with the exception of introducing process gasses). There is capactiy for six cusps sharing two DC power sources and one RF power source allowing for cosputtering of up to 3 targets.

Substrates are first pumped down in the load lock to UHV before being coupled with the sample stage. The stage can be heated to 500°C to further dry the sample and prepare the surface. Before deposition on the sample the consistency of sputter rates are tested on a retractable quartz crystal monitor while the sample is shuttered also removing any contamination or impurity at the target surface. Ar is fed to the cusps bringing the chamber pressure to around 1×10^{-3}mbar. The stage is rotated at 20rpm for homogeneous exposure across the surface before opening the shutters and carrying out the deposition.

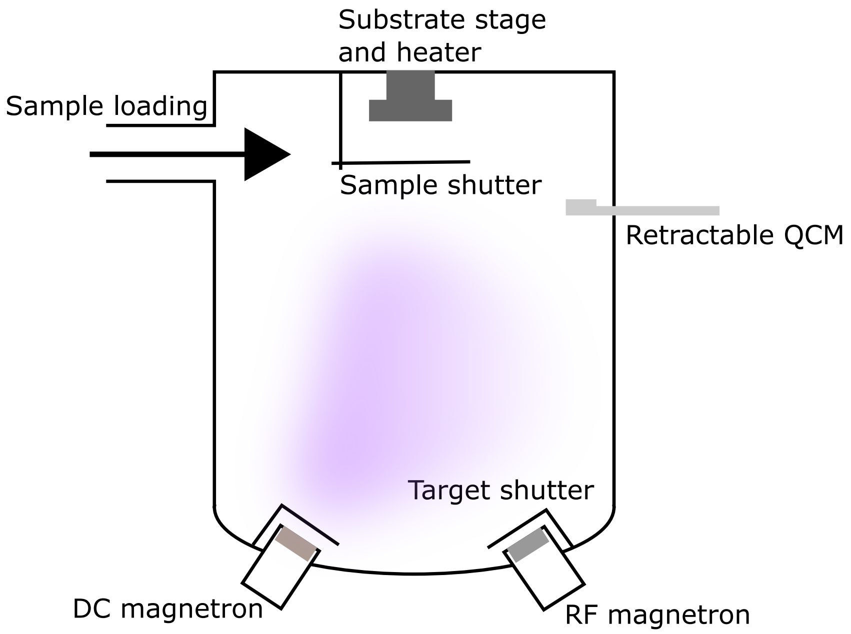

Fig. 2.7 Schematic cross section of the MANTIS magnetron sputter machine illustrating the arrangement of sample, cusps and other components.

2.2 Characterisation Techniques

2.2.1 X-Ray Diffraction

Diffraction in crystallography relies on elastic (Thomson) scattering of radiation by atomic crystal spacings of size akin to the wavelength resulting in characteristic peaks and patterns from the constructive and destructive interference of coherent rays. Results describe the reciprocal space of the crystal - taking the Fourier transform will describe the averaged real space order of the lattice. For crystalline materials the lattice can be probed by radiation in the X-ray regime of the electromagnetic spectrum following Bragg's law, with the lattice acting as a grating to produce the diffraction peaks and patterns. Other inelastic scattering can occur but is not discussed in the following work. The resulting diffraction pattern can be used to determine the size, quality and atomic arrangement of the sample material.

X-rays incident on a sample scatter coherently off electrons moving in-plane with the electromagnetic radiation adding a phase shift according to the path between different scattering centres. A simple 2D model of this additional path can be seen in fig. 2.8. Scattered X-rays will interfere to form a diffraction pattern characteristic of the structure of the crystal. The crystal lattice plane is described in terms of the Miller indices (hkl) that are the reciprocal of the intercept along the lattice vectors. These indices can be used to determine either the lattice parameter or interplanar spacing given knowledge of one of the two.

Basic geometric conditions for diffraction are encapsulated in Bragg's law. Reflection must be specular i.e. the angle ω between the incidence beam and sample surface and the angle θ between the reflected beam and sample surface are the same as in fig. 2.8. Further conditions are that reflected and incident angle are not parallel to atomic planes and the diffraction vector is parallel to the plane normal d_{hkl}. Reflection is efficient when the wavelength and interplanar spacing are of a similar order. In a simple 2D geometry as in fig. 2.8 depicting the reflection from two successive planes at the specular angle θ between the plane and beam the additional path $2dsin\theta$ for the second plane can be seen. All specular reflection from planes will interfere constructively is the distance d is an integer multiple n of the wavelength λ leaving the Bragg equation,

$$2d_{hkl}sin\theta = n\lambda. \tag{2.4}$$

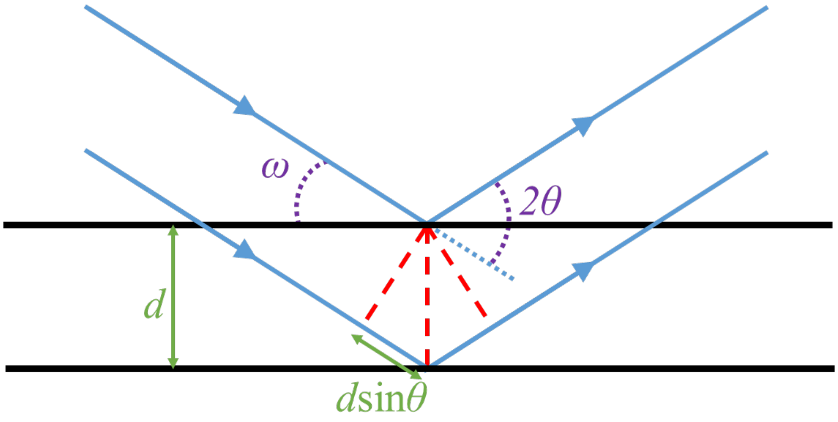

Fig. 2.8 The additional path allowing for constructive interference under Bragg's law for a beam of X-rays undergoing specular reflection from successive crystal planes, the fundamental basis for XRD. Here the incident angle between beam and plane is given as ω. Twice the angle of the reflected beam and the crystal plane, θ, is the angle between transmitted and reflected beams.

Further conditions rely on the atomic and geometric scattering factors, characteristic properties of the constituent atoms and crystal lattice that affect X-ray-electron interactions. The atomic scattering factor is a number defined by the ratio of the wavelength to the diameter of the atomic electron distribution

$f \approx \frac{\lambda}{D_e}$ accounting for the number and density of an atom's electrons available for scattering interactions. Bonds between outer electrons in condensed matter affect f but outside of the lightest elements, rarely encountered in XRD, the figure is closely approximated by a standalone atomic model.

The geometric structure factor considers the atomic form and arrangement of atoms in the unit cell and beyond Bragg's law is a significant determinant of the viability and strength of diffraction peaks where the geometry adds out of phase destructive interference. For example in in cubic systems all reflections are allowed for simple cubic lattices. For a body centred cubic Bravais lattice the structure factor is 0 if the sum of h, k and l is an odd integer. The structure factor is only non-zero for a face centred cubic Bravais lattice if h, k and l are either all even or all odd.[97]

PANalytical X'Pert Diffractometer

X-Ray crystallography in this work was performed using a Philips PANalytical X'Pert Materials Research Diffractometer equipped with a Cu target X-ray source. The beam was conditioned with a parabolic X-ray mirror and 0.02 radian soller slits to reduce divergence and collimate the rays. A symmetrical Ge220 monochromator selects for the Cu K_α photoemission of wavelength $\lambda = 1.54$Å. Two detectors are available for XRD: the PIXcel solid state detector from PANaltical and a high resolution crystal analyser gas cell. The path of the beam from source to detector is illustrated schematically in fig. 2.9a.

Chips of material between 10mmx10mm up to a 1/4 wafer were mounted onto a Eulerian stage, capable of linear movement in x, y and z as well as rotation in three axes. Rotation perpendicular to the xy plane of the sample is defined as φ, rotation perpendicular to the xz plane of the beam is ψ. Although rotation of the sample in the xz plane of the beam is θ movement in this dimension is achieved by movement of the source and detector optics. These cartesian directions and axes of rotation with respect to the sample are shown in fig. 2.9b. A linear resolution of 0.1mm can be achieved and angular resolution in θ is up to 0.0003° and 0.01° in φ and ψ.

Measurement

$2\theta/\omega$ line scans

Diffraction from the (00l) reflection was a relatively straightforward procedure

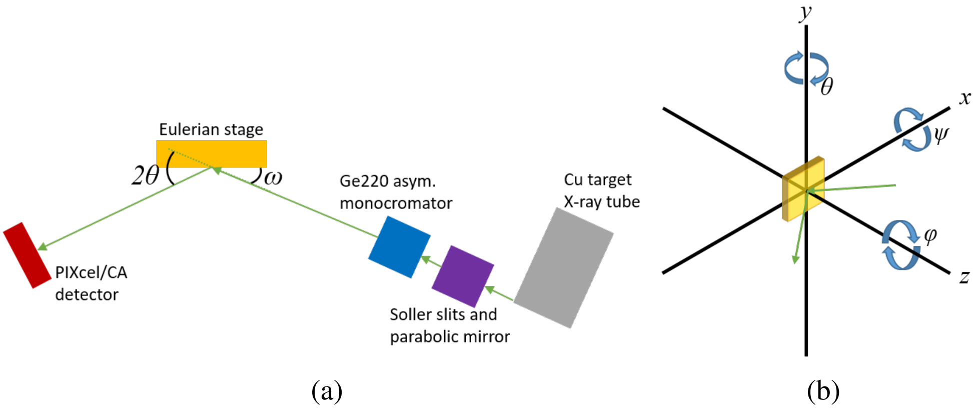

Fig. 2.9 (a) A simple schematic of the key apparatus from X-ray beam (green) generation to detection (b) spatial coordinate system of XRD stage centred at the sample

that allowed access to the d-spacing and c lattice parameter in the growth direction for all materials studied in this work. Samples were mounted on the stage and the 2mm×4mm beam aligned by optimising the high intensity (004) substrate peak. A small (typically $<0.1^{\circ}$) offset accounting for tilt in the sample, stage, source and detector alignment in the θ plane results in two angular parameters 2θ and ω that are illustrated at the sample in 2.9a. The source and detector then sweep through range associated with the layer (00l) peaks synchronously to maintain an equal angle with respect to sample surface.

Reciprocal Space Maps

Line scans offer a slice of the reciprocal lattice where the angle is defined by the average spacing and breadth of the peak can inform the spread and quality. However, by varying the offset in ω the reciprocal space around the peak can be mapped.Performing reciprocal space maps (RSMs) requires crystals of quality between defect free single crystal epitaxy to at worst mosaic domains with low angular divergence in 'textured' epitaxy. Usually RSMs are taken over both a substrate and layer peak for assessment of strain, however, in this case they are useful in accessing high angle reflections of low intensity that are difficult to achieve alignment upon. As a result in-plane *ab* lattice parameters could be determined with confidence.

2.2.2 X-Ray Reflectivity

X-ray reflectivity (XRR) is a fast technique for assessment of crystalline thin film surfaces and interfaces. The nondestructive technique focuses on the collection and analysis of intensity curves from reflected X-rays incident on the sample at a grazing angle and can determine thickness, density and roughness for films and multi-films from 1nm up to a few hundred nm in thickness.

Most condensed matter has a refractive index of less than 1 in the X-ray regime. As a result, below a certain critical angle - dependent on electron density - (usually <2°) the X-rays undergo total external reflection at the surface. Above the critical angle penetration below the surface increases rapidly with incident angle ω with the reflected intensity dropping several orders of magnitude. From this angle assessment of the density of a layer can be made. Roughness at surfaces and interfaces gives rise to diffuse scattering and loss of specular intensity and the rate of signal decay provides an estimate of the interface quality. Coherent surface reflection occurs both at and beneath the surface for multilayers and interference between elastically scattered rays produces interference fringes with θ. The frequency of fringes in θ is proportional to the spacing between interfaces providing measurement of layer thickness.

Measurement and Simulation

Measurements were also performed on the PANalytical X'Pert machine used for XRD with the substitution of some X-ray optics. The Ge220 monochromator was removed and beam moderated by an automatic Ni attenuator shuttered up to the critical angle. The beam footprint is reduced close to that of the sample by a 10mm brass beam mask. A gas cell detector is used to measure the reflected intensity, preconditioned by a parallel plate collimator and broadband graphite monochromator. These changes make for a high intensity to background ratio. [98]

The beam is aligned parallel to the sample so that it is half obscured from the detector at $\omega = 0$. The source and detector then synchronously sweep from $\sim 0.5^\circ$ to $\sim 6^\circ$ from parallel to the sample plane in a specular scan measuring intensity with incident angle. Results compared with simulated XRR fringe curves employing the proprietary X'Pert reflectivity v1.1 software that uses an iterative fitting algorithm to match the critical angle, intensity decay and fringe frequency with density, roughness and thickness respectively.

2.2.3 Atomic Force Microscopy

Surfaces of thin films can be mapped as 3D relief images by scanning probe microscopy, resolving the nanoscale by using an atomic force microscope (AFM). AFM operates by probing the sample surface with an ultra-sharp tip at the free end of a spring like cantilever controlled through a simple yet delicate feedback loop. Whether in contact or near touching non-contact modes the tip, with radius of curvature of tens of nm, is scanned across the sample surface. Forces due to interaction with the surface, predominantly Van der Waals forces, deflect the tip and bend the cantilever. The feedback loop begins with a laser spot on the order of the cantilever width (tens of microns) reflected off the back of the cantilever free end onto a split photodiode. As the cantilever is deflected the reflected spot shifts between the portions of the photodiode producing a difference in voltage between them proportional to the tip displacement. Movement of the tip on the scale of nanometers is amplified by the path of the laser beam, typically several millimetres, to produce such high resolution. The shift in balance on the photodiode is passed onto x, y and z piezoelectric controllers of the tip holder or sample to react to the surface features.

For the specific case of tapping non-contact mode, illustrated in fig. 2.10, the cantilever is oscillated near its resonant frequency while the tip is in close proximity to the surface. With the xy scanning of the tip rises and falls in the surface increase or decrease the damping on the cantilever oscillation. The frequency change is detected on the split photodiode and feeds back to the z piezo to adjust the mean height of the tip above the surface and maintain a constant oscillation amplitude. Compared to contact modes this technique reduces damage to the tip and surface. In the simplest case of imaging the surface the z piezo input is inferred as the sample topography, however, material properties and fields around the sample surface can also be examined in other modes. [84]

MFP-3D AFM

Use of AFM in this work was primarily concerned with observing surface features and obtaining a quantitative measure of roughness. This was performed using the Asylum Research MFP3D AFM head with Bruker OTESPA Al coated Si AFM tips operating with tapping in air mode .

The bulk of the active AFM components are contained in the head, which contains the tip, laser, photodiode resonant piezo and z piezo. Additionally

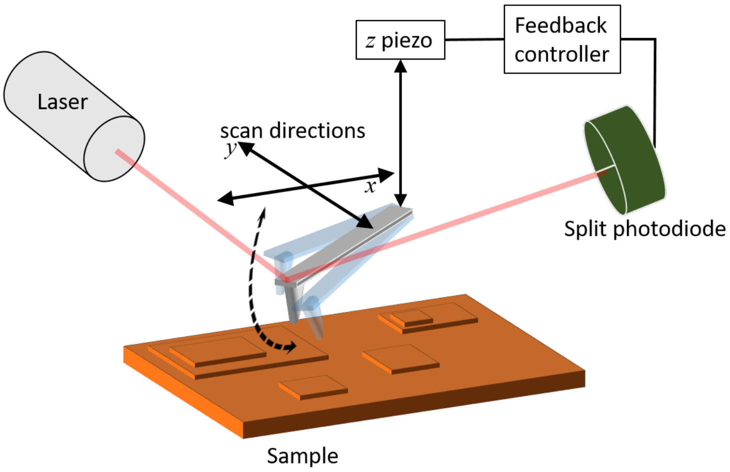

Fig. 2.10 A schematic of the operating principle of non-contact tapping mode AFM where the cantilever at the centre is oscillated in the z axis at a resonant frequency set point as it's scanned across the sample. Surface features shift the oscillation away from the set point, seen as a change in the deflection of the laser by the photodiode.

there microscope optics for a camera and fibreoptic cables for illumination. The tip is loaded into the head, and inverted over the sample placed on the scanner below. The scanner has x and y piezoelectric actuators for lateral movement of the sample relative to the tip with a maximum displacement of 90μm. The scanner and head are housed in an acoustic enclosure to exclude and damp noise, vibrations and air currents to the system. Feedback for the head and scanner is routed through the AFM controller outside the enclosure along with the computer for interface with the user.

2.2.4 SQUID Magnetometry

Measurement of samples' magnetic moment was carried out on a commercial Quantum Design MPMS XL superconducting quantum interference device (SQUID) magnetometer. The system is highly sensitive, capable of sensitivity down to $\sim 1 \times 10^{-8}$emu.

A SQUID itself is composed of a superconducting (SC) ring interrupted by one or two Josephson junctions, thin non-SC breaks in the ring. The system relies on the Josephson effect whereby SC Cooper pairs can tunnel across the junction.

In the MPMS the SQUID is coupled with an unbroken SC ring that surrounds the sample space, the detecting coil. The tunnelling across the Josephson junction is proportional to the magnetic flux through the detecting coil. As the sample is moved through the detecting coil the change in tunnelling current manifests as interference fringes equating to quantised changes in magnetic flux. With a feedback loop to offset the change and hold the tunnelling signal constant a feedback voltage is obtained as the readout signal for measurement. The feedback voltage is proportional to the magnetic flux and calibrated against a Pd reference sample.

In carrying out magnetometry, sample chips 5mm×5mm or smaller were cleaned with isopropol alcohol before being mounted and loaded for in-plane reciprocal sample oscillation measurements. Reciprocal sample oscillation moves the sample through the detector coil at constant frequency for several cycles allowing the signal to be locked, improving the signal to noise ratio. Measurements consisted of magnetisation with applied field carried out at a sample temperature of 300K or 2K. Additionally, during heating after low temperature measurements remnant magnetisation of the sample in the absence of an applied field was observed up to a maximum of 400K.

2.2.5 Neutron Diffraction

Neutron diffraction is a technique involving the elastic scattering of neutrons by a material to determine its crystal and magnetic structure. This practice harnesses the de Broglie wave like behaviour that follows $\lambda = \frac{h}{p}$ where h is Planck's constant and p the particle momentum. Similar to XRD a beam of neutrons is incident upon and penetrates a sample material, interacting with regular structures. Neutrons of wavelength akin to the atomic or moment spacing can be diffracted as if the material were a grating ($\lambda \sim 1$Å) following Bragg's law. Unlike X-rays, neutrons interact with the nucleus via the strong nuclear force rather than the electrons. In the absence of magnetic interactions neutron diffraction is sensitive to the arrangement of atoms, producing a diffraction pattern representing the reciprocal space image of the crystal.

All fermions including neutrons possess half integer spin angular momentum and therefore a magnetic moment. They can therefore interact with magnetic moments within a material and where there is magnetic order the scattering will be coherent and reveal the structure of the magnetic order.[99]

There are two practical sources for a neutron beam, either a fission source drawing on the nuclear reactor of a power plant or a spallation source. Spallation is the ejection of nuclear matter as a result of a high energy impact on the material. Work detailed below involving neutron diffraction of a $CuMnAs_{0.8}Sb_{0.2}$ film was performed at ISIS Neutron and Muon Source generating a pulsed beam by spallation. There, spallation is achieved by accelerating a pulsed beam of protons to high energies (800MeV) in a synchrotron before being directed at the target, a Ta coated W plate, ejecting neutrons from the W nuclei. The resulting bursts of neutrons are brought to the appropriate energy spectrum by a cryogenic solid methane tube moderator, producing neutrons of wavelengths between 2Å and 6Å. An illustration of this process along with a schematic of the WISH end station at ISIS is shown in fig.2.11.

The range of energies in the burst that go on to be refracted is resolved by time of flight measurements. The path, L, of the neutrons from spallation and moderation to the sample and detection is well defined. Substituting the de Broglie wavelength into Bragg's law and expressing the momentum in terms of neutron mass (m), displacement over the path L and time to the detector (t_d) we can obtain the effective wavelength from the elapsed time to the detector.

$$t_d = \frac{mL}{nh} 2dsin\theta \tag{2.5}$$

Detection of neutrons is complicated by their lack of charge. Instead detectors facilitate nuclear reactions with atoms to release energy. At ISIS's WISH end station 1520 tubes of ^{3}He, contained at 15bar, each 8mm wide and 1m tall surround the sample space spread across two semi-circular arrays. Upon incidence the ^{3}He nucleus is split into a free proton and tritium atom along with a free electron. The free, charged subatomic particles are accelerated to an anode and cathode that can be detected as a current. [100] Additionally, WISH possess a furnace sample environment able to heat samples to several hundred degrees (>500K). Commensurate heating and diffraction are able to show the emergence or disappearance of the magentic signal with heating or cooling through a magnetic phase transition critical temperature.

2.2.6 Transmission Electron Microscopy

Transmission electron microscopy (TEM) is an imaging technique capable of resolving features down to the atomic scale with the passage of an electron beam through a sample onto a detector screen. As with RHEED, XRD and neutron diffraction the resolution surpasses that of visible light due to the comparatively short wavelength of electrons. Samples consist of an ultra thin ($\sim$ 100nm) lamella to allow the transmission of the electron beam.

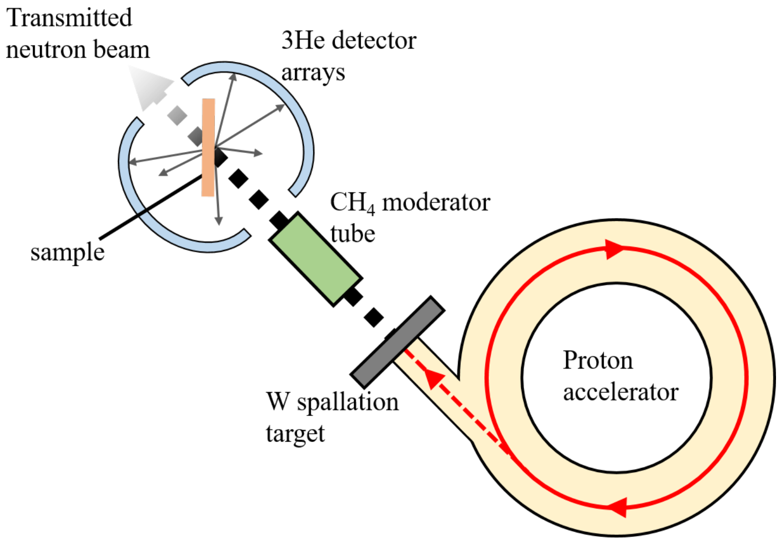

Fig. 2.11 A simplified top down depiction of neutron diffraction from a spallation source such as at the WISH endstation at ISIS Neutron and Muon Source.

An electron gun emits the electron beam at a well-defined energy, operating between 100keV and 400keV, through a vacuum. Apertures and electromagnetic lenses narrow and focus the beam. As the beam passes through the lamella interactions between the sample and electrons within the beam give rise to a multitude of scattered species and secondary radiation that is sensitive to distinct material characteristics, providing a wealth of dispersed information each of interest for isolated study. Further lenses magnify the beam before incidence on the detector. Commonly in modern TEMs, this is formed of a fluorescent screen or scintillator and CCD.

The direct beam makes up the bright field image in which contrast arises from the shadow of matter and scattered electrons that diverged from the beam. The degree of contrast in the bright field imaging mode is sensitive to compositional density.

In dark field imaging mode the diffracted pattern, made up of elastically scattered electrons, is selected by adjustment of the optics after the sample. For a crystalline sample the detector will obtain the reciprocal lattice, which can be transformed into a real space image of the sample structure. The contrast is opposite to that of the bright field, regions of little or no diffraction appear dark while regions producing scattering are light. The dark field mode is useful in the assessment of crystal quality and detection of defects.[101]

An evolution on the basic TEM configuration is a narrowed convergent beam and scanning mechanism that builds up a raster image from incremental measurement of elements of the sample. Scanning transmission electron microscopy (STEM) allows for a development on the conventional dark field imaging mode. Rather than adjusting the optics beyond the sample the direct beam is preserved passing to the typical detector and a dedicated annular detector collects the scattered electrons that diverge at higher angles. The incident electrons in this regime have largely undergone Rutherford scattering by the atomic nuclei making the technique sensitive to atomic number Z.[102]

Energy Dispersive X-Ray Spectroscopy

A further benefit of STEM is the highly localised signal that can be obtained from the sub-nanometre beam footprint on the sample. As the beam is incident on atoms they have sufficient energy to promote bound electrons in the inner shell, creating an electron hole. An outer shell electron with higher potential energy, relative to the nucleus, fills the hole releasing energy as a photon within the X-ray spectrum and characteristic to the shell migration. Detection of these characteristic X-rays by a spectrometer allows elemental analysis of the spot, this is the basic principle of energy dispersive X-ray spectroscopy often referred to as EDS or EDX. Complementary imaging and EDX of regions allows correlation of the two signals to map material features with elemental composition.[103]

2.2.7 Synchrotron X-Ray Microscopy

Wavelength resolved X-ray microscopy can produce images, including features down to the nanoscale, with chemical and magnetic contrast. The absorption of high energy X-rays by tightly bound inner shell electrons can promote them to available higher orbital states. The promotion follows the selection rule $\Delta l = \pm 1$ and spin is conserved. In transition metals this allows for the probing of the 2p to 3d excitation but not a spin flip transition.

Measurement of the absorption of X-rays at specific wavelengths by a material reveals resonances corresponding to specific atomic element binding energies of inner shell electrons. In transition metals the promotion from 2p to 3d orbitals has two absorption peaks due to the core level spin-orbit coupling between $J = \frac{1}{2}$ and $J = \frac{3}{2}$ in the 2p orbitals referred to as L_2 and L_3 respectively. The promotion of an electron from an inner shell orbital leaves a vacancy that is quickly filled by another electron with higher potential energy. This leads to the emission of secondary electrons, the predominant mechanism by which absorption incidents are detected. Synchrotron facilities are electron accelerator rings that provide a source of broadband high energy X-rays. Beams of appropriate narrow energy can selected by a beamline end station for X-ray microscopy.[104]

X-Ray Magnetic Circular Dichroism

Probing the magnetisation in XAS microscopy is possible with control of the X-ray polarisation, specifically circular polarisation for FMs. Circularly polarised X-rays have an electric field vector that rotates in the plane perpendicular to the direction of propagation of the wave **k**. The chirality of the rotation can be clockwise (CW) or anticlockwise (ACW) with respect to **k** and both carry angular momentum. The angular momentum is characterised by the photon spin, which has the same direction as **k** for ACW and opposite for CW.

Where the photoelectron originates from the spin split core level the photon angular momentum is transferred to inner shell electrons' spins via spin-orbit coupling. The two circular polarisation chiralities transfer angular momentum of opposite direction to the photoelectrons. The promotion of electrons from the 2p orbitals discriminates between CW and ACW X-ray absorption, with the two spin-orbit coupling split orbitals preferentially promoting spin of the same direction as the beam angular momentum vector.

In a two step process, illustrated in fig. 2.12(a) the portion under examination is exposed to an ACW polarised beam, is parallel to the 2p orbital moment preferentially exciting electrons in the spin up state. A beam of CW polarisation is then incident on the same portion and preferentially excites electrons in the spin down state. In both cases the photoelectron cannot undergo a spin flip and the XAS peak intensity is proportional to the number of available matching spin states around the 3d band. For a d shell transition metal with a spin moment arising from a bias between spin up and spin down states at the Fermi level there is a difference between the ACW and CW XAS spectra, shown in fig. 2.12(b). The difference between the two spectra is the X-ray magnetic circular dichroism (XMCD). The size of the dichroism scales with $\cos\xi$ where ξ is the angle between the polarisation angular momentum vector and the magnetisation.

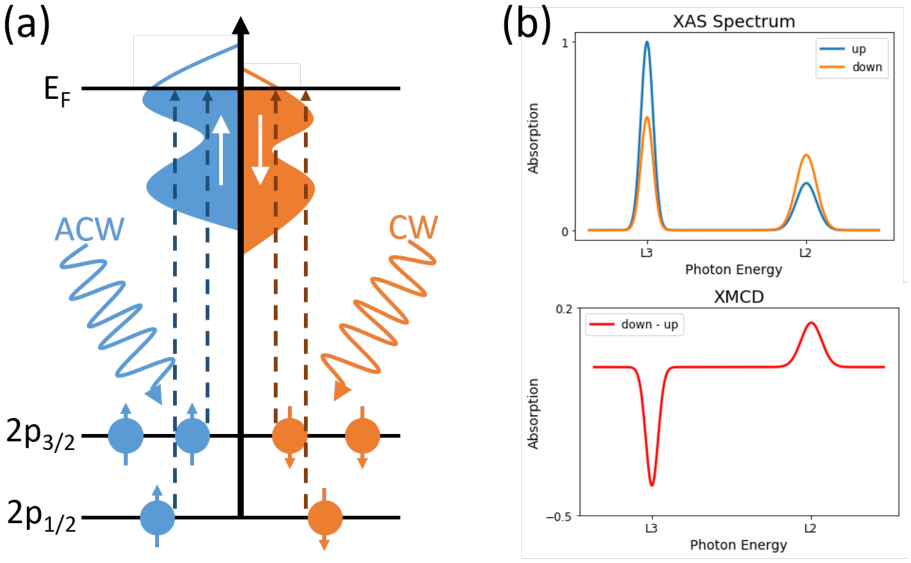

Fig. 2.12 The process of X-ray magnetic circular dichroism (a) two step exposure of the sample to ACW then CW polarised X-ray beam preferentially promotes electrons from the core level spin-orbit coupling split 2p level to the 3d band of a d shell transition metal with a spin bias around the Fermi level. (b) The two polarisations produce XAS spectra with different peak intensities, which after taking the difference leave an XMCD signal.

X-Ray Magnetic Linear Dichroism

Dichroism does not arise from circularly polarised X-ray absorption in AFs due to their magnetic ordering that preserves time reversal symmetry globally. However, the axial magnetic order parameter can be probed via another mechanism of dichroism using linearly polarised X-rays. In X-ray magnetic linear dichroism (XMLD) linearly polarised X-rays' are composed of electric field oscillations perpendicular to the direction of propagation within a single fixed plane. Two orthogonal planes of electric field oscillation can be termed horizontal and vertical.

Linearly polarised X-rays are sensitive to charge anisotropy. Typically in cubic systems charge distribution lacks sufficient asymmetry. However, in a system with magnetic order spin orbit coupling leads to preferential charge distribution along the axis of the magnetic order parameter. In collinear AFs moments are aligned antiparallel, typically along the easy axis at equilibrium. Where the X-ray polarisation is parallel to the moments a maximum of X-ray absorption transitions occur. The XMLD is obtained from the difference between the horizontal and vertical polarisation and varies with $\cos^2 \zeta$ where ζ is the angle between the polarisation and the axis of magnetic order.

While the effect is present in both AFs and FMs XMCD is preferable in FMs for its greater size and full direction rather than simply axial resolution. The detection of secondary electrons is the predominant means of measuring X-ray absorption from XMCD and XMLD processes. While the X-ray penetration depth of the sample is high the scattering of secondary electrons within below the surface is the critical constraint on the probing depth, typically between 2nm and 10nm. XMCD and XMLD are therefore highly surface sensitive processes. Although this is a limitation in bulk characterisation the technique is particular suited to the study of thin films.[104]

Photoemission Electron Microscopy

Images can be generated in X-ray microscopy by spatially resolving the emission of secondary electrons from the sample, which are generated by the X-ray beam with the requisite photon energy. This technique, involving the imaging of photoelectrons, is known as photoemission electron microscopy (PEEM) and a reduced schematic of the absorption imaging operation is presented in fig. 2.13. Detection on a pixelated CCD coupled with a scintillator is preceded by electron optics that focus the electrons. Lateral resolution is optimal at high electron speeds, necessitating a large accelerating voltage bias between the sample and microscope. At a voltage above 10kV resolution down to 25nm is feasible. To avoid arcing, as well as reducing the probability of scattering of electrons, PEEM is performed at UHV.

Contrast in the image can be elemental with the selection of a specific absorption peak, imaging of composition maps can be useful for inhomogeneous samples. With control of beam polarisation XMCD and XMLD PEEM is possible. In these images contrast is derived from orientation of the magnetic order parameter making domains, domain walls and topological features apparent. Additionally the (axial) direction of the magnetic order parameter can be determined allowing vector mapping of the spin texture.[104, 105]

2.3 Fabrication

Electron transport measurements demanded the fabrication of union jack (UJ) microdevices, material reliefs in the form of a cross with 8 arms of 10μm width, each terminating at a 200μm contact pad. A microscope image depicts one such device in fig. 2.14.

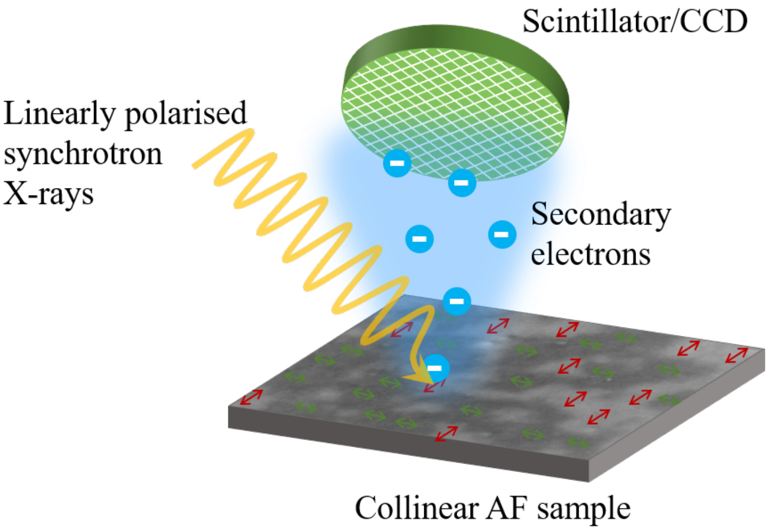

Fig. 2.13 An illustration of a linearly polarised X-ray incident upon a collinear AF sample with domains of orthogonal Néel vectors in green and red, the latter being parallel to the polarisation. Absorption of the X-rays induces secondary electrons of similar energy, which are spactially resolved by the CCD to produce an XMLD-PEEM image.

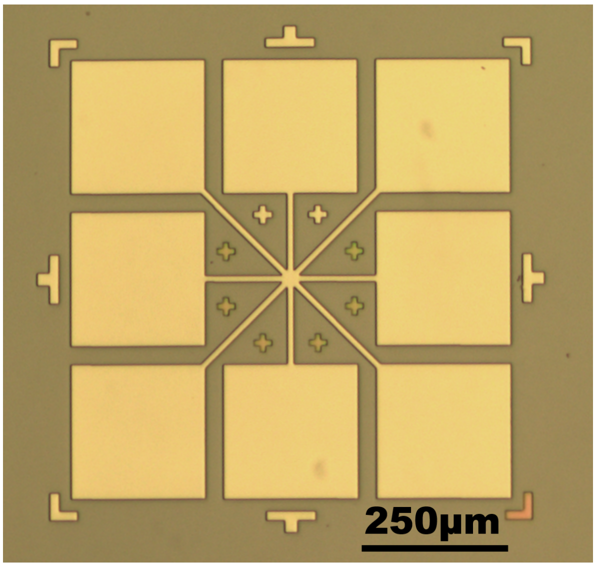

Fig. 2.14 5x optically magnified image of an UJ cross device including scale bar taken with a microscope camera.

Chips were scribed from the sample wafers for fabrication along the $\langle 110 \rangle$ GaAs cleave axes using a diamond tipped Dynapert scriber. They were cleaned with a series of solvents in a PTFE beakers placed in a sonic bath for 2 minutes. Beginning with Ethyl Lactate followed by Methanol, Acetone and finally IPA before drying under N_2 gas. A layer of BPRS100 photoresist was pippetted onto the chip before spin coating at 4000rpm for 30s. Any beading of the photoresist at the edge was wiped away with a foam cleaning swab. Chips were then left covered overnight for the photoresist to off gas and dry.

For the 10μm rounded union jack devices a chrome on soda lime glass stencilled in was used. This was cleaned with IPA and acetone before loading both the mask and chip into a Suss MJB-3 photolithography aligner. The chip was exposed to UV light of intensity 9.5mWcm^{-2} for 6s. The photoresist was developed in a a 9:1 solution of H_2O and AZ400K, submerging the chip for $\sim$10s before plunging into deionised water to arrest the development.

In the case of CuMnAsSb the K in AZ400K removes the Al cap for subsequent chemical wet etching. This was done in a 400:10:1 parts etch solution of H_2O, H_2O_2 and H_3PO_4 with an etch rate of CuMnAs of $\sim$1nms^{-1} etching for at least 60s to reach the substrate leaving the only material in the device geometry below the photoresist. Again the chips were plunged into deionised water to arrest the etchant. After confirming sufficient etch step height on a line profiler the photoresist was washed off with acetone.

Fe and FeGa UJ devices for magnetotransport measurements were ion milled by Dr A. Rushforth before removing the photoresist with acetone.

Devices were mounted onto 12-pin PCB headers using GE varnish and the pins bonded to the contact pads with an Al wire wedge bonder.

2.4 Measurement Instruments

2.4.1 Lateral Magneto-Thermoelectric System

Lateral measurements of the ordinary Seebeck effect along with magneto-Seebeck experiments were performed on a table top system built in house at the University of Nottingham by Dr M. Weir and the author with assistance from Dr O. Makarovskiy and Dr A. Rushforth. The system held the ends of a long chip between two heat baths maintained by Peltier devices at a temperature difference to induce thermoelectric effects detected by voltage probes on the surface. The addition of a horseshoe electromagnet with Fe pole pieces was used to induce a magnetic field transverse to the thermal gradient for magneto-Seebeck measurements. A schematic illustration of the lateral system is depicted in fig. 2.15.

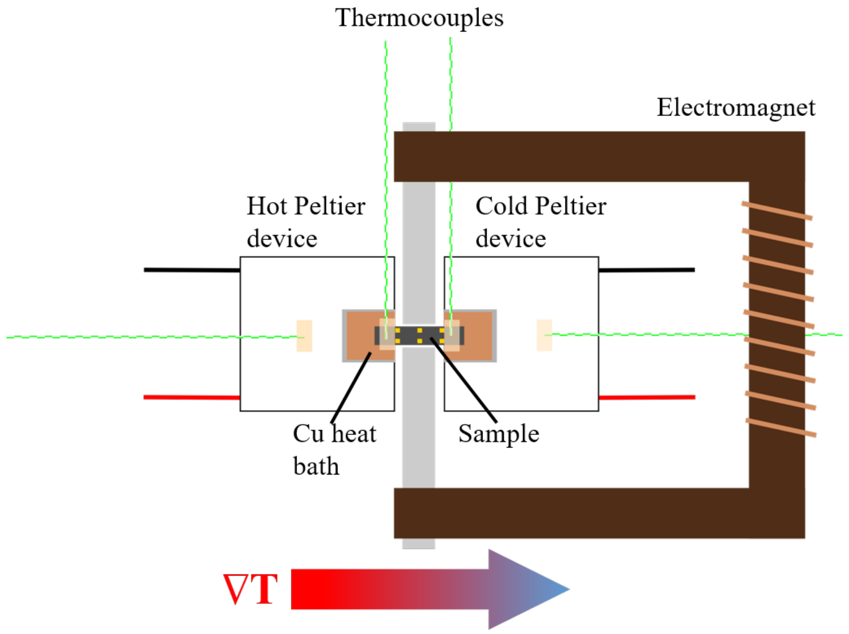

Fig. 2.15 A top down perspective of the lateral magneto-Seebeck measurement setup illustrating the arrangement of components around the sample at the centre.

Thermal gradients are generated by two Adaptive® Peltier devices, the hot side on the left and cold driven with reversed polarity on the right. Both Peltier devices were bonded to an Al heat sink with silicone thermal paste to exchange heat efficiently. A simple feedback loop was integrated using K-type thermocouples bonded to the middle of each Peltier with Kapton® polyamide tape and read with a USB I/O DAQ via a 5V thermocouple amplifier chip.

The 20mm×5mm sample, bridging the left and right Peltier, was seated with GE varnish on 1cm^3 cubes of Cu, themselves bonded to the edge of the Peltier with silver paint. The Cu acts as a buffer and thermal bath whilst also raising the sample into the region of the applied magnetic field. The field was induced between two soft Fe pole pieces of a Fe horseshoe electromagnet drawing from a dedicated polarity switching power supply. The 10V/10A source was controlled via an analogue input from a Keithley K2450 multimeter and could achieve maximum stable fields of ±120mT.

Seebeck measurements were made with micropositioning needle probes connected to a Keithley K2182 nanovoltmeter with stated instrument noise as low as 50nV. The probes were placed in contact with 1mm^2 Au pads 6mm apart longitudinally and 3mm transverse, which were deposited on the sample surface using photolithography microfabrication techniques. The Au pads, 70nm in thickness, improve contact resistance and demark fixed lengths of measurement from sample to sample.

To monitor the thermal gradient across the sample a K-type thermocouple was held to the sample surface with kapton tape above the ‘inner’ edge of the Cu block. A bespoke LabView VI controlled the thermal gradient but also synchronously triggered the magnetic field and voltmeter. The thermal gradient control hinges on the midpoint being held at ambient temperature T and takes in a user defined ΔT. Each heat bath is then held at $T \pm \frac{\Delta T}{2}$ as opposed to one side of the system being T_0 and the other $T_0 + \Delta T$. This extended the Peltier device range to a maximum temperature difference of 15K while avoiding bias towards ambient temperature across the chip.

2.4.2 Longitudinal Spin Seebeck Effect System

Measurement of the longitudinal spin Seebeck effect (LSSE) and the anomalous Nernst effect (ANE) in Fe and FeGa thin films were carried out at the University of Loughborough on an in house system developed by Prof. K. Morrison. [106] Samples were sandwiched between two Peltier devices, one active and one passive, that provided the heat pump (P_H) to generate a temperature gradient and heat flux monitor (P_Q) respectively. The arrangement of components in the LSSE system sandwich are illustrated in fig. 2.16. The system is calibrated in the absence of a sample to establish the a Peltier calibration factor c_P. The calibration factor allows conversion of the voltage V_P induced in P_Q for a given heat flow Q driven by P_H. A Keithley K2200 sourcemeter is connected to P_H applying between 0 and 0.8A while a Keithley K2110 multimeter reads out the heat flux monitor voltage.

In the middle of the face that is in contact with the sample on each Peltier device is the end of a thermocouple. Two thermocouples are used in differential mode to provide a low noise voltage signal proportional to the temperature difference.[107] One junction is on the heat pump side and one on the sensing side of the sample. The two are then united at an isothermal point with the remaining connection to another K2110 multimeter for readout.

For each measurement a 10mm×10mm chip of the sample was scribed from the wafer. Enamelled copper wire was bonded to the midpoint on opposite

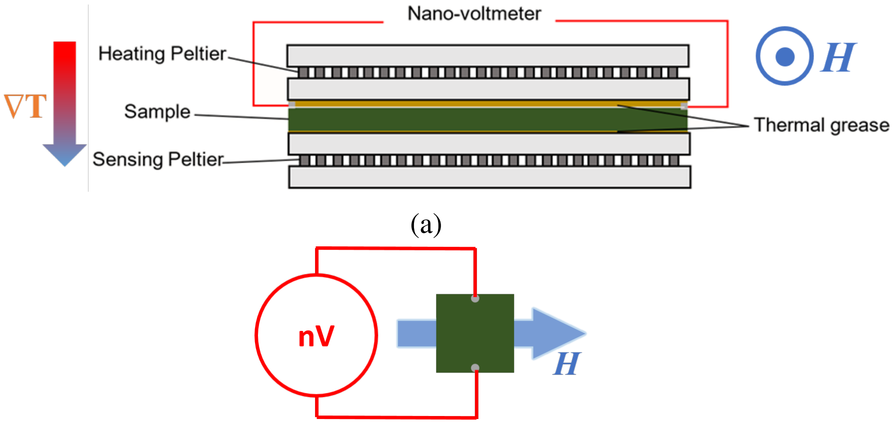

(a)

(b)

Fig. 2.16 (a) A profile view of the sample sandwiched between the active heat pump Peltier device and passive heat flux sensing Peltier device. The stack was clamped together and placed at the centre of the air gap of an electromagnet. (b) A reduced planar illustration of the voltage measurement across the sample surface, orthogonal to the applied magnetic field.

edges of the layer with silver paint, typically with 9mm separation s. The chip was then placed upon the lower passive Peltier device and the wire soldered to BNC connectors on a PCB circuit board. Coaxial shielded cabling connected to the Keithley K2182 nanovoltmeter for readout of the planar thermoelectric voltage V_{raw} from the layer surface.

To improve homogeneous thermal coupling between the chip and P_H a Cu spacer is bonded to the sample side of P_H, covered with paper as an insulating barrier and insulating thermal grease was applied for even contact across the faces. With the placement of the P_H on top the entire sandwich is tightened with two nylon screws until ‘snug’ without heavy clamping, which risks cracking the sample.

The sandwich device was held at the centre of a watercooled electromagnet with soft Fe pole pieces. Driven by a Kikusui power supply with reversible polarity the electromagnet produced a maximum high field of ±200mT. During measurement the field was swept from zero to positive high field, down to negative high field and back to positive high field to include the full hysteresis loop.

Heat Flux Method

In many studies, particularly early work on the SSE and LSSE the coefficient S was simply defined as the voltage V_{ISHE} (assuming a purely spin Hall contribution) scaled with the temperature difference ΔT. However this fails to take into account temperature drops at the interfaces, critical in the determination of the LSSE in thin films, and led to drastic variation in results between different LSSE systems. An approach reported by A. Sola [108] considers scaling the voltage with the heat Q flowing through the sample of area A, which provides much closer reproducibility between LSSE systems of disparate design and specification. By also normalising for the contact separation the LSSE coefficient can then be described by

$$S_{LSSE} = \frac{V_{ISHE}A}{sQ} = \frac{V_{ISHE}}{sI_Q} \tag{2.6}$$

where I_Q is the heat flux obtained from the sensing Peltier device.

2.4.3 Room Temperature Electrical Transport System

The Room Temperature System (RTS) is a table top electron transport environment designed by S. Poole to provide high thermal stability between -8°C and 65°C for measurements with the option of pumping to pressures as low as 1×10^{-6}mbar. Thermal control is delivered via a 20W 20mm×20mm Peltier device coupled to the sample header on one face and a thermal feedthrough to a heat sink on the other. The system has been optimised to operate around room temperature to perform stable antiferromagnetic switching experiments on CuMnAs. Thermal deviation from the set point is less than 2mK with an overshoot of just 4mK during ramping.

The Peltier device is sandwiched between the Cu sample stage and Cu thermal feedthrough block for efficient heat pumping from the sink to sample. The Cu feedthrough is connected to a large passive heat sink by Cu pipes below the main body of the vacuum chamber. The sample stage offers 12 pin header socket connected to exterior instruments along single core enamelled wires leading to a feedthrough. A Cu lid is bolted above the sample after loading to enclose the sample environment. The Peltier device power and Pt100 thermometer run to another flange opposite the device signal feedthrough. The top orifice allows for connection to a vacuum pumping rig, typically a tabletop diaphragm and TMP rig. A full illustration of the components and arrangement is depicted in fig. 2.17.

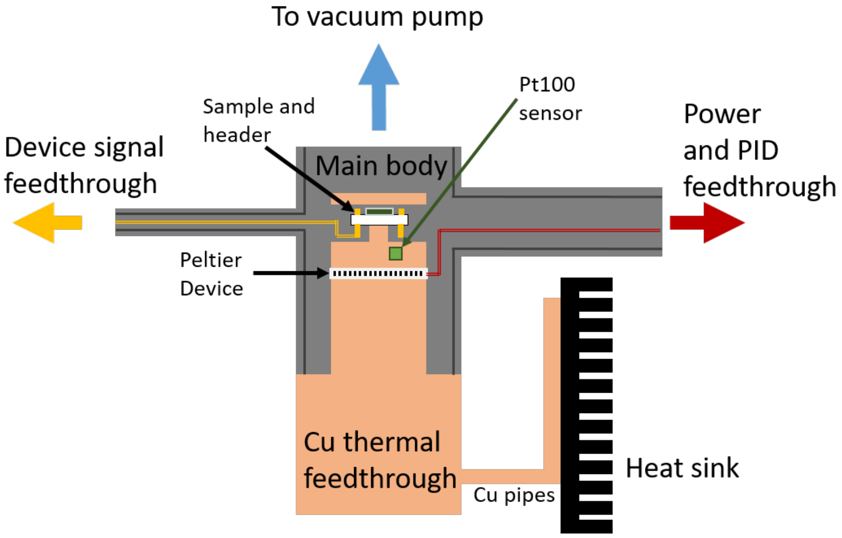

Fig. 2.17 A simplified schematic cross section of the RTS depicting the key components and their arrangement.

2.4.4 High Temperature Electrical Transport System

A high temperature transport environment capable of low pressures was used for transport measurements in the region of the Néel temperature of CuMnAs(Sb). The system is capable of reaching temperatures between ambient room temperature and 230°C. Background pressure of $1 \times 10^{-}6$mbar prevents a large degree of the sample degradation from oxidisation.

Devices and chips can be mounted on ceramic 12 pin headers with silver paint or GE varnish with electrical contact made between chip and pin by Al microwires made on a wedge bonder. The Cu sample environment is at the end of a stainless steel stem, which all slots into the steel vacuum chamber. The stem is removed for sample loading at a nitrogen overpressure and header inserted into the Cu enclosure. Within the sample environment is a halogen bulb that makes up the heat source and is shielded from the sample by a thin Cu wall for even radiative and conductive heating. A cross section of the sample environment showing these components is depicted in fig. 2.18. Heating is controlled by power to the bulb using a Eurotherm PID temperature controller with feedback from a type T thermocouple adjacent to the header socket. The arrangement of these components is depicted in fig. 2.18

Electrical contact to the header is fed to the exterior via ceramic bead insulated Cu wires, connecting to sourcemeter instruments by BNC coxial shielded cables. 8 connections are available on the breakout box allowing 4-wire probing and access to device multiple arms.[15]

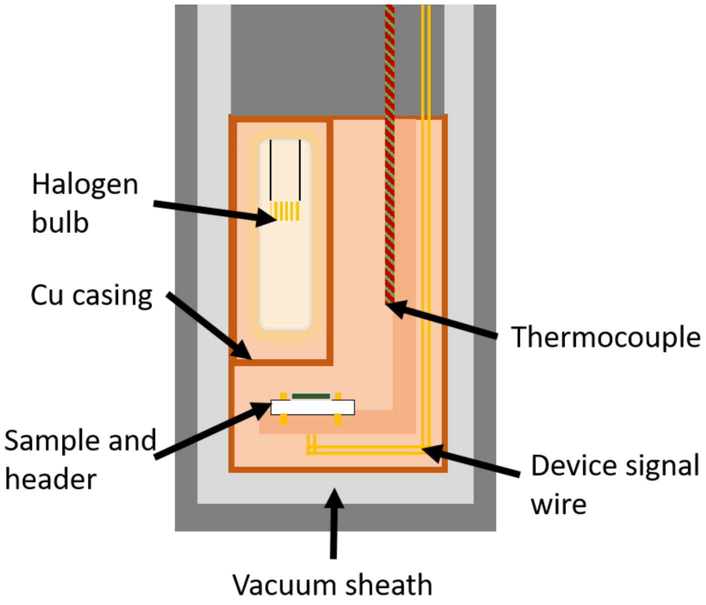

Fig. 2.18 The cross section of the end of the tubular vacuum chamber showing the Cu sample environment in the high temperature transport system.

Chapter 3

MBE Growth and Characterisation of CuMnAs$_{1-\alpha}$Sb$_{\alpha}$ Thin Films

3.1 Introduction

This chapter outlines the work carried out to grow and characterise CuMnAs$_{1-\alpha}$Sb$_{\alpha}$ thin films. Preceding these experimental growths, work to recommission the "mini MBE" system and grow control CuMnAs layers is detailed. Material characteristics associated with crystal growth are discussed. However, more in depth probing of the properties of CuMnAsSb is left for the succeeding chapter.

The collinear antiferromagnet (AF) CuMnAs has been a convenient testbed for many AF spintronic experiments. Most notably being the first AF to demonstrate electrical switching of the anisotropic magnetoresistance (AMR). Prior to this study CuMnAs had been grown in two MBE systems by Dr R. Campion and Dr V. Novak. While the first material was grown on single crystal GaAs(001) substrates, the highest quality material in terms of epitaxy, crystal order and AF domain size had been grown on GaP(001). The improvement between the two substrate materials is due to the difference in lattice mismatch with bulk CuMnAs of 4.3% for GaAs and just 0.7% for GaP. However, GaP wafers of equivalent quality to GaAs are less readily available, more costly and require more MBE infrastructure for their preparation. Consequently there is interest in manipulating the lattice parameter of CuMnAs with the substitution group V elements, while maintaining the overall tetragonal phase and magnetic order for well matched, high quality heteroepitaxial layer on GaAs.

Work by Dr. V. Hills [15] established that the substitution of P at the As site reduces the *ab* lattice parameter and so Sb was chosen as a candidate to increase the *ab* lattice parameter. Sb and As compete for the group V lattice site and the incorporation of Sb should lead to a larger atomic separation in the unit cell and a larger lattice parameter, which may lead to a decreased band gap as well as a lowering of Néel temperature (T_N). However, there was a concern that the relatively high vapour pressure of Sb below 400^{o}C would create issues with back emission from hot MBE components and contaminate non-Sb growths. Additionally, the Sb_4 tetramer is corrosive to some metals. Without a high temperature cracker, Sb will interfere with a mixed application MBE machine and so a dedicated or sacrificial test system is best suited. Therefore the 'mini-MBE', an older system that was idle at the time, was repurposed for this task.

The process of growing CuMnAs and later $CuMnAs_{1-\alpha}Sb_{\alpha}$ in the 'new' system will be broken down into three key steps for discussion. Beginning with the initial work to bring the "mini MBE" back into commission for GaAs including the crucial changes made, calibration of instruments and finding growth conditions. This served as a precursor to any growth of CuMnAs material and demonstration of the system's viability.

The second key step for discussion is the first growths of CuMnAs on GaAs. This work includes the fine calibration of fluxes for stoichiometry and optimisation of lower temperature growth conditions. Before the introduction of Sb, the ability of the MBE system to produce CuMnAs of sufficient quality was established. Characterisation of CuMnAs layers was carried out with XRD, AFM and SQUID measurements for comparison to well-studied growths of equivalent layers from the Gen III MBE system. While material grown in the two systems bears differences, the quality of CuMnAs grown in the "mini MBE" is judged to be of reasonable quality for the study given the limitations of the machine.

Description of the growth of $CuMnAs_{1-\alpha}Sb_{\alpha}$ at three Sb fluxes with in situ RHEED feedback are included. These three layers are characterised by the same methods listed above for crystal structure, surface topography and composition with the additional employment of TEM-EDS elemental maps and high resolution imaging of the crystal for one layer. With the aide of the latter, it was possible to confirm the incorporation of Sb and assess it's distribution through the layer. An increase in ferromagnetic crystal precipitates at the surface and changes in unit cell volume are found with increasing Sb flux. A comparative discussion of the layers is undertaken with speculation on the growth mechanics that lead to their varying quality.

3.2 Calibration for MBE Growth of CuMnAs

In order to grow CuMnAs$_{1-\alpha}$Sb$_{\alpha}$ (henceforth simply CuMnAsSb) it was first necessary to accomplish two things: convert the system to III-V group system and to grow CuMnAs as a benchmark against the established Gen III system operated by Dr R. Campion. The steps and results involved in this work are described below. In brief, the first objective was achieved by reconfiguring several parts and beginning to grow homoepitaxial GaAs on GaAs. Once instruments were calibrated stoichiometric fluxes and optimal growth conditions for CuMnAs were found over the course of five separate layer depositions.

3.2.1 Recommissioning for GaAs

The "mini MBE" was idle at air for two years before efforts to adapt it for CuMnAs. Before that time it had been used for growth of III-V nitride semiconductors including anion modulation epitaxy. The adulterants of the system were unknown and without a mass spectrometer the best attempt at mitigation involved prolonged UHV pumping, internal baking, burial under As and deposition of reactive ‘getters’ such as Al. This limited the presence of potential contaminants and ultimately, with the LN cryopanels at -150^{o}C, allowed base pressures in the region of 10^{-9}mbar.

In order to grow GaAs, a K-cell was refurbished in-house by A. Solomon with new Ta heat shields and a PCB crucible and installed. A needle valve As source with a cracker was also installed with the As reservoir run at constant power around 400^{o}C and the cracker at 650^{o}C on PID control. A limiting factor on the temperature of the cracker was knock on radiant heating of the sample stage due to the relatively small geometry of the chamber. This temperature was high enough to prevent condensation of As around the needle valve while avoiding extraneous radiant heating of the sample. A side effect of this relatively low cracker temperature was the presence of a significant proportion of As$_4$ tetramer in the As flux, however this was deemed permissible based on prior CuMnAs growth under similar conditions with the tetramer typically breaking up at the surface.

Further K-Cells were refurbished or fabricated for Cu, Mn, Al and Sb. Unlike the As, the Sb source was a shuttered source without a cracker. The use of a cracker was prohibited by both cost and geometry of the machine. Without the use of a mass spectrometer the proportion of Sb_2 and Sb_4 effused from the Sb cell are not known. The role of oligomers of Sb is outside the scope of this study and conditions at the growth surface were assumed to be consistent between layers.

After the system was dry and Ga and As sources prepared, growth was attempted. The first attempt at this was sample 'Test 1', largely following a procedure used in the Gen III system. Initially using GaAs(001) wafers surface oxide removal was determined by in situ RHEED feedback, observing the change from a hazy image to a bright spotty pattern as depicted in fig. 3.1. This process occurs rapidly at a surface temperature of 630^{o}C and allowed for a calibration point of the sample heater and surface temperature in the absence of substrate thermometry at that time.

Given the volatility of As, the needle valve was opened fully for the first growths. During high temperature GaAs growth, an excess of As above stoichiometry will be ejected from the growth surface. The Ga flux was set within a reasonable range of the ion gauge sensitivity such that 2 significant figures could be resolved. Commencing growth the RHEED feedback deteriorated quickly becoming faceted. After 2 minutes the Ga was shuttered but it was not possible to recover the surface with an As overpressure.

Several attempts encountered the same issue before using a higher As reservoir temperature, lower Ga flux and higher growth temperature. Sample 'Test 4' while initially appearing faceted on the RHEED feedback became streaky, typical of an As over-pressure. It was possible to determine the approximate stoichiometry of As and Ga from the appearance of 3x RHEED streaks at a ratio of 8:1 on the BFM.

Another growth, sample Calib 4, followed to determine the growth rate of GaAs and AlAs. This was achieved by first preparing the substrate with heat assisted oxide removal followed by growing a GaAs buffer. An AlAs layer and layer of GaAs were then grown for examination by XRR. The top two layers offer interfaces for XRR thickness analysis with results shown in fig. 3.2 where AlAs and GaAs layers are 28.5nm and 33.5nm respectively. Knowing the stoichiometric ratio of As, it was possible to calibrate 3 sources in single growth and measurement.

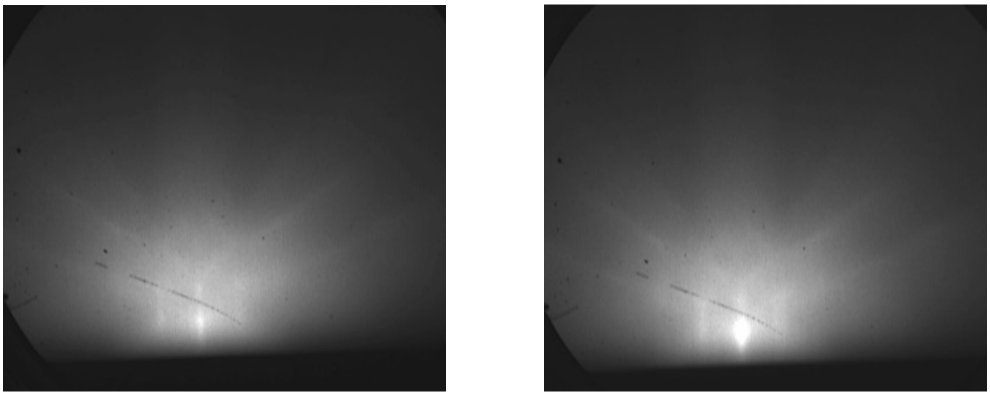

(a) 380^{o}C (b) 450^{o}C

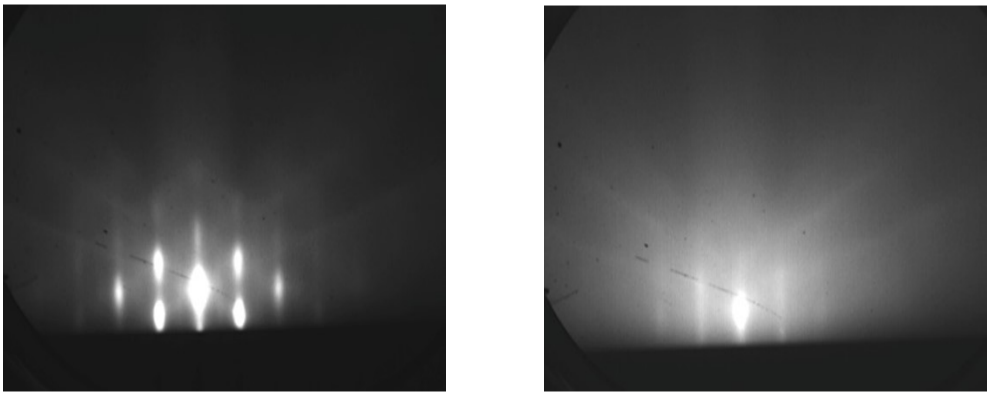

(d) 640^{o}C (c) 600^{o}C

Fig. 3.1 RHEED pattern along the GaAs [110] direction for an substrate undergoing thermal oxide removal increasing in temperature clockwise from 380^{o}C (top left) to full oxide removal at 640^{o}C. Images captured on GaAs(001) by Dr. R Campion.

Flux rates for the Mn source were calibrated via a similar method. A 10mm×10mm MgO chip was heated to 500^{o}C, allowed to cool to 250^{o}C and exposed to a Mn flux. After further cooling to 5^{o}C on the thermocouple the layer was capped with Al. The thicknesses of the layers were again determined via XRR given in fig. 3.3 in order to calibrate the deposition rate of Mn.

XRR measurements of a similar test for Cu were impeded by surface roughness. However, an approximate gauge from the extinction of the GaAs RHEED pattern in attempted growths provided enough information to begin efforts to grow tetragonal CuMnAs.

Sb was also resistant to smooth deposition on GaAs quickly exhibiting rough 3D growth incompatible with XRR. Instead, glass slides were prepared with photoresist developed to leave stencils of micron shapes. After deposition

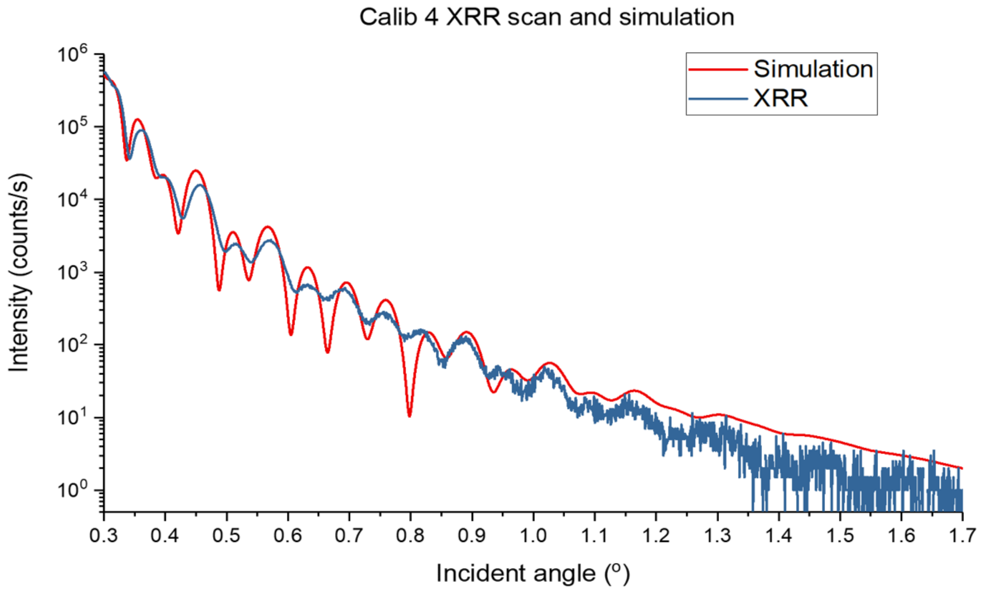

Fig. 3.2 XRR scan of Calib 4 AlAs/GaAs layer to determine growth rates. Scan data is given in blue and a simulated sample XRR curve plotted in red.

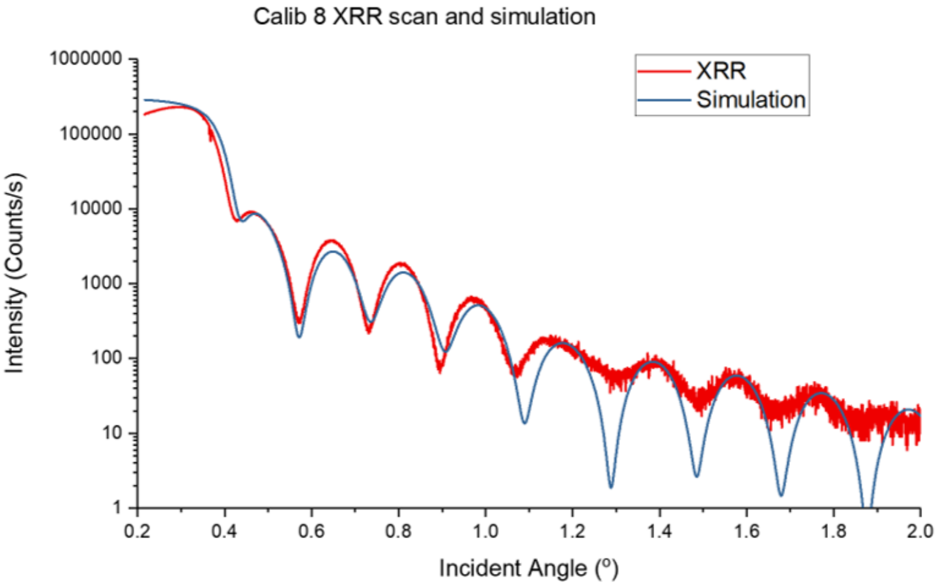

Fig. 3.3 XRR scan of Calib 8 Mn/Al layer to determine deposition rates. Scan data is given in red and a simulated sample XRR curve plotted in blue.

of Sb on the cold surface the photoresist was removed and the step height shown in fig. 3.4 measured via AFM.

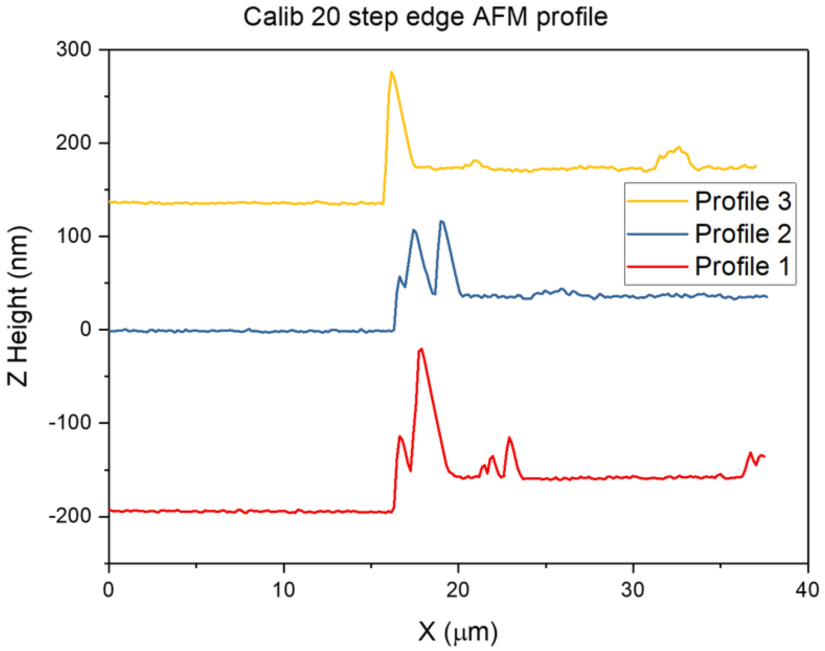

Fig. 3.4 AFM line profiles (offset in Z height) from a 3D scan across the step between the Sb and the previously masked substrate. The peaks near the edge are due to feedback overcompensation, tip contact and photo resist lift-off. Background plane levelling was performed by subtracting the same linear fit of the lower glass substrate baseline from all profiles.

3.2.2 Growth of CuMnAs

Following the growth of GaAs and the calibration of Mn and As sources, attention was turned to growing the first tetragonal CuMnAs in the mini MBE. The first growths would need to establish a suitable surface preparation, growth temperature and the stoichiometric ratio of Cu, Mn and As. Quality was assessed via in situ RHEED, AFM, XRD and later SQUID. The last growth in the series has been directly compared to an equivalent layer from the well-studied Gen III system to determine the suitability of the mini-MBE to grow CuMnAsSb.

The first attempt at growth, LXB012, began with substrate oxide removal at a heater temperature of 980^{o}C. GaAs was grown before allowing the surface to cool to 292^{o}C on the thermocouple. Without substrate thermometry an approximately 30% difference between thermocouple and surface temperatures was assumed to leave the substrate in the optimal window for tetragonal growth. Knowing the rate of flux for Mn, the ratio on the BFM from the Gen III was taken for Cu along with a slight overpressure of As. During growth RHEED feedback indicated the presence of a cubic order along with the emergence of spots, possibly growth of hexagonal crystal structures. The sample was capped with Al at low temperature before characterisation.

This first sample allowed a fair assessment of thickness via XRR in fig. 3.5 to establish a growth rate for CuMnAs at the given fluxes of 80nm/hr. XRD seen in fig. 3.6 also confirmed the epitaxial growth of tetragonal CuMnAs with a $2\theta/\omega$ scan of the 00L peaks. The sample was found to be rough in AFM. Table 3.1 gives the RMS and average maximum height of roughness for each layer along with growth notes. While the RMS roughness is 2.0±0.4nm the average maximum height of 5.7±0.9nm indicates that the peaks are severe for an epitaxial thin film.

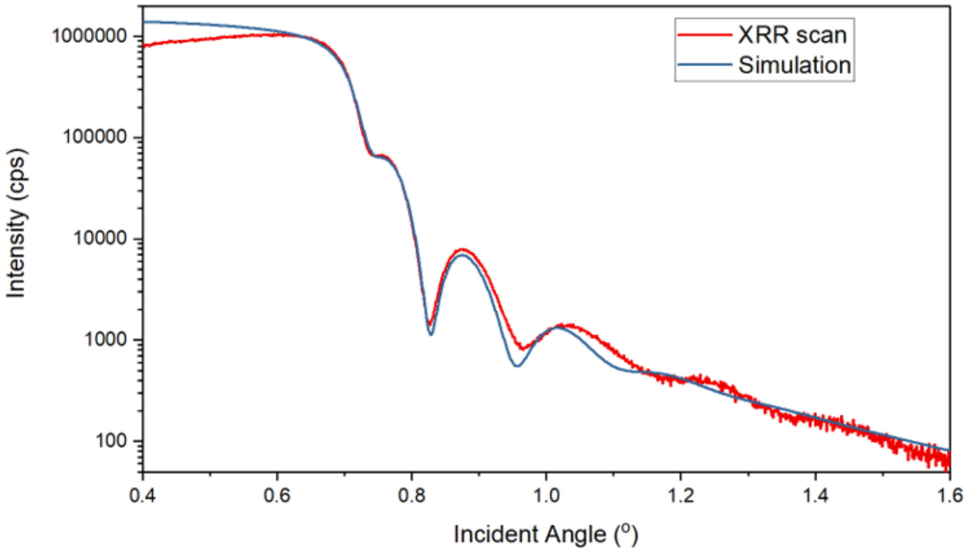

Fig. 3.5 XRR scan of LXB012 CuMnAs layer to determine layer thickness. Scan data is given in red and a simulated sample XRR curve plotted in blue.

The succeeding growth, LXB013, benefitted from the addition of band edge thermometry using a kSA BandiT to better understand the surface conditions in preparation and growth. Growth temperatures henceforth refer to values measured using substrate band edge thermometry. Without elemental analysis for determination of excesses in the stoichiometry this layer was a test of where improvement could be found in the material ratio space. Since Mn excesses lead to growth of ferromagnetic MnAs this was reduced in the first instance.

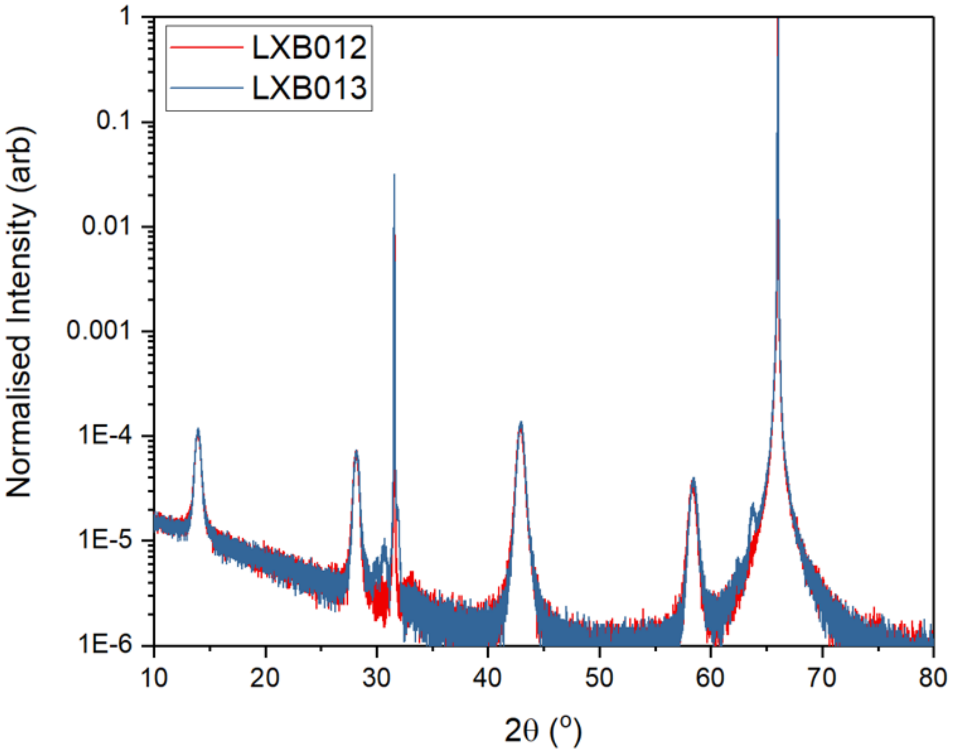

Fig. 3.6 $2\theta/\omega$ XRD lines scans of the out of plane 00L diffraction peaks for LXB012 (red) and LXB013 (blue). Intensity has been normalised to the substrate 004 peak.

Substrate band edge thermometry showed a difference in temperature between the edge and centre of up to 50^{o}C during oxide removal. Hence, for this sample the substrate was heated to high temperature with the As valve open to prevent loss and formation of Ga droplets as the centre reached 700^{o}C on the BandiT. After cooling to grow a homoepitaxial GaAs buffer layer, fluxes were set with 5% reduced Mn as measured on the BFM. Nucleating at 223^{o}C substrate temperature the heater was set to ramp down at a slow rate (0.5^{o}C per minute) to prevent runaway heating. This was hotter than contemporary Gen III growths but had proven successful previously. Uncertainty in the stoichiometric flux of As made a slight As overpressure preferable and higher CuMnAs growth temperatures held the advantage of less risk of As inclusions. RHEED feedback during the 23 minute growth showed a diffuse spotty RHEED patterm with the emergence of other orders at around 16 minutes. Subsequent AFM characterisation of the layer as detailed in table 3.1 found it to be rougher than LXB012. An XRD scan in fig.3.6 showed that whilst the tetragonal CuMnAs phase was maintained there are is also a low intensity peak at around 64° showing the presence of another crystal phase. The occurrence of the peaks coincides with powder diffraction peaks of Ga, possibly formed at the centre during the high temperature oxide removal. Due to the roughness of the sample the XRR data was of poor quality.

Many of the issues in LXB013 were presumed due to the high temperatures reached attempting to remove the substrate oxide from the edge of the wafer. The following growths focused on preserving good growth conditions around the centre. LXB014 was heated a substrate temperature of around 620^{o}C before growing the GaAs buffer. Given the poor surface quality and accumulation of material seen in RHEED and XRD the ratio of Cu on the BFM was reduced by approximately 7%. Nucleating slightly higher at 230^{o}C the RHEED still began as a diffuse spotty RHEED pattern, however, within 5 minutes exhibited smooth streaks that were maintained for around 10 minutes of growth. Later, extra spots were faintly visible on the RHEED and the temperature had risen slowly by 10^{o}C. Optimising surface preparation and growth conditions for the central region of the wafer greatly reduced the roughness. AFM results presented in table 3.1 show the improvement in LXB014 and close results in subsequent layers. While XRR was of better quality it posed little change to the growth rate.

A further growth, higher in Cu flux, showed no improvement but coincided with SQUID magnetometry becoming operational. A plot of the magnetisation with applied field is given in fig.3.7 with very little ferromagnetic response allowing the determination that a higher proportion of Mn was likely needed to achieve stoichiometry. Thus, LXB016 was prepared following the methods of LXB014 with 10% more Mn for a ratio to Cu of 1.5 on the BFM. Nucleating slightly lower at 220^{o}C to avoid higher temperatures seen at the end of growth the RHEED feedback was good. Within a minute the RHEED pattern typical of the CuMnAs reconstruction was discernible, smooth a minute later and at 4 minutes, streaky. Reducing the BandiT lamp power kept the surface temperature around 230^{o}C and the streaky pattern was preserved throughout the growth.

Initial results between RHEED and magnetometry suggested an improvement in the quality of the layer. In fig. 3.7a(a) small ferromagnetic response is present in the MH loop not seen in the previous sample. The remnant ferromagnetic moment of LXB016 in fig. 3.7b decays from 2K to 300K where it levels off to a very low signal below 5×10^{-8} emu. This is indicative of a Mn excess with the formation of MnAs with a Curie temperature (T_C) of 330K. Given the moment in fig. 3.7(a) the thickness of MnAs is equivalent to 40pm around 1% of the total layer thickness. The MnAs actually appears as 3D islands on the layer, however, the small quantity indicative of being near stoichiometry. It was judged that improvement was outside the resolution of the BFM and such trace margins were permissible.

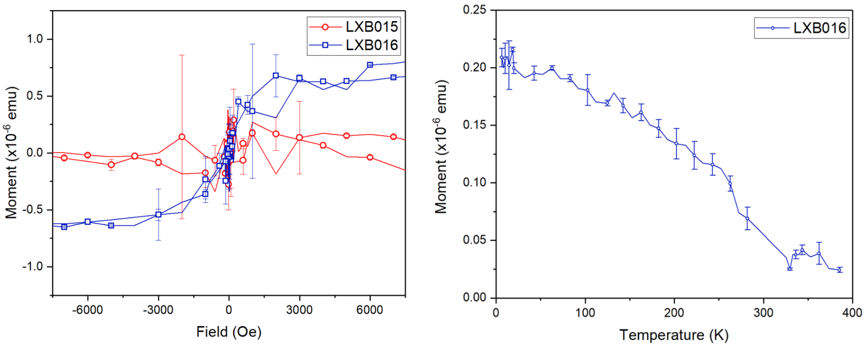

(a) (b)

Fig. 3.7 (a) Magnetic moment of the sample with applied field at 300K. (b) Remnant magnetic moment of the sample at zero field with increasing temperature.

Sample	**Aim**	**RHEED notes**	**Flux (e-8 Torr)**			**Temperature (^{o}C)**		**AFM (nm)**		**Outcome**
			Cu	Mn	As	Deoxidising	Start	RRMS	Rtm	
LXB012	1st attempt at CuMnAs	Some pattern, additional hexangonal	1.4	2	25	980*	<292	2.0±0.4	5.7±0.9	low quality, CuMnAs present
LXB013	With BandiT, test less Mn for stoichiometry	Some streaks, additional spots later	1.4	1.9	23	700	223	4±1	10±2	Poor, rough, requires better surface preparation.
LXB014	Prioritise conditions at the centre of wafer	Streaks good, additional spots later	1.3	1.9	23	620	230	0.6±0.4	2.3±0.8	Improved, likely still off stoichiometry.
LXB015	Higher Cu for stoichiometry	Streaks good, additional spots later	1.4	1.85	23	620	230	0.6±0.4	2.6±0.6	Fair but no significant improvement
LXB016	Higher Mn for stoichiometry	RHEED very streaky, consistent and smooth	1.4	2.1	22	660	220	0.6±0.1	2.1±0.4	Good, useful material

Table 3.1 CuMnAs growth notes in refinement of optimal growth conditions for the Mini MBE. *substrate heater thermocouple temperature.

3.2.3 CuMnAs Quality Comparison

Given initial results for LXB016 further material characterisation was carried out, comparing the results with a benchmark layer grown in the Gen III MBE system. LXB010 is an Al capped 30nm layer of CuMnAs grown on GaAs and useful as a control to assess the readiness of the machine before the introduction Sb.

XRD

Comparing $2\theta/\omega$ scans on both layers along the (00L) shows the CuMnAs peaks LXB016 to be sharper. Fig. 3.8 illustrates the 003 peak where fitting of peaks reveals FWHMs of 0.71^{o} for LXB010 and 0.54^{o} in LXB016. This difference is an indicator of a narrower spread in d-spacing of the unit cells making up the layer, an encouraging sign of good crystal quality in LXB016.

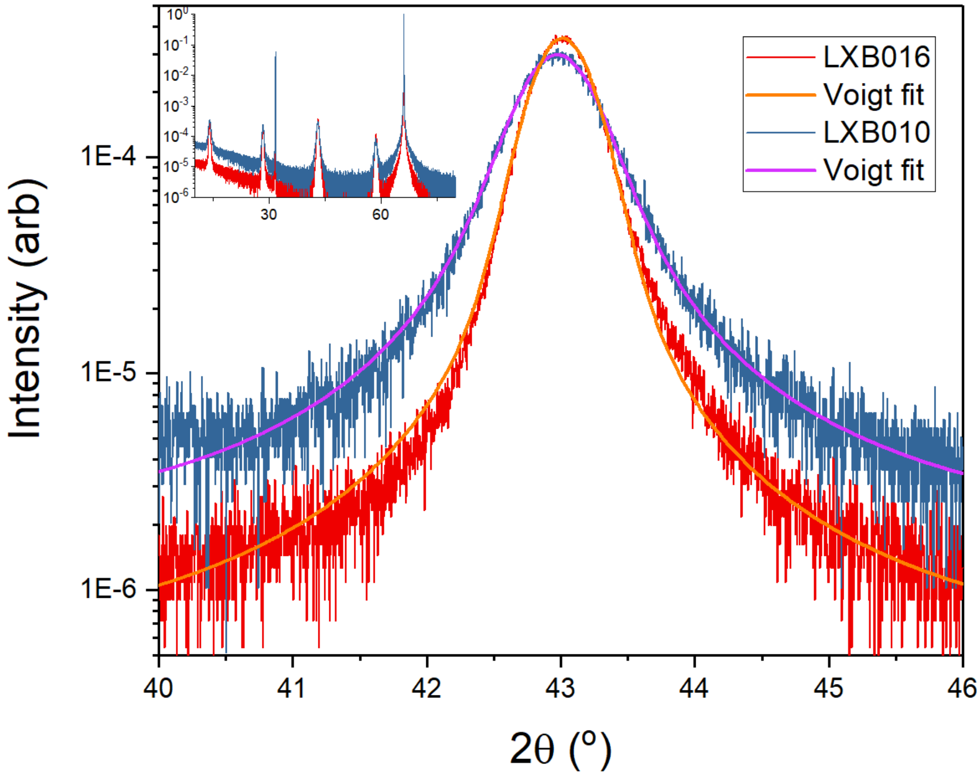

Fig. 3.8 $2\theta/\omega$ XRD line scans of the CuMnAs (003) diffraction peaks and respective Voigt fits for LXB016 (red/orange) and LXB010 (blue/magenta). The intensity has been normalised to the common GaAs 004 substrate peak.

AFM

Surface topography revealed a more stark difference between the two layers. While both exhibited roughness of the order of 4nm peak to trough, the difference was seen in their character and likely origin. Raster images are given for LXB016 and LXB010 in fig. 3.9(a) and (b) respectively, where a general roughness across the wafer is clear in the "mini MBE" layer the Gen III equivalent suffers from fissures. This is illustrated as 3D projections in fig. 3.9(c) where crystallite spikes make up the highest peaks on LXB016 and in (d) LXB010 is dominated by a singular hole in the scan, deeper than any feature on the "mini MBE" layer.

Fissures in LXB010 have been well studied by Dr V. Hills, Dr R. Campion [15] and Dr F. Krizek [16]. The holes are a product of the island growth of CuMnAs as it forms localised islands with the deposition of the first 3 unit cells of flux before growing outward. Within 4nm thickness the islands encroach on their neighbours leaving holes, elongated along the substrate [110]. With further growth the holes disappear from the surface, with a significantly lower density by 20nm and essentially vanished by 50nm. Profiles away from the fissure in fig. 3.10 show that the background roughness is of a similar order.

In the case of LXB016 the spikes are likely MnAs crystal precipitates based on the trace ferromagnetism seen in SQUID. The background roughness may occur for several reasons. Off stoichiometric growth may, in addition to MnAs peaks, disrupt the ideal 2D growth of CuMnAs and form islands. Most likely roughness may have developed during oxide removal and buffer layer deposition that impacts the growth of subsequent layers. It can be speculated that roughness in LXB016 gives way to strain relaxation before the formation of fissures further explaining the characteristic difference in roughness between the two layers.

Poorer overall roughness and trace presence of MnAs demonstrate that LXB010 and LXB016 are not of equal quality. However, the limitations of the "mini MBE" over the Gen III must allow for some margin of deterioration. The smaller heater size, designed for work on ¼ waters that inhibited homogenous oxide removal. Additionally, the sensitivity of the BFM over the background limited the degree of control over the stoichiometry. Under such circumstances the material and procedures for LXB016 were judged to be of sufficient quality to observe any likely change with the addition of Sb to CuMnAs.

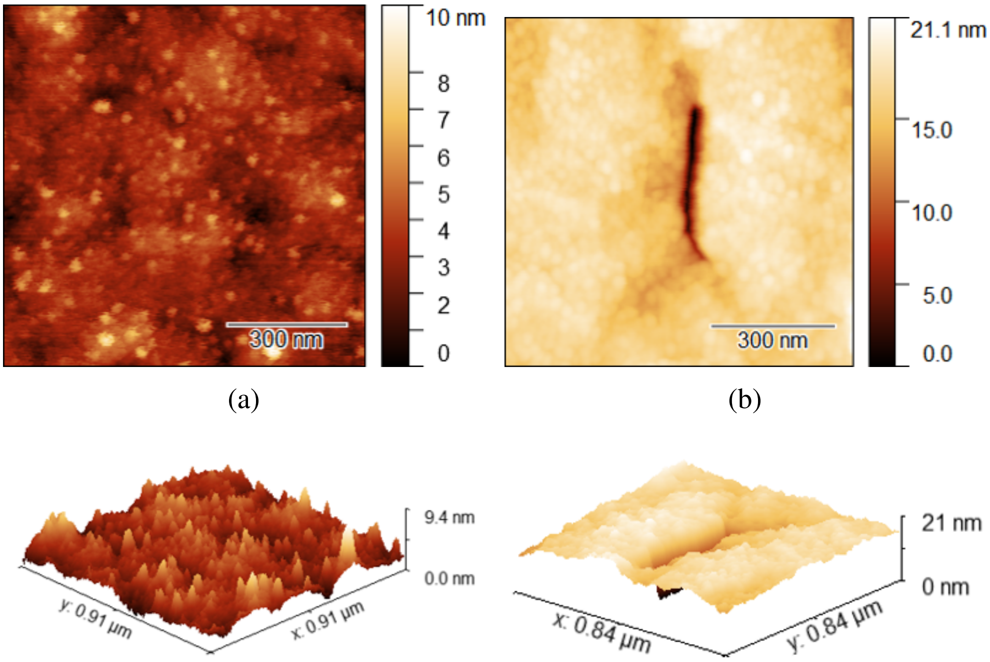

(a) (b)

(c) (d)

Fig. 3.9 AFM raster images of (a) LXB016 and (b) LXB010 and the respective 3D projection in (c) and (d) illustrating the order of roughness between CuMnAs samples.

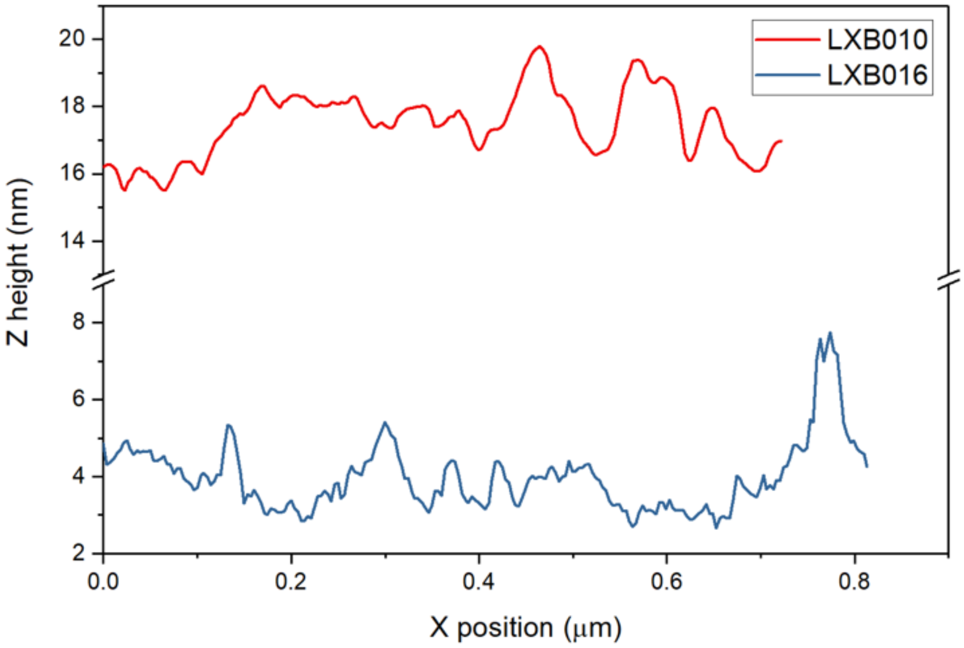

Fig. 3.10 AFM line profiles of LXB010 (red) and LXB016 (blue) along the flat of the layer away from large fissures.

3.3 Growth with Sb and Characterisation

Layers at three levels of Sb flux were grown in this study with an additional thicker growth at the median concentration for neutron diffraction experiments. Below, the details of growth including conditions, motivation and in situ RHEED feedback are presented. After growth, the material was characterised by similar methods to the previous section using SQUID magnetometry, AFM scanning probe microscopy and XRD crystallography. The latter technique was extended to include reciprocal space maps (RSMs) useful for measurement of d-spacing at high angles and quantitative assessment of crystal quality.

The quality of material varied significantly with Sb concentration, with an increase in lattice parameter at lower concentrations before a breakdown of the crystal order at the highest. Crystal precipitates, initially assumed to be alloys between Mn and group V elements, are present at the surface and increase with Sb concentration. Some control over strain and lattice parameter was found and would benefit from additional study to examine if further refinement is feasible.

3.3.1 MBE Growth of CuMnAsSb

After the work described previously to grow CuMnAs in the "mini MBE" some components of the machine began to fail including the continuous rotation of the substrate and Cu shutter. In spite of these issues growth was still feasible, however, due to the lack of rotation, the composition would be less homogeneous across the wafer. While the effects could not be entirely known or circumvented all data described below was performed on the central 20mm×20mm area of the wafer. Homogeneity was most likely to coincide there and as described in the previous section growth conditions were the most consistent. To address the broken Cu shutter the sample holder shutter was held in place until immediately before growth, raising the surface temperature before growth by up to 18^{o}C. However, this was not considered detrimental since excess As, already at a slight overpressure and competing with Sb, would be more likely to re-evaporate from the surface.

The only other change to the methods followed to grow LXB016 was the addition of the Sb flux. The flux was set in increments of 10% of the relative As in the layer. This figure was chosen for the resolution and sensitivity of the BFM, previous group V substitution of CuMnAs and consideration of the average dispersion within the layer. Work by Dr. V. Hills had found that fluxes of P above 1.5×10^{-8} Torr began to phase separate into binary alloy compounds, particularly MnP. With a background chamber pressure in growth of the order 1×10^{-9} Torr fluxes below 1×10^{-8} Torr proved difficult to reliably set on the BFM. The lowest figure feasible was set at 7×10^{-9} Torr, a deposition rate approximately 10% of the constituent As in a CuMnAs layer at calibrated fluxes. This was taken for the first growth (LXB023) and subsequent higher concentrations multiplied by two (LXB024, LXB025) and three times (LXB026) respectively. For a fully incorporated flux of 7×10^{-9} Torr on average there would be 1 Sb atom per 5 unit cells of otherwise tetragonal CuMnAs. Details for all the growths are summarised in table 3.2.

The first growth, LXB023, nucleated at 230^{o}C as recorded on the BandiT. The CuMnAs RHEED pattern emerged within 2 minutes and was streaky after another minute. The middle streak in the RHEED patter, typical of the (2×2) reconstruction along the CuMnAs [100] direction as previously determined [109] began to appear 4 minutes into growth. It grew was stronger after 7 minutes and the pattern is shown in fig. 3.11a. Notes taken during growth describe the RHEED pattern as exceptional after 13 minutes and is also shown in fig. 3.11(b). As the surface became more metallic the BandiT lamp was gradually reduced in power from 37% to 5% by the time the growth stopped after 40 minutes and approximately 60nm of material. After cooling to near 0^{o}C an Al cap was deposited. Based on RHEED feedback the growth was considered good and work to study the layer and continue Sb growths deemed of interest.

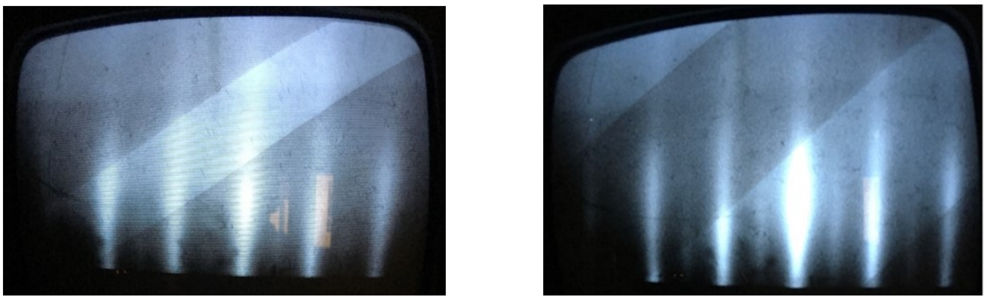

(a) (b)

Fig. 3.11 RHEED images of the growth of LXB023 at (a) 7 minutes and (b) 13 minutes showing the development of the (2×2) reconstruction.

Two growths were carried out at a higher flux of 1.4×10^{-8} Torr. The first, LXB024, was a thicker layer for T_N determination via neutron diffraction. This layer nucleated at 233^{o}C due to the reduced shutter control. The RHEED pattern became mixed within a minute and the CuMnAs streaks were visible a minute later. After 3 minutes of growth the middle streak of the (2×2) reconstruction pattern appeared and continued to improve for several minutes. After 22 minutes the RHEED began to become hazy and the middle streak faded ten minutes later. Some faceting could be seen 36 minutes however the development was slow. The growth was stopped after 97 minutes approximately 120nm thickness before Al capping at low temperature.

The second thinner sample at the same flux, LXB025, was nucleated marginally higher at 234^{o}C. The CuMnAs RHEED pattern emerged at 2 minutes and signs of a middle streak of the (2×2) reconstruction pattern along the CuMnAs [100] direction appeared after 4 minutes. The temperature began to rise after 8 minutes, addressed by reducing the BandiT lamp power gradually to 5% over 22 minutes. The growth was stopped at 40 minutes with a good RHEED pattern and again capped with Al.

The final growth to be carried out, LXB026, was at 2.1×10^{-8} Torr Sb flux. This layer nucleated at 238^{o}C and the RHEED pattern developed slowly. After 12 minutes the CuMnAs reconstruction RHEED pattern had developed but was not strong, 4 minutes later it had become spotty. At 24 minutes of growth the pattern was described as deteriorating but growth continued to 40mins to preserve equivalent thicknesses between the layers. Finally the layer was capped with Al at low temperature.

Sample name	Layer structure	Layer thickness (nm)	RHEED notes	Sb flux $[\times 10^{-8}]$ (Torr)
LXB023	CuMnAs$_{0.9}$Sb$_{0.1}$	60	Quickly streaky, exceptional pattern	0.7
LXB024	CuMnAs$_{0.8}$Sb$_{0.2}$	120	Quickly streaky, good, faceting at $\sim$ 30min	1.4
LXB025	CuMnAs$_{0.8}$Sb$_{0.2}$	60	Quickly streaky, good pattern	1.4
LXB026	CuMnAs$_{0.7}$Sb$_{0.3}$	60	Slow pattern, weak, spotty and deteriorating	2.1

Table 3.2 Details of the growth of each layer of CuMnAsSb

3.3.2 Material Characterisation of CuMnAsSb

X-Ray Crystallography

00L Line Scans

The $2\theta/\omega$ scan taken of the 00L inset in fig. 3.13 collected with a narrow detector confirm the preservation of the tetragonal crystal structure of CuMnAs. From the [003] peak of the main plot in fig. 3.13 the c lattice parameter and FWHM are determined via Voigt fitting and plotted in fig. 3.13(a) and (b) respectively. The out of plane c parameter is typically employed as a gauge of strain in the layer. There is little change between the lower Sb growths LXB023 and LXB025, however the highest Sb growth clearly shows a shift in c and broadening of the spread. Given the feedback from RHEED and broad peak width this layer's growth mechanics appear to have been disrupted, leading to the malformation of the tetragonal crystal phase. For CuMnAs grown on GaAs the mismatch typically leads to tensile strain on the layer, thus, a c parameter of 6.318Å is associated with a relaxation of the crystal. The relaxed thicker layer LXB024 is taller suggesting there is some tensile strain for thin layers at low Sb concentration.

The sharpness of the thin low Sb growths is consistent with a 50nm growth of CuMnAs on GaAs with little change in the out of plane lattice parameter. While this corroborated the assumptions of good quality from RHEED little could be said of the change to the crystal due to Sb. Further scans of the in plane crystal axes revealed more on the change between CuMnAs and CuMnAsSb.

Reciprocal Space Maps

Two dimensional reciprocal space maps (RSMs) of the [112] CuMnAs peak were acquired with a high resolution crystal analyser. Scanning the [112] peak provided access to the a and b in plane lattice parameters as well as a further measure of the crystal quality. RSMs for the three 60nm layers are shown in fig. 3.14. While LXB023 and LXB025 appear relatively sharp there is clear broadening of LXB026 and a deterioration is immediately apparent as in the 00L line scans. Taking the d spacing from the peaks and applying a simple calculation using the previously obtained c parameter provides the a and b parameter in fig. 3.15a(a). When compared to the relaxed LXB024 a and b values for the lower Sb layers LXB023 and LXB025 confirmed they are under tensile strain. As with the c parameter, the relaxed CuMnAs a and b parameter (3.82Å) is marginally smaller than that of LXB024 indicating that the unit

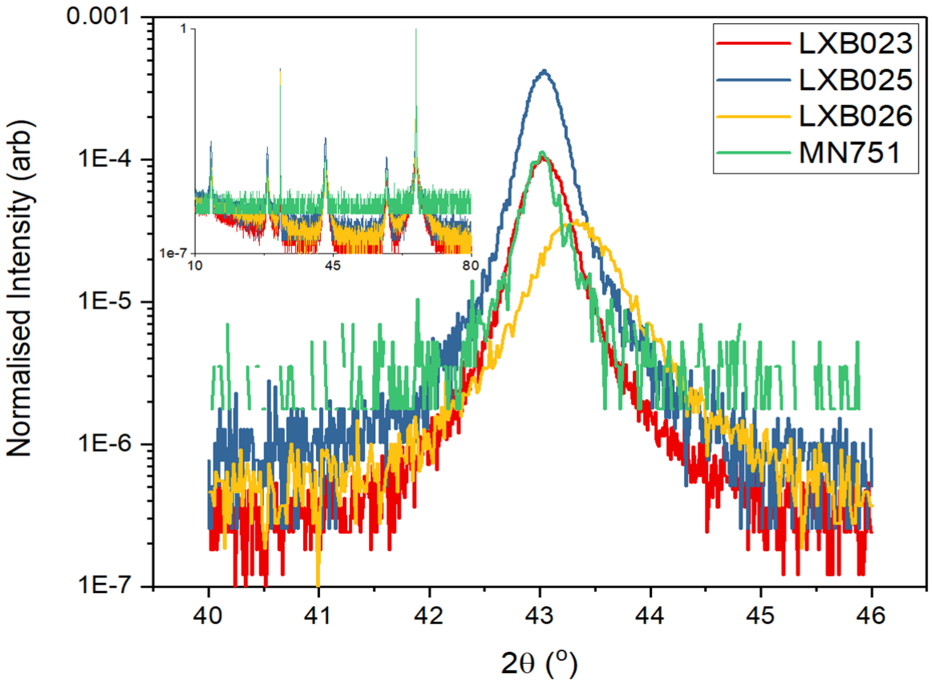

Fig. 3.12 $2\theta/\omega$ line scan of the [003] CuMnAs(Sb) peak with the 00L family depicted in the inset plot. All intensities are normalised to the 004 GaAs substrate peak. Juxtaposing the CuMnAsSb scans in green is MN751, an equivalent CuMnAs layer grown on GaAs.

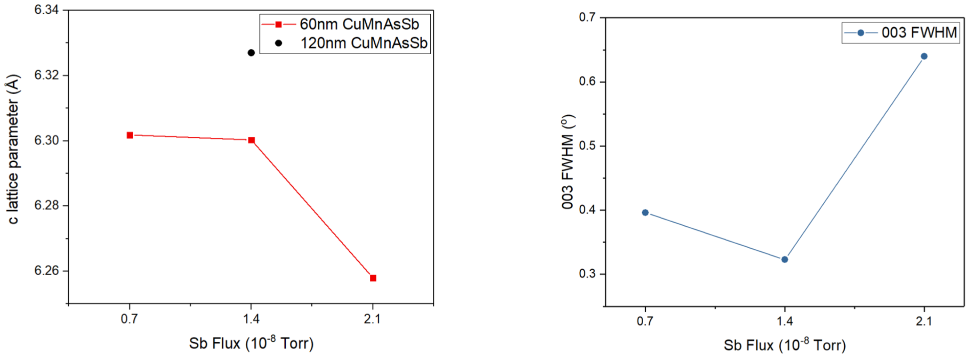

(a) (b)

Fig. 3.13 (a) out of plane lattice parameter c with Sb flux including the relaxed thick layer LXB024 in black and (b) the FWHM of the [003] XRD peak with Sb flux from which c was obtained.

cell was expanded with the addition of Sb. However, the a and b parameters are still in deficit of the GaAs leaving a sizeable mismatch. Comparing the sharpness of the peaks across both $2\theta/\omega$ and ω in fig. 3.15b(b) it was again clear that while the lower Sb concentrations were consistent the highest flux of Sb showed a broader spread. The assessment of LXB026 was increasingly poor indicating a limit to the Sb concentration at this series' conditions.

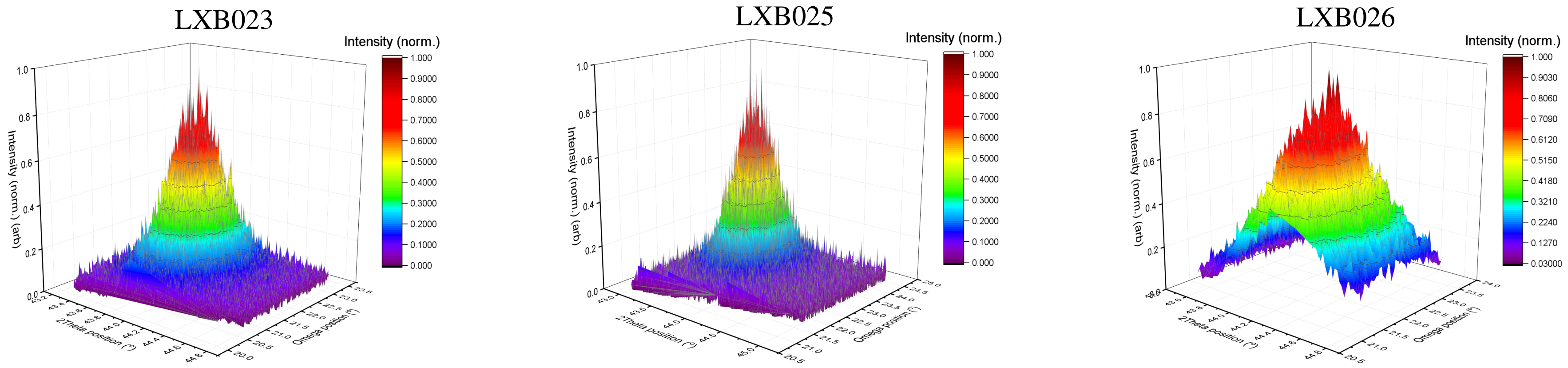

Fig. 3.14 2D RSMs of the (112) CuMnAsSb peak for each Sb flux. While source and detector parameters are fixed colour spectrums indicated are individual to each scan and are not normalised between differing scan settings and backgrounds.

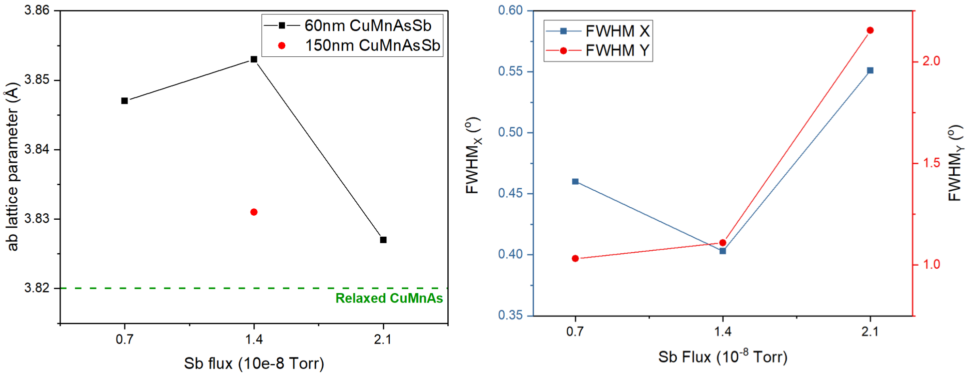

(a) (b)

Fig. 3.15 (a) a and b lattice parameter of CuMnAsSb layers determined from [112] RSM with Sb flux. The point in red is the lattice parameter of LXB024 a thicker less strained layer of CuMnAsSb and the green dashed line marks relaxed CuMnAs as grown on GaAs.[109] (b) the FWHM$_X$ ($2\theta/\omega$ line scan) in blue and FWHM$_Y$ (ω rocking curve) of CuMnAsSb layers with Sb flux.

Surface Scanning Probe Microscopy

Non-contact tapping AFM was carried out on each 60nm layer to obtain a raster image of the surface topography. The images, along with a 3D projection, are compared in fig. 3.16 where crystallite peaks on the surface can be seen in all three layers with a significant increase at high Sb concentration. Counting the area density of the peaks, fig. 3.17, found a 7 fold increase between the lowest Sb samples and LXB026. The highest Sb flux sample, similarly to the crystal analysis seen previously, is reaching a concentration that leads to a breakdown in the material and the formation of these precipitates.

While the conventional growth mechanism has certainly been disrupted, the origin and composition of these crystallites has not been determined by AFM and is investigated in greater detail in the following chapter via TEM elemental analysis. Beyond the tall features of the surface the background roughness of LXB023 and LXB025 consistent with the calibration layer of LXB016 with RMS of 0.5nm. Probing the background of LXB026 was not forthcoming due to the frequency of peaks that in a small scan area causing damage to the tip.

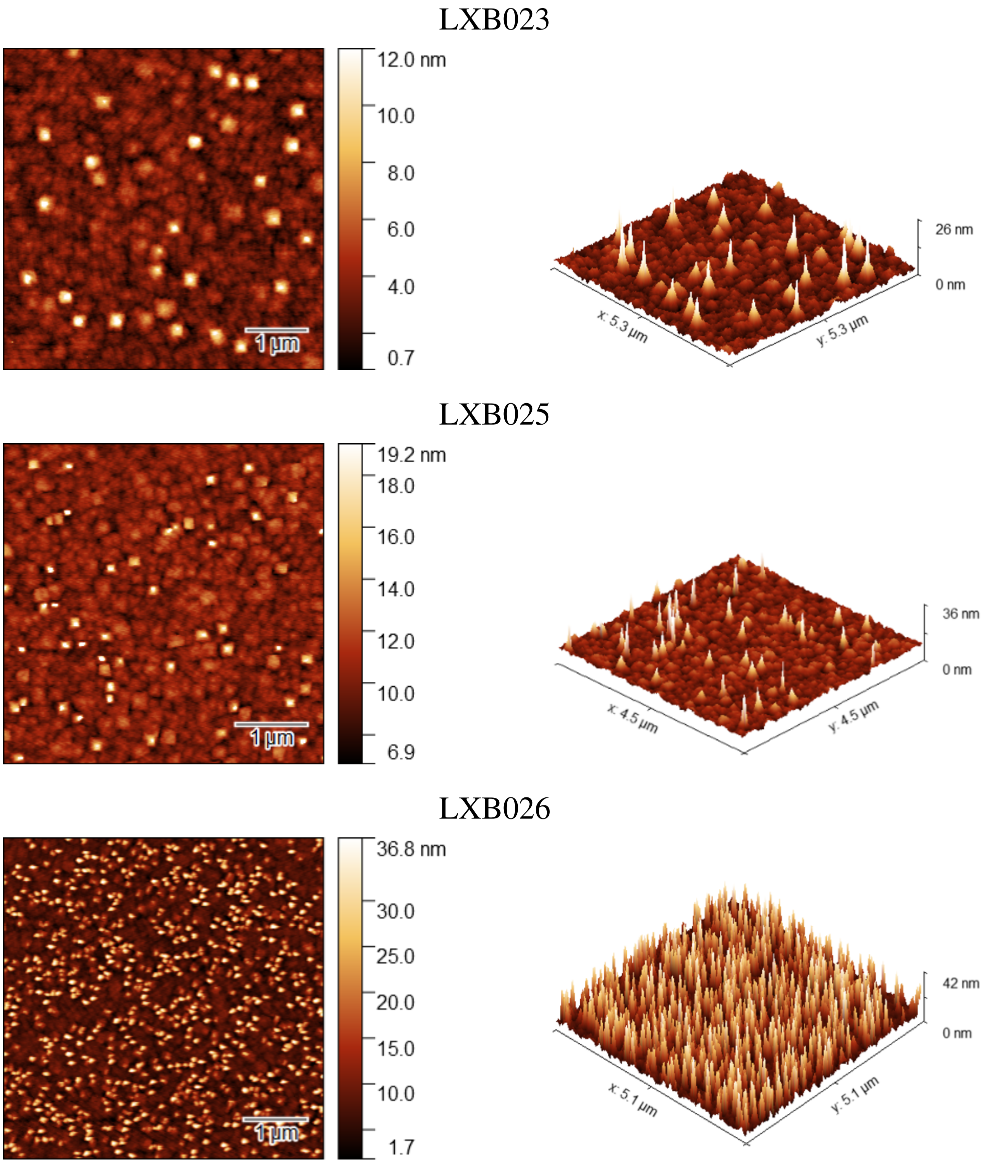

Fig. 3.16 AFM raster images of each CuMnAsSb layers at each flux and a 3D projection of the height trace.

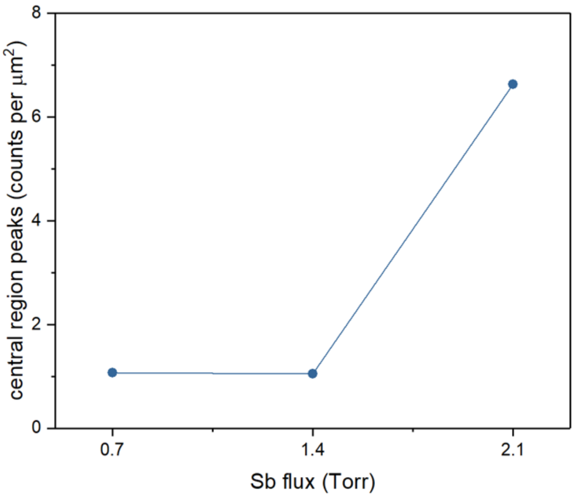

Fig. 3.17 Density of crystallite peaks that precipitated to the surface of CuMnAsSb layers with Sb flux determined using MATLAB regionprops function.

SQUID Magnetometry

Sample chips were measured in +10kOe (1T) field sweep scans at 300K and the remnant magnetisation at zero field from 2K to 370K after a 10kOe saturating applied field. All layers measured via SQUID magnetometry displayed a FM response with hysteresis loops in fig. 3.18(a). As shown in the inset plot the magnetisation is proportional to the Sb flux, indicating a direct role of the Sb concentration in growth and formation of FM material.

Previous studies of nonstoichiometric CuMnAs by Dr. V. Hills found MnAs appeared as islands on the surface. It was assumed that the precipitates seen in AFM were the origin of the FM signal, however, the density of peaks in AFM is not proportional to the Sb flux as is seen in the magnetisation. Rather, the FM material may well originate from material in the layer. Further investigation of the cross section of layers including elemental mapping is carried out in the next chapter.

A simple calculation assuming that the FM material is entirely MnAs with a bulk magnetisation of 500emu/cm^3 reveals that the thickness would range from 0.4nm to 1.6nm for these samples. While these quantities appear reasonable differences in the remanence suggest MnAs is not the sole FM. In fig. 3.18(b), above the T$_C$ of MnAs at 320K the magnetisation was not entirely extinguished. Another FM signal persists, likely MnSb with a higher T$_C$ of 590K.

Establishing that, while a likely candidate, MnAs is not the sole FM present it is also clear that the coercive field of LXB023 is markedly higher than the latter two layers. The FM composition is likely different at this lower flux possibly composed FM MnSb or a multiple other alloys of Mn. Owing to the 5 unpaired electrons of Mn a multitude of FM compounds such as Heusler alloys are readily formed.

Another feature of note in the remnant magnetisation is an increase in the rate of decay between 150K and 200K. This was speculated to originate from either an unknown FM compound or alternatively a spin reorientation transition (SRT), the change of easy axis from one crystal axis to another, which could occur in this region. Thermally driven SRTs have been described in variants of tetragonal Mn$_2$Sb based intermetallic compounds. While Mn$_2 - x$Cu$_x$Sb has not been well studied it is discussed as a candidate in the Mn-pnictide family. One such study found a Mn1.95Cr0.05Sb alloy with a SRT during cooling in the same region as the change in fig. 3.18(b) between 150K and 200K. [110]

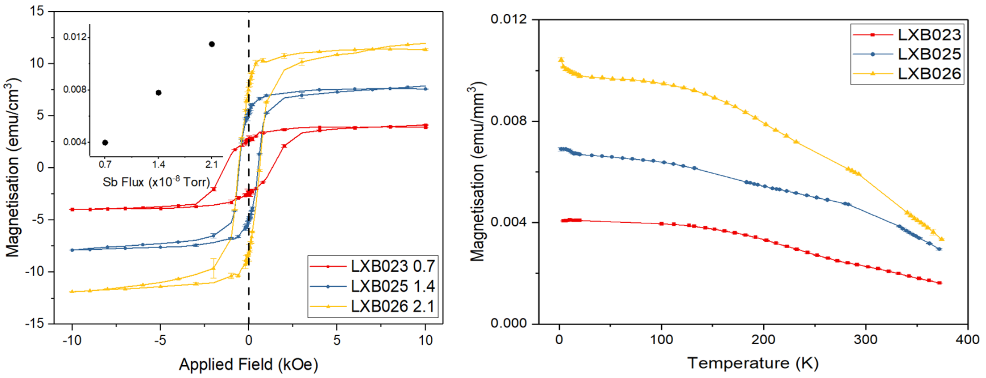

(a)

(b)

Fig. 3.18 (a) Magnetisation with applied field for all three 60nm CuMnAsSb samples at 300K. The inset plot depicts the magnetisation at saturating field with Sb flux. The diamagnetic background signal due to the GaAs substrate has been subtracted. (b) Remnant magnetisation with temperature for each sample.

3.4 TEM-EDS

Two ultrathin lamellae of LXB025 were prepared and imaged in transmission electron microscopy (TEM) by F. Kriezek at Charles University in Prague on a Thermo Fisher Scientific TEM Titan Themis 60-300 including elemental mapping and atomic resolution. The images present greater insight into the substrate layer interface, elemental dispersion and crystallographic defects not treated by prior material characterisation.

The two lamellae L1 and L2 were prepared by FIB/SEM milling down to a thickness on the order of (100±50)nm making the TEM signal an average of approximately 100-300 atoms. Concerns over loss of material at the surface during the milling of L1 were addressed with deposition of a protective carbon cap on L2 albeit with a subsequent loss of clarity of the surface. Three imaging modes bright field, dark field and high angle annular dark field were available offering atom Z sensitivity, strain sensitivity and high resolution to atomic length scales respectively. Additionally, elemental dispersive X-ray spectroscopy (EDS) raster scans were obtained for the mapping of growth materials and secondary phase composition.

Results showed the successful incorporation of Sb with some inhomogeneity around defects and secondary phase growth. Examples of defects including lattice mismatch slips, microtwin defects and substrate step antiphase domain boundaries are illustrated in discussion below. Secondary phase growth is shown in and at the surface of the layer along with EDS maps of their predominant constituents.

3.4.1 EDS Element Maps

Sb Incorporation

Selecting the dispersion peak of Sb, raster images of the Sb distribution in L1 are depicted in fig. 3.19(a) and (b) superimposed over the HAADF and BF images. It's clear that the Sb has been incorporated into the bulk of the layer with some inhomogeneity. Notably the presence of a secondary phase inclusion is largely devoid of Sb. The same process for L2 fig. 3.19(c) above the HAADF image (d) also shows exclusion of Sb from defects. Here antiphase domain boundaries (APDB), defects described in greater detail below, appear as dark lines in the HAADF image and can be directly mapped to regions of low Sb concentration in the EDS map.

Material Dispersion and Secondary Phases

The full collection of constituent elemental maps for L1 in fig. 3.20 clearly shows the secondary phase inclusion in the bulk is Mn rich and Cu poor with little variation in As. This correlates with the FM response of SQUID samples

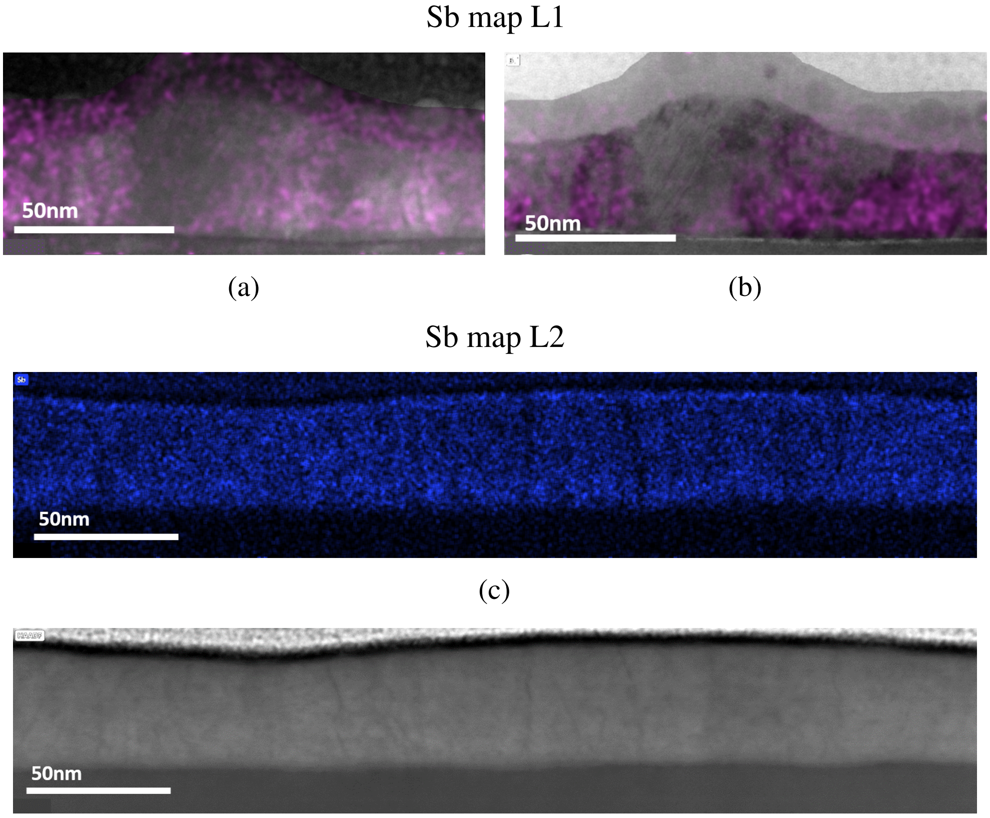

Sb map L1

(a)

(b)

Sb map L2

(c)

(d)

Fig. 3.19 (a) L1 Sb EDS map in magenta superimposed on the HAADF TEM image at x580k magnification and (b) the same EDS map on the BF TEM image of the equivalent region. (c) L2 Sb EDS map in blue at x290k magnification above (d) the HAADF TEM image of the same region.

at room temperature, falling above 330K typical of MnAs based FM alloys. A feature shared between L1 and L2 in fig. 3.21 is the presence of Sb and Cu at the surface. The surface Cu in L1 is likely responsible for the short range roughness seen in AFM. Also visible in both fig. 3.20 and fig. 3.21 is the distinct layer-substrate interface seen in the transition metals in contrast to the overlapping As map. However, some undulation in the epilayer can indicate incomplete or poor oxide removal, a flaw predicted in growth for some regions of the wafer due to lack of stage rotation and small heater footprint. Exclusive to maps in fig. 3.21, Cu, Mn and As do not exhibit the exclusion from APDB previously highlighted in Sb.

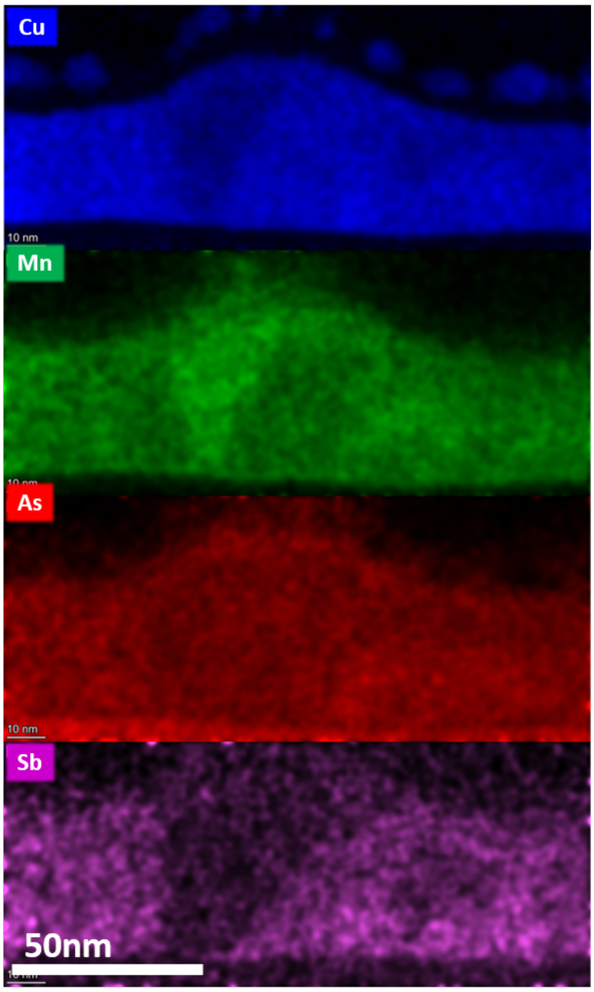

Fig. 3.20 TEM-EDS elemental maps at x580k magnification of L1 for Cu (blue), Mn (green), As (red) and Sb (magenta).

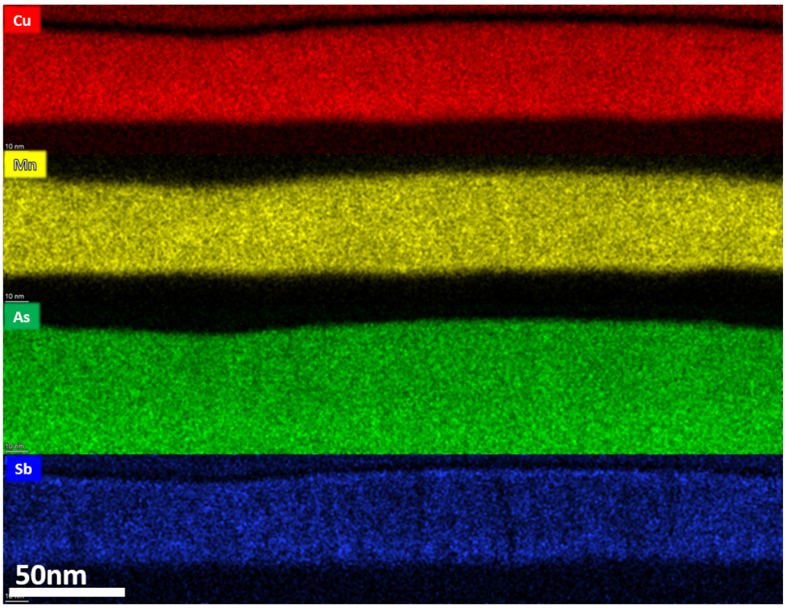

Fig. 3.21 TEM-EDS elemental maps at x290k magnification of L2 for Cu (red), Mn (yellow), As (green) and Sb (blue).

3.4.2 Layer Defects

Substrate Step APDB

The process of substrate oxide removal and 3D island growth of the buffer GaAs layer both contribute to steps forming at the substrate surface. These steps, 5.65Å in height, create nucleation points for APDBs between crystal domains of CuMnAsSb growth such that when the two lattices meet their sublattices are opposite. Typically these defects persist from the substrate to the surface propagating at 60^o from the substrate surface or meet another APDB and annihilate.[16] An example in L1 in fig. 3.22(a) shows the two crystal domains meeting and competing as they form at a step in the substrate. By applying a mask to the fast Fourier transform domain (FFT) of the original HAADF image, where regular atomic positions are isolated, an inversion back to the image state highlights those atomic positions from the background as in fig. 3.22(b). The difference in atomic arrangement and offset between the crystal planes is highlighted in the inset with points indicating specific atomic model positions.

APDBs do influence AF domains as the offset breaks the continuous Mn plane that makes up a sublattice typically inducing an AF domain wall. While the density of APDBs does correlate with non-stoichiometric growth their occurrence cannot be eliminated under the given growth conditions. Consistent with both GaP and GaAs growth of CuMnAs, multiple examples of APDBs exist in both lamellae, however, unlike prior reports[16] they do not necessarily propagate at 60^o from the substrate, rather 'interlacing' vertically. In order to determine if this occurrence is sample specific or driven by Sb incorporation a broader HR-TEM study including all three layers and CuMnAs on GaAs material would be required.

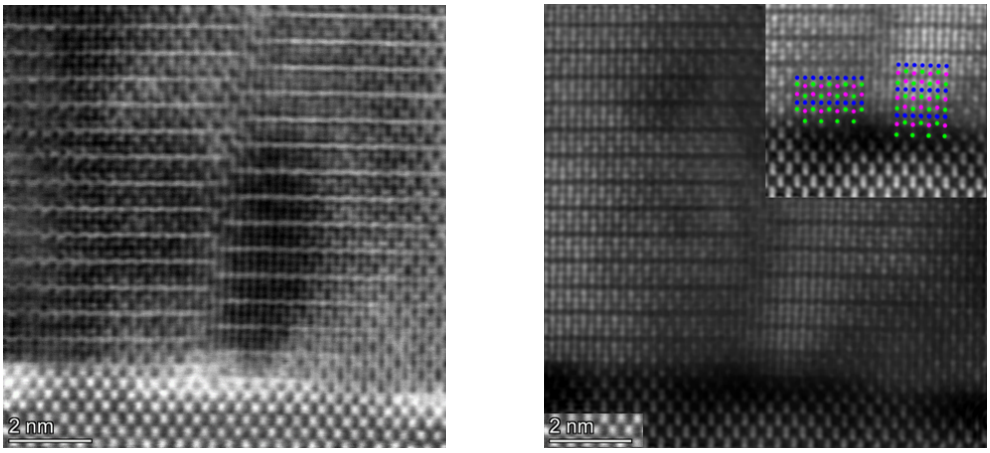

Fig. 3.22 BF TEM image at x9.2M magnification of a GaAs step and resulting of a CuMnAsSb APDB in L1 and the same step and APDB in Fourier filtered HAADF image the difference in atomic arrangement across the APDB is illustrated in the inset where Cu points are blue, Mn pink and As or Sb green.

Nucleation APDB

Within tetragonal CuMnAs the As bonds with both Cu and Mn, the surface As site can therefore nucleate on either of the transition metals but the growth of the two will be out of phase. In the case that two crystal domains of opposite nucleating metal neighbour one another they will form an APDB at the interface.[16] A clear example is highlighted by the two offset crystal domains in red and blue of fig. 3.23. Similarly to the APDBs described above these are typical of tetragonal CuMnAs growth on III-V substrates and cannot be eliminated in typical growth.

Microtwin Defects

Another growth defect, well-studied in CuMnAs,[16] is microtwins typically also occurring at the GaAs step edge where additional lattice sites are exposed along the step where growth can nucleate off axis and result in secondary

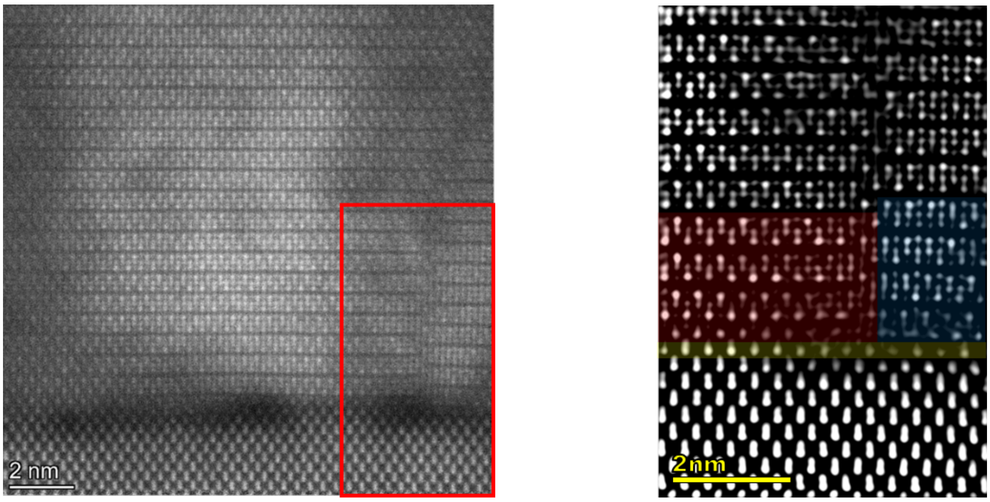

Fig. 3.23 HAADF TEM image at x1.6M magnification of a nucleation APDB in L1 including a Fourier filtered close up of the region in the red box.

twinned crystal growth of the same phase. Their density correlates with local crystal strain as well as off stoichiometric growth. Microtwin slabs are depicted in fig. 3.24 of no more than 2nm width and the reorientation is highlighted in the inset by coloured atomic positions and the respective *c* axis in orange intersecting to illustrate the 60^{o} reorientation. Microtwins seen in the Fourier filtered TEM image are curtailed and do not persist to the surface as is seen on CuMnAs/GaP layers. Strain relaxation and disorder are likely to contribute to their extinction.

Lattice Mismatch Slip

Due to the lattice mismatch between the layer and substrate there is a significant degree of strain at the interface. Such strain can be relieved by a slip in the epilayer where, in the case of this tetragonal system, an additional atom regular to the lattice of the layer is incorporated interstitially and not associated with a regular atomic site on the substrate. Regular heteroepitaxy and the occurrence of a slip are seen in the Fourier filtered image fig. 3.25 taken from the red box of the HAADF image. The slip, nominally singled out by the green fork, is seen to deviate from the ideal arrangement in red, ultimately leaving the substrate and layer arrangements out of phase. The heteroepitaxy does recover with some deformation and local strain visible in surrounding volume of the layer. This is important evidence of the strain between the layer and substrate,

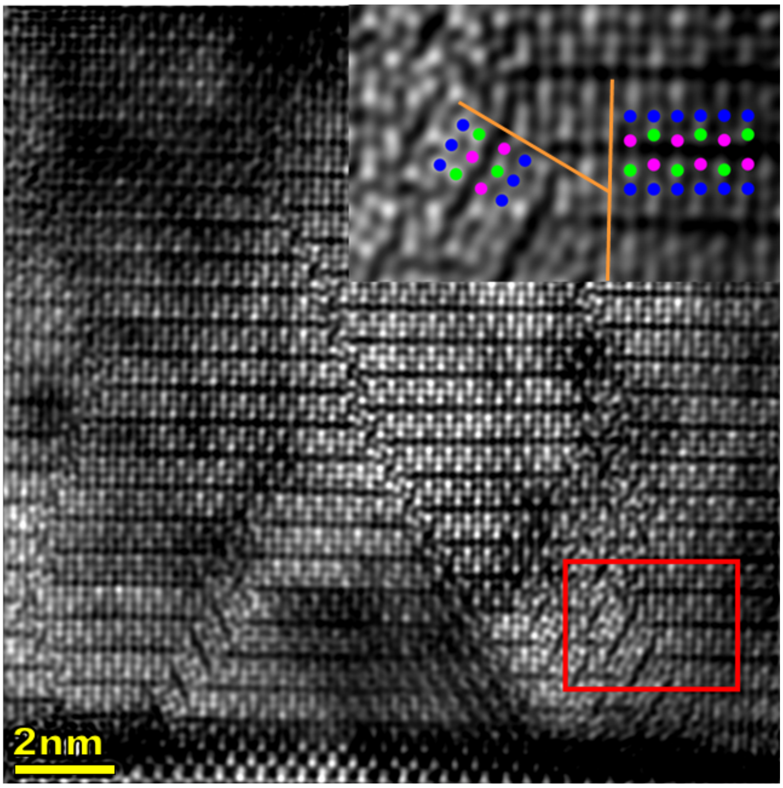

Fig. 3.24 A Fourier filtered HAADF TEM image of L1 depicting microtwin defects. The inset taken from the red box highlights the 60^o c axis offset between the two twinned crystals along with atomic positions highlighted by blue, magenta and green points for Cu, Mn and As or Sb respectively.

which had been sought to be matched with Sb's inclusion but has ultimately persisted.

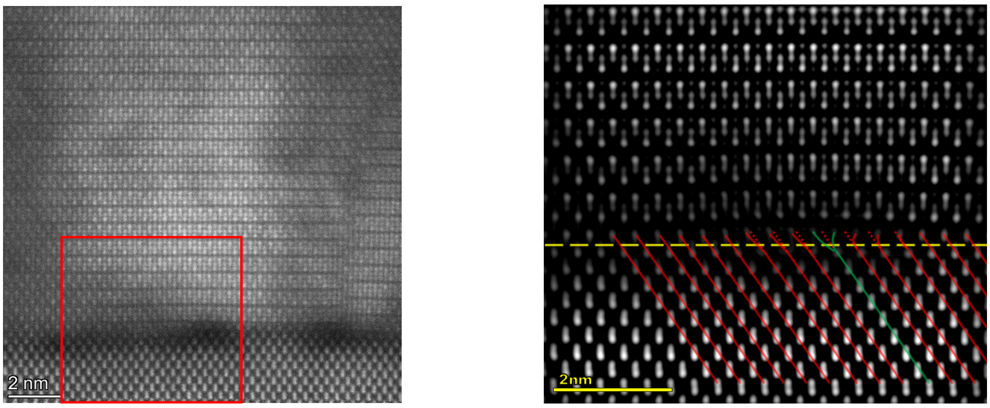

Fig. 3.25 HAADF TEM image of a slip dislocation in L1 at x6.5M magnification with the red box Fourier filtered image on the right. The yellow dashed line indicated the layer/substrate interface along with the 1:1 lattice matching in red, before divergence from the ideal dashed red line and slip in green.

3.5 Summary and Conclusion

The above work details the successful recommission and conversion of the "mini MBE" system to CuMnAs growth. XRD has shown that there is a similar out of plane lattice parameter and narrower spread over equivalent material grown in other systems confirming the feasibility of equivalent or better quality single crystal epitaxial growth of CuMnAs in the "mini MBE" machine. In scanning probe microscopy surface roughness is of a similar order albeit with some difference in the cause. Finally, magnetometry showed that although exact stoichiometry was not achieved a reasonably close ratio with minimal ferromagnetic secondary phase was established.

Growths of CuMnAs incorportating an Sb flux were then undertaken. Growths that preserved the tetragonal crystal structure and were of similar structural quality to that of CuMnAs grown on GaAs were successfully carried out. Measurement of the out of plane and high angle diffraction peaks in XRD confirmed good quality at lower Sb fluxes. The Sb flux with the best matched lattice with the GaAs substrate was at a nominal 20% of the As flux while higher flux led to the deterioration of the crystal structure. This is likely due to strain relaxation interfering with the conventional growth mechanism.

Rough surface features appear at the surface in AFM measurements of all layers. Some drift in stoichiometry, whether cell behaviour or static growth, may have led to such precipitates. However, the severe density of crystal precipitates at high Sb flux was likely a result disruption in growth and phase separation.

From magnetometry of the Sb layers multiple secondary FM compounds, likely alloys of MnAs and MnSb, were measured. The addition of Sb may make secondary phases more likely. It may be that Sb alloys with Mn in preference to incorporation in the layer Sb may eject other adatoms from the typical tetragonal crystal disrupting stoichiometry locally. A proportional rise in magnetisation with Sb flux suggested a direct role in formation of FM material. Unlike prior material characterisation there was not a severe worsening at the highest Sb flux, indicating a continuous development of material, possibly within the layer.

While EDS mapping indicates the successful incorporation of Sb into the tetragonal phase it does appear somewhat inhomogeneous in the layer due to exclusion from defects. The maps also reveal Sb and Cu rich material at the surface of LXB025 alongside Mn and As rich inclusions from substrate to surface, likely forming the FM signature seen in magnetic characterisation. There is a reasonable separation of substrate and layer despite waviness and steps in the buffer, possibly also associated with uneven oxide removal.

Numerous crystal defects have been identified including APDBs forming due to steps and offset nucleation on available As sites and microtwins. All expected from prior CuMnAs on III-V substrate studies, however crucially strain induced slips due to the lattice mismatch were not resolved by the incorporation of Sb.

This study shared some results observed by Dr. V. Hills on CuMnAsP. Principally a refinement of the crystal structure to improve a detrimental unit cell mismatch. CuMnAsSb, by comparison, was not able to preserve the surface or offer FM free material even at lower fluxes.

Chapter 4

Spintronic Properties of $\mathbf{CuMnAs}_{1-\alpha}\mathbf{Sb}_{\alpha}$

4.1 Introduction

In Chapter 3 the growth and material properties of CuMnAsSb were discussed in relative isolation from the application of the material in spintronics. Here the same layers are examined for their candidacy for spintronics applications, testing against the comparatively well-studied CuMnAs to establish any change or indeed improvement as envisioned in the inception of the study.

The antiferromagnetic (AF) ordering of Mn spins was verified by neutron diffraction experiments in addition to determining the Néel temperature (T_N) via neutron diffraction and electron transport temperature dependent experiments. The spin texture and domain structure of LXB025 was imaged in XMLD-PEEM, providing qualitative insight into the spontaneous anisotropy. Finally, electron transport experiments pulsing devices fabricated on the layers evaluate the functionality of the material for electrical writing and reading of the spin state for use in information technologies.

4.2 Determination of Magnetic Phase Transition

In this section a 120nm layer of $\mathrm{CuMnAs}_{0.8}\mathrm{Sb}_{0.2}$ (LXB024) is investigated to establish the magnetic ordering and T_N via two corroborative experiments. The first is an electron transport measurement with heating developed on CuMnAs by V. Hills [15] to find T_N. The second is neutron diffraction detection of magnetic and nuclear ordering with heating beyond T_N. A counterpart transport T_N determination measurement was carried out on LXB023.

4.2.1 High Temperature Transport

As a magnetic conductor undergoes a magnetic phase change it exhibits critical behaviour. This can be detected electrically as a change in longitudinal resistance (R_{xx}) due to the changing interaction of itinerant spins and lattice spins. At a second order phase transition the change from AF to paramagnetic sees a continuous fall in the magnetic order parameter to zero, which can be detected. Taking the derivative of R_{xx} with respect to temperature around T_N reveals a pronounced cusp where the AF ordered spins cease to be so aligned and electrons display a difference in their transport characteristics.[111]

Chips of LXB023 and LXB024 with dimensions of 5mm×5mm were each mounted onto PCB headers and wire-bonded to create an inline 4 point probe configuration of contacts. Utilising the high temperature transport system in a vacuum as described in section 2.4.4 a current of 500μA was applied continuously with simultaneous readout of the V$_{xx}$ voltage. Concurrently the heating halogen bulb was driven by a Eurotherm controlled power supply from lab temperature of 295K to 485K at a ramp rate of 2K/min. The sampling rate for LXB023 was approximately 1Hz resulting in more than 5000 data points and for LXB024 300mHz giving ∼1800 points. During passive cool down V_{xx} measurement continued over a much longer timescale resulting in up to 10000 data points.

A graph of the variation in R_{xx} on first heating and cooling of LXB023 and LXB024 is given in fig. 4.1 to show the form of the change in R_{xx} with temperature. There is a discernible increase in the linear gradient of the resistance above 420K. A non-reversible difference after heating is evident in both plots despite operating in a vacuum at pressures below 10^{-3}mbar. This has been observed previously for CuMnAs layers and is attributed to annealing. The Al cap, which is deposited at low temperature, is likely to diffuse and alloy with the top of the layer.[15]

The derivative of the voltage signal with temperature is highly sensitive to noise. Given sampling rate and large data set smoothing it was feasible to obtain the derivative with respect to temperature via a 1000 point linear interpolation. This is depicted in fig. 4.2 for both layers, each normalised to the inflection at T_N. The derivatives show a commensurate steep decline beyond

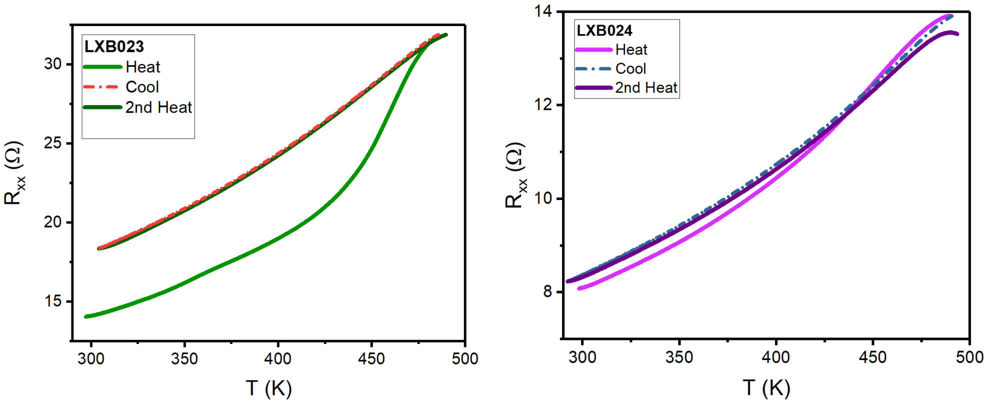

(a) (b)

Fig. 4.1 Changes in longitudinal resistance with temperature of (a) LXB023 and (b) LXB024 both interpolated for differentiation.

465K although the broader cusp of LXB024 onsets at a lower temperature, associated with greater disorder and inhomogeneity. With bigaussian fitting of the cusp a value for the peak centre of 451.5±0.7K is obtained. The point of inflection of the lower Sb flux LXB023 is narrower and occurs at a higher temperature, 462.1±0.2K from fitting, both are lower than values reported for CuMnAs grown on GaP of 480±5K.[112] A fall in T_N may be due to the substitution of Sb into the unit cell increasing the separation of Mn sublattices and reducing exchange. Alternatively, the Sb may occur as an inclusion disrupting the lattice and perturbing the exchange interaction.

From the dashed lines in fig. 4.2 there is a significant broadening in the change in R_{xx} with temperature for both layers after the first heating cycle due to irreversible annealing. T_N is taken as the peak of $\frac{dR}{dT}$ with the second measurement confirming that the inflection is, although broader, repeatable and not due to any thermally induced deformation.

There are also cusps in fig. 4.2 apparent at lower temperatures: at 310K in both samples and an additional cusp in LXB023 at 350K. These are likely associated with the T_C of alloys of Mn, As and Sb that were also measured previously in SQUID magnetometry in section 3.3.2.

4.2.2 Neutron Diffraction

On the ISIS neutron source Wish instrument a semi-circular half wafer of LXB024 was loaded into a furnace sample environment at an angle of 51° incidence to the neutron beam allowing access to (h00) and (00l) reflections.

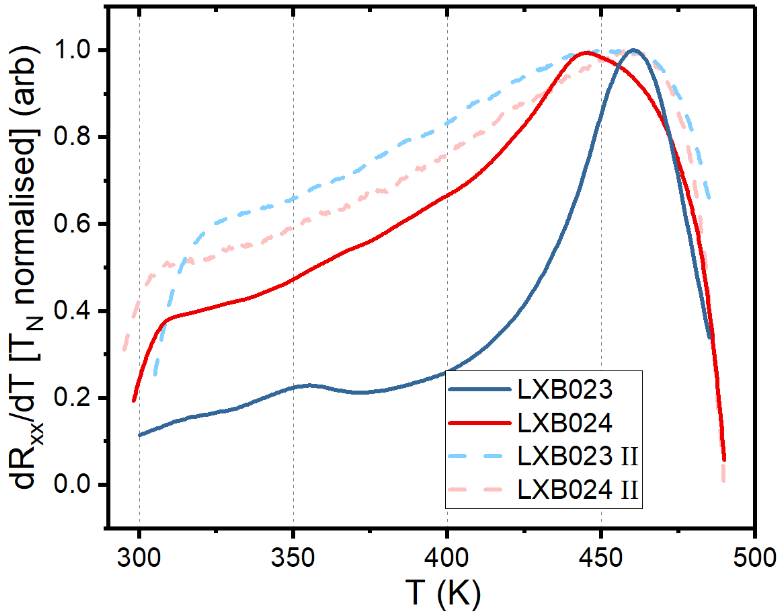

Fig. 4.2 Derivative of the R_{xx} with temperature taken of the interpolated R_{xx} each normalised to the inflection point of the critical behaviour. The change in resistivity after the first heating and cooling cycle is shown by the dashed line.

The sample environment was then heated from 300K to 503K settling at 12 steps to perform diffraction measurements. Due to the low interaction rate of neutrons LXB024 was grown thicker than other samples in the series and a high intensity beam is exposed to the sample for 30 minutes for each step in temperature. This work was performed by Dr P. Manuel, Dr D. Khalyavin, Dr M. Wang, S. Poole and the author.

Incident neutrons are sensitive to magnetic moments as well as matter and will be diffracted by both the nuclear and magnetic reflections. Magnetic scattering occurs when moments are perpendicular to the scattering vector. In CuMnAs, Mn sublattices are coupled FM in-plane and coupled AF out of plane $\langle 001 \rangle$ with a propagation vector of zero. Since the in-plane nuclear (100) reflection of P4/nmm space group that tetragonal CuMnAs belongs to is forbidden, the diffraction peak can be said to be purely magnetic. FM sublattices lying in the plane of the film also occur perpendicular to the scattering vector leading to a mixed magnetic and nuclear peak in the (001) reflection. The diffraction peak acts as a helpful control to monitor the preservation of the material during measurement.

Neutron diffraction peaks observed at ISIS are shown in fig. 4.3(a) and (b) for the (100) and (001) reflections respectively. The presence of the (100) confirms the AF ordering of the moments in-plane. There is a large SNR in the (100) reflection due to the absence of a nuclear component and only a fraction of the Mn spins aligned perpendicular to the scattering vector. The (100) diffraction peak is almost entirely extinguished at 463K.

While some loss of intensity at higher temperatures in fig. 4.3(b) is due to the suppression of the magnetic order a significant fall is due to the thermal degradation of the material. Ultimately, heating in atmospheric air led to significant structural deterioration of the sample. However, some signal is preserved in contrast to the 463K extinction of the purely magnetic (100) diffraction peak, a working upper value of the magnetic phase transition T_N. The intensity and sharpness continue to drop beyond 463K rather than remaining constant, which is assumed to be further purely structural deterioration. The result beyond 463K does offer a cautionary higher temperature for the stability of the material in an air environment.

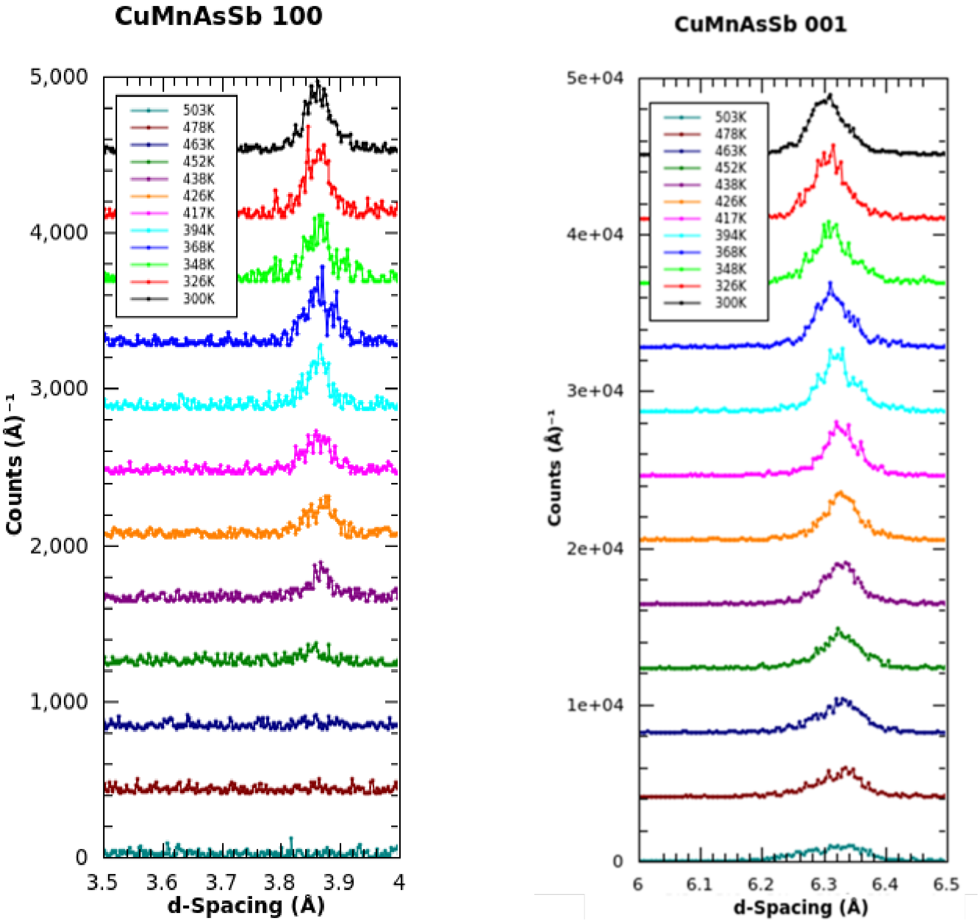

(a) (b)

Fig. 4.3 Neutron diffraction peaks with temperature for the (a) (100) purely magnetic reflection compared with (b) the mixed structural and magnetic (001) reflection.

Diffraction peaks in fig. 4.3(a) were fitted with a Voigt profile in order to extract the integrated area under the intensity curve. These values are shown in fig. 4.4 with transport data overlaid for comparison of the critical behaviour. The magnetic phase transition T_N can be interrogated by fitting integrated intensity data with the function:

$$I = A(T_N - T)^{\beta} + c \tag{4.1}$$

where A is an arbitrary instrumental constant, c is an offset for nuclear and background signal and β is the material specific critical exponent both only valid below T_N. Fitting both peak's integrated intensity with temperature arrives at a T_N of 460±10K. The critical exponent is relevant to the statistical mechanics descriptions of the material and determines the universality class governing the system. In undoped CuMnAs this was found to be 0.4037[15] placing it within the Heisenberg universality class (between 0.34 and 0.44).[113]

Values of T_N from neutron diffraction and transport in fig. 4.4 are in relative agreement with a small depression of T_N in transport due to influence of long range disorder and inhomogeneity on the transport measurement. Here both fits find an exponent of 0.6±0.2. The large uncertainty over previous measurement is ascribed to the measurement in air deteriorating the material where previous work was performed at vacuum or in a He environment. The level of noise in the (100) diffraction peak contributes to a high uncertainty in the Voigt peak fitting and inhomogeneity across the layer has previously been observed to leave a ‘tail’ of mixed T_N beyond the predominant value in magnetic phase transition studies on the ferromagnetic semiconductor GaMnAs.[114]

4.3 XMLD-PEEM Imaged Spin Texture

Insight into the AF domain and spin texture as well as the anisotropy of LXB025 was obtained via XMLD-PEEM imaging. An unadulterated chip of LXB025 was loaded into the XMLD-PEEM end station at Diamond Light Source’s (DLS) I06 magnetic materials nanoscience beamline. The following section covers the passive imaging with rotation of the beam carried out to determine the domain and spin texture of LXB025, performed by Dr S. Reimers with support from Dr O. Amin and DLS’s Dr F. Maccherozzi and Dr S. Dhesi. Characteristic electron emission by X-ray absorption illustrates the spontaneous resting AF domain texture including their size and shape allows a

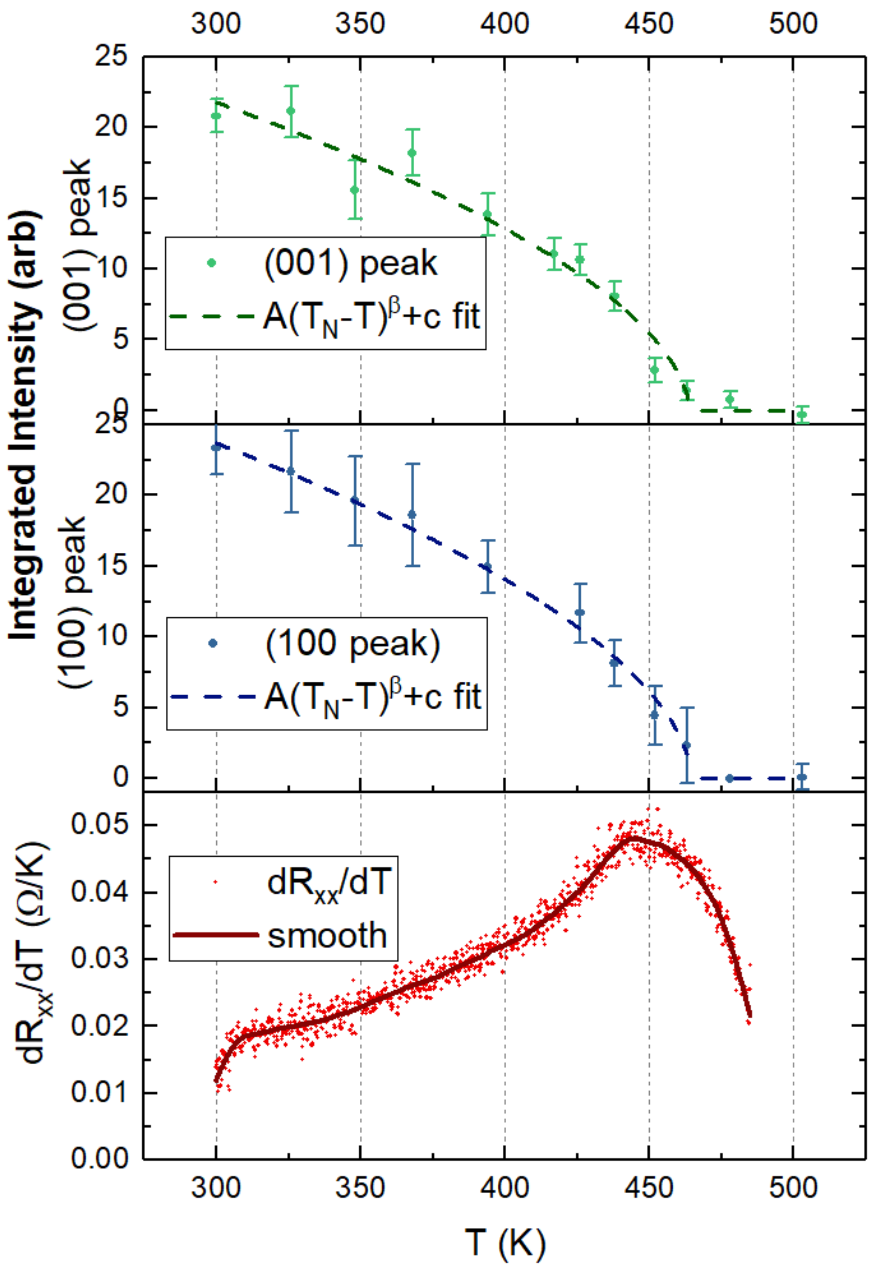

Fig. 4.4 Integrated intensity with ramping temperature in neutron diffraction demonstrating the fall in (001) and (100) reflections along with fits following eqn. 4.1. In red is the R_{xx} derivative and 100 point Savitzky Golay smooth for comparison around T_N.

qualitative comparison with other layers. By rotating the X-ray polarisation patterns in the alignment of AF domains can reveal dominant anisotropic directions within the layer.

In expansion of the particular experimental configuration of DLS's I06 endstation described in 2.2.7 there is a 16° angle of incidence by the X-ray beam above the plane of the sample surface. The linear polarisation **E** of the wave is in-plane parallel to the film for observation of in-plane moments. The angles between **E** and the CuMnAsSb [100] crystal axis and spin axis are defined as ϕ and ψ respectively. The two are related by the offset between the [100] direction and local spin axis orientation $\alpha = \phi - \psi$. ϕ is controlled with the rotation of the sample with the XMLD varying as,

$$I_{PEEM}(\psi) = A + Bcos(2\psi) = A + Bcos(2\phi - 2\alpha) \tag{4.2}$$

where A is the background electron emission and B is the amplitude of the XMLD signal. Between two domains with spin axis oriented along the [100] direction in one and [010] direction in another the contrast is the difference due to XMLD between them, given as C_{100} it follows,

$$C_{100} = Bcos(2\phi) - B(cos2\phi - \frac{3\pi}{2}) = 2Bsin(2\phi) \tag{4.3}$$

so that the contrast reverses between 45° and 135° images.

4.3.1 Domain Structure

XMLD-PEEM images taken when the X-ray polarisation is out of plane showed no contrast, indicating spins are aligned in-plane. Imaging with polarisation along the [100] and [010] CuMnAs crystal directions depicted in fig. 4.5 shows biaxial spin axis alignment along the same directions with $\alpha = 0°, 90°$. Domains on the lengthscale of $\sim 1\mu$m are larger than typically seen in CuMnAs/GaAs (10-100μm) but smaller than some CuMnAs/GaP layers previously imaged on length scales an order larger.[17] Inversion of the contrast in image processing, represented on the right hand side of fig. 4.5, demonstrates the consistent reversal of XMLD contrast with ψ associated with orthogonal domains.

As the sample is rotated with respect to the X-ray polarisation the contrast becomes granular as seen with the polarisation aligned along the [110] and [$1\bar{1}0$] in XMLD-PEEM images on the left hand side of fig. 4.6. Such granular

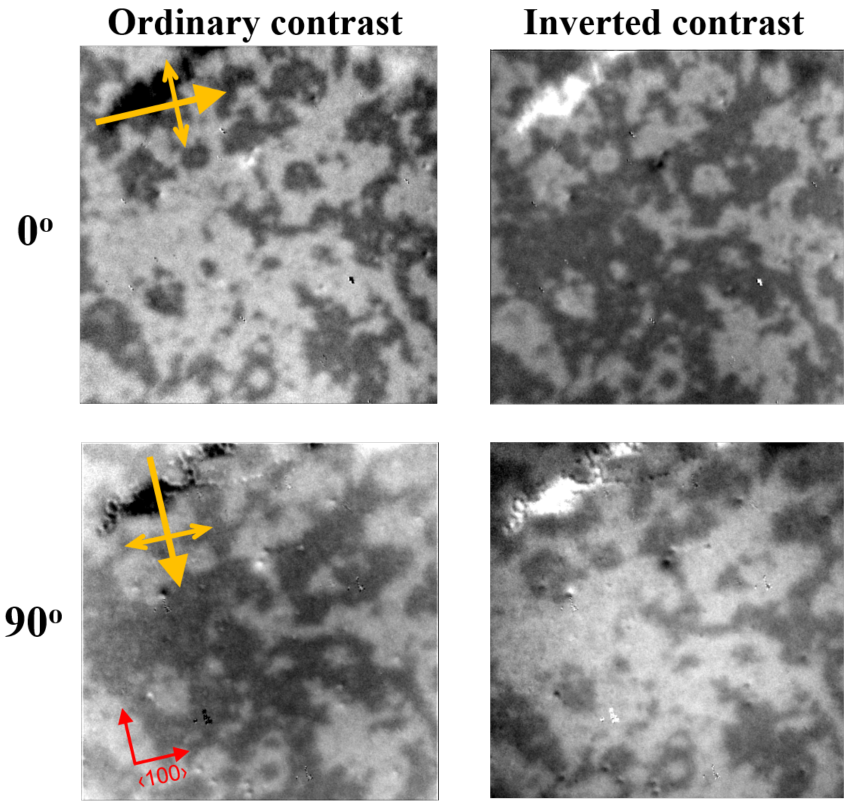

Fig. 4.5 XMLD-PEEM images over a 10μm field of view with the X-ray polarisation along the [010] and [100] directions. The orange arrow indicates the X-ray beam's direction, with the linear polarisation axis orthogonal as represented by the double headed arrow. The given angles refer to the clockwise offset between the X-ray beam direction in the xy plane and CuMnAsSb [100] crystal direction. On the left hand side is a measured domain pattern with contrast narrowed to highlight the domain texture. On the right hand side the contrast is inverted for comparison with the diagonal image, which demonstrates the reverse in contrast with 90° rotation in ϕ

texture can be observed with varying degrees of angular offset and does not necessarily indicate orthogonal domains after contrast adjustment. In a ‘perfect’ biaxial sample domains would be expected to lack any contrast aside from domain walls when the X-ray polarisation and both spin axes are offset by 45°. Considering a small divergence from the magnetic easy axes within a domain the change in contrast with rotation of the sample $\frac{dC_{100}}{d\phi}$ is at a maximum at a 45° offset to the spin axis. Therefore, for the imaged chip of LXB025 the high sensitivity to divergence occurs with the polarisation aligned along the [110] and [$\bar{1}$10] crystal directions, giving rise to the texture on the left hand side images of fig. 4.6. Therefore, within domains with spin axis largely aligned along the crystal [100] and [010] the local α is not strictly confined to 0° or 90°. As in fig. 4.5 the contrast reverses with the expected 90° rotation of the sample with respect to the polarisation vector.

From these images it can be determined that AF spin pairs in LXB025 lie in the plane of the layer and at equilibrium orient along biaxial easy axes along the [100] and [010] CuMnAsSb crystal directions with some divergence.

4.4 Electrical Switching Behaviour

4.4.1 Trends in Antiferromagnetic Electrical Switching

Electrical control via spin orbit torques (SOTs) and spin transfer torques (STTs) to ‘switch’ the magnetisation in FMs with read out using AMR has long been studied and employed in technologies such as MRAMs.[5] More recently, analogous mechanisms to switch the Néel vector and read out an AMR change in AFs were theorised and for the first time harnessed experimentally in CuMnAs.[13, 14]

Electrical switching of AFs was conceived as analogous to relativistic spin orbit torques (SOTs) seen in FMs with either broken bulk or structural inversion symmetry.[13] These bulk or structural broken symmetry conditions lead to energy band splitting, the Rashba or Dresselhaus effect respectively, and with the application of a charge current a transverse spin accumulation. This inverse spin galvanic effect exerts a torque on the magnetisation of the FM domains as described in more depth in section 1.4.3.[80]

For a collinear AF with two spin sublattices that form inversion partners local broken inversion symmetry exists that gives rise to the same inverse spin galvanic effect and Néel order relativistic spin orbit torques (NSOTs).[13]

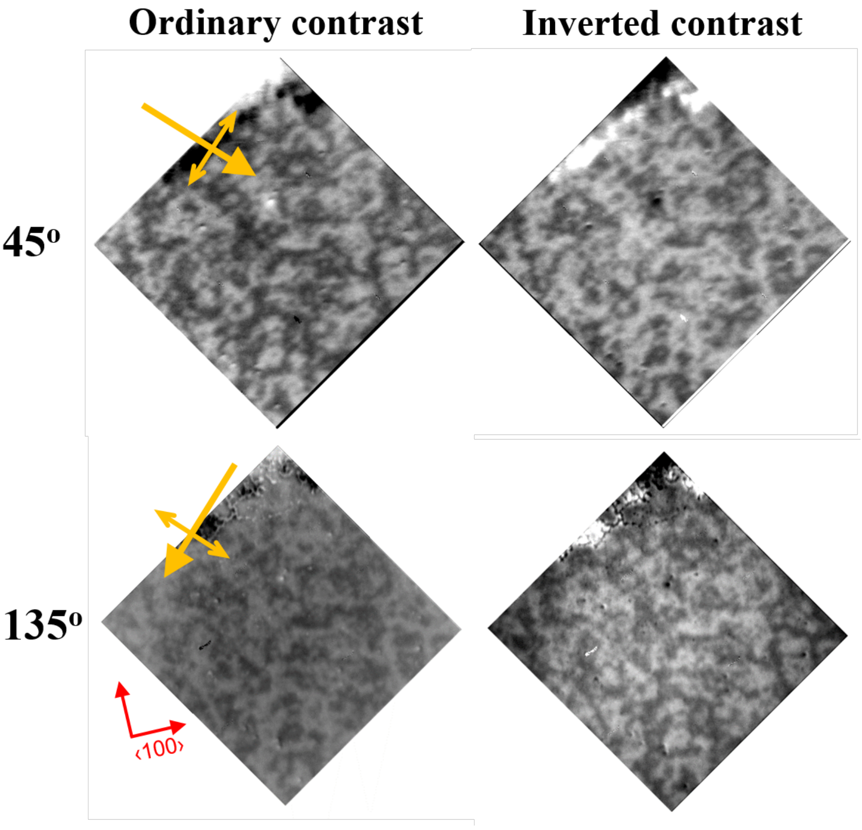

Fig. 4.6 XMLD-PEEM images over a 10μm field of view with the X-ray polarisation along the [110] and [$\bar{1}$10] directions, the orange arrow indicates the X-ray beam's direction with the lateral arrow heads the linear polarisation, angles refer to the clockwise offset between the X-ray beam and CuMnAsSb [100]. On the left hand side the contrast, narrowed for XMLD features, measured in PEEM is shown. The granular pattern can be attributed to divergence of AF spin pairs within the domain from the magnetic easy axes. The expected reversal of contrast with 90° rotation in ϕ is seen through comparison with the inverted contrast image on the right hand side.

The field like torques, distinct from long established anti-damping like non-relativistic spin transfer torques, alternate in sign between the two spin sublattices and are transverse to the sublattice magnetisation vector acting to rotate the spins 90°.

AF current driven domain reorientation was demonstrated in XMLD-PEEM images of CuMnAs alongside reversible AMR readout correlating with the change in domains. The currents applied along the [110] and [$1\bar{1}0$] CuMnAs crystal directions as 275ms orthogonal pulses, were particularly low density of 4.5MAcm^{-2} in comparison to FM SOTs, which are typically two orders of magnitude higher. However, the induced change in resistance due to the AMR totalled less than 0.1% with each pulse.[14]

Larger AMR response was later observed in another collinear AF meeting the symmetry conditions, Mn$_2$Au. In this study larger current densities of 14MAcm^{-2} were applied in trains of 1ms and it was found that with successive pulse trains on the order of 500 pulses, the change in resistance due to the AMR could surpass 6%.[115]

Subsequent work on CuMnAs highlighted distinguishing attributes of AF switching such as the terahertz writing speeds [116] as well as more explicit demonstration of NSOT action on the AF texture.[117, 118] Pulses along the hard axis with current density as low as 0.5MAcm^{-2} were demonstrated to manipulate domain walls with a commensurate change in the local domains and AMR in a reduced two contact geometry. Imaging of the change via XMLD-PEEM showed the current polarity dependence of the domain wall change, matching the expected behaviour of NSOTs and further evidencing their existence.[117]

Similarly, specific NSOT effects were successfully tested in a uniaxial CuMnAs thin film. Composed of 180° domains, and therefore imperceptible via the AMR, this cross device was both switched and read utilising NSOTs. Applying a 20ms writing pulse of the order 10MAcm^{-2} to the thin film cross device was shown to induce a change in the second order magneto-resistance detected in the transverse resistance of a 1MAcm^{-2} probe, associated with an 180° Néel vector reversal. The probe current exerts a deterministic and transient tilt on the Néel vector accessible as the coefficient of the second order term in the transverse probe resistance.[118] These two studies described long lasting AMR far in excess of the readout timescales and associated with stable changes in the domain structure of the material, in the latter explicitly cited as more than a day.

With the proliferation of switching techniques and parameters, in particular the emergence of switching via anti-damping like spin transfer torques in systems such as Pt/NiO bilayers at much higher current densities, studies began to examine the temporal dynamics of the AMR in greater depth. Transport measurements when applying short higher current density (in excess of 10MAcm^{-2}) orthogonal pulses to CuMnAs displayed a high resistivity AMR, decaying on the order of seconds, going beyond simple thermal effects shown to dissipate within 100μs. This was characterised as a distinct switching regime, in which the material was brought close to the magnetic transition point by Joule heating from the high energy pulse, domains and walls were fragmented and with time, typically seconds to minutes, relaxed to a stable resistive state.[119, 120]

The process of fragmentation and relaxation, has been well documented in three distinct magnetic imaging techniques and is commensurate with the transverse resistance change. The increase in domain wall density with fragmentation from a current pulse and subsequent decrease with reformation of domains correlated with changes in the transverse resistance. Described as a quenching of the AF texture, the higher current regime can produce larger transient AMR signals - as much at 100% in certain geometries - as well as a long lasting AMR typical of prior low current density NSOT switching. Prior studies[120, 121] found no signs of electromigration or structural transition of the crystal from the application of pulses in the quenching regime.

In order to better understand the decaying signal the changes in transverse resistance with time were treated with Kohlrausch stretch exponential relaxation (SER) fitting. SER is a functional form that describes many electromagnetic relaxation dynamics [122] that with fitting to a relaxation signal provide quantitative insight to the amplitude, A, and relaxation time, τ. SERs follow the form,

$$Aexp[-(t/\tau)^{0.6}]+c \tag{4.4}$$

where c is a constant offset representing the value after return to equilibrium. Multiple terms can be utilised to describe concurrent effects in the relaxation. In CuMnAs undergoing switching in the quench regime, a two term SER function was fitted to the decay signal to distinguish relaxation dynamics in a fast (<20s) and slow (~250s) regime. This SER function followed the form,

$$A_1 exp[-(t/\tau_1)^{0.6}] + A_2 exp[-(t/\tau_2)^{0.6}] + c \tag{4.5}$$

where the coefficients of the first term describe the fast component of relaxation and second term describe the slow component of relaxation. A study across several CuMnAs layers switched at multiple temperatures between 270K and 320K and extrapolated both τ_1 and τ_2 in the limit of $1/T \rightarrow 0$ to find the material dependent attempt time. The result correlated with expected picosecond timescales of spin dynamics in AFs.[121]

Together the imaging and temperature studies demonstrate the coincidence of current pulse domain fragmentation and reformation dynamics with resistive changes and that those changes can be modelled as operating on the timescale of AF spin dynamics. However, the mechanism behind the deterministic AMR change and potential role of NSOTs is not yet well understood and has not been conclusively linked to the fragmentation and reformation of AF domains.

4.4.2 Introduction to Electrical Switching Results

While advancement of open questions in current pulse switching goes beyond the scope of this study devices patterned from CuMnAsSb layers grown at three Sb fluxes were subject to electrical current pulsing measurements in work outlined below. This work sought to demonstrate electrical switching in the three CuMnAsSb layers and observe the AMR in comparison with previous AF switching studies. A plan of commensurate spin flop AMR measurements of samples could not be successfully carried out due to technical and resource constraints. This unfulfilled component demanded an experimental fabrication step of surface etching in attempt to remove FM material on the layer identified in SQUID magnetometry, which was pre-emptively carried out before the curtailment of the study. Electrical current pulse switching was carried out and demonstrated the characteristic decaying signal in the transverse resistance broadly consistent with previous work on CuMnAs.[120, 121] Following the same procedure of the quench switching model the decay signals are fitted with bespoke stretched exponential relaxation (SER) functions to obtain the amplitude, relaxation time and constant offset. The novel surface etched fabrication was shown to largely preserve material properties for transport and removed some surface adulterants, however, FM material was also found to exist within the layer that was not removed.

4.4.3 Dip Etching

Prior to fabrication of transport devices chips of material were treated to an experimental process in an effort to remove unwanted surface material seen in SQUID and TEM. The adulterants, believed to be ferromagnetic material existing on the sample surface, would interfere in proposed magneto-transport experiments.

Prior to fabricating devices on CuMnAsSb layers a similar chip of CuMnAs RC134 was used as an etch rate calibration. Chips patterned with photoresist were dipped in a solution of HCl and water for 10s and the height of features measured on a line profiler. The resulting step depicted on three sweeps at both 10mg and 8mg of tip pressure in fig. 4.7 was determined as (10 ± 2)Å/s. A chip of LXB025 that was treated by an HCl etch wash was also measured via SQUID magnetometry. Compared with the original sample described in the previous chapter, the FM signal at room temperature was found to be reduced by around 80% as depicted in fig. 4.8. However, the low temperature magnetisation is similar with some reduction in the coercivity likely due to material deterioration. The difference between high and low temperature magnetisation curves suggests that room temperature FM material such as MnAs has been affected by the etching step, but low Curie temperature FM material has been preserved and correlates with its presence in the bulk of the layer as has been seen from inclusions in TEM outlined in the previous chapter. Differences in the coercivity are attributed to arbitrary changes between the two chips' shape and orientation.

Material was dipped in a concentrated solution of HCl and water for 10s before rinsing in deionised water. Typical fabrication steps outlined in section 2.3 were otherwise followed to develop 10μm arm rounded union jack (UJ) micro-devices as depicted in fig. 4.9(a). Prepared devices were mounted on 12-pin ceramic headers with contacts connected by Al microwire bonds.

4.4.4 Switching and Decay

Utilising the Room Temperature System (RTS) described in 2.4.3 devices were individually loaded into the sample environment held at 21°C and evacuated to a pressure of 1×10^{-5} mbar. A Keithley K2461 source meter delivered voltage controlled top-hat pulses of 1ms width. After each pulse, the V_{xx} was measured with a 200μA probe in a 4 wire configuration by the K2461 and the V_{xy} by a dedicated Keithley K2000 multimeter for a minimum of 40s for low

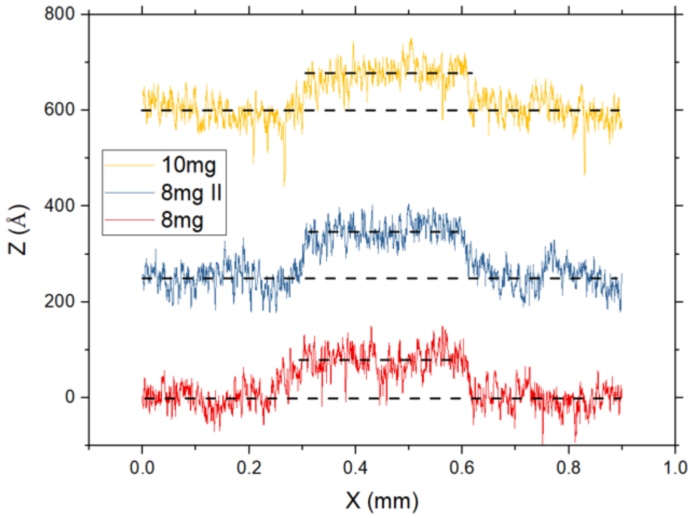

Fig. 4.7 Step height as measured on a microdevice line profiler of a feature etched in CuMnAs by a HCl solution for 10s at two tip pressures. Dashed lines indicate the height extracted via fitting.

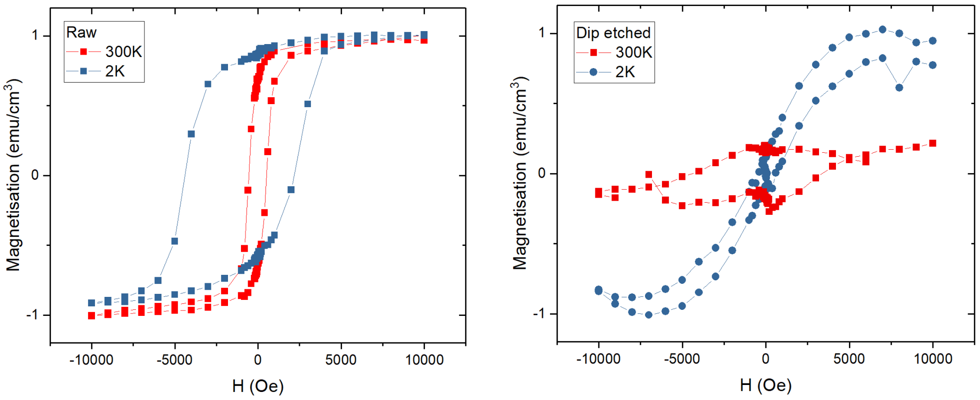

Fig. 4.8 Magnetisation with sweeping field for two chips of LXB025 one raw as grown (left) and another (right) dipped in an HCl solution for 10s measured at 300K (red) and 2K (blue) via SQUID magnetometry. Linear diamagnetic background from the substrate and mounting apparatus has been subtracted.

amplitude pulses and upwards of 9 minutes for higher pulse amplitudes.The primary configuration alternated pulses between two orthogonal arms of the device along the [110] and [1$\bar{1}$0] CuMnAsSb crystal directions (at 45° to the equivalent direction in the substrate lattice). Relative pulse, probe and measurement orientations are depicted schematically in fig. 4.9(b). The voltage of the pulses was ramped up from 1V to an amplitude of 30V in small increments equating to a current densities between approximately 0.4MAcm^{-2} and 11MAcm^{-2} - varying with the resistivity of the device. Further pulses

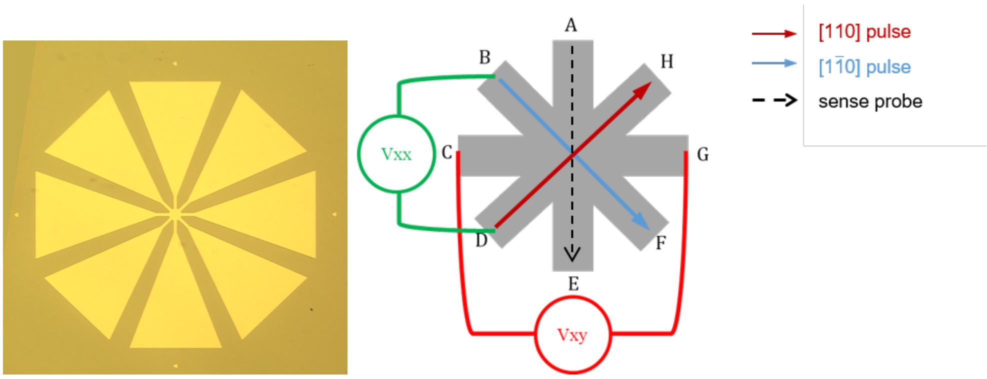

(a) (b)

Fig. 4.9 (a) microscope image at 10x magnification of a 10μm rounded union jack device fabricated on LXB025 dip etched. (b) the pulse and probing configuration at the centre of union jack microdevices, indicated pulse directions refer to the CuMnAsSb layer crystal directions.

offset by 45° pulsing along the [0$\bar{1}$0] and [100]CuMnAsSb directions were applied at 30V in a demonstration of the pulse response along both the easy and hard magnetic axes.

The transverse and longitudinal resistance response of each layer to orthogonal pulses of 22V, 26V and 30V are depicted in fig. 4.10. All show the transient and deterministic form of decaying R_{xy} signal associated with spin relaxation AMR in the quench switching regime where the transient signal in R_{xy} varies with sign between orthogonal pulses while changes in R_{xx} carry the same decay form but do not change sign between orthogonal pulses.[120]

The R_{xy} signal of the same form is also observed following 30V orthogonal pulses along the [0$\bar{1}$0] and [100] directions as shown in fig. 4.11. This apparent isotropic in-plane pulsing result is unexpected for NSOT action in biaxial AF material, which discriminates between pulses along the easy and hard axes based on domain reorientation or domain wall motion respectively as described in section 4.4.1. The result is consistent with the high resistivity quench switching model in which the approach to the magnetic phase transition temperature is motivated purely by Joule heating.

An unambiguous difference in the form of the R_{xy} decay is apparent between LXB023 and the two higher Sb layers. In LXB023 the sign of $\frac{dR_{xy}}{dt}$ changes within a single decay signal, first deviating from the mean R_{xy} for around 5s before decaying back towards it over a longer period. In LXB025 and LXB026 the $\frac{dR_{xy}}{dt}$ after a pulse has a constant sign, relaxing toward the mean value of R_{xy}. In the quench switching regime such differences in the form of decay between samples are known to occur and ascribed to two distinct decay components that may be of opposite or like sign.

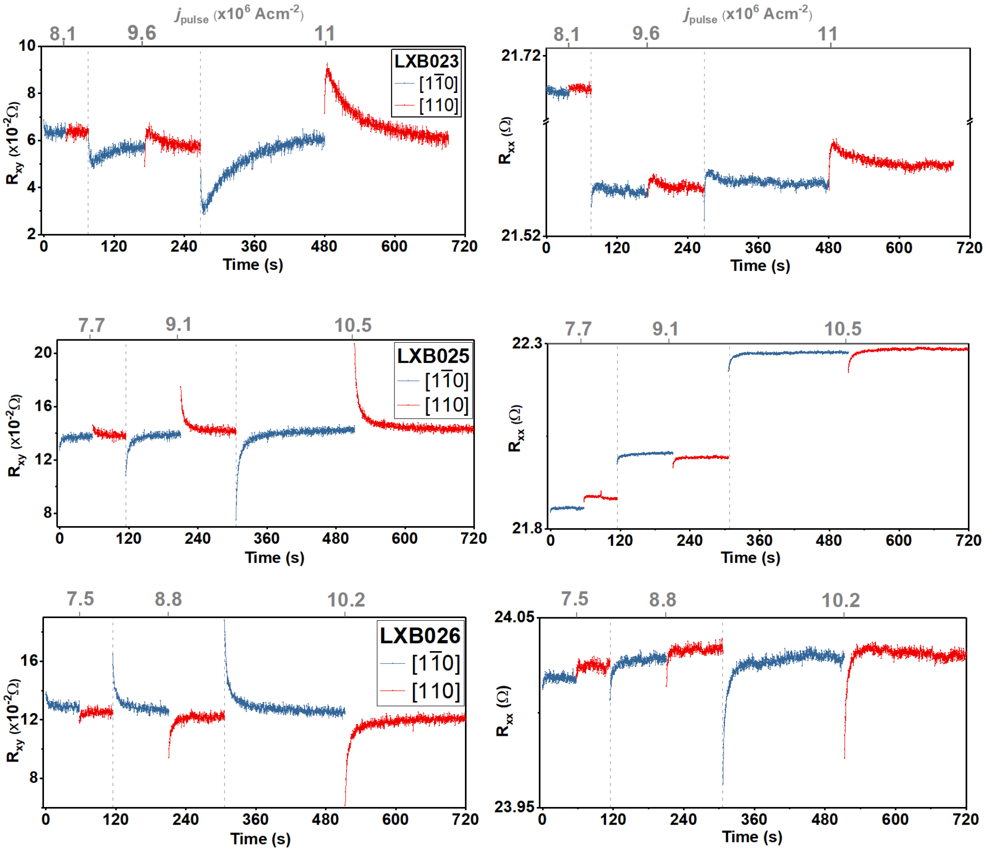

Fig. 4.10 Response of transverse resistance to orthogonal pulses along the layer [1$\bar{1}$0] (blue) and [110] (red) for each layer with the longitudinal resistance depicted on the right hand side. The switching signal on the left shows the response to pulses at three current densities to demonstrate the size of the relaxation with pulse amplitude.

4.4.5 Stretched Exponential Fitting

Studies on CuMnAs have used SER fitting to model the relaxation of transverse resistance after electrical switching in the quench regime. Although, results obtained in the measurements described in section 4.4.4 are insufficient to draw insight into the mechanism of quench switching by following the same procedure comparison of the decay after pulsing in CuMnAsSb with those earlier studies is feasible. SERs offer access to the amplitude and relaxation time of the transient R_{xy} signal as well as the constant offset between orthogonal pulses after decay.

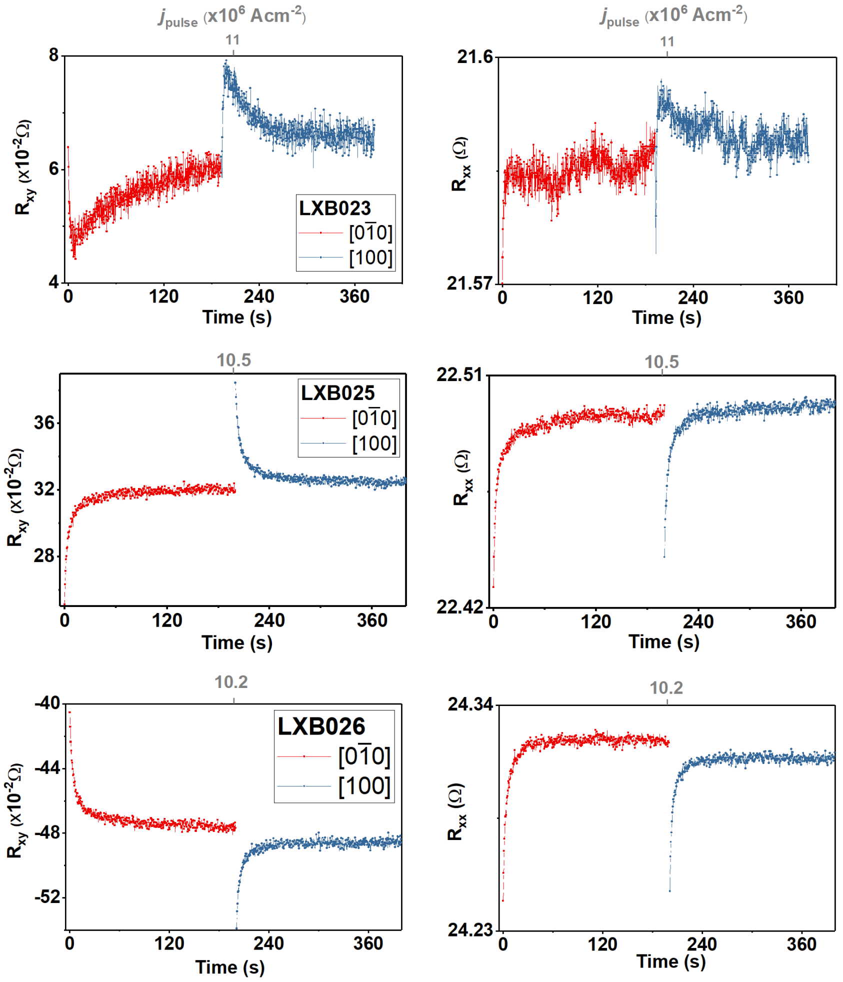

Fig. 4.11 Response of transverse resistance to orthogonal pulses along the layer [100] (blue) and $[0\bar{1}0]$ directions (red) for each layer with the longitudinal resistance depicted on the right hand side. The switching signal on the left shows the response to pulses at three current densities to demonstrate the size of the relaxation with pulse amplitude.

The R_{xy} responses of all three layers was treated with SER fits. However, the difference in form seen in LXB023 over LXB025 and LXB026 required a distinct approach. Fitting for LXB025 and LXB026 followed the previously established two component decay model characterised by the linear combination of two SER terms as in eqn. 4.5. Such fitting over the full R_{xy} response for LXB023 results was not feasible due to the change in sign of dR_{xy}dt. Instead the R_{xy} signal for LXB023 was truncated from the start of the probe to the first point of inflection i.e. omitting up to the first 5s of data. The reduced dataset was then fit with a single term SER function as in eqn. 4.4 to model the signal that converges on the mean R_{xy}. This approach loses some information, only producing one figure for the decay amplitude and time period. However, in the two component decay model the first term was associated with decay in the first seconds of the R_{xy} signal, with the remaining signal dominated by evolution over a timescale of up to 250s and so the single term approach is assumed to solely model the latter decay component.

In following the approach of [120] and [121] the same exponent value of 0.6 was preserved in the fitting of CuMnAsSb results. Fitting was performed using CFTool developed by Dr R. Campion with a Levenberg-Marquardt algorithm using initial values as checks on the sign of the terms and to avoid local minima. From examples of the fitting shown in fig. 4.12 for LXB025 and LXB026 the improvement in fitting around the first seconds of decay with a two term SER function over the single term function is clear. This is further highlighted by the base 10 logarithmic scale residual below to data plot.

Relaxation Time

From SER fitting the relaxation time, τ, provides a quantitative assessment of the timescale over which the R_{xy} response returns to an equilibrium state. Values of τ extracted from fitting are plotted at multiple pulse amplitudes for each CuMnAsSb layer in fig. 4.13. For results fit with a two term SER function (LXB025 and LXB026) the values of τ_1 and τ_2 broadly fall within two distinct timescales that is a fast decay component below $\sim$5s and a slower decay component generally characterised as between 10s and 250s with some statistical deviation.

LXB023, which was cropped and fitted with a single SER term demonstrate relaxation time from 10s to 53s. With the exclusion of the initial response below 5s the remaining signal bears an affinity with the slower decay component found in two term SER fitting of LXB025 and LXB026.

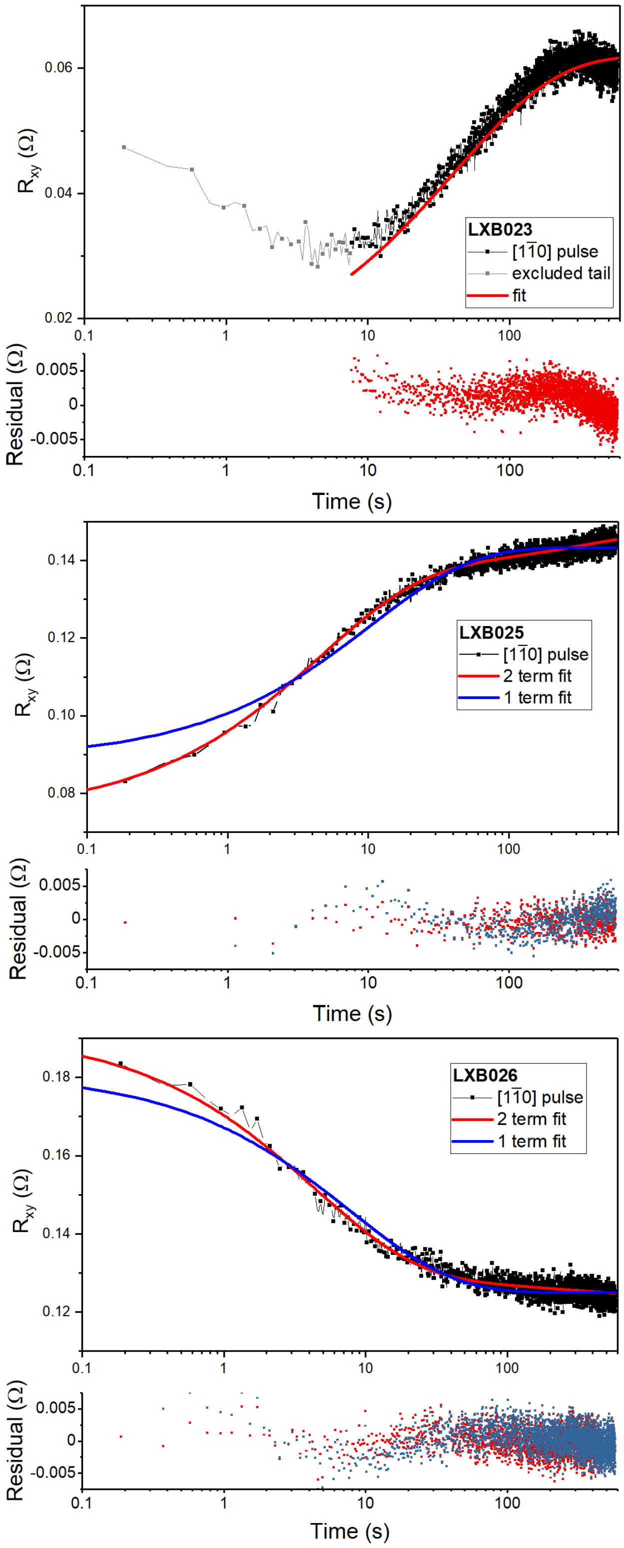

Fig. 4.12 Logarithmic plot of the [1$\bar{1}$0] 30V pulse for each layer with the associated fitting applied in red along with lower order SERs in blue and residuals illustrated below.

In the physical picture of fragmentation and reformation postulated to relate to the quench switching regime the relaxation time corresponds to the timescale of AF domain and wall reformation in response to the current pulse, however, other interpretations cannot be ruled out based on results obtained in this work. Rather, the relaxation time coincides with behaviour observed with commensurate magnetic contrast imaging in prior quench switching work by Kaspar et al.[120] For comparison values of τ determined in [120] were of the order $\sim$ 10ms and $\sim$ 10s for the fast and slow decay components at 300K respectively. Work conducted over three CuMnAs layers in [121] found that at 290K the two components could be separated into windows of $\sim$ 20s and $\sim$ 250s.

Amplitude and Offset

The amplitude extracted from SER fitting provides the size of the relaxation for a given current pulse. Amplitude coefficients extracted from SER fitting for all three CuMnAsSb layers are presented in fig. 4.14 against the pulse current density.

Beyond a threshold pulse current density j_0 a discernible change and relaxation in R_{xy} follows the pulse, however at low amplitudes the uncertainty in fitting becomes large beyond efficacy. The amplitude is however proportional to the pulse power following the polynomial relationship,

$$A_{1,2} = a_{1,2}(j - j_0)^2 \tag{4.6}$$

where $\mathrm{a}_{1,2}$ is the parabola steepness for the first and second amplitude term and relates the relaxation amplitude to the pulse current. Comparison of the amplitude with pulsing current, given in table 4.1, can then be made between layers. For the quench switching model, the threshold current density may be lower in LXB025 and LXB026 due to a reduction in T_N with Sb inclusion or disruption of the crystal lattice. Comparison with literature ranks the threshold current density of CuMnAsSb amongst other collinear AFs with broken inversion symmetry such as CuMnAs and $\mathrm{Mn_2Au}$ and significantly less than bilayer insulator systems.[123]

The offset term c represents the equilibrium R_{xy} value after relaxation. The difference in c between successive orthogonal pulses is the persistent change in R_{xy} or 'switch' signal. These values for each layer with current density are presented in fig. 4.15. The persistent offset in R_{xy} following a pulse is small in

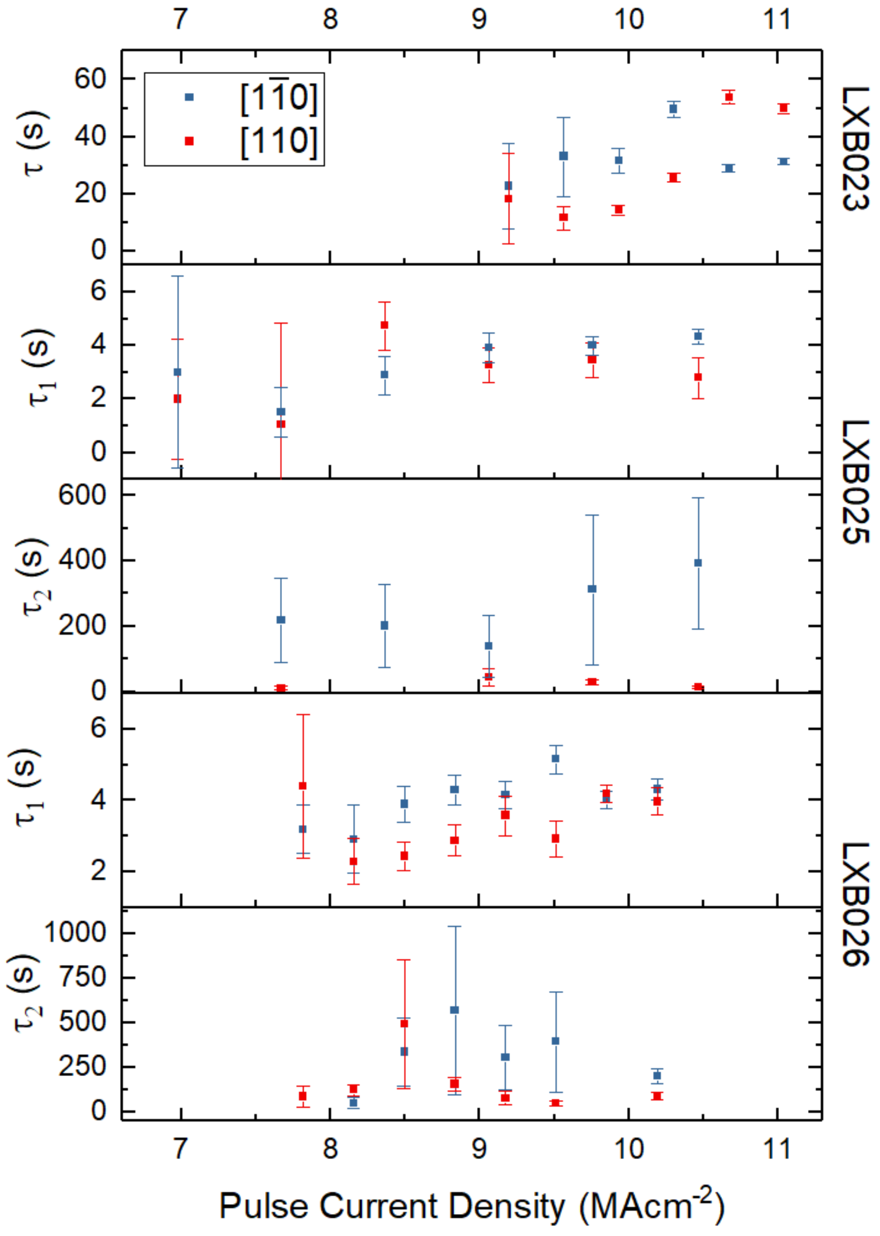

Fig. 4.13 Decay time from SER fitting with current pulse amplitude for each layer. LXB023 has only one component due to the truncation of the fast decay component from the fitting procedure. Orthogonal pulse crystal directions are relevant to the CuMnAsSb layer.

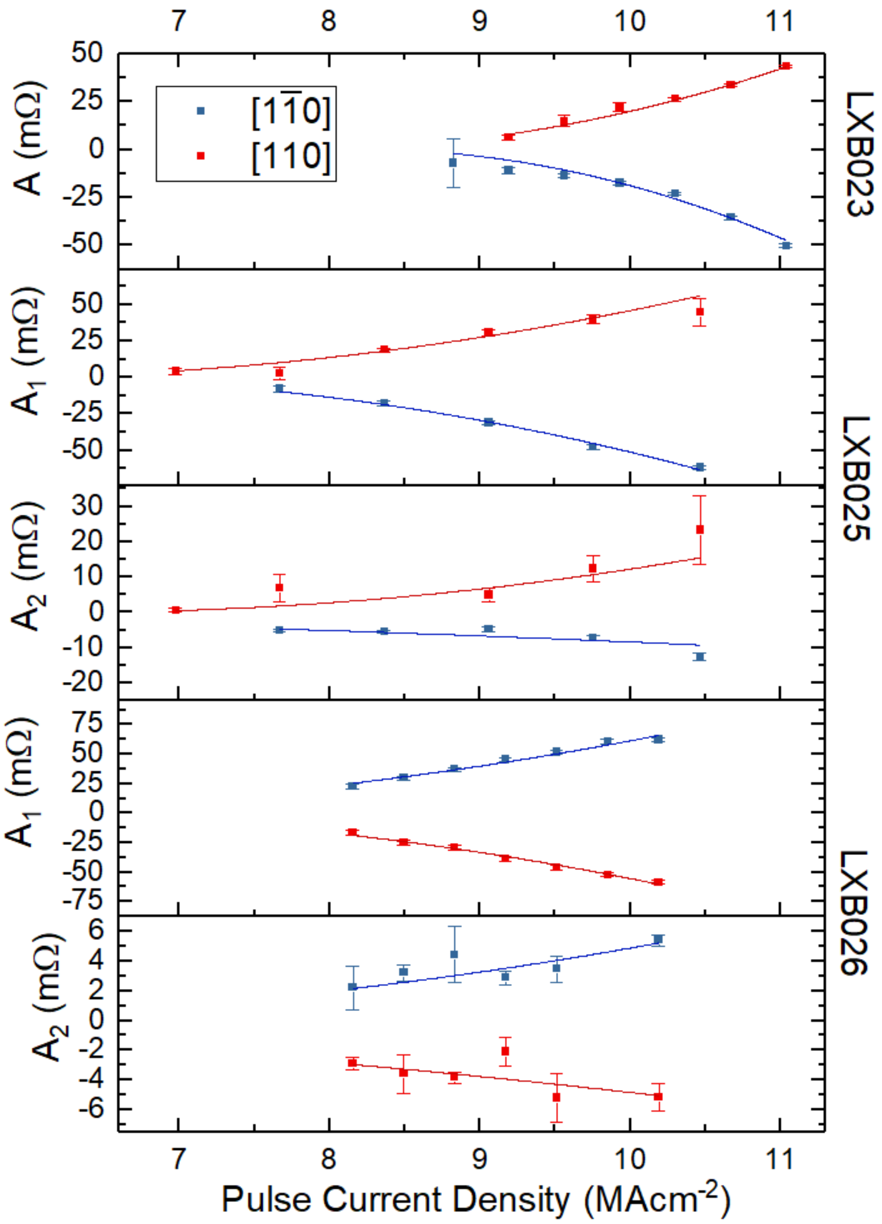

Fig. 4.14 SER fitting amplitude coefficient with applied current pulse amplitude. LXB023 has only one component due to the truncation of the fast decay component from the fitting procedure. Polynomial fits following eqn. 4.6 are overlaid to depict the typical evolution of decay amplitude with pulse amplitude. Orthogonal pulse crystal directions are relevant to the CuMnAsSb layer.

Sample	nominal Sb flux (%)	R_s (Ω/sq)	j_0 (MAcm^{-2})	a_1 $\times 10^{-15}$ (%/A^{2}cm^{-4})	a_2 $\times 10^{-15}$ (%/A^{2}cm^{-4})
LXB023	10	99.5	8.0±0.1	-	32±1
LXB025	20	100	5.8±0.2	23±2	5.4±0.9
LXB026	30	110	5.6±0.2	15±0.4	1.5±0.2

Table 4.1 Threshold switching pulse amplitudes by current density j_0 for CuMnAsSb layers along with sheet resistivity R_s along with relaxation amplitude parabola steepness $a_{1,2}$ as an AMR percentage.

comparison with the maximum change after the pulse. Additionally compared to the 0.1% resistive signal in current pulsing within the NSOT regime for CuMnAs the persistent change proportional to the R_{xx} here is at most a mere 0.02%. Insight into the relationship between current pulse amplitude and offset is limited with no clear trend across the three CuMnAsSb samples. Additionally the substitution of Sb does not appear to pose a significant improvement in the persistent change in R_{xy} over electrical switching in CuMnAs.

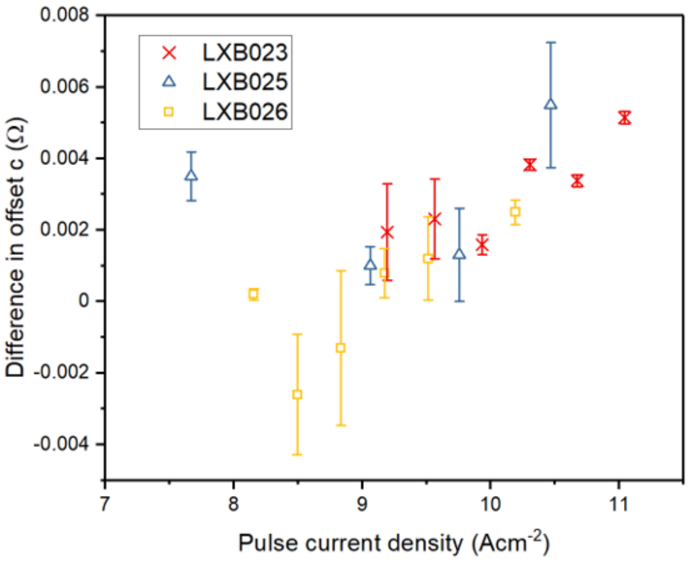

Fig. 4.15 Difference in offset found by SER fitting between orthogonal current pulses with current pulse amplitude for each layer.

4.5 Summary and Conclusion

Characterisation of the magnetic and transport properties of CuMnAsSb were described in this chapter.

Electron transport investigation of the Néel temperature indicated a magnetic phase transition at 451.5±0.7K for a 120nm thick layer with Sb flux at 20% of stoichiometric As and a similar value within error of 462.1±0.2K for lower (10%) Sb flux, at thicknesses utilised in microdevices. Transport and neutron diffraction methods were found to corroborate to a reasonable degree with a value of 460±10K obtained from the latter on the same 120nm thick layer grown at 20% Sb flux. Neutron diffraction also confirmed the in-plane AF ordering of spins. Although there was a depression of T_N between 19K and 28K as compared to CuMnAs in transport measurements a margin of 160K above room temperature was preserved.

XMLD-PEEM imaging has confirmed in-plane AF ordering in LXB025. Domains larger than seen in CuMnAs grown on GaAs but smaller than high crystal quality CuMnAs grown on GaP were observed. Rotation of the sample with respect to the X-ray polarisation revealed biaxial domain texture in the layer where the spin axes to lie in-plane predominantly along the [100] and [010] crystal directions of CuMnAsSb. Some small divergence of spin axes within the domain is indicated by granular XMLD contrast in images with the X-ray polarisation at a 45° offset to the AF easy axes.

Current pulse transport measurements on CuMnAsSb microdevices exhibited a characteristic resistive response of the same form as CuMnAs pulsed in the quench switching regime when pulsed along any arm. Following the same SER fitting procedure as in work by Kaspar et al,[120] which found the same two characteristic relaxation timescales and comparable threshold current densities. The persistent 'switch' in R_{xy} was small and evidence of NSOT induced AMR like that in low current density pulsing in CuMnAs was not shown here, however, use of trains of repeating pulses along one direction may illicit an NSOT AMR signal.

The novel HCl dip etch fabrication step has preserved switching phenomena in transport and removed some contribution of MnAs, however, transport at high field was not feasible and might still suffer a FM contribution at the low temperatures employed by superconducting magnetic field systems.

Chapter 5

Nernst and Spin Seebeck Effects in Fe and FeGa Thin films

5.1 Introduction

The following work discusses the investigation of $Fe_{0.79}Ga_{0.21}$ (referred to simply as FeGa henceforth) thin films as a candidate spin caloritronic material, with simultaneous comparison to elemental Fe layers. The spin Seebeck effect is a nascent approach for waste thermal energy harvesting devices. Key to quantitatively ranking candidate materials efficiency is measuring the spin Seebeck coefficient and obtaining the figure of merit.

First for discussion is how samples were synthesised via sputter deposition and their properties assessed for crystallinity, composition, and morphology. This procedure utilised XRD, magnetometry, AFM, TEM-EDS, and electrical transport measurements. TEM-EDS work was carried out by Loughborough Materials Characterisation Centre with assistance from Dr C. Cox.

Attention is then directed to the principal experiment aiming to obtain a spin Seebeck coefficient and figure of merit for FeGa in the longitudinal temperature gradient, that is, a gradient perpendicular to the plane of the layer and in-plane magnetisation. These longitudinal spin Seebeck effect (LSSE) experiments stimulate a spin current in the ferromagnet, which is detected via the inverse spin Hall effect (ISHE) in a heavy metal overlayer. Although separation of spin Seebeck effects from other thermally driven galvanic phenomena proved infeasible, due to conduction path mixing, it was possible to corroborate contemporary work and further investigation of Fe layers was stimulated. This work was carried out in part by the author, Prof. K. Morrison and Dr C. Cox with support from Dr G. Venkat.

The chapter goes on to outline the efforts to understand anomalous peaks in the in-plane voltage of Fe samples around the coercive field seen during measurement of the LSSE. Beginning with the assembly of a new lateral thermoelectric setup, which demonstrated the excitation of planar magneto-Seebeck effects, it was determined that the anomalous peaks were an experimental artefact, which serves as a cautionary tale for experimentalists investigating thermo-galvanic phenomena in thin magnetic films.

Finally, electron transport experiments on microfabricated devices of each ferromagnet confirmed the mechanism of magnetisation reversal giving rise to the planar signals originally seen in the longitudinal geometry. These results demonstrated the difference in signal between Fe and FeGa layers is inherent to the magnetisation reversal behaviour rather than relating to a specific thermal effect.

5.2 Characteristics of Fe and FeGa thin films

5.2.1 Samples and Synthesis

A total of 13 samples were made, all following the same method with changes in choice of cap material, thickness and ferromagnet (FM) composition. Wafer Tech (100) undoped single crystal GaAs substrates, 2” in diameter were used for their high-quality epitaxy with Fe given a lattice parameter mismatch is 1.4% between a pair of BCC Fe unit cells and GaAs. Prior to loading the substrate into the UHV of the sputter machine, the oxide layer was etched away in an HCl acid bath. The loaded substrate was then annealed at high temperature of 500^oC for 1 hour to reduce surface contamination. With the heating off the substrate was allowed to cool to below 35^oC as recorded on the thermocouple for several hours before starting deposition. 20nm of the FM layer were deposited, established in previous studies as the optimal thickness without degradation of crystallinity [124] followed by 2nm or 5nm caps of a ‘normal’ metal (NM) for protection from oxidation and as an ISHE spin current converter.

The archetypal ISHE layer, Pt has a high spin Hall angle θ (SHA) [63] amongst transition metals and is highly unreactive whilst Cr is abundant and self-limiting to oxidation, although, it’s SHA is not well studied. Later samples used Al as a low SHA cap to test for purely ANE signal and a cap of Ta was employed with a negative SHA to determine whether the anomalous Nernst effect (ANE) and LSSE signals could be enhanced by matching their directions. A full list of sputtered samples including their cap composition and thickness by assigned sample name is given in table 5.1.

Cap →		Pt($0<\theta \leqslant 0.11$)		Cr(θ -)		Al($0<\theta \leqslant 0.0003$)		Ta($\theta \leqslant -0.07$)	
FM ↓	tcap →	2nm	5nm	2nm	5nm	2nm	5nm	2nm	5nm
FeGa		-	S667	S670	S672	S690	S689	S740	S688
Fe		S735	S668	S732	-	S680	S686	S741	S685

Table 5.1 Fe and FeGa samples synthesised by sputter deposition by capping material and cap thickness, each deposition is named sequentially. values of θ from [63]

5.2.2 Crystal Qaulity

XRD

In order to determine the crystal order and quality of the sputtered layers, demonstrative x-ray diffraction line scans were carried out. Performed across the surface to obtain the out of plane $\langle 001 \rangle$ peaks these $2\theta/\omega$ scans reveal the lattice parameter, mosaicity and strain. The line scan shown in fig. 5.1 at the relevant angle for Fe and FeGa. All four samples exhibit a diffraction peak confirming the FM layer broadly follows the BCC Fe structure and the varying shapes allow for comparison between samples. The full scan, in the inset plot, shows the two out of plane substrate peaks and an additional broad peak of the Pt cap in S667 at 46^o.

The Fe diffraction peaks are both sharper than the FeGa peaks, the extracted FWHM is given in table 5.2 along with lattice parameter and normalised intensity. The results show there is up to a 5-fold improvement in the FWHM of the Fe over the FeGa. This is consistent with the expected integration of Ga, as the material maintains the overall BCC Fe crystal structure with either interstitial Ga atoms or inhomogeneous Ga cluster inclusions forming.[35, 36] Both would disrupt and degrade the BCC Fe crystal order manifesting in the data as a spread in the size of Fe cubic cells and a broader diffraction peak. This is also apparent in the nearly 10-fold higher yield diffracted X-rays at the Fe peak. Taking the centre of the peaks as the c axis lattice parameter it can be determined that the Fe layer is marginally taller undergoing some compressive strain with two unit cells of bulk BCC Fe 1.1% greater than the lattice constant of the GaAs substrate.[125] Although broad the peak position of FeGa places the lattice constant close to the bulk FeGa lattice constant, determined to be 2.906Å. [126]

Sample	Composition	Intensity BG norm. (x10^{-5})	Lattice Parameter (Å)	FWHM (^{o})
S667	FeGa/Pt	1.6	2.91	4.3
S670	FeGa/Cr	1.1	2.90	3.6
S680	Fe/Al	9.8	2.87	1.8
S685	Fe/Ta	5.6	2.88	0.79

Table 5.2 XRD line scan results for two FeGa and two Fe thin films

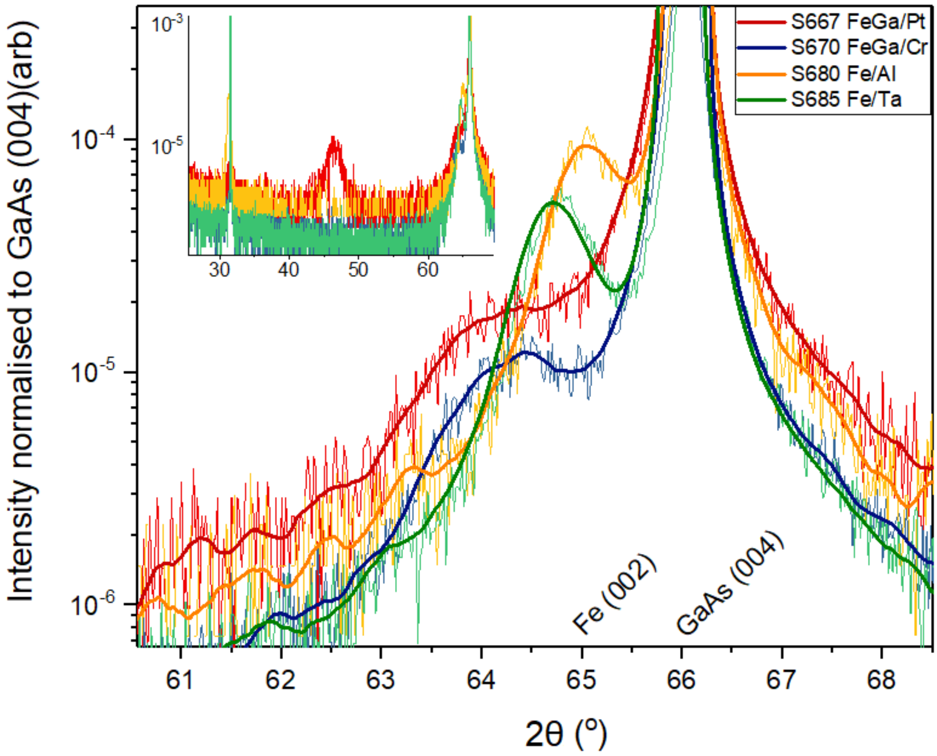

Fig. 5.1 $2\theta/\omega$ line scans as measured and smoothed (bold) taken in the out of plane direction of the four samples covering all deposition materials. The intensity in counts has been normalised to the dominant GaAs(004) substrate peak common between them at 66^{o}. The bulk Fe (002) peak is indicated at 65^{o}.

TEM EDS

Lamellae of S667 and S668 were examined under HRTEM to observe the structure and quality of the layers. In this phase contrast imaging technique the periodicity of atoms can be observed, however, specific information is predominantly derived from a counterpart simulation as opposed to contrast in the image. Both layers exhibit crystallinity within the FM layer, the periodicity of the lattice can be enhanced with FFT image processing. By isolating the highest intensity points in the FFT transform and reverting back to the real space image irregular information is removed. The distance between atomic spacings can then be measured given enough knowledge of the crystal. In this case the sample is examined along the [110] direction, diagonal to the unit cell. Multiple spacings were measured by number of pixels to obtain an average of the unit cell *ab* hypotenuse, converting to a length by calibration against the inset scale bar. The measured spacing of columns in S668 is consistent for heteroepitaxy of BCC Fe on the cubic Zincblende GaAs substrate layer, where the GaAs unit cell is twice the width of Fe with a 1.5% mismatch. The spacing of FeGa however is closer, likely due to disruption of the Fe lattice by Ga. There is a perceived improvement in contrast and clarity of the Fe over the FeGa images, however, with the absence of proper simulation little can be said with confidence besides a difference in crystal quality is consistent with the XRD.

Sample	Composition	FM d-spacing $\sqrt{a^2+b^2}$ (Å)	GaAs d-spacing $\sqrt{a^2+b^2}$ (Å)	Mismatch (%)
S667	FeGa/Pt	4.12	8.26	-0.2
S668	Fe/Pt	4.18	8.24	1.5

Table 5.3 HRTEM determined in plane d-spacing, averaged over multiple atomic columns. Since the lamellae are taken along the diagonal [110] direction the d-spacing represents the hypotenuse of the planar lattice parameters a and b.

EDS was performed with a TEM reference to provide elemental mapping of cross sections. These maps reveal the distribution of sputtered material through the sample including integration of Ga within Fe and quality of interfaces between layers. Specifically of interest is the presence of Ga throughout the FM layer and an absence of diffusive mixing between the cap and the FM layer. The ISHE is a highly interface-sensitive phenomenon and a mixing of

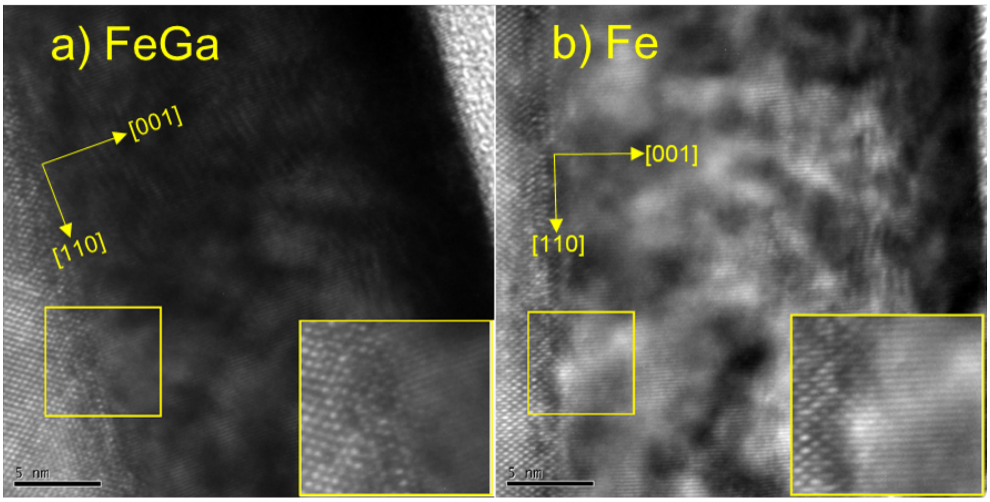

Fig. 5.2 HRTEM image of (a) FeGa sample S667 and (b) Fe sample S668. A close up of the region of interest in yellow is given for both highlighting the perceptible crystallinity of the substrate on the left and FM layer to the right.

Fe and Pt would dampen the LSSE signal. As shown in fig. 5.3(b) a drop off in Ga concentration closely follows the deposition of Fe and is present throughout with a clear boundary of Fe on the substrate in fig. 5.3(c). Figure 5.4(b) shows the absence of Ga beyond the substrate and on the overlapped maps in fig.5.4(c) the clear boundaries between GaAs, Fe and Pt cap.

5.2.3 Material Properties

Composition

The fractional concentration of Ga x in $Fe_{1-x}Ga_x$ layers, optimal in terms of magnetostriction at 21%, can be determined from the magnetic moment in a saturating magnetic field by taking the room temperature ratio of moment per unit volume between the layer. This approach assumes the moment per Fe atom ($2.15\mu_B$) remains constant with Ga substitution of 21% and excluding magnetic depletion region at the substrate interface from the FM volume. This has been shown to the case in work by Dr. S. Roy [124] for samples grown and characterised in the same systems. The moment per Fe atom at 20% Ga content was measured as $2.0\pm0.2\mu_B$ and a 1nm magnetic depletion layer was calculated from comparison of layer volume magnetisation in SQUID and ferromagnetic resonance measurements, which was performed coupled to the layer surface.[124]

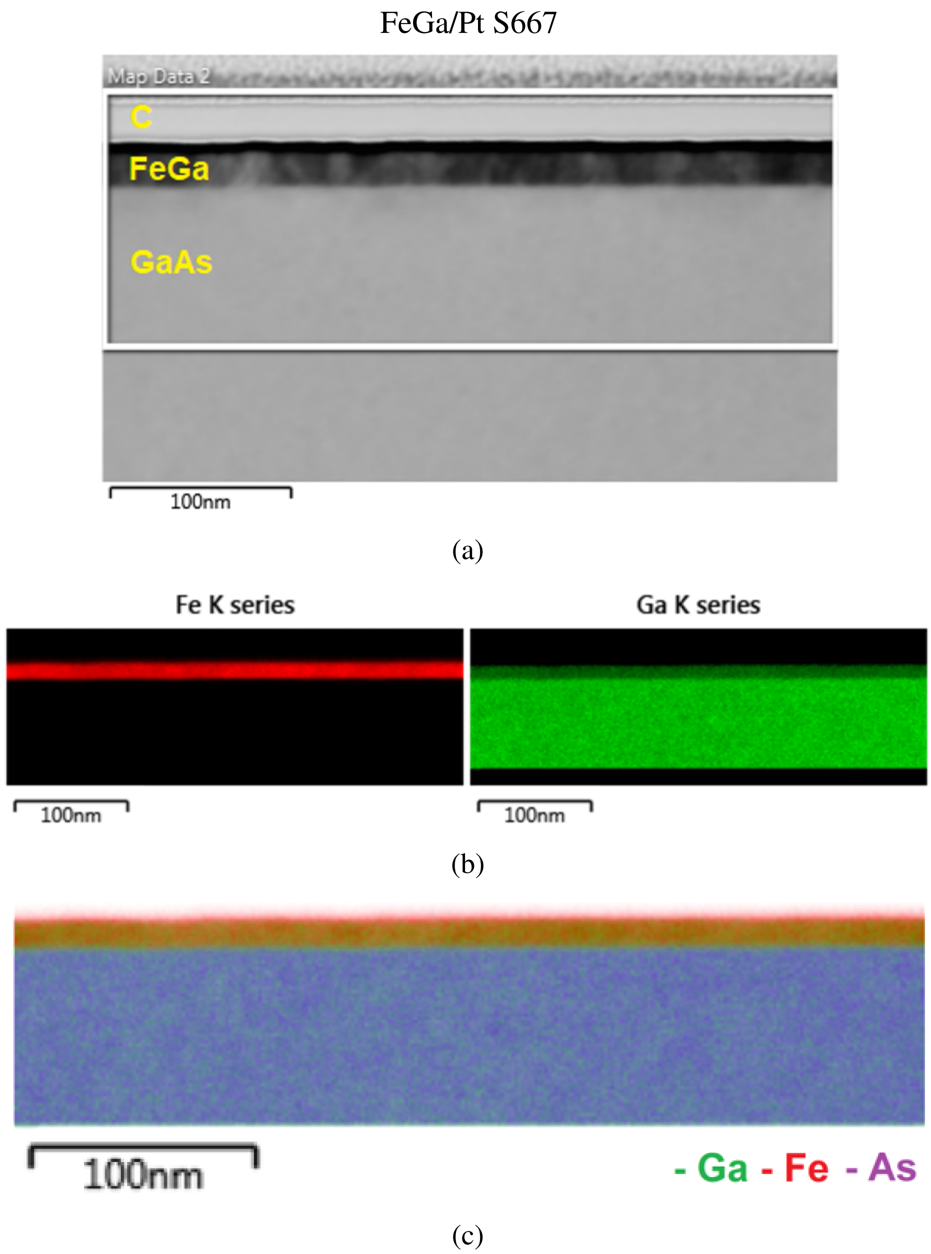

Fig. 5.3 Here (a) shows the TEM region of the S667 FeGa/Pt sample under EDS analysis. In (b) individual maps of Fe and Ga are given and in (c) the same maps along with As overlaid.

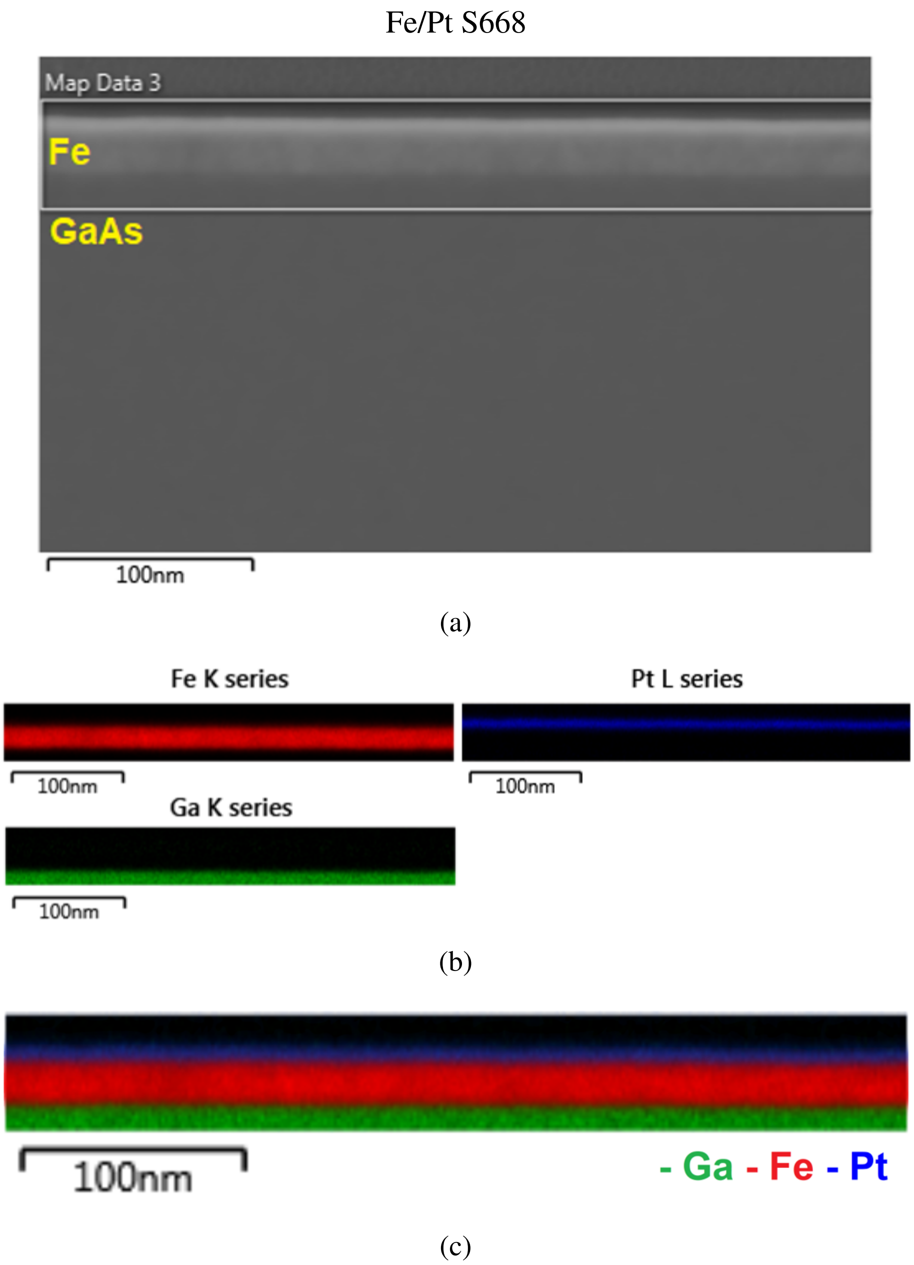

(a)

(b)

(c)

Fig. 5.4 Here (a) shows the TEM region of the S668 Fe/Pt sample under EDS analysis. In (b) individual maps of Fe, Pt and Ga are given and in (c) the same maps along with As overlaid.

SQUID measurements were performed, at 300K, to ensure the stoichiometry during synthesis was in line with expected values. Sweeping between a ±1T field these measurements also provided information on the coercive and saturating field strength generally ±8mT and ±50mT respectively as discernable in fig. 5.5. Notably also the Cr capped FeGa appears offset toward the negative field, exhibiting exchange bias due to the AF magnetic order of Cr. Composition results, equivalent to % Fe concentration, are given in fig. 5.6. There is some variation in the concentration skewed toward Fe, however, repeating growths was not always feasible under time, access and material constraints.

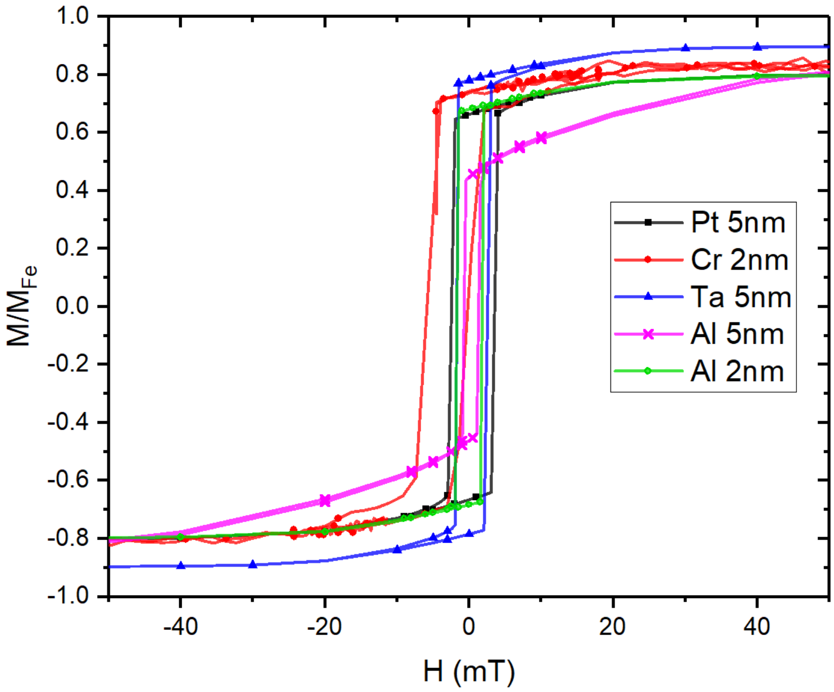

Fig. 5.5 Magnetisation with field hysteresis loops for FeGa samples as a ratio of elemental Fe magnetisation. Measurement performed at 300K with a sweep between ±50mT

Surface Topography

Surface topography was studied with AFM to ensure the caps were smooth and without defect as well as an early and convenient assessment of sample quality. Smooth surfaces are preferable for simplifying the electron transport phenomena, as indicators of good interfaces between FM and cap needed for ISHE and that conditions in sputtering are appropriate with consistent results.

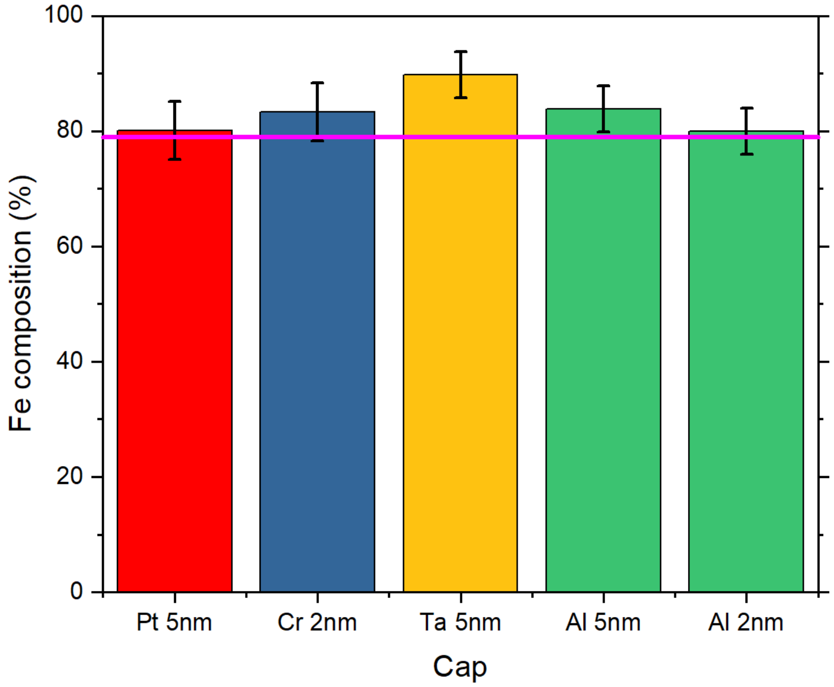

Fig. 5.6 ratio of sample FM layer magnetisation to magnetisation of Fe as measured in SQUID with samples grouped in colour by capping material. The magenta line marks the ideal 21% Ga to 79% Fe ratio to optimise magnetoelastic properties of FeGa.

While a sample might exhibit features on the order of 1nm or greater in R_z here a measure of the average roughness over a scanned area R_{RMS} and R_{av} below 1nm is considered adequate.

Results from AFM are given in table 5.4 and show that there is good sub nm roughness for Cr and Pt but Al is far rougher. This is illustrated visually in fig. 5.7(a) where profiles of the three caps can be seen on the same plot and fig. 5.7(b) shows a 3D projection of the AFM image for Al and Cr. The low level of roughness for Pt and Cr are good for the experimental applications and consistent with sputtered metallic thin films. Rougher Al however is poor but still has some use since it is not a SSE detection candidate possessing a small spin Hall angle. The roughness is likely due to 3D growth of Al occurring at high surface temperatures. Given a warm surface, even after several hours cooling after annealing of the substrate, Al is highly mobile and surface energy allows it to accumulate in a preferential crystal phase oriented out of plane. Despite allowing the sample to cool from annealing for several hours no thermometry of the sample is available and further cooling is infeasible due to gradual contamination of the surface and lab access rules.

Cap	Roughness R_{RMS} (nm)	Av max. height R_z (nm)	Roughness average R_{av} (nm)
Pt	0.2	0.7	0.2
Cr	0.3	1	0.2
Al	2	8	2

Table 5.4 Measures of roughness for three different cap materials determined from AFM line profiles of a 1-2μm length-scale.

Resistivity

Sheet resistance was obtained from Van Der Pauw measurements on 10mmx10mm chips, positioning brass microprobe pins at the corner to measure the horizontal and vertical resistance. These measurements are useful in comparing longitudinal thermoelectric results and necessary for the calculation of the lateral thermoelectric power factor. There is a large difference between Fe and FeGa samples as seen between the plots in fig. 5.8, with Fe far more conductive, consistent with an elemental metal layer with fewer scattering centres than the FeGa. An apparently anomalous result exists for the thicker 5nm Ta capped Fe sample, which has a higher resistance than the counterpart thin cap, a result not observed in the FeGa sample. This may be explained by the high resistance of Ta compared to Fe and degree of contact with the pin, where the pins may make direct contact with the more conductive Fe through abrasion of the cap on the thin cap sample, with the current passing largely through the Fe layer. Contrastingly, the thicker Ta cap may make up more of the contact interface with the pin and contribute more to the measurement. In the FeGa the FM layer resistance is higher making a more conductive path bypassing the cap unlikely.

Crucially, there is significant change in conductivity between caps and cap thickness for FeGa and to a lesser extent in Fe layers. Consequently in FeGa samples the cap material and thickness has a large influence over measured voltage, particularly relevant to the ANE signal that predominantly originates in the FM but is detected via conduction through the cap. The need for a model of the conduction path and contribution of the cap, made evident in the initial LSSE measurements is described later in the chapter.

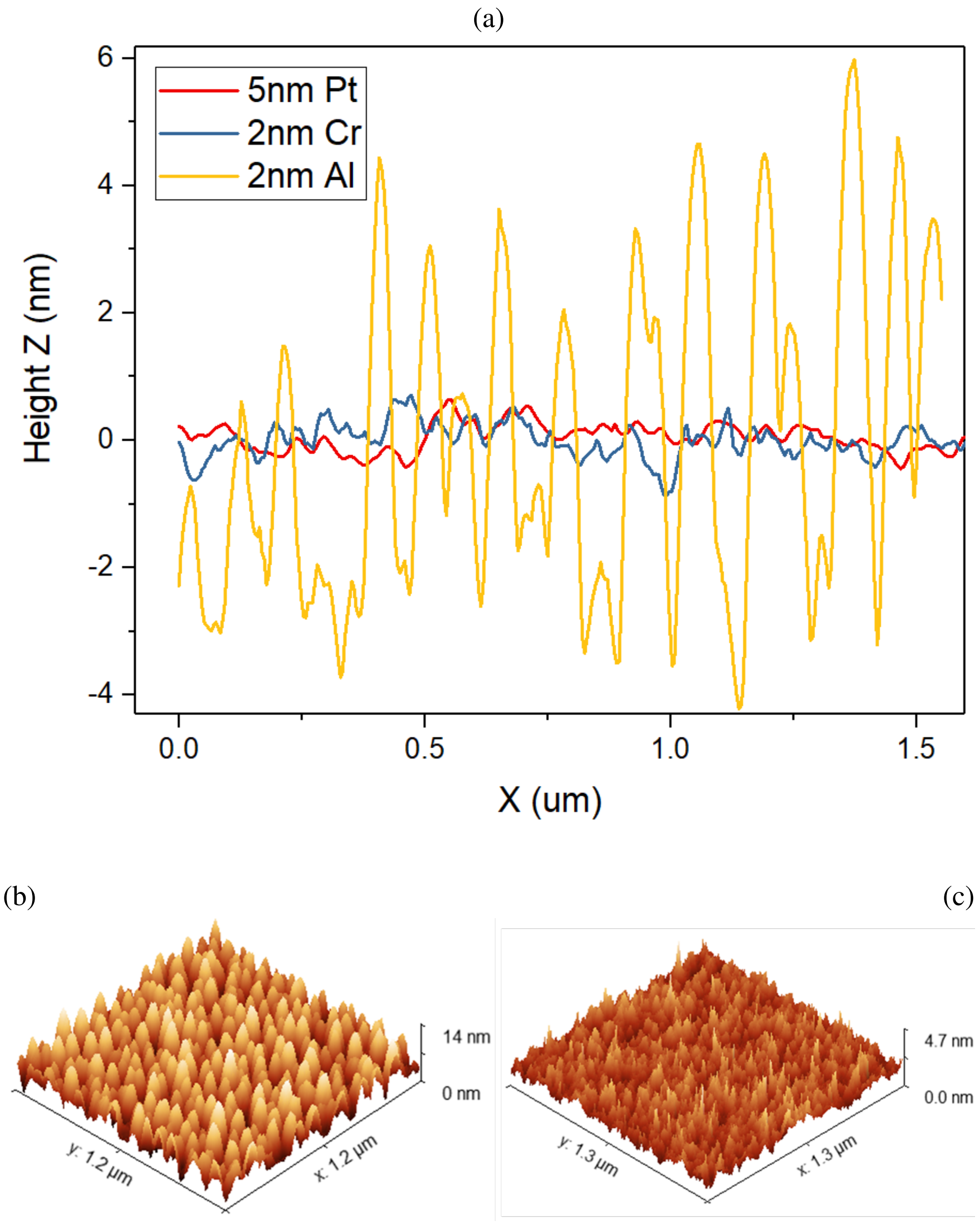

Fig. 5.7 (a) AFM line profiles of 3 different cap materials (b) left Al capped surface with large 3D features and right Cr capped surface with lower roughness.

5.3 Longitudinal Spin Seebeck Effect Experiments

5.3.1 Comparison between Fe and FeGa

Utilising a vertical stack of Peltier devices and a Helmholtz coil electromagnet it is possible to induce the longitudinal spin Seebeck effect in the previously

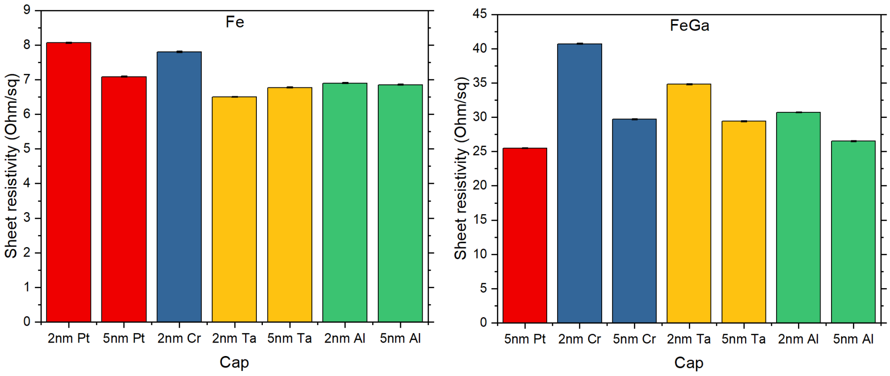

Fig. 5.8 Bar charts for sheet resistance measured via 4 probe Van Der Pauw for Fe (left) and FeGa (right) samples. Cap materials are grouped by colour.

described sputtered samples. In this section results are shown from such an experiment for both FeGa and Fe, which resolved to produce vastly different responses.

Using the setup described in 2.4.2 10mmx10mm chips were held at a temperature difference from 4K up to a maximum of 30K above room temperature, while the applied magnetic field, orthogonal to the Peltier stack, is swept between saturating fields in excess of ±40mT. Probing the in plane voltage orthogonal to the magnetic field and vertical temperature difference galvanic responses of thermal origin are detected. Two effects of principle interest are dependent on sample magnetisation as well as thermal gradients, the longitudinal spin Seebeck effect and the anomalous Nernst effect. Another occurs when in plane temperature gradients give rise to ordinary Seebeck effects. These extraneous gradients have arbitrary, unknown direction and are not easily controlled. In most spin caloritronic experiments this background is not considered of interest and subtracted to make the midpoint of the hysteresis response zero.

Assessment is made based on the electric field E, which aside from the ordinary Seebeck background is composed of the anomalous Nernst effect existing largely in the FM and the ISHE generated by the spin injection of the LSSE into the NM.

The ISHE is defined by the spin Hall angle θ_{SH} and cap resistivity ρ_{cap} intrinsic to the selection of the NM capping material and the injected spin current $\mathbf{j_s}$ itself originating in the FM and contingent on material factors such as the spin mixing conductance. While the spin current direction is controlled by the temperature gradient the unit spin polarisation vector σ is parallel to the FM magnetisation **M**. The equation for electric field contribution of the ISHE is presented in eqn. 5.1.

$$E_{ISHE} = (\theta_{SH}\rho_{cap})\sigma \times \mathbf{j_s} \tag{5.1}$$

The anomalous Nernst effect component emerges largely from the FM and is defined simply by the cross product of the temperature gradient $\nabla\mathbf{T}$ and magnetisation related to electric field by the Nernst coefficient $\mid N \mid$of the FM as in eqn. 5.2.

$$E_{ANE} = |N|(\nabla\mathbf{T} \times \mathbf{M}) \tag{5.2}$$

It is therefore possible for the two effects to be the same or opposing signs leading to either a higher or diminished total electric potential. In fig. 5.9 the heat flux normalised voltage described in 2.4.2 for each capping material is shown directly comparing the FeGa and Fe. It is immediately apparent the FeGa exhibits a far greater response and is of the opposite sign to equivalent Fe samples. Between all the FeGa samples absolute V_{J_Qs} falls within the range 58 and 100 $\mathrm{nVmW^{-1}}$ whilst the greatest absolute V_{J_Qs} from Fe is seen in the capped Ta S685 at just 12.2 $\mathrm{nVmW^{-1}}$ around 10% of the corresponding FeGa response.

Looking at Al, which has the smallest magnitude Spin Hall angle and little ISHE contribution, it is possible to make a comparison of the ANE in the two FMs. The ANE in Fe is indeed far smaller than the equivalent FeGa at just 6% of the measured V_{J_Qs} in FeGa/Al and of opposite sign. This is largely owing to two factors, enhancement of the transverse thermoelectric coefficient with Ga substitution [33] and the difference in electron transport between the systems.

Two previous studies on the ANE in Fe and FeGa thin films found that there was a large increase in the magnitude of the ANE signal with Ga substitution.[33, 34] Based on DFT calculations, the change was ascribed to tuning of the Fermi surface with the addition of Ga up to 32% of the composition, resulting in the enhancement of the transverse thermoelectric coefficient. The study also found a change in sign and greater magnitude Seebeck coefficient with Ga substitution, reversing with as little at 4% of the content. This change is corroborated by results in fig. 5.9.

The difference in V_{J_Qs} from electron transport is complicated by the bilayer, whilst the ANE occurs predominantly in the FM the respective contribution to the electron's mean free path by FM and NM is not known. Since FeGa is far more resistive than Fe (around 5 times higher sheet resistance for thin caps in fig. 5.8) the difference is presumed to be significant and electron transport between NM and FM cannot be assumed to be the same in comparative Fe and FeGa systems. That question became a recurrent point throughout the study and obscured a good assessment of the ANE and LSSE of FeGa particularly when attempting to compare the 4 capping materials as described in the following section.

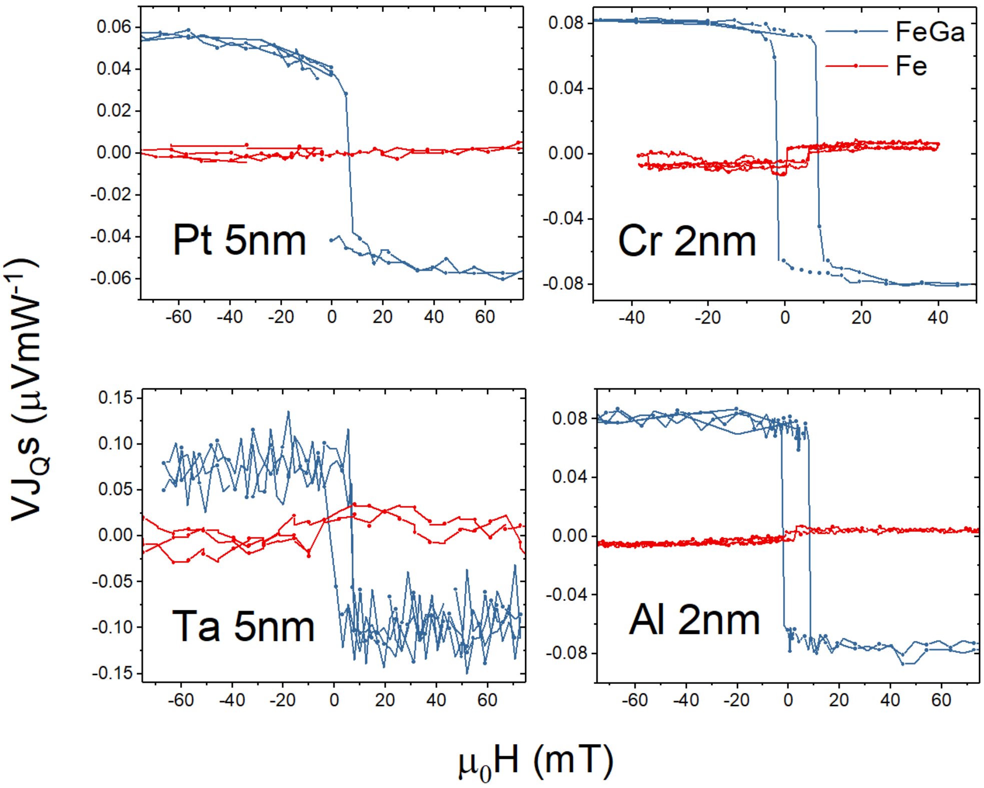

Fig. 5.9 Voltage response normalised for heat flux and contact separation of 10mmx10mm chips under a vertical temperature gradient undergoing orthogonal magnetic field sweeps. Each cap material is shown for both Fe and FeGa layers in red and blue respectively. The response at saturation equates to the electric field response per unit of heating power through the layer.

5.3.2 Comparison between FeGa capping material

Whilst the Fe-derived signal is relatively low and difficult to discern accurately, a comparison on the V$_{J_Qs}$ signal of the FeGa layers and the differing caps is feasible. There are two key factors influencing the V$_{J_Qs}$ values represented in fig. 5.10: the resistance of the cap with subsequent effects on electron transport behaviour and the competition between ANE and LSSE. While the value of

V$_{J_{Qs}}$ between samples of the same capping material follow agree with the trend of the superimposed sheet resistance values different capping materials do not. The 2nm Cr capped samples is the most resistive but elicits a lower V$_{J_{Qs}}$ than both Ta samples. There is therefore some additional difference in the voltage between systems other than competition amongst the magneto-thermal effects.

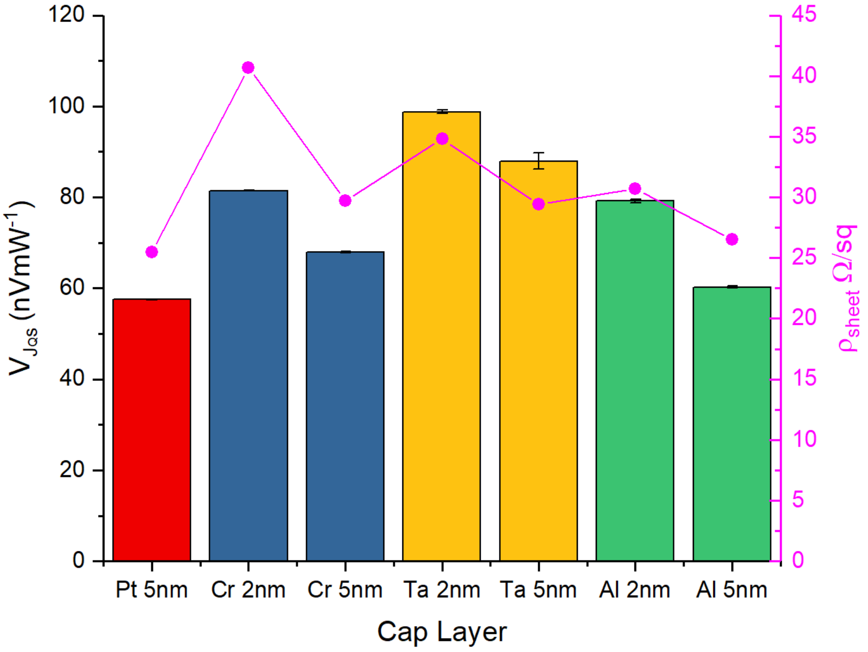

Fig. 5.10 Bar chart of heat flux normalised voltage for FeGa layers grouped by capping material with sample sheet resistivity plotted in pink.

In order to obtain the Spin Seebeck coefficient of a sample the ANE signal must be well known. Given Al's role as a low SHA cap the thinner 2nm sample can be taken as the closest to a pure ANE signal. However, the thicker cap response is far lower. The 5nm Al cap, more conductive than FeGa, likely shunts Nernst current, originating in the FM, lowering the measured voltage by more than is proportional to the lower overall sheet resistance. Current path mixing cannot be modelled without first establishing the electron mean free path. Therefore comparing between cap thicknesses produces complex results, obscuring the magnitude of LSSE and ANE effects for the FM.

The question of the capping material's contribution to the measured voltage can be tested to demonstrate that the ANE cannot reliably be measured across samples of differing composition. It should be true that given the same FM the ANE should not depend on the electrical nature or presence of the capping layer because it doesn't change the heat flow through the FM layer using the heat flux method. The voltage will only depend upon the cap due to shunting.

This test is done as an exercise below, taking the experimental dimensions and results of FeGa layers with each capping material that are provided in table 5.5.

Taking the FeGa layers with the thinnest cap Al 2nm and Cr 2nm, which are expected to present the least shunting and ISHE, it is possible to make a reasonable estimate of the ANE by assuming the cap is negligable i.e. they are "uncapped".

For FeGa capped with 2nm Cr:

$$R = 0.76 \times 40.7\Omega/\square = 30.9\Omega$$

$$I_{ANE}^{Cr} = \frac{V_{meas}}{R} = 0.185\mu A$$

For FeGa capped with 2nm Al:

$$R = 0.61 \times 30.8\Omega/\square = 18.7\Omega$$

$$I_{ANE}^{Al} = \frac{V_{meas}}{R} = 0.256\mu A$$

Assuming still that the ANE in the FM is the same irrespective of capping material it should be possible to work out the voltage of the thicker 5nm Cr and Al capped FeGa samples due entirely to shunting.

For FeGa capped with 5nm Cr:

$$R = 0.88 \times 29.7\Omega/\square = 26.1\Omega$$

If as above $I_{ANE}^{Cr} = 0.185\mu A$ then:

$$V_{calc} = 4.83\mu V$$

where $V_{meas} = 5.14\mu V$

For FeGa capped with 5nm Al:

$$R = 0.63 \times 26.5\Omega/\square = 16.7\Omega$$

If $I_{ANE}^{Al} = 0.256\mu A$ then:

$$V_{calc} = 4.27\mu V$$

where $V_{meas} = 3.71\mu V$

This is already poses an inconsistency between both the two thin caps and their equivalent measured voltage for a thicker cap of the same material. However, extending it further still assuming the above is the ANE contribution to the measured current the ISHE contribution for higher θ_{SH} caps Pt and Ta should be ascertainable.

For FeGa capped with 5nm Ta:

$$R = 0.65 \times 29.4\Omega/\square = 19.1\Omega$$

$$\text{If } I_{ANE}^{Cr} = 0.185\mu A \text{ then } V_{calc}^{Ta} = 3.53\mu V$$

$$\text{or } I_{ANE}^{Al} = 0.256\mu A \text{ then } V_{calc}^{Ta} = 4.89\mu V$$

Whereas $V_{meas}^{Ta} = 6.21\mu V$ so:

$$I_{ISHE} = 0.140\mu A \text{ or } 69nA$$

For FeGa capped with 5nm Pt:

$$R = 0.71 \times 25.5\Omega/\square = 18.1\Omega$$

$$\text{If } I_{ANE}^{Cr} = 0.185\mu A \text{ then } V_{calc}^{Pt} = 3.35\mu V$$

$$\text{or } I_{ANE}^{Al} = 0.256\mu A \text{ then } V_{calc}^{Pt} = 4.63\mu V$$

Whereas $V_{meas}^{Pt} = 3.94\mu V$ so:

$$I_{ISHE} = 33nA \text{ or } -38nA$$

This is not consistently as expected with a difference in sign for Pt and large difference in magnitude for Cr. The ANE cannot reliably be extracted from the thin capped samples to make any confident assessment of the ISHE.

The aim of acquiring a LSSE figure of merit Z as shown in eqn. 5.3 relies on knowledge of the spin Seebeck coefficient α_s and ferromagnet thermal conductivity κ_{FM}. For FeGa and Fe a spin Seebeck coefficient free of the ANE was prohibited by cap shunt resistance and current path mixing as described above. While it was not in the scope of the experiment to determine κ_{FM} of FeGa there is purpose in establishing Z^{LSSE} with κ_{FM} as an unknown constant factor to compare geometries and materials of a similar order. In one of the most ubiquitous SSE systems that takes advantage of insulator yttrium iron

Sample:	FeGa/Cr	FeGa/Al	FeGa/Cr	FeGa/Al	FeGa/Pt	FeGa/Ta
Thickness (nm)	20/2	20/2	20/5	20/5	20/5	20/5
R_s ($\Omega/\Box$)	40.7	30.8	29.7	26.5	25.5	29.4
Chip area A (mm^2)	97	100	98	96	104	98
s (mm)	8.6	7.8	9.3	7.8	8.6	8
Geometric factor (s^2/A)	0.76	0.6	0.88	0.63	0.71	0.65
J_Q (W/m^2)	8200	8200	8650	8130	8000	8650
V$_{meas}$ (μV)	5.72±0.01	4.79±0.04	5.14±0.02	3.71±0.04	3.94±0.01	6.2±0.2

Table 5.5 Experimental results and parameters for four layers of FeGa with different caps used in the calculation of the ANE. R_s is the sheet resistance, s denotes the contact separation, J_Q is the heat current through the sample measured by the Peltier device and V$_{meas}$ the voltage above background transverse to a saturating magnetic field with the given heat current applied.

garnet, YIG/Pt, the Z^{LSSE} has been recorded as high as 4×10^{-4} at around 60K but on the order of 10^{-5} at 300K.[127]

$$Z^{LSSE} = \frac{(\alpha_S \theta_{SH})^2}{\kappa_{FM} \rho_{NM}} \tag{5.3}$$

Comparison of the ANE of FeGa seen in other experiments is complicated by their temperature difference approach and transverse configuration. However, it is noted that for the thin, low θ_{SH} samples the relative ANE signal was 324±2nVK^{-1} for 2nm Cr cap and 250±3nVK^{-1} for 2nm Al capped FeGa. These figures are roughly an order lower than the seen in [33] at 1.4±0.2μVK^{-1} for 21% Ga substitution and in [34] at around 6μVK^{-1} for a Fe$_3$Ga based ANE thermopile device. The discrepency is largely attributed to the geometry, whereby the ANE in the longitudinal configuration is draw from a thermoelectric response out of plane to the sample meaning it is across just 20nm material in a stack a little over 1mm thickness. The temperature difference seen by the FM layer is expected to be much lower than the measured difference.

5.3.3 Coercive Field Peaks

Not shown above is the intermittent appearance of peaks in the in-plane voltage of Fe samples around the coercive field. The effect, sporadic in its appearance, was not apparent until some time into the study and was first observed in 5nm Al capped Fe S686 as shown in fig. 5.11. It is possible to see how on the red field sweep, from negative to positive field, the voltage falls suddenly from the dashed line at around 10mT before returning to the typical voltage at positive saturation magnetisation. The effect is mirrored in the down sweep in blue at around 0mT as the magnetisation begins to reverse in the opposite direction. The peaks magnitude 0.5μV is approximately twice the saturation magnetisation signal after removing the ordinary Seebeck background of -3.1μV. The size of the spikes together with the simple structure of the layer make the result surprising and novel thermal effects were speculated as the origin. Further study to characterise and isolate the signal was carried out.

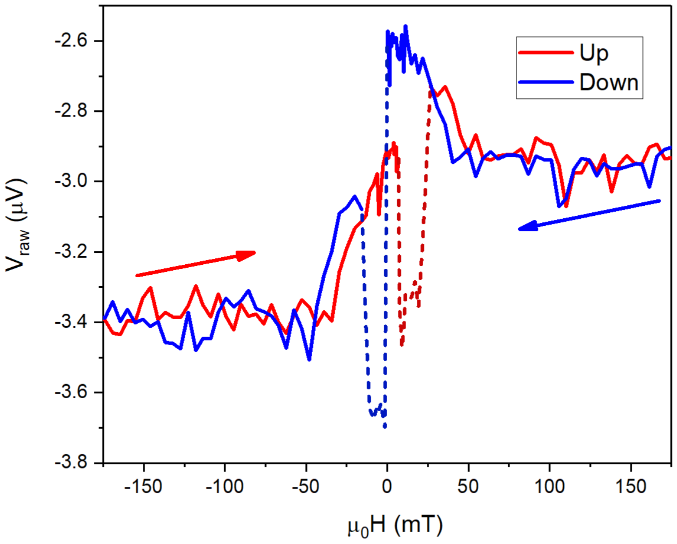

Fig. 5.11 Line plot of the measured in plane voltage over a field sweep on S686 5nm Al capped Fe sample where top and bottom Peltier devices are held at a temperature difference of 18K. The up and down sweep are shown in red and blue respectively and spikes in the voltage around 0mT indicated by dashed lines.

Attempts to Isolate Coercive Behaviour

In order to establish the origin of the spikes the first factor to be tested was the temperature difference, varied by running the top heat pump Peltier device at a series of currents to find the change in amplitude. This result is depicted in fig. 5.12. The change in voltage, relative to the voltage at saturation, increases linearly with Peltier current with an offset from 0 allowing for the dynamic performance of the Peltier device. In the inset of fig. 5.12 the voltage signal and spike at each driving current can be seen in like colours illustrating the emergence and growth of the voltage change with increasing temperature.

The angular dependence of the effect was another factor for examination. By incrementally rotating the sample with respect to the applied field it would

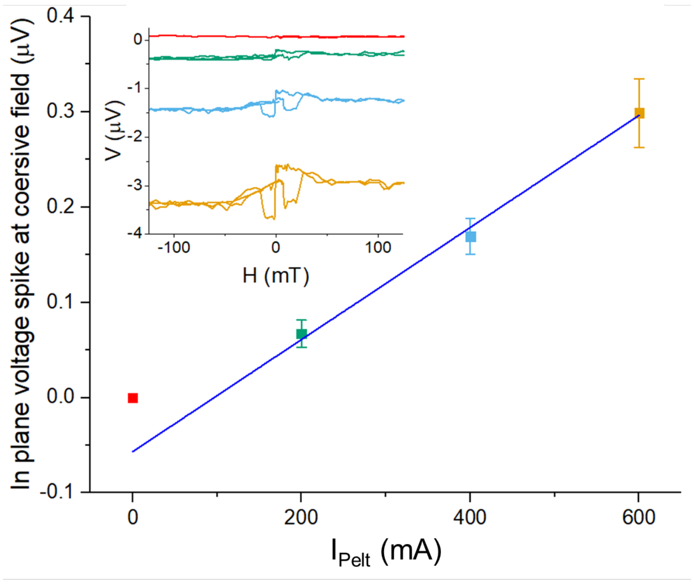

Fig. 5.12 Change in voltage with heat pump Peltier device driving current carried out on 5nm Al capped Fe layer S686.

be possible to ascertain if the effect was consistent or varied in another non-orthogonal geometry. If consistent and the effect remained largely the same then it is more likely the origin lies in planar Hall like effects with magnetisation reversal intrinsic to the sample as an applied field changes sign. As the field passes through zero and the sample magnetisation reverses it will always step along the typical magnetic easy axes of the crystalline Fe sample, which is 45^o to the voltage probe contacts. Alternatively an angular dependence may indicate a novel thermally driven effect other than the ANE that is not being detected in the orthogonal geometry of the probes. From the results seen in fig. 5.13 as the sample is rotated in 15^o increments the amplitude of the spike is the same relative to the ANE voltage and stepped magnetisation reversal appears likely. The discrepancy at 90^o seen in red is due to a change in sign of the peaks, from a spike increased to a drop in the voltage signal. This is assumed to be a difference in the path of the reversing magnetisation vector, stepping at the opposite direction of the easy axis as it becomes favourable with the rotation of the sample.

In the interest of a complete study, counterpart lateral magneto-Seebeck experiments were undertaken to fully explore the in-plane effects in addition to work in the perpendicular scheme outline above. This revealed the ordinary Seebeck coefficient for both Fe and FeGa samples as a multilayer system and allowed direct observation of any planar magneto-Seebeck. Ultimately these additional measurements would also aid in determining the origin of the coercive field peaks.

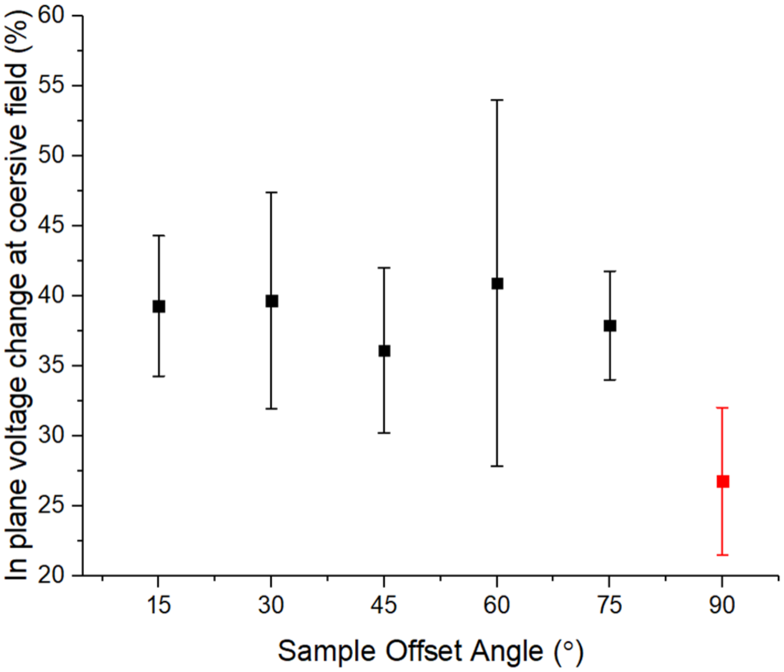

Fig. 5.13 Angular dependence of changes in voltage as a percentage of the in-plane background voltage at the coercive field for 2nm Al capped Fe layer S680. The point at 90^o shown in red has the opposite sign change in voltage.

5.4 Lateral Magneto-Seebeck Experiments on Fe and FeGa Thin Films

Utilising the measurement setup described in 2.4.1 a lateral temperature gradient was applied to 20x5mm chips of each Fe and FeGa layer and an orthogonal applied field was swept around the central region. Gold contact pads deposited onto the layers allowed for probing the voltage along either the temperature gradient or field direction. One of the aims of the experiment was to obtain the Seebeck coefficient for each system in a planar geometry. The other key aim is to confirm the magneto-Seebeck effect (MSE) origin of the spikes in voltage around magnetisation reversal seen in spin caloritronic experiments of Fe layers.

To determine the Seebeck response of layers a temperature differential of 5K, 10K and 15K created between Cu blocks at either end of the chip with the central region at ambient lab temperature (typically 21^{o}C). This range was within linear steps in voltage driving the Peltier device and was limited by the formation of condensation at the cold bath beyond the difference of 15K. The Seebeck voltage was probed between Au contacts 3mm either side of the midpoint. Due to mixed thermal conduction via the substrate, FM and NM as well as thermal losses from the surface this method does not yield a pure Seebeck coefficient of the FM alone, but rather the relative Seebeck of the system in an analogous state to the spin caloritronic setup with the benefit of a defined geometry.

The MSE originates in the magnetic dependence of the Seebeck coefficient S in FMs. It varies with the angle ϕ between the magnetisation vector **M** and the temperature gradient ∇_xT such that the transverse voltage V$_{xy}$ is at a maximum when the magnetisation is offset by 45^{o} from ∇_xT. For a planar geometry the phenomenological form of longitudinal voltage V$_{xx}$ and V$_{xy}$ is described by the equations eqn. 5.5 and eqn. 5.6:

$$V_{xx} = S\nabla_x T + S_{xx}\nabla_x T\cos 2\phi \tag{5.4}$$

$$V_{xy} = S_{xy}\nabla_x T\sin 2\phi \tag{5.5}$$

Where S$_{xx}$ and S$_{xy}$ are the longitudinal and transverse anisotropic magneto-thermopower.

In measuring the MSE the same configuration was used as above with the inclusion of electromagnetic pole pieces sweeping between positive and negative 130mT whilst V$_{xy}$ was measured in line with the applied field between 2 Au contact pads 2mm apart. This performs the same role as the Helmholtz coil in the longitudinal measurements, rotating **M** through the easy axis along the [100] or [010] at 45^{o} to V$_{xx}$ and V$_{xy}$.

5.4.1 Seebeck Response

Seebeck coefficients measured in the lateral system in fig. 5.14 show the positive and negative response from Fe and FeGa respectively as seen in [33]. There is a significant variation of S with cap composition for samples especially in FeGa where the standard deviation from the Seebeck coefficient is 25% compared to 10% in the Fe samples measured. The Seebeck voltage due to the FM alone is obscured partly by mixed conduction channels described in the previous section 5.3.2. Note that the random error associated with the measurement in fig. 5.14 is small and does not appear on the scale of the graph. However, there is a systematic error associated with the temperature drop off between the thermocouple and contact, along with thermal conduction through the substrate, is not considered in the error calculation.

The relatively conductive Fe layer is between 4× and 10× the thickness of the cap with a large S_{bulk} as seen in table 5.6 so it is assumed the thermoelectric voltage predominantly originates in the Fe with some shunting and an additional contribution from the cap, more so where they are 5nm thick.

While the Pt capped layers are similar a small increase in the 5nm thick Pt cap sample is somewhat anomalous given its low resistivity and opposite bulk Seebeck coefficient in table 5.6. However, bulk Seebeck effects may not be preserve in ultra thin films as in Fe which changes sign with thickness below 5nm [128]. Shunting is evident in Al and Ta capped layers where the thicker caps diminish the longitudinal Seebeck voltage.

In the FeGa layers the 2nm and 5nm capped samples differ by $4.5\mu V/K$. Both shunting and competing Seebeck voltages are likely at play given the large S_{bulk} of Cr. The expected diminishing of the thermoelectric voltage by shunting through 5nm Ta and Al as compared to the thinner caps appears to be moderated. This may be due to complimentary Seebeck effects of the same sign as FeGa from the cap.

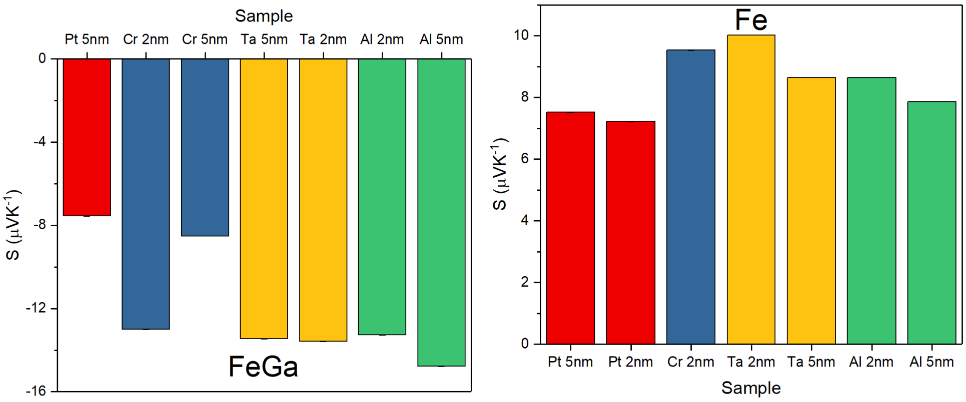

Fig. 5.14 Bar graphs of the Seebeck coefficient of FeGa (left) and Fe (right) thin films on GaAs chips as measured in the lateral thermoelectric system.

Metal	Bulk Resistivity (nΩ.m)	Bulk Seebeck Coefficient (300K) (μV/K)
Al	26.5	-1.66
Cr	125	21.8
Pt	105	-5.3
Ta	131	-1.9
Fe	96.1	15

Table 5.6 Bulk properties of cap materials as well as Fe [129]

5.4.2 Magneto-Seebeck Response

Applying the magnetic field sweeping in steps of 1.42mT between approximately 120mT positive and negative field the magneto-Seebeck effect could be reliably observed in all Fe chips with magnetisation reversal. This is shown for each sample measured in fig. 5.15 where a spike in the V_{xy} signal equivalent to around -1% of the V_{xx} is seen around the coercive field for all samples. The spike amplitude as a percentage of the longitudinal Seebeck voltage is given in fig. 5.16. The measurements presented in fig. 5.15 were taken at the greatest temperature difference of 15K and sweeps were performed at 2 lower temperature gradients for each chip each giving a proportional magneto-Seebeck response. The effect was not observed in any of the FeGa layers, all of which were measured under the same conditions.

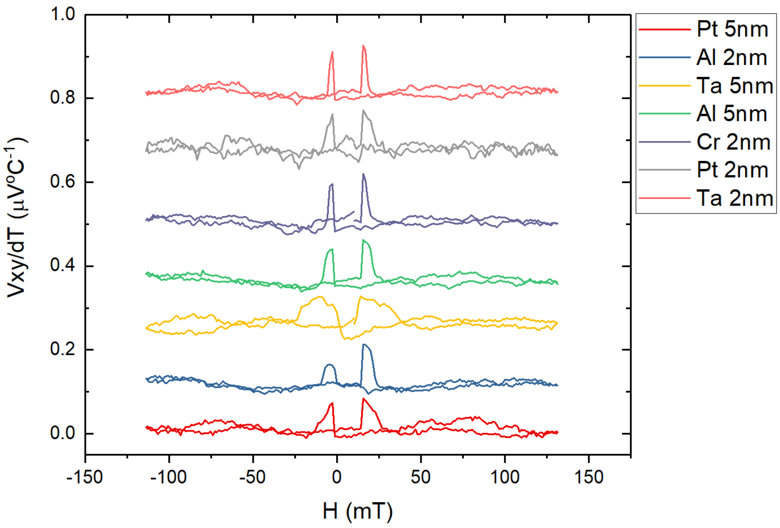

Fig. 5.15 V_{xy} response for each Fe layer scaled to temperature difference with an arbitrary offset in the scale.

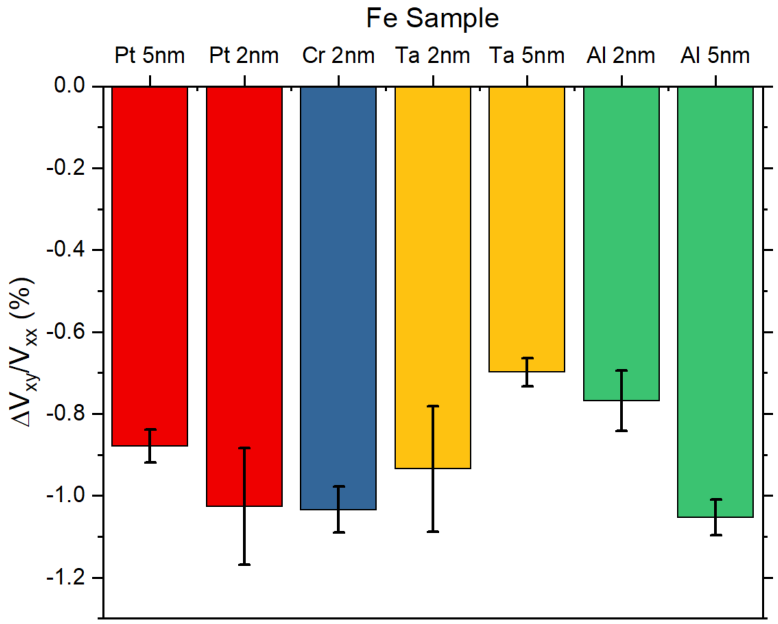

Fig. 5.16 Magneto-Seebeck peak amplitude in V_{xy} as a percentage the average V_{xx} for each Fe layer. All measurements were at a target temperature gradient of 15K.

The peak amplitude is directly proportional to the temperature gradient applied to the sample. This is shown in fig. 5.17 for the 2nm Al capped sample S680 where the peaks, seen in (a), increase linearly with temperature gradient as depicted in (b).

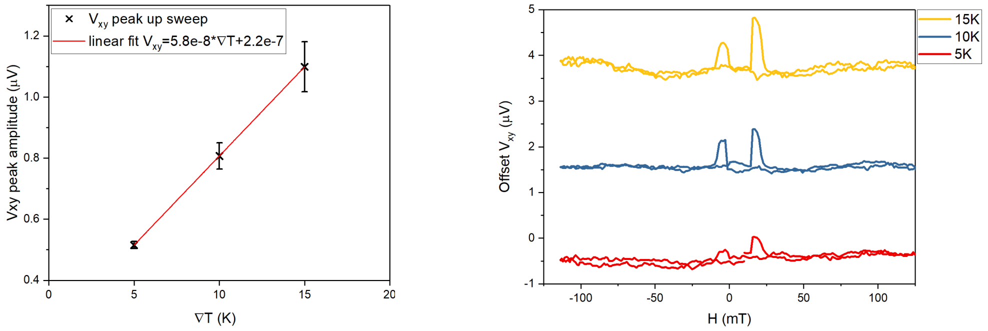

(a) (b)

Fig. 5.17 (a) Magneto-Seebeck peak in V_{xy}, taken from like sweeps from negative to positive field in Al capped Fe layer S680. The fitting represents the S_{xy} magneto-Seebeck coefficient in the case of the magnetisation lying along the easy axis. (b) V_{xy} Magneto-Seebck response on S680 at 3 temperature gradients showing the increase in coercive field peaks with temperature. The two peaks have different amplitude likely due to the magnetisation reversal path as well as some drift affecting individual peaks.

The reliable appearance of magneto-Seebeck effects with magnetisation reversal in Fe and not FeGa, as well as their direct relation to the temperature difference and ordinary Seebeck voltage all indicate the origins, speculated on in longitudinal measurements, of a MSE derived from extraneous in plane gradients, which appeared intermittently when the requisite geometry was satisfied.

Estimation of extraneous in plane Seebeck voltages

Referring back to the peaks described in the longitudinal setup of the previous section, 5.3.3, in fig. 5.11 the 5nm Al capped Fe sample exhibited coercive field peaks of amplutide -0.6μV. By considering the results obtained from the lateral magneto-Seebeck measurments it is possible to estimate the ordinary Seebeck voltage and temperature difference that might give rise to the -0.6μV peak.

Extraneous in plane thermal gradients and associated ordinary Seebeck voltage from uneven thermal coupling between the sample and heat pump Peltier device are known to occur in the LSSE system, appearing as a background voltage without magnetic dependence when parallel to the wire contacts. Assuming the case that the ordinary Seebeck voltage in the LSSE setup occurs orthogonal to the contacts, then as the magnetisation reverses stepping along the $\langle 100 \rangle$ typical Fe easy axis it will be at 45° to the extraneous Seebeck voltage and produce the maximum transverse voltage, following eqn. 5.5.

Referring then to the controlled in plane thermoelectric signal measured here in the same layer, a transverse peak amplitude equating to -1.05% of the ordinary Seebeck voltage is obtained as given in fig. 5.16. Given the conditions in the assumed ideal case for the signal in fig. 5.11 above, the -0.6μV amplitude would equate to an extraneous in plane ordinary Seebeck voltage of 57μV. Further, taking the quotient of the Seebeck voltage estimate and S for the layer in fig. 5.14 of -7.86μVK^{-1} the estimated temperature difference due to uneven heating is 7.3K. In the specific LSSE measurement under consideration the sample was held at an out of plane temperature difference of 18.28±0.05K between the two Peltier devices.

While the estimated temperature difference is within physical means the largest background in plane Seebeck voltage detected parallel to the LSSE contacts in any measurement was a mere 15μV, significantly less than the 57μV. The discrepancy between this estimated value and typical background planar Seebeck voltages is ascribed to differences between the experimental geometries producing different relative transverse thermopower S_{xy}. Additionally, a systematic error of the relative Seebeck coefficient measurement may exist. Sample thermocouple readings are likely to produce higher temperature difference than that at the voltmeter probes, underestimating the thermopower of the layer and here inflating the estimated temperature difference.

5.5 Electron Transport in Fe and FeGa Thin Films

5.5.1 Anisotropic Magnetoresistance

Electron transport experiments using the experimental setup described in section 2.4 reveal the characteristic AMR of system. This is useful for demonstrating how the magnetisation reverses via the cubic axes and explain the appearance of planar magneto-Seebeck effects subject to the same magnetisation dynamics.

For a magnetic conductor thin film with uniaxial and cubic anisotropy it is possible to obtain the anisotropy coefficients from the longitudinal and transverse AMR of the form given in eqn. 5.6 and 5.7 respectively. The coefficients C_I, C_U, C_C, and $C_{I,C}$ refer to the non-crystalline term, uniaxial crystalline term, cubic crystalline term and crossed non-crystalline/crystalline term respectively. The angle ψ refers to the angle between the magnetisation and the [110] crystal direction.

$$\frac{\Delta\rho_{xy}}{\rho_{av}} = C_I sin2\phi - C_{I,C} sin(4\psi - 2\phi) \tag{5.6}$$

$$\frac{\Delta\rho_{xx}}{\rho_{av}} = C_I cos2\phi + C_U cos2\psi + C_C cos4psi + C_{I,C} cos(4\psi - 2\phi) \tag{5.7}$$

For AMR measurements 8 arm star devices were microfabricated on the 2nm Al capped samples S680, (Fe) and S690 (FeGa) via the processes described in section 2.3 with an example device and schematic diagram of the device configuration depicted in fig. 5.18. These offer a well-defined current path along the 20um arms with access to directions offset by 45^o. The devices, held within a 300mT saturating field were rotated 200^o with a constant 1mA current along each arm in turn, probing the V_{xx} and V_{xy} simultaneously. To obtain a symmetric dataset the probe current was reversed and field rotated back through 200^o, mathematically the same as a 180^o magnetisation reversal.

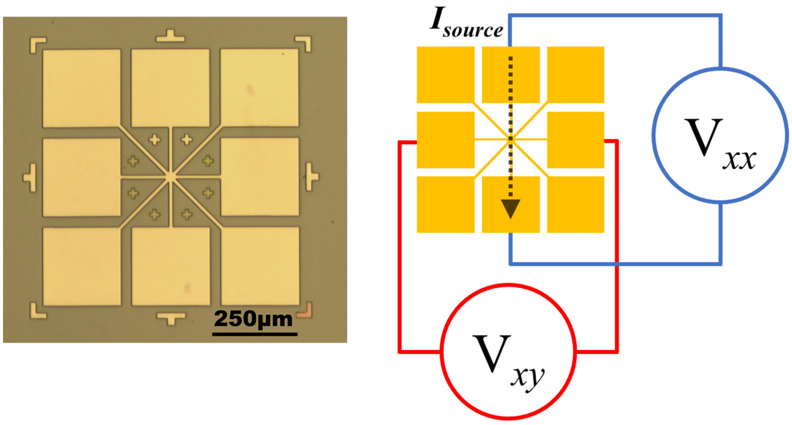

Fig. 5.18 Microscope image at 5x magnification of a UJ device along with a schematic diagram of the current source, longitudinal and transverse voltage probe directions during and AMR measurement. The magnetic field was applied in the plane of the device.

An extraneous out of plane Hall component, originating in a tilt on the PCB header has been fitted with an additional $cos(\psi + w)$ where there is also an arbitrary phase factor w term and subtracted from the data on S690.

The change in R_{xy} for both samples takes the same form of eqn 5.6 as shown in fig. 5.19 and are of a similar magnitude with the AMR in Fe S680 slightly larger and an offset in the FeGa S690 due to alignment of around 10^o. Crucially the signal agrees with the postulated effect from thermoelectric experiments where the transverse voltage peaks when the magnetisation is at 45^o to the current direction. From eqn. 5.6 the noncrystalline and crossed crystalline-noncrystalline AMR coefficients can be extracted from fitting the data with respect to phi and substituting the results. The results of fitting and final AMR coefficients from change in R_{xy} are given in table 5.7. These effectively describe the behaviour of the transverse resistivity with rotating magnetic field for the system and are presented on the plot in reasonable agreement with the data, bar the offset in S690.

The dR_{xx}/Rav signals in fig. 5.20 show the inverse response with the minimum when the magnetisation is oriented 45^o offset to the current, consistent with the form of eqn 5.7. Again there is an offset in S690 of around 10^o. While there is a clear difference in the size of the AMR between the crystal axes the longitudinal resistivity data is subject to significant noise, such upon combination of the results to cancel terms the uniaxial or cubic crystalline AMR coefficients are obscured. Therefore, it is not feasible to reveal the difference in contribution to AMR from crystalline anisotropy for Fe and FeGa layers from the data.

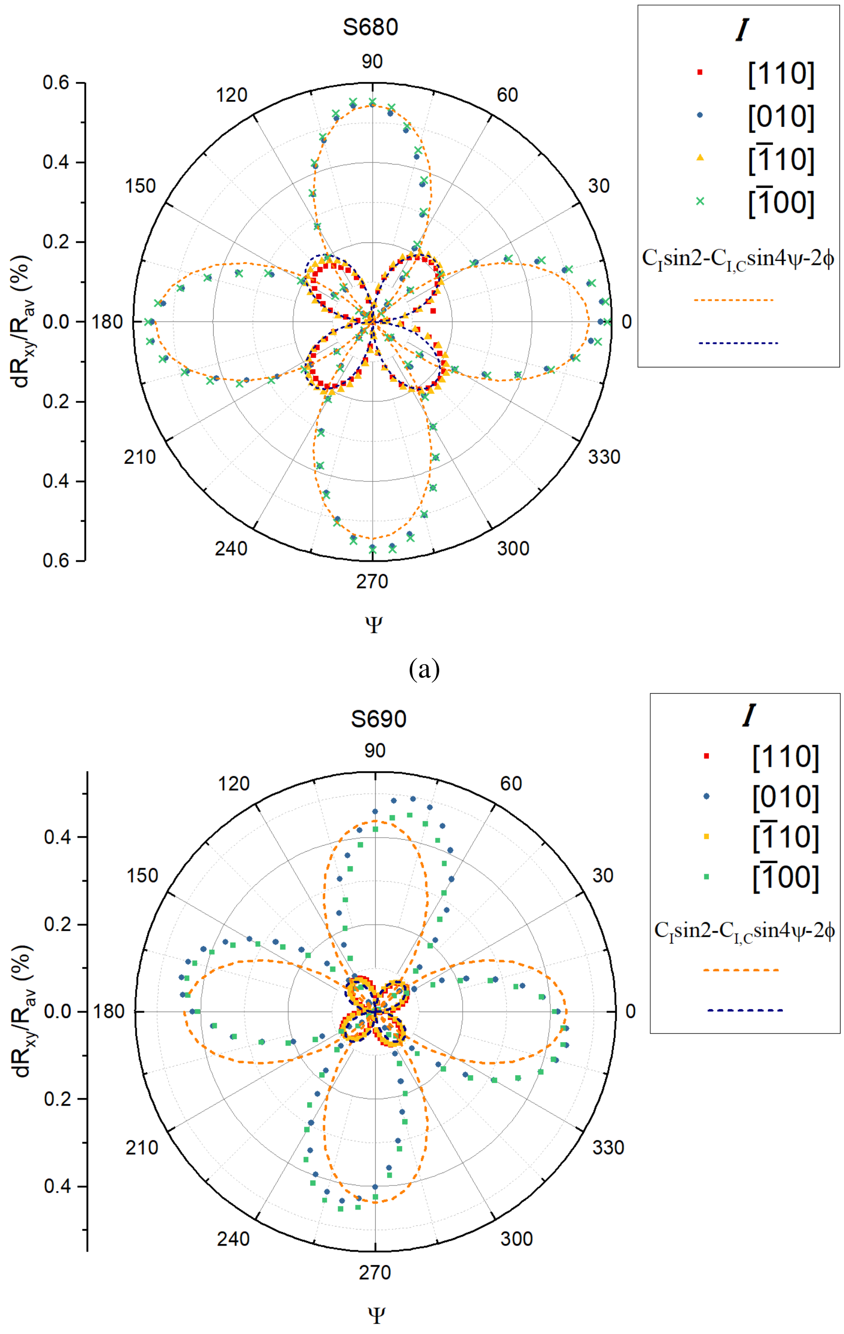

(a)

(b)

Fig. 5.19 Polar representation of transverse AMR (a) in Fe S680 and (b) FeGa S690 at 300mT. The angle ψ represents the angle between the magnetisation and the [110] crystal direction. Each one of 4 colour plots represents current along a particular crystal axis. Data for S690 was skewed by an out of plane Hall voltage and through fitting background has been subtracted.

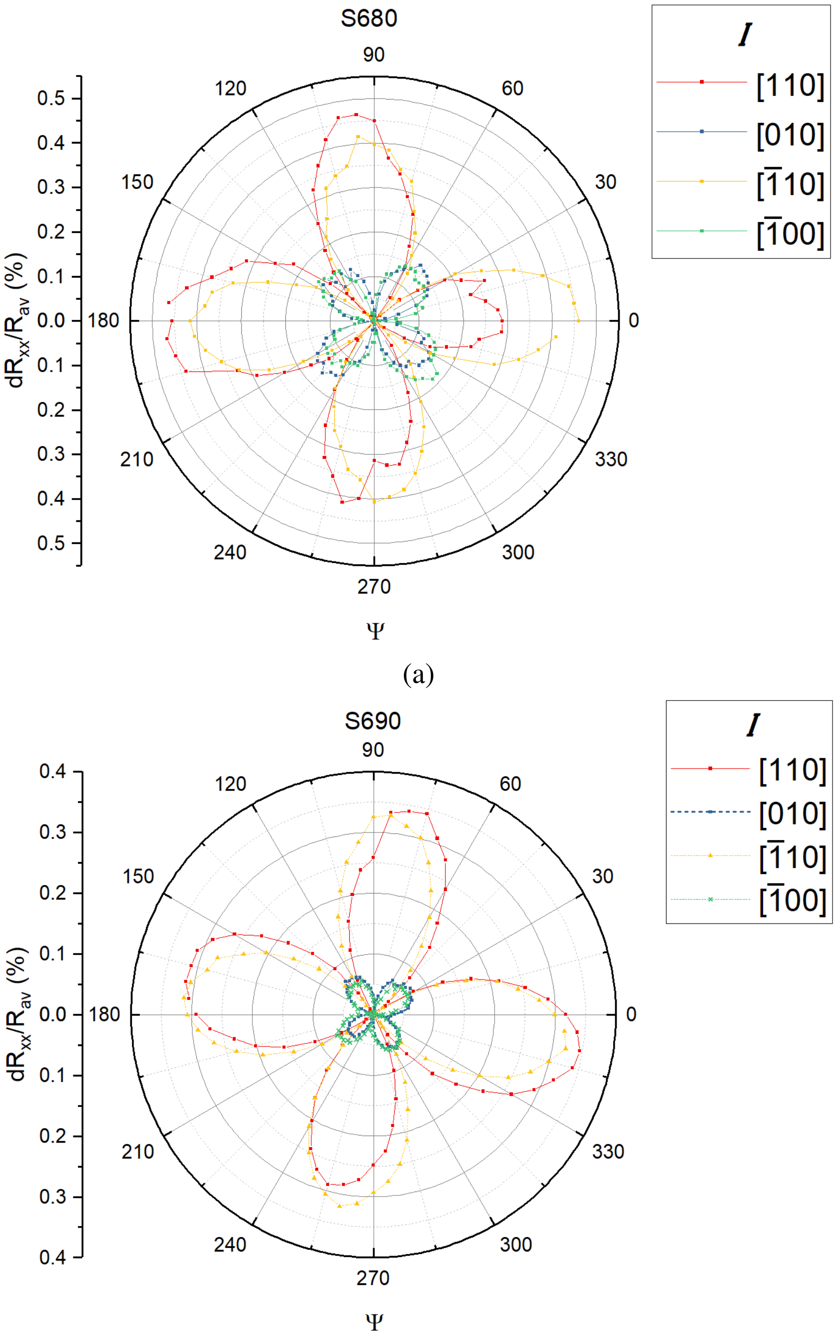

(a)

(b)

Fig. 5.20 Polar representation of longitudinal AMR in Fe S680 (left) and FeGa S690 (right) at 300mT. The angle ψ represents the angle between the magnetisation and the [110] crystal direction. Each one of 4 colour plots represents current along a particular crystal axis

R_{xy}	C_I+$C_{I,C}$	C_I-$C_{I,C}$	C_I	$C_{I,C}$
S680	-0.543±0.005	-0.219±0.004	-0.381±0.006	-0.162±0.006
S690	0.437±0.00003	0.091±0.00005	0.264±0.00006	0.173±0.00006

Table 5.7 Values extracted from R_{xy} of AMR along with non-crystalline and crossed crystalline non-crystalline term.

5.5.2 Ramped Magnetic Field Sweeps

Field-sweep measurements employed the same setup and microfabricated devices as above with a fixed geometry and applied field ramped between ±300mT in increments of 2.5mT. With the applied field perpendicular in plane to the probe current along the [110] crystal direction, with the exception the geometry mirrors the lateral magneto-Seebeck setup with an applied current rather than thermoelectric effects.

Results for Fe S680 in fig. 5.21(a) show the AMR is in good agreement with the field rotation measurements with around 0.2% change in transverse R_{xy} and 0.4% change in R_{xx} between zero field and saturation field. The presence of peaks in Fe sweeps along with the agreement in the AMR signal supports the role of the magnetisation stepping to a cubic crystalline magnetic easy axes along the [100] or [010] 45^o to the [110] direction during magnetisation reversal thus giving rise to a maximum from the MSE. While SQUID magnetometry was not undertaken for Fe layers results in fig. 5.22 for the FeGa layer S690 has a coercivity of less than +10mT, bringing the window for magnetisation reversal precisely around the peaks in the Fe R_{xy} signal. Similarly the magnetisation is largely saturated at +50mT, where the field dependent change in resistivity begins to go through an inflection point.

No such peaks appear at low field in the FeGa layer, where the in plane cubic anisotropy is likely deteriorated by the incorporation of Ga. As such the magnetisation reverses swiftly without a detectable MSE voltage. While the difference in crystal anisotropy has not been determined the result does demonstrate the difference in transport around the coercive field is characteristic of their electron transport behaviour and not owing to any novel thermal effect.

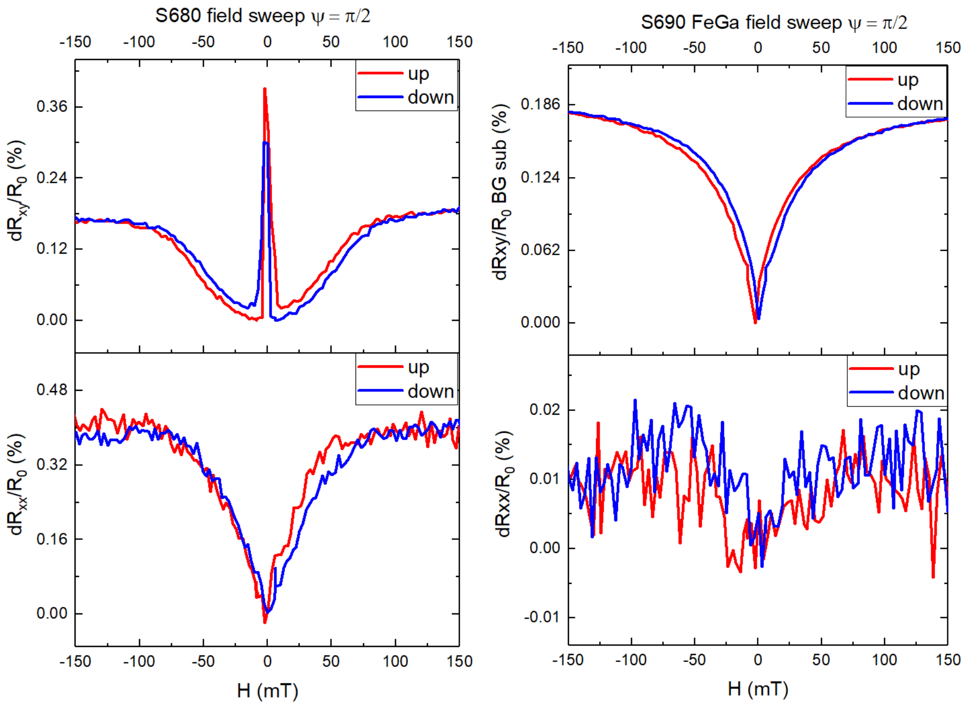

(a) (b)

Fig. 5.21 (a) AMR of Fe S680 device in a stationary sweeping field. The longitudinal (blue) and transverse (red) signal show the current along the [110] crystal direction are orthogonal to the applied magnetic field. Present in the transverse R_{xy} is the coercive field peaks. (b) AMR of Fe S680 device in a stationary sweeping field. Some features are skewed by the background out of plane Hall voltage subtraction, some by removing a linear fit to the saturated signal above 100mT.

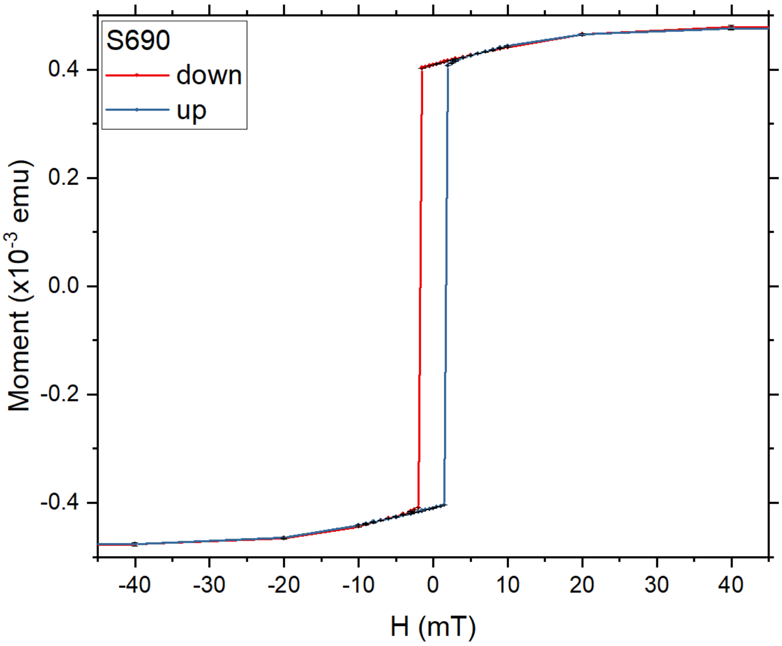

Fig. 5.22 SQUID magnetometry of S690 FeGa Al sample.

5.6 Summary and Conclusion

This chapter on Fe and FeGa thin films has covered the synthesis and characterisation of material for spin caloritronic experiments and subsequent investigation of extraneous effects' origins within those results. In characterisation, layers were found to be of reasonably good quality for the work undertaken. The following LSSE and ANE measurements were carried out with the aim of establishing FeGa's candidacy for thermal energy harvesting in the move towards more efficient technologies. Large difference in ANE between Fe and FeGa have been found in good agreement with other studies.[33, 34]

Where work by other groups to obtain S_{LSSE} for metallic FMs reported success in disentangling ANE and LSSE contributions from field dependent thermoelectric signal [28, 32] obstacles in this approach have been identified in the work presented here. Specifcally in [32] 10nm $NiFe_2$ permalloy films are tested for the ANE and LSSE by measuring both with and without a Pt cap following the Sola heat flux method. The ANE and proximity Nernst effect (due to the magnetisation of the Pt in the region of the FM) are then separated assuming that the two layers act as parallel resistors. However, the use of different caps of varying thickness and composition has shown that without accounting for scattering at the interface of current mixing when the electron mean free path is greater than the thickness of the layer this model breaks down.

Not observed in section 5.3 was any sign of resonant magnetoelastic enhancement of the LSSE as reported in [42, 44, 45] speculated based on the strong magnetoelastic coupling of FeGa. Field sweeps of fine increment up to higher fields, as was employed in the work referenced, might have more success in observing an increase in LSSE at specific applied magnetic field values. Experiments described above were limited from thorough exploration of these effects by the operational ability of the instruments used.

While undertaking the measurements peaks in the in-plane voltage of Fe layers were observed and attributed to the magneto-Seebeck effect arising from a stepped magnetisation reversal along the Fe easy axis influencing in-plane ordinary Seebeck currents. This was further corroborated in lateral MSE measurements where it was also shown that the effect only presented itself in Fe and not FeGa layers with the specific conditions to allow the appearance of peaks. AMR measurements confirmed the mechanism of magnetisation reversal giving rise the coercive field peaks. These measurements also demonstrated that it was a thermoelectric interaction with the magnetisation analogous to electron transport effects that appeared rather than novel galvanic phenomena. Given XRD results this is assumed to be the result of stronger crystal anisotropy in Fe, however, results of the AMR in field rotation measurements proved inadequate to show this. The question of differences in crystal anisotropy could also be approached with further SQUID magnetometry. By measuring a chip along orthogonal crystal directions it is possible to determine the anisotropy of the FM layer. This would confirm the role of crystal anisotropy in stepped magnetisation reversal and subsequent coercive field peaks.

Further, the spin caloritronic work, which was unable to disentangle the LSSE and ANE could be improved by varying the thickness of the FM and NM cap then applying the Fuchs-Sondheimer theory to create a model that would reveal the systems mean free path and reflection coefficient.[130] If successful then additional studies involving different caps may lead to the optimisation of the large ANE in FeGa with a complementary LSSE.

Chapter 6

Summary and Further Work

6.1 Summary of Key Results and Further Work

6.1.1 Growth and characterisation of Antiferromagnetic $\mathbf{CuMnAs}_{1-\alpha}\mathbf{Sb}_{\alpha}$

In an effort to improve upon the lattice mismatch of CuMnAs on GaAs towards the high crystal quality observed when grown on GaP, material was grown on GaAs with an additional Sb flux. Three levels of flux at 10%, 20% and 30% as a proportion of the As content were tested. Material characterisation provided feedback on crystal structure and quality, secondary phases and defects with Sb flux. Magnetic and transport characterisation confirm the antiferromagnetic ordering of CuMnAsSb, the AF domain texture and resistive response to current pulses.

Composition mapping in electron microscopy demonstrated the successful incorporation of Sb in $\mathrm{CuMnAs}_{0.8}\mathrm{Sb}_{0.2}$. With the incorporation of Sb the tetragonal unit cell of CuMnAs was preserved in all growths, however, $\mathrm{CuMnAs}_{0.7}\mathrm{Sb}_{0.3}$ flux was found to deteriorate the crystal structure and lead to acute defect density. This serves as an upper limit under the explored growth conditions for CuMnAsSb. Growths at lower Sb flux remained under tensile strain from the substrate lattice mismatch at 60nm thickness, however, 120nm thickness was sufficient to induce strain relaxation.

However, all layers exhibited the formation of ferromagnetic (FM) secondary phases including species of MnAs. The FM signal detected in magnetometry is proportional to the Sb flux during growth, at 300K magnetisation of 4×10^{-4}emu/cm^{-3} per % Sb flux as a proportion of the As flux. Secondary phase growth manifested as roughness on the surface with island peaks present in all layers and increasing in number density with stoichiometric drift away from the wafer centre. In material grown at 10% and 20% Sb flux, the region of lowest number density contained one peak in every square micrometre. For those layers, the RMS roughness away from the peaks was consistent with benchmark CuMnAs from the same system at a value of 0.5nm. Crystal defects consistent with those seen in CuMnAs persisted within the 20% Sb layer observed in TEM.

Neutron diffraction of CuMnAsSb confirmed the magnetic ordering to be AF in-plane as in CuMnAs. Values of T_N were found at 10% and 20% Sb flux by electron transport at high temperature and corroborated by neutron diffraction for the sample at 20%. Both presented a depression of T_N in electron transport compared to CuMnAs, at 462.1±0.2K for 10% Sb and 451.5±0.7K for 20% as compared to 480K in CuMnAs.

XMLD-PEEM imaging revealed a biaxial in-plane AF domain texture with domains of 1μm width in a sample of $\mathrm{CuMnAs_{0.8}Sb_{0.2}}$. Spin axes aligned along the CuMnAsSb [100] and [010] directions with some divergence of spins within the domains.

Electrical current pulses produced transient resistivity response in the resistivity of microdevices fabricated from each sample. These bore the functional fingerprint of the high resistivity quench switching regime observed in current pulse measurements in CuMnAs. Stimulated by Joule heating the transient decay and persistent offset cannot conclusively be demonstrated to possess spintronic origins and pose little advancement of their interpretation.

With the demonstration of Sb incorporation in CuMnAsSb, future work may benefit from an Sb source with a cracker to effuse the more mobile and less corrosive Sb_2 dimer. Other useful features in growth might include constant sample rotation and improvements in substrate preparation for oxide removal to reduce inhomogeneity across the wafer. These additions present an opportunity to carry out more growths to establish if CuMnAsSb free of secondary phases compositional defects might be feasible. Reduction in defects and flaws may foster clearer trends with Sb incorporation for a growth study as well as removing parasitic FM material that complicates the magnetoelectric transport picture.

6.1.2 Spin Caloritronic study of Fe and FeGa thin films

Thin films of Fe and FeGa were deposited by sputter deposition with caps of Pt, Ta, Cr and Al before material characterisation and assessment of spin caloritronics properties. During spin caloritronics measurements extraneous voltage signals were observed in Fe thin films, and subsequent investigation found evidence supporting planar magnetisation reversal effects as the origin.

A large enhancement of the in-plane voltage in $Fe_{0.79}Ga_{0.21}$ over Fe under an orthogonal in-plane magnetisation and out of plane thermal gradient corroborated work by Nakayama et al. Disentangling the spin Seebeck effects from anomalous Nernst effects between samples of different caps was not feasible. The parallel resistor approach pursued by Bougiatioti et al was found to be flawed and a more thorough model considering the mean free path of charge carriers and interface resistance effects, such as in the Fuchs Sondhiemer theory, would be more appropriate.

The appearance of peaks in the planar voltage during measurement of ANE and LSSE in Fe layers probably occur as a result of stepped magnetisation reversal around the coercive field inducing magneto-Seebeck effects from planar thermal gradients. The effects were replicated in a lateral magneto-Seebeck measurement and AMR measurements obtained by electron transport confirmed the mechanism of magnetisation reversal. Quantitative comparison of the differences in anisotropy between Fe and FeGa that promote and inhibit the stepped magnetisation respectively would be aided by further SQUID magnetometry along orthogonal crystal directions.

References

[1] W. Thomson, “XIX. on the electrodynamic qualities of metals: Effects of magnetization on the electric conductivity of nickel and of iron,” *Proceedings of the Royal Society of London*, vol. 8, pp. 546–550, 1857.

[2] N. F. Mott, “Electrons in transition metals,” *Advances in Physics*, vol. 13, no. 51, pp. 325–422, 1964.

[3] M. N. Baibich, J. M. Broto, A. Fert, F. N. Van Dau, F. Petroff, P. Etienne, G. Creuzet, A. Friederich, and J. Chazelas, “Giant magnetoresistance of (001)Fe/(001)Cr magnetic superlattices,” *Phys. Rev. Lett.*, vol. 61, pp. 2472–2475, Nov 1988.

[4] G. Binasch, P. Grünberg, F. Saurenbach, and W. Zinn, “Enhanced magnetoresistance in layered magnetic structures with antiferromagnetic interlayer exchange,” *Phys. Rev. B*, vol. 39, pp. 4828–4830, Mar 1989.

[5] C. Chappert, A. Fert, and F. Van Dau, “The emergence of spin electronics in data storage,” *Nature materials*, vol. 6, no. 11, 2007.

[6] J. S. Moodera, L. R. Kinder, T. M. Wong, and R. Meservey, “Large magnetoresistance at room temperature in ferromagnetic thin film tunnel junctions,” *Phys. Rev. Lett.*, vol. 74, pp. 3273–3276, Apr 1995.

[7] T. Miyazaki and N. Tezuka, “Giant magnetic tunneling effect in Fe/Al_2O_3/Fe junction,” *Journal of Magnetism and Magnetic Materials*, vol. 139, no. 3, pp. 231–234, Jan. 1995.

[8] J. M. Daughton, “Magnetic tunneling applied to memory (invited),” *Journal of Applied Physics*, vol. 81, no. 8, pp. 3758–3763, 04 1997.

[9] F. J. Albert, J. A. Katine, R. A. Buhrman, and D. C. Ralph, “Spin-polarized current switching of a Co thin film nanomagnet,” *Applied Physics Letters*, vol. 77, no. 23, pp. 3809–3811, 12 2000.

[10] P. Gambardella and I. M. Miron, “Current-induced spin–orbit torques,” *Philosophical Transactions of the Royal Society A: Mathematical, Physical and Engineering Sciences*, vol. 369, no. 1948, pp. 3175–3197, 2011.

[11] I. M. Miron, T. Moore, H. Szambolics, L. D. Buda-Prejbeanu, S. Auffret, B. Rodmacq, S. Pizzini, J. Vogel, M. Bonfim, A. Schuhl, and G. Gaudin, “Fast current-induced domain-wall motion controlled by the Rashba effect,” *Nature materials*, vol. 10, no. 6, pp. 419–423, 2011.

[12] T. Jungwirth, X. Marti, P. Wadley, and J. Wunderlich, “Antiferromagnetic spintronics,” *Nature nanotechnology*, vol. 11, no. 3, pp. 231–241, 2016.

[13] J. Železný, H. Gao, K. Výborný, J. Zemen, J. Mašek, A. Manchon, J. Wunderlich, J. Sinova, and T. Jungwirth, “Relativistic Néel-order fields induced by electrical current in antiferromagnets,” *Phys. Rev. Lett.*, vol. 113, Oct 2014.

[14] P. Wadley, B. Howells, J. Železný, C. Andrews, V. Hills, R. P. Campion, V. Novák, K. Olejník, F. Maccherozzi, S. S. Dhesi, S. Y. Martin, T. Wagner, J. Wunderlich, F. Freimuth, Y. Mokrousov, J. Kuneš, J. S. Chauhan, M. J. Grzybowski, A. W. Rushforth, K. W. Edmonds, B. L. Gallagher, and T. Jungwirth, “Electrical switching of an antiferromagnet,” *Science*, vol. 351, no. 6273, pp. 587–590, 2016.

[15] V. A. Hills, “MBE growth, characterisation and physics of antiferromagnetic copper manganese arsenide,” Ph.D. dissertation, University of Nottingham, December 2016.

[16] F. Krizek, Z. Kaspar, A. Vetushka, D. Kriegner, E. M. Fiordaliso, J. Michalicka, O. Man, J. Zubac, M. Brajer, V. A. Hills, K. W. Edmonds, P. Wadley, R. P. Campion, K. Olejnik, T. Jungwirth, and V. Novak, “Molecular beam epitaxy of CuMnAs,” *Phys. Rev. Mater.*, vol. 4, Jan 2020.

[17] S. Reimers, “Antiferromagnetic domain structure in tetragonal CuMnAs films: A picturebook of domains, domain walls and everything in between,” Ph.D. dissertation, University of Nottingham, August 2022.

[18] B. Howells, M. Wang, K. W. Edmonds, P. Wadley, R. P. Campion, A. W. Rushforth, C. T. Foxon, and B. L. Gallagher, “Crystalline anisotropic magnetoresistance in quaternary ferromagnetic semiconductor (Ga,Mn)(As,Sb),” *Applied Physics Letters*, vol. 102, no. 5, 02 2013.

[19] B. Howells, “Studies of spin-orbit coupling phenomena in magnetic semiconductors,” Ph.D. dissertation, University of Nottingham, July 2015.

[20] G. E. W. Bauer, “Spin Caloritronics,” in *Spin Current*. Oxford University Press, 09 2017.

[21] C. Kittel, *Introduction to Solid State Physics*, 8th ed. Wiley, 2004.

[22] C. Goupil, H. Ouerdane, K. Zabrocki, W. Seifert, N. F. Hinsche, and E. Müller, *Thermodynamics and Thermoelectricity*. John Wiley and Sons Ltd, 2016, ch. 1, pp. 1–74.

[23] E. Saitoh, M. Ueda, H. Miyajima, and G. Tatara, “Conversion of spin current into charge current at room temperature: Inverse spin-Hall effect,” *Applied Physics Letters*, vol. 88, no. 18, 05 2006.

[24] K. Uchida, S. Takahashi, K. Harii, J. Ieda, W. Koshibae, K. Ando, S. Maekawa, and E. Saitoh, “Observation of the spin Seebeck effect,” *Nature*, vol. 455, no. 7214, p. 778–781, 2008.

[25] K. Uchida, J. Xiao, H. Adachi, J. Ohe, S. Takahashi, J. Ieda, T. Ota, Y. Kajiwara, H. Umezawa, H. Kawai, G. E. W. Bauer, S. Maekawa, and E. Saitoh, “Spin Seebeck insulator,” *Nature materials*, vol. 9, no. 11, p. 894—897, November 2010.

[26] K. Uchida, H. Adachi, T. Ota, H. Nakayama, S. Maekawa, and E. Saitoh, “Observation of longitudinal spin-Seebeck effect in magnetic insulators,” *Applied Physics Letters*, vol. 97, no. 17, 10 2010.

[27] K. Uchida, M. Ishida, T. Kikkawa, A. Kirihara, T. Murakami, and E. Saitoh, “Longitudinal spin Seebeck effect: from fundamentals to applications,” *Journal of physics. Condensed matter*, vol. 26, no. 34, 2014.

[28] R. Ramos, T. Kikkawa, K. Uchida, H. Adachi, I. Lucas, M. H. Aguirre, P. Algarabel, L. Morellón, S. Maekawa, E. Saitoh, and M. R. Ibarra, “Observation of the spin Seebeck effect in epitaxial Fe_3O_4 thin films,” *Applied Physics Letters*, vol. 102, no. 7, 02 2013.

[29] Z. Duan, B. Miao, L. Sun, D. Wu, J. Du, and H. Ding, “The longitudinal spin Seebeck coefficient of Fe,” *IEEE Magnetics Letters*, vol. 10, pp. 1–5, 2019.

[30] J. Holanda, O. Alves Santos, R. O. Cunha, J. B. S. Mendes, R. L. Rodríguez-Suárez, A. Azevedo, and S. M. Rezende, “Longitudinal spin Seebeck effect in permalloy separated from the anomalous Nernst effect: Theory and experiment,” *Phys. Rev. B*, vol. 95, Jun 2017.

[31] K.-D. Lee, D.-J. Kim, H. Yeon Lee, S.-H. Kim, J.-H. Lee, K.-M. Lee, J.-R. Jeong, K.-S. Lee, H.-S. Song, J.-W. Sohn, S.-C. Shin, and B.-G. Park, “Thermoelectric signal enhancement by reconciling the spin Seebeck and anomalous Nernst effects in ferromagnet/non-magnet multilayers,” *Scientific reports*, vol. 5, no. 1, pp. 10 249–10 249, 2015.

[32] P. Bougiatioti, C. Klewe, D. Meier, O. Manos, O. Kuschel, J. Wollschläger, L. Bouchenoire, S. D. Brown, J.-M. Schmalhorst, G. Reiss, and T. Kuschel, “Quantitative disentanglement of the spin Seebeck, proximity-induced, and ferromagnetic-induced anomalous Nernst effect in normal-metal–ferromagnet bilayers,” *Phys. Rev. Lett.*, vol. 119, Nov 2017.

[33] H. Nakayama, K. Masuda, J. Wang, A. Miura, K. Uchida, M. Murata, and Y. Sakuraba, “Mechanism of strong enhancement of anomalous Nernst effect in Fe by Ga substitution,” *Phys. Rev. Mater.*, vol. 3, Nov 2019.

[34] A. Sakai, S. Minami, T. Koretsune, T. Chen, T. Higo, Y. Wang, T. Nomoto, M. Hirayama, S. Miwa, D. Nishio-Hamane, F. Ishii, R. Arita, and S. Nakatsuji, “Iron-based binary ferromagnets for transverse thermoelectric conversion,” *Nature*, vol. 581, pp. 53–57, 2020.

[35] J. R. Cullen, A. E. Clark, M. Wun-Fogle, J. B. Restorff, and T. A. Lograsso, “Magnetoelasticity of Fe-Ga and Fe-Al alloys,” *Journal of Magnetism and Magnetic Materials*, vol. 226, no. 2001, pp. 948–949, May 2001.

[36] R. Wu, “Origin of large magnetostriction in FeGa alloys,” *Journal of Applied Physics*, vol. 91, no. 10, pp. 7358–7360, May 2002.

[37] D. E. Parkes, S. A. Cavill, A. T. Hindmarch, P. Wadley, F. McGee, C. R. Staddon, K. W. Edmonds, R. P. Campion, B. L. Gallagher, and A. W. Rushforth, “Non-volatile voltage control of magnetization and magnetic domain walls in magnetostrictive epitaxial thin films,” *Applied Physics Letters*, vol. 101, no. 7, 08 2012.

[38] A. E. Clark, K. B. Hathaway, M. Wun-Fogle, J. B. Restorff, T. A. Lograsso, V. M. Keppens, G. Petculescu, and R. A. Taylor, “Extraordinary magnetoelasticity and lattice softening in bcc Fe-Ga alloys,” *Journal of Applied Physics*, vol. 93, no. 10, pp. 8621–8623, 05 2003.

[39] H. Cao, P. M. Gehring, C. P. Devreugd, J. A. Rodriguez-Rivera, J. Li, and D. Viehland, “Role of nanoscale precipitates on the enhanced magnetostriction of heat-treated galfenol ($Fe_{1-x}Ga_x$) alloys,” *Phys. Rev. Lett.*, vol. 102, Mar 2009.

[40] Y. Zhang and R. Wu, “Mechanism of large magnetostriction of galfenol,” *IEEE Transactions on Magnetics*, vol. 47, no. 10, pp. 4044–4049, 2011.

[41] H. Adachi, K. Uchida, E. Saitoh, and S. Maekawa, “Theory of the spin Seebeck effect,” *Reports on Progress in Physics*, vol. 76, no. 3, feb 2013.

[42] T. Kikkawa, K. Shen, B. Flebus, R. A. Duine, K. Uchida, Z. Qiu, G. E. W. Bauer, and E. Saitoh, “Magnon polarons in the spin Seebeck effect,” *Phys. Rev. Lett.*, vol. 117, Nov 2016.

[43] K. Uchida, R. Ramos, and E. Saitoh, “Spin Seebeck effect,” in *Spin Current*. Oxford University Press, 09 2017, pp. 322–348.

[44] R. Ramos, T. Hioki, Y. Hashimoto, T. Kikkawa, P. Frey, A. J. E. Kreil, V. I. Vasyuchka, A. A. Serga, B. Hillebrands, and E. Saitoh, “Room temperature and low-field resonant enhancement of spin Seebeck effect in partially compensated magnets,” *Nature Communications*, vol. 10, no. 1, nov 2019.

[45] W. Xing, Y. Ma, Y. Yao, R. Cai, Y. Ji, R. Xiong, K. Shen, and W. Han, “Facet-dependent magnon-polarons in epitaxial ferrimagnetic Fe_3O_4 thin films,” *Phys. Rev. B*, vol. 102, Nov 2020.

[46] S. Blundell, *Magnetism in condensed matter*, ser. Oxford master series in condensed matter physics. Oxford: Oxford University Press, 2001.

[47] R. O’Handley, *Modern Magnetic Materials: Principles and Applications*. Wiley, 1999.

[48] B. Cullity and C. Graham, *Introduction to Magnetic Materials*. Wiley, 2011.

[49] E. V. Gomonaj and V. M. Loktev, “On the theory of equilibrium magnetoelastic domain structure in easy-plane antiferromagnet,” *Low Temperature Physics*, vol. 25, no. 7, pp. 520–526, 07 1999.

[50] T. McGuire and R. Potter, “Anisotropic magnetoresistance in ferromagnetic 3d alloys,” *IEEE Transactions on Magnetics*, vol. 11, no. 4, pp. 1018–1038, 1975.

[51] W. Döring, “Die Abhängigkeit des Widerstandes von Nickelkristallen von der Richtung der spontanen Magnetisierung,” *Annalen der Physik*, vol. 424, no. 3, pp. 259–276, 1938.

[52] A. W. Rushforth, K. Výborný, C. S. King, K. W. Edmonds, R. P. Campion, C. T. Foxon, J. Wunderlich, A. C. Irvine, P. Vašek, V. Novák, K. Olejník, J. Sinova, T. Jungwirth, and B. L. Gallagher, “Anisotropic magnetoresistance components in (Ga,Mn)As,” *Phys. Rev. Lett.*, vol. 99, Oct 2007.

[53] A. Rushforth, K. Výborný, C. King, K. Edmonds, R. Campion, C. Foxon, J. Wunderlich, A. Irvine, V. Novák, K. Olejník, A. Kovalev, J. Sinova, T. Jungwirth, and B. Gallagher, “The origin and control of the sources of AMR in (Ga,Mn)As devices,” *Journal of Magnetism and Magnetic Materials*, vol. 321, no. 8, pp. 1001–1008, 2009, current Perspectives: Spintronics.

[54] J. M. D. Coey, *Magnetism and Magnetic Materials*. Cambridge University Press, 2010.

[55] C. Goldberg and R. E. Davis, “New galvanomagnetic effect,” *Phys. Rev.*, vol. 94, pp. 1121–1125, Jun 1954.

[56] L. Ejsing, M. F. Hansen, A. K. Menon, H. A. Ferreira, D. L. Graham, and P. P. Freitas, “Planar Hall effect sensor for magnetic micro- and nanobead detection,” *Applied Physics Letters*, vol. 84, no. 23, pp. 4729–4731, 05 2004.

[57] L. Landau and E. Lifshitz, “On the theory of the dispersion of magnetic permeability in ferromagnetic bodies - reprinted from physikalische zeitschrift der sowjetunion 8, part 2, 153, 1935.” in *Perspectives in Theoretical Physics*, L. Pitaevski, Ed. Amsterdam: Pergamon, 1992, pp. 51–65.

[58] T. Gilbert, “A phenomenological theory of damping in ferromagnetic materials,” *IEEE Transactions on Magnetics*, vol. 40, no. 6, pp. 3443–3449, 2004.

[59] J. Sinova, D. Culcer, Q. Niu, N. A. Sinitsyn, T. Jungwirth, and A. H. MacDonald, “Universal intrinsic spin Hall effect,” *Phys. Rev. Lett.*, vol. 92, Mar 2004.

[60] N. Nagaosa, J. Sinova, S. Onoda, A. H. MacDonald, and N. P. Ong, “Anomalous Hall effect,” *Rev. Mod. Phys.*, vol. 82, pp. 1539–1592, May 2010.

[61] M. Dyakonov and V. Perel, “Current-induced spin orientation of electrons in semiconductors,” *Physics Letters A*, vol. 35, no. 6, pp. 459–460, 1971.

[62] J. E. Hirsch, “Spin Hall effect,” *Phys. Rev. Lett.*, vol. 83, pp. 1834–1837, Aug 1999.

[63] J. Sinova, S. O. Valenzuela, J. Wunderlich, C. H. Back, and T. Jungwirth, “Spin Hall effects,” *Rev. Mod. Phys.*, vol. 87, pp. 1213–1260, Oct 2015.

[64] Y. K. Kato, R. C. Myers, A. C. Gossard, and D. D. Awschalom, “Observation of the spin Hall effect in semiconductors,” *Science*, vol. 306, no. 5703, pp. 1910–1913, 2004.

[65] T. Moriyama, K. Oda, T. Ohkochi, M. Kimata, and T. Ono, “Spin torque control of antiferromagnetic moments in NiO,” *Scientific Reports*, vol. 8, 2017.

[66] A. v. Ettingshausen and W. Nernst, “Ueber das Auftreten electromotorischer Kräfte in Metallplatten, welche von einem Wärmestrome durchflossen werden und sich im magnetischen Felde befinden,” *Annalen der Physik*, vol. 265, no. 10, pp. 343–347, 1886.

[67] S. Y. Huang, X. Fan, D. Qu, Y. P. Chen, W. G. Wang, J. Wu, T. Y. Chen, J. Q. Xiao, and C. L. Chien, “Transport magnetic proximity effects in platinum,” *Phys. Rev. Lett.*, vol. 109, Sep 2012.

[68] K. Uchida, “Transport phenomena in spin caloritronics,” *Proceedings of the Japan Academy, Series B*, vol. 97, no. 2, pp. 69–88, 2021.

[69] V. D. Ky, “Planar Hall and Nernst effect in ferromagnetic metals,” *Physica Status Solidi B-basic Solid State Physics*, vol. 22, pp. 729–736, 1967.

[70] M. Schmid, S. Srichandan, D. Meier, T. Kuschel, J.-M. Schmalhorst, M. Vogel, G. Reiss, C. Strunk, and C. H. Back, “Transverse spin Seebeck effect versus anomalous and planar Nernst effects in permalloy thin films,” *Phys. Rev. Lett.*, vol. 111, Oct 2013.

[71] R. Winkler, *Spin-orbit Coupling Effects in Two-Dimensional Electron and Hole Systems*, ser. Springer Tracts in Modern Physics. Berlin: Springer, 2003.

[72] A. Manchon, H. Koo, J. Nitta, S. Frolov, and R. Duine, “New perspectives for Rashba spin-orbit coupling,” *Nature materials*, vol. 14, 07 2015.

[73] G. Bihlmayer, O. Rader, and R. Winkler, “Focus on the Rashba effect,” *New Journal of Physics*, vol. 17, no. 5, may 2015.

[74] Y. A. Bychkov and E. I. Rashba, "Oscillatory effects and the magnetic susceptibility of carriers in inversion layers," *Journal of Physics C: Solid State Physics*, vol. 17, no. 33, nov 1984.

[75] H. Zhang, Z. Ma, and J. Liu, "Equilibrium spin current in graphene with Rashba spin-orbit coupling," *Scientific Reports*, vol. 4, 2014.

[76] G. Dresselhaus, "Spin-orbit coupling effects in zinc blende structures," *Phys. Rev.*, vol. 100, pp. 580–586, Oct 1955.

[77] A. Manchon, J. Železný, I. M. Miron, T. Jungwirth, J. Sinova, A. Thiaville, K. Garello, and P. Gambardella, "Current-induced spin-orbit torques in ferromagnetic and antiferromagnetic systems," *Rev. Mod. Phys.*, vol. 91, Sep 2019.

[78] E. L. Ivchenko and G. E. Pikus, "New photogalvanic effect in gyrotropic crystals," *Soviet Journal of Experimental and Theoretical Physics Letters*, vol. 27, p. 604, Jun. 1978.

[79] V. Edelstein, "Spin polarization of conduction electrons induced by electric current in two-dimensional asymmetric electron systems," *Solid State Communications*, vol. 73, no. 3, pp. 233–235, 1990.

[80] A. Manchon and S. Zhang, "Theory of nonequilibrium intrinsic spin torque in a single nanomagnet," *Phys. Rev. B*, vol. 78, Dec 2008.

[81] M. Henini, *Molecular Beam Epitaxy: From Research to Mass Production*. Elsevier Science, 2012.

[82] M. Herman and H. Sitter, *Molecular Beam Epitaxy: Fundamentals and Current Status*, ser. Springer Series in Materials Science. Springer Berlin Heidelberg, 1996.

[83] W. Braun, *Applied RHEED: reflection high-energy electron diffraction during crystal growth*, ser. Springer tracts in modern physics ; v. 154. Berlin: Springer Science, 1999.

[84] J. L. Hall, "Growth and structural characterisation of novel III–V semiconductor materials," Ph.D. dissertation, University of Nottingham, July 2010.

[85] J. A. Venables, *Introduction to Surface and Thin Film Processes*. Cambridge University Press, 2000.

[86] F. Frank and J. van der Merwe, "One-dimensional dislocations. I. static theory," *Proceedings of the Royal Society of London A: Mathematical, Physical and Engineering Sciences*, vol. 198, no. 1053, pp. 205–216, 1949.

[87] I. Markov, *Crystal growth for beginners: fundamentals of nucleation, crystal growth and epitaxy*, 2nd ed. Singapore; River Edge, N.J.: World Scientific, 2003.

[88] P. Larsen and P. Dobson., Eds., *Reflection high-energy electron diffraction and reflection electron imaging of surfaces*, ser. NATO Science Series B:. New York: Plenum Press, 1988, vol. 188.

[89] M. Volmer and A. Weber, “Nucleus formation in supersaturated systems,” *Z. Phys. Chem.*, vol. 119, pp. 277–301, 1926.

[90] I. N. Stranski and L. Krastanow, “Zur theorie der orientierten ausscheidung von ionenkristallen aufeinander,” *Monatshefte für Chemie und verwandte Teile anderer Wissenschaften*, vol. 71, pp. 351–364, 1937.

[91] M. Henzler, “Growth modes in homo- and heteroepitaxial growth,” *Progress in Surface Science*, vol. 42, no. 1, pp. 297–316, 1993.

[92] L. Daweritz and R. Hey, “Reconstruction and defect structure of vicinal GaAs(001) and Al$_x$Ga$_{1x}$As(001) surfaces during MBE growth,” *Surface Science*, vol. 236, no. 1, pp. 15–22, 1990.

[93] Y. Horikoshi, H. Yamaguchi, F. Briones, and M. Kawashima, “Growth process of III–V compound semiconductors by migration-enhanced epitaxy,” *Journal of Crystal Growth*, vol. 105, no. 1, pp. 326–338, 1990.

[94] M. D. Pashley and K. W. Haberern, *The Role of Surface Reconstructions in MBE Growth of GaAs*. Dordrecht: Springer Netherlands, 1993, pp. 63–73.

[95] Y. P. Varshni, “Temperature dependence of the energy gap in semiconductors,” *Physica*, vol. 34, no. 1, pp. 149–154, jan 1967.

[96] S. Rossnagel, *Sputtering and Sputter Deposition*. William Andrew, 12 2001, pp. 319–348.

[97] J. S. Blakemore, *Solid State Physics*, ser. Saunders physics books. W. B. Saunders Co., 1969.

[98] J. Daillant and A. Gibaud, *X-Ray and Neutron Reflectivity: Principles and Applications*, ser. Lecture Notes in Physics Monographs. Springer Berlin Heidelberg, 1999.

[99] T. Chatterji, Ed., *Neutron scattering from magnetic materials*, 1st ed. Elsevier, 2006.

[100] D. Duxbury, D. Khalyavin, P. Manuel, D. Raspino, N. Rhodes, E. Schooneveld, and E. Spill, “Operational performance characteristics of the WISH detector array on the ISIS spallation neutron source,” *Journal of Instrumentation*, vol. 9, no. 12, dec 2014.

[101] D. Williams and C. Carter, *Transmission Electron Microscopy: A Textbook for Materials Science*, ser. Cambridge library collection. Springer, 06 2009.

[102] M. T. Otten, “High-angle annular dark-field imaging on a TEM/STEM system.” *Journal of electron microscopy technique*, vol. 17, pp. 221–30, 1991.

[103] J. I. Goldstein, D. E. Newbury, J. R. Michael, N. W. Ritchie, J. H. Scott, and D. C. Joy, *Scanning Electron Microscopy and X-ray Microanalysis*, J. I. Goldstein, Ed. New York: Springer, 01 2003, vol. XIX.

[104] J. Stöhr, H. Padmore, S. Anders, T. Stammler, and M. Scheinfein, “Principles of X-Ray Magnetic Dichroism Spectromicroscopy,” *Surface Review and Letters*, vol. 5, no. 6, pp. 1297–1308, Jan. 1998.

[105] O. Amin, S. Poole, S. Reimers, L. Barton, F. Maccherozzi, S. Dhesi, V. Novák, F. Krizek, J. Chauhan, R. Campion, A. Rushforth, T. Jungwirth, O. A. Tretiakov, K. Edmonds, and P. Wadley, “Antiferromagnetic half-skyrmions electrically generated and controlled at room temperature,” 07 2022, accepted.

[106] K. Morrison, A. Caruana, and C. Cox, “Towards a standard spin Seebeck measurement,” 05 2017, Preprint. [Online]. Available: https://www.researchgate.net/publication/316779869_Towards_a_standard_spin_Seebeck_measurement

[107] K. C. Sloneker, D. N. Polsky, A. Zhagrov, and V. Lutsenko, “High-Resolution Differential Thermocouple Measurements Using an Improved Noise Cancellation and Magnetic Amplification Technique,” in *Temperature: Its Measurement and Control in Science and Industry*, ser. American Institute of Physics Conference Series, D. C. Ripple, Ed., vol. 684, Sep. 2003, pp. 997–1002.

[108] A. Sola, P. Bougiatioti, M. Kuepferling, D. Carsten, G. Reiss, M. Pasquale, T. Kuschel, and V. Basso, “Longitudinal spin Seebeck coefficient: heat flux vs. temperature difference method,” *Scientific Reports*, vol. 7, 04 2017.

[109] P. Wadley, V. Novák, R. Campion, C. Rinaldi, X. Martí, H. Reichlová, J. Zelezný, J. Gazquez, M. Roldan, M. Varela, D. Khalyavin, S. Langridge, D. Kriegner, F. Máca, J. Mašek, R. Bertacco, V. Holý, A. Rushforth, K. Edmonds, B. Gallagher, C. Foxon, J. Wunderlich, and T. Jungwirth, “Tetragonal phase of epitaxial room-temperature antiferromagnet CuMnAs,” *Nature communications*, vol. 4, 2013.

[110] Y. Cao, K. Xu, Z. Li, Y. Zhang, X. He, Y. Kang, W. Sun, T. Gao, Z. Qian, C. Liu, M. Ye, and C. Jing, “Interplay between spin reorientation and magnetoelastic transitions, and anisotropic magnetostriction in the $\mathrm{Mn}_{1.95}\mathrm{Cr}_{0.05}\mathrm{Sb}$ single crystal,” *Journal of Magnetism and Magnetic Materials*, vol. 487, 2019.

[111] L. W. Shacklette, “Specific heat and resistivity of iron near its Curie point,” *Phys. Rev. B*, vol. 9, pp. 3789–3792, May 1974.

[112] P. Wadley, V. A. Hills, M. R. Shahedkhah, K. W. Edmonds, R. P. Campion, V. Novák, B. Ouladdiaf, D. Khalyavin, S. Langridge, V. Saidl, P. Nemec, A. W. Rushforth, B. L. Gallagher, S. S. Dhesi, F. Maccherozzi, J. Železný, and T. Jungwirth, “Antiferromagnetic structure in tetragonal CuMnAs thin films,” *Scientific Reports*, vol. 5, 2015.

[113] M. Campostrini, A. Pelissetto, P. Rossi, and E. Vicari, “25th-order high-temperature expansion results for three-dimensional Ising-like systems on the simple-cubic lattice,” *Phys. Rev. E*, vol. 65, Jun 2002.

[114] M. Wang, R. A. Marshall, K. W. Edmonds, A. W. Rushforth, R. P. Campion, and B. L. Gallagher, “Determining Curie temperatures in dilute ferromagnetic semiconductors: High Curie temperature (Ga,Mn)As,” *Applied Physics Letters*, vol. 104, no. 13, 04 2014.

[115] S. Y. Bodnar, L. Šmejkal, I. Turek, T. Jungwirth, O. Gomonay, J. Sinova, A. A. Sapozhnik, H.-J. Elmers, M. Kläui, and M. Jourdan, “Writing and reading antiferromagnetic Mn_2Au by Néel spin-orbit torques and large anisotropic magnetoresistance,” *Nature Communications*, vol. 9, no. 1, jan 2018.

[116] K. Olejník, T. Seifert, Z. Kašpar, V. Novák, P. Wadley, R. P. Campion, M. Baumgartner, P. Gambardella, P. Němec, J. Wunderlich, J. Sinova, P. Kužel, M. Müller, T. Kampfrath, and T. Jungwirth, “Terahertz electrical writing speed in an antiferromagnetic memory,” *Science Advances*, vol. 4, 2018.

[117] P. Wadley, S. Reimers, M. J. Grzybowski, C. Andrews, M. Wang, J. Chauhan, B. L. Gallagher, R. P. Campion, K. W. Edmonds, S. S. Dhesi, F. Maccherozzi, V. Novák, J. Wunderlich, and T. Jungwirth, “Current polarity-dependent manipulation of antiferromagnetic domains,” *Nature Nanotechnology*, vol. 13, pp. 362–365, 2018.

[118] J. Godinho, H. Reichlova, D. Kriegner, V. Novak, K. Olejnik, Z. Kaspar, Z. Soban, P. Wadley, R. P. Campion, R. M. Otxoa, P. E. Roy, J. Železny, T. Jungwirth, and J. Wunderlich, “Electrically induced and detected Néel vector reversal in a collinear antiferromagnet,” *Nature Communications*, vol. 9, 2018.

[119] T. Matalla-Wagner, J.-M. Schmalhorst, G. Reiss, N. Tamura, and M. Meinert, “Resistive contribution in electrical-switching experiments with antiferromagnets,” *Phys. Rev. Res.*, vol. 2, Jul 2020.

[120] Z. Kaspar, M. Surynek, J. Zubac, F. Krizek, V. Novak, R. P. Champion, M. S. Wörnle, P. Gambardella, X. Marti, P. Němec, K. W. Edmonds, S. Reimers, O. J. Amin, F. Maccherozzi, S. S. Dhesi, P. Wadley, J. Wunderlich, K. Olejnik, and T. Jungwirth, “Quenching of an antiferromagnet into high resistivity states using electrical or ultrashort optical pulses,” *Nature Electronics*, vol. 4, no. 1, pp. 30 – 37, 2021-01.

[121] O. Amin, “Electrical control of antiferromagnetic CuMnAs,” Ph.D. dissertation, University of Nottingham, 2022.

[122] J. C. Phillips, “Stretched exponential relaxation in molecular and electronic glasses,” *Reports on Progress in Physics*, vol. 59, no. 9, sep 1996.

[123] O. J. Amin, K. W. Edmonds, and P. Wadley, "Electrical control of antiferromagnets for the next generation of computing technology," *Applied Physics Letters*, vol. 117, no. 1, 07 2020.

[124] S. Roy, "The magnetic properties of epitaxial $Fe_{100-x}Ga_x$ thin films: the role of gallium composition and film thickness," Ph.D. dissertation, University of Nottingham, November 2020.

[125] W. P. Davey, "Precision measurements of the lattice constants of twelve common metals," *Phys. Rev.*, vol. 25, pp. 753–761, Jun 1925.

[126] Z. Nie, Z. Wang, Y. Liang, D. Cong, G. Li, C. Zhu, C. Tan, X. Yu, Y. Ren, and Y. Wang, "Structural investigations of Fe-Ga alloys by high-energy X-ray diffraction," *Journal of Alloys and Compounds*, vol. 763, pp. 223–227, 2018.

[127] R. Iguchi, K. Uchida, S. Daimon, and E. Saitoh, "Concomitant enhancement of the longitudinal spin Seebeck effect and the thermal conductivity in a Pt/YIG/Pt system at low temperatures," *Phys. Rev. B*, vol. 95, May 2017.

[128] T. C. Chuang, P. L. Su, P. H. Wu, and S. Y. Huang, "Enhancement of the anomalous Nernst effect in ferromagnetic thin films," *Phys. Rev. B*, vol. 96, Nov 2017.

[129] D. Rowe, *CRC Handbook of Thermoelectrics*. CRC Press, 1995.

[130] G. Gould and L. Moraga, "A method for fitting the Fuchs-Sondheimer theory to resistivity-thickness measurements for all film thicknesses," *Thin Solid Films*, vol. 10, pp. 327–330, 1972.